Direct numerical simulation of droplet-laden isotropic turbulence

Michael S. Dodd

A dissertation
submitted in partial fulfillment of the
requirements for the degree of

Doctor of Philosophy

University of Washington

2017

Reading Committee:

Antonino Ferrante, Chair

James C. Hermanson

James J. Riley

Program Authorized to Offer Degree:
Aeronautics & Astronautics

University of Washington

Abstract

Direct numerical simulation of droplet-laden isotropic turbulence

Michael S. Dodd

Chair of the Supervisory Committee:
Associate Professor Antonino Ferrante
Aeronautics & Astronautics

Interaction of liquid droplets with turbulence is important in numerous applications ranging from rain formation to oil spills to spray combustion. The physical mechanisms of droplet-turbulence interaction are largely unknown, especially when compared to that of solid particles. Compared to solid particles, droplets can deform, break up, coalesce and have internal fluid circulation. The main goal of this work is to investigate using direct numerical simulation (DNS) the physical mechanisms of droplet-turbulence interaction, both for non-evaporating and evaporating droplets.

To achieve this objective, we develop and couple a new pressure-correction method with the volume-of-fluid (VoF) method for simulating incompressible two-fluid flows. The method's main advantage is that the variable coefficient Poisson equation that arises in solving the incompressible Navier-Stokes equations for two-fluid flows is reduced to a constant coefficient equation. This equation can then be solved directly using, e.g., the FFT-based parallel Poisson solver. For a 1024^3 mesh, our new pressure-correction method using a fast Poisson solver is ten to forty times faster than the standard pressure-correction method using multigrid.

Using the coupled pressure-correction and VoF method, we perform direct numerical simulations (DNS) of 3130 finite-size, non-evaporating droplets of diameter approximately equal to the Taylor lengthscale and with 5 % droplet volume fraction in decaying isotropic turbulence at initial Taylor-scale Reynolds number $\mathrm{Re}_\lambda = 83$. In the droplet-laden cases, we vary one of the following three parameters: the droplet Weber number based on the r.m.s. velocity of turbulence ($0.1 \leq We_{\mathrm{rms}} \leq 5$), the droplet- to carrier-fluid density ratio ($1 \leq \rho_d/\rho_c \leq 100$) or the droplet- to carrier-fluid viscosity ratio ($1 \leq \mu_d/\mu_c \leq 100$). We derive the turbulence kinetic energy (TKE) equations for the two-fluid, carrier-fluid and droplet-fluid flow. These equations allow us to explain the pathways for TKE exchange between the carrier turbulent flow and the flow inside the droplet. We also explain the role of the interfacial surface energy in the two-fluid TKE equation through work performed by surface tension. Furthermore, we derive the relationship between the power of surface tension and the rate of change of total droplet surface area. This link allows us to explain how droplet deformation, breakup and coalescence play roles in the temporal evolution of TKE.

We then extend the code for non-evaporating droplets and develop a combined VoF method and low-Mach-number approach to simulate evaporating and condensing droplets. The two main novelties of the method are: (i) the VOF algorithm captures the motion of the liquid gas interface in the presence of mass transfer due to evaporation and condensation without requiring a projection step for the liquid velocity, and (ii) the low-Mach-number approach allows for local volume changes caused by phase change while the total volume of the liquid-gas system is constant. The method is verified against an analytical solution for a Stefan flow problem, and the D^2 law is verified for a single droplet in quiescent gas.

Finally, we perform DNS of an evaporating liquid droplet in forced isotropic turbulence. We show that the method accurately captures the temperature and vapor fields in the turbulent regime, and that the local evaporation rate can vary along the droplet surface depending on the structure of the surrounding vapor cloud. We also report the time evolution of the mean Sherwood number, which indicates that turbulence enhances the vaporization rate of liquid droplets.

TABLE OF CONTENTS

Page

LIST OF FIGURES

NOMENCLATURE

Upper-case Roman

A	total droplet surface area	[m^2]
C	VoF function (volume fraction)	
D	droplet diameter	[m]
$\hat{D}$	equivalent spherical diameter of droplet	[m]
D_0	initial droplet diameter	[m]
D_{gv}	binary mass diffusion coefficient between the gas and vapor species [m^2 s^{-1}]	
$\mathbf{F}_\nu$	viscous force vector	[N]
$\mathbf{F}_p$	pressure force vector	[N]
Fr	Froude number ($= U^2/(gL)$) and non-dimensional gravity	
H	VOF height function or Heaviside function	
I	identity tensor	
L	edge length of cubic computational domain	[m]
La	Laplace number ($= \sigma\rho L/\mu^2$)	
Le	Lewis number ($= \alpha/D_{gv}$=Sc/Pr)	
M	molar mass	[kg mol^{-1}]
$\dot{M}$	rate of change of droplet mass	[kg s^{-1}]
Ma	Mach number ($= V/c$)	
N_d	number of droplets	
$N_{gp/d}$	number of grid point per diameter	
Oh	Ohnesorge number ($= \mu/\sqrt{\rho\sigma L}$)	
Pr	Prandtl number ($= \nu/\alpha$)	
R_u	universal gas constant	[J mol^{-1} K^{-1}]
Re	Reynolds number ($= \rho U L/\mu$) and inverse of non-dimensional kinematic viscosity	
Re$_\ell$	Reynolds number based on the integral lengthscale	
Re$_\lambda$	Reynolds number based on the Taylor lengthscale	
S	strain-rate tensor	[s^{-1}]
Sc	Schmidt number ($=\nu/D_{gv}$)	
Sh	Sherwood number ($=h_{\text{mass}}L/D_{gv}$)	
St	Stefan number ($=c_pT/\Delta h_v$)	

$\mathrm{Ste_c}$	pseudo Stefan number $(=R_u T/(\Delta h_v M_v))$	
T	temperature	[K]
T	viscous stress tensor	
T_{boil}	normal boiling point of liquid phase	[K]
T_{dvm}	period of the fundamental droplet vibration mode	[s]
T_ν	rate of energy transfer due to work by viscous stresses	[J $\mathrm{s^{-1}}$]
T_p	rate of energy transfer due to pressure work	[J $\mathrm{s^{-1}}$]
$\mathbf{V}_d$	droplet velocity vector	[m $\mathrm{s^{-1}}$]
$\mathcal{V}$	volume of computational domain	[m $\mathrm{s^{-1}}$]
$\mathcal{V}_c$	volume of carrier fluid	[$\mathrm{m^3}$]
$\mathcal{V}_d$	volume of droplet fluid	[$\mathrm{m^3}$]
We	Weber number $(=\rho U^2 L/\sigma)$	
$\mathrm{We_{rms}}$	Weber number based on r.m.s. velocity of turbulence and droplet diameter $(=\rho U_{\mathrm{rms}}^2 D/\sigma)$	
Y_v	vapor mass fraction	

Lower-case Roman

c_p	specific heat at constant pressure	[J $\mathrm{kg^{-1}}$ $\mathrm{K^{-1}}$]
c_p	specific heat at constant volume	[J $\mathrm{kg^{-1}}$ $\mathrm{K^{-1}}$]
e	specific internal energy	[J $\mathrm{kg^{-1}}$]
$\mathbf{f}_\sigma$	force due to surface tension per unit volume	[N $\mathrm{m^{-3}}$]
h	grid spacing	[m]
h_{mass}	convective mass transfer coefficient	[m $\mathrm{s^{-1}}$]
k	thermal conductivity	[W $\mathrm{m^{-1}}$ $\mathrm{K^{-1}}$]
ℓ	integral lengthscale	[m]
$\dot{m}''$	mass flux	[kg $\mathrm{m^{-2}}$ $\mathrm{s^{-1}}$]
$\dot{m}$	volumetric mass flux	[kg $\mathrm{m^{-3}}$ $\mathrm{s^{-1}}$]
$\mathbf{n}$	interface normal vector directed towards the droplet fluid	
p	pressure (dynamic)	[N $\mathrm{m^{-2}}$]
p_0	thermodynamic pressure	[N $\mathrm{m^{-2}}$]
t	time	[s]
$\mathbf{u}$	mass-average velocity vector, $=(u,v,w)$	[m/s]
u	x-component of velocity	[m/s]
v	y-component of velocity	[m/s]
w	z-component of velocity	[m/s]
$\mathbf{x}$	position vector	
x	Cartesian coordinate	
y	Cartesian coordinate	

z	Cartesian coordinate	

Upper-case Greek

Δh_v	enthalpy of vaporization	[J kg^{-1}]
Δt	time step	[s]
Δx	grid spacing in the x-direction	[m]
Ψ_σ	power of the surface tension force	[J s^{-1}]

Lower-case Greek

α	thermal diffusivity	[m^2 s^{-1}]
δ	Dirac delta function	[m^{-1}]
δ_{ij}	Kronecker delta	
ε	rate of dissipation of turbulent kinetic energy	[J s^{-1}]
η	Kolmogorov lengthscale	[m]
θ_ν	angle between droplet velocity $\mathbf{V}_d$ and viscous force $\mathbf{F}_\nu$	
θ_p	angle between droplet velocity $\mathbf{V}_d$ and pressure force $\mathbf{F}_p$	
γ	ratio between the carrier- and droplet-fluid viscosity ($= \mu_c/\mu_d$) or ratio of specific heats ($= c_p/c_v$)	
κ	wave number or interface curvature	[m^{-1}]
λ	Taylor lengthscale	[m]
μ	dynamic viscosity	[kg m^{-1} s^{-1}]
ν	kinematic viscosity	[m^2 s^{-1}]
ω_d^2	enstrophy inside droplet	[s^{-2}]
ϕ_v	droplet volume fraction ($\mathcal{V}_d/\mathcal{V}$)	
ρ	density	[kg m^{-3}]
σ	surface tension coefficient	[N m^{-1}]
$\boldsymbol{\tau}$	stress tensor	[N m^{-2}]
τ_d	droplet response time	[s]
τ_ℓ	integral timescale	[s]
τ_η	Kolmogorov timescale	[s]
τ_λ	timescale based on the Taylor lengthscale	[s]
φ	density ratio between droplet fluid and carrier fluid (ρ_d/ρ_c)	

Superscripts

$\tilde{Q}$	dimensional quantity	

$\overline{Q}$	ensemble-averaged quantity

Subscripts

Q_a	ambient gas quantity (e.g. air)
Q_c	carrier-fluid quantity
Q_d	droplet-fluid quantity
Q_g	gas-phase quantity (e.g. air and water vapor mixture)
Q_l	liquid-phase quantity
Q_{ref}	reference quantity
Q_{rms}	root-mean square quantity
Q_{sat}	quantity at saturation conditions
Q_v	vapor-phase quantity (e.g. water vapor mixture)
Q_Σ	interfacial quantity

Symbols

∇	gradient operator
∇_s	surface gradient operator $(\nabla - \mathbf{n}(\mathbf{n} \cdot \nabla))$
$\nabla \cdot$	divergence operator
∇^2	Laplacian operator
$\times$	vector cross product
$\cdot$	vector dot product

Abbreviations

DNS	direct numerical simulation
FFT	fast Fourier transform
LES	large-eddy simulation
MPI	message passing interface
p.d.f.	probability density function
r.m.s.	root-mean square
SGS	subgrid scale
TKE	turbulent kinetic energy
VOF	volume of fluid

ACKNOWLEDGMENTS

The research presented in this work would not have been possible without the support and guidance of many people. I would like to begin by thanking my advisor, Prof. Antonino Ferrante. His advice and high standards have played an invaluable role in my success.

I would also like to thank the members of my supervisory committee for their time and suggestions along the way. In particular, I would like to thank Prof. Jim Riley and Prof. Alberto Aliseda who expressed interest in my work early on. Thank you for your support and guidance over the years. Thank you to Prof. Jim Hermanson for providing helpful comments on a draft of this dissertation. I am also grateful for conversations with Dr. Philippe Spalart on a topic unrelated to this work. His perspectives and knowledge of turbulence have undoubtedly influenced and improved the present work.

I would also like to acknowledge the many friends and colleagues I have met during my time at the University of Washington. I have learned so much from you, and I will always value the time we spent together. Special thanks to the undergraduate students that worked in the Computational Fluid Mechanics Group. I am grateful for the trust you placed in me and for the joy and inspiration you provided.

I thank my family for their support and for always believing in me. I can not adequately express how much that has meant to me at times. Finally, I would like to thank my fiancée, Kara, who has been with me from the beginning of this journey. She has read nearly every paper and viewed nearly every slide. More often than not, her feedback was among the most valuable I received. Thank you for your love and support.

This work was supported by the National Science Foundation (NSF) CAREER Award, Grant No. ACI-1054591. M.S.D. was also partially supported by the Clairmont Egtvedt Fellowship and the Louis and Katherine Marsh Fellowship from the College of Engineering at the University of Washington (UW), Seattle. The numerical simulations were performed in part on Hyak, high-performance computer cluster at UW, and in part on the Extreme Science and Engineering Discovery Environment (XSEDE, [1]) under XRAC Grant No. TG-CTS100024. XSEDE is supported by National Science Foundation Grant No. ACI-1053575. We specifically acknowledge the Texas Advanced Computing Center (TACC) at The University of Texas at Austin (http://www.tacc.utexas.edu) and the University of Tennessee and Oak Ridge National Laboratory's Joint Institute for Computational Sciences (http://www.jics.utk.edu) for providing HPC resources that have contributed to the research results reported within this paper. Also, we specifically acknowledge the assistance of the XSEDE Extended Collaborative Support Service (ECSS, [2]) team members, Jay Alameda and Darren Adams, of the National Center for Supercomputing Applications (NCSA) at the University of Illinois at Urbana-Champaign. The author also acknowledges support from NSF REU Grant No. ACI-1528430.

Chapter 1

INTRODUCTION

1.1 Background and Motivation

The interaction of dispersed droplets and turbulence is important in many natural, biological, and industrial processes, e.g. rain formation [3], sneezing and coughing [4], liquid-liquid emulsion [5], spray cooling [6] and spray atomization in combustors [7, 8]. In these flows the droplet volume fraction is typically of the order of 1–10 % such that the turbulence is altered by droplet feedback on the surrounding fluid and by droplet-droplet interactions, placing the flow in the four-way coupling regime [9]. Oftentimes, evaporation and condensation play an important role in the process. Consider, for example, the formation of rain in warm clouds. Here, droplets grow from diameters on the order of microns to millimeters in about one hour. Turbulence plays a critical role in droplet growth by producing fluctuating supersaturations of water vapor necessary for condensational growth and by creating collisions and preferential concentrations leading to growth by coalescence. This is just one example in which momentum, heat, and mass transfer between droplets and the surrounding turbulent flow combine to form a complex multiphysics problem.

Evaporating droplets include all the physical effects experienced by solid particles and additional complexities. In addition to the drag force, evaporating droplets participate in mass and thermal energy transfer with the carrier phase. The evaporation rate, and therefore droplet diameter, is closely tied to the local flow conditions, hence the droplet lifetime can vary greatly in time and space. Thus evaporating droplets create polydisperse flows which result in preferential concentrations and flow modulations that are expected to be markedly different than for solid particles.

Direct numerical simulation (DNS) has proven to be an invaluable tool in understanding turbulence modulation in two-phase flows [10], because it resolves the full range of temporal and spatial scales present in the flow at the continuum level. Spherical particles (or droplets) in isotropic turbulence can be broadly classified by their diameter D relative to the smallest turbulent lengthscale (the Kolmogorov scale, η) as sub-Kolmogorov size ($D \ll \eta$) or *finite-size* ($D > \eta$). For $D \ll \eta$, the extent to which solid particles modulate isotropic turbulence, for fixed volume fraction and mass loading, is fully characterized by the Stokes number $St = \tau_p/\tau_\eta$ [11, 12], where τ_p is the particle response time and τ_η is the Kolmogorov time scale. If $D > \eta$, St is no longer an appropriate indicator of turbulence modulation [13].

1.2 Challenges in simulating droplet-laden turbulent flows

There have been four main physical challenges identified in simulating droplet-laden turbulent flows [14]; they are: (i) resolving the smallest turbulent eddies (Kolmogorov scale), (ii) resolving the velocity gradients in the interfacial boundary layer (iii) resolving the flow between droplets and (iv) resolving the flow in the droplet interiors. In addition, we have identified three primary numerical challenges in simulating droplet-laden turbulent flows; they are: (i) developing a mass-conserving algorithm to track/capture the droplet volumes in space and time, (ii) developing a time integration scheme and spatial discretization that is stable for large density and viscosity ratios and (iii) accurately modeling the effects of surface tension. With the exception of resolving the thin (tens of nanometers) liquid film that develops during droplet coalescence and breakup, we have overcome the physical and numerical challenges by developing a mass conserving VoF scheme [15] and a two-fluid pressure-correction method [16]. This has enabled us to perform DNS of droplet-laden isotropic turbulence [17].

1.3 Objectives

The primary goals of the present work are to (i) advance the current computational methods for gas-liquid flows with phase change and (ii) improve the understanding of the interaction of evaporating droplets and turbulence. Specific aims are:

- Develop an efficient, accurate, robust, and scalable numerical method to perform DNS of non-evaporating droplets in turbulence. The method should accurately capture the motion of the droplet interface, account for surface tension, fully-resolve the flow inside and outside the droplets, and be accurate and stable at high density and viscosity ratios.

- Determine the effects of varying the following parameters on non-evaporating droplet-laden decaying isotropic turbulence: density ratio, viscosity ratio, and droplet Weber number.

- Extend the method for non-evaporating droplets to be able to simulate evaporating and condensing droplets. The method should full-resolve the process of momentum, heat, and mass transfer between the gas and liquid.

- Investigate the interaction of evaporating droplets and isotropic turbulence.

Chapter 2

MATHEMATICAL FORMULATION FOR NON-EVAPORATING DROPLETS

2.1 Governing equations

The non-dimensional governing equations for the incompressible flow of two immiscible fluids are

$$\nabla \cdot \mathbf{u} = 0, \tag{2.1a}$$

$$\frac{\partial \mathbf{u}}{\partial t} + \nabla \cdot (\mathbf{u}\mathbf{u}) = \frac{1}{\rho}\left[-\nabla p + \frac{1}{\mathrm{Re}}\nabla \cdot (2\mu \mathsf{S}) + \frac{1}{\mathrm{We}}\mathbf{f}_\sigma\right] + \frac{1}{\mathrm{Fr}}\mathbf{g} \tag{2.1b}$$

where $\mathbf{u} = \mathbf{u}(\mathbf{x}, t)$ is the fluid velocity, $p = p(\mathbf{x}, t)$ is the pressure, $\rho = \rho(\mathbf{x}, t)$ is the density, $\mu = \mu(\mathbf{x}, t)$ is the dynamic viscosity, $\mathsf{S} = \mathsf{S}(\mathbf{x}, t)$ is the strain-rate tensor ($\mathsf{S} = \frac{1}{2}[\nabla\mathbf{u} + (\nabla\mathbf{u})^T]$), $\mathbf{f}_\sigma$ is the force due to surface tension, and $\mathbf{g}$ is the gravitational acceleration vector of unit length. Re, We, and Fr are the Reynolds, Weber, and Froude numbers, respectively, which are defined as:

$$\mathrm{Re} = \frac{\tilde{U}\tilde{L}\tilde{\rho}_c}{\tilde{\mu}_c}, \qquad \mathrm{We} = \frac{\tilde{\rho}_c \tilde{U}^2 \tilde{L}}{\tilde{\sigma}}, \qquad \mathrm{Fr} = \frac{\tilde{U}^2}{\tilde{g}\tilde{L}}, \tag{2.2}$$

where $\tilde{U}$, $\tilde{L}$, $\tilde{\rho}_c$, $\tilde{\mu}_c$, $\tilde{\sigma}$, and $\tilde{g}$ denote, in order, the reference dimensional velocity, length, carrier-fluid density, carrier-fluid dynamic viscosity, surface tension coefficient, and gravitational acceleration used to non-dimensionalize the governing equations (2.1a) and (2.1b). The subscripts c and d indicate the carrier fluid and droplet fluid, respectively. We have chosen to non-dimensionalize the density and dynamic viscosity in (2.1b) by choosing the carrier fluid as the reference phase, i.e. $\rho_c = 1$ and $\mu_c = 1$. Also, we note that Re^{-1}, We^{-1}, and Fr^{-1} are equivalent to the non-dimensional kinematic viscosity ν, surface tension coefficient σ, and gravitational acceleration magnitude g respectively, and are used interchangeably

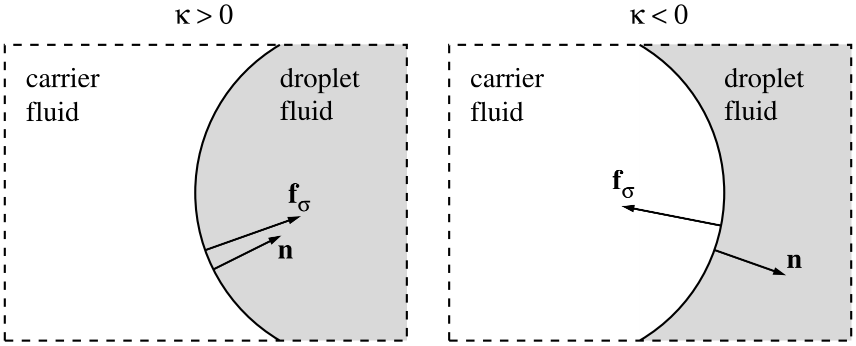

Figure 2.1: Schematic of the interface between two fluids which shows the surface tension force ($\mathbf{f}_\sigma$), interface normal ($\mathbf{n}$) and the sign convention of the curvature (κ).

throughout this work. $\mathbf{f}_\sigma = \mathbf{f}_\sigma(\mathbf{x}, t)$ is the force per unit volume due to surface tension,

$$\mathbf{f}_\sigma = \kappa\delta(\mathbf{x} - \mathbf{x}_s)\mathbf{n} \tag{2.3}$$

where $\kappa = \kappa(\mathbf{x}, t)$ is the curvature of the interface between the carrier fluid and the droplet, $\mathbf{n} = \mathbf{n}(\mathbf{x}, t)$ is the unit vector that is normal to the interface and directed towards the interior of the droplet and δ is the Dirac δ-function that is needed to impose the force only at the interface position $\mathbf{x}_s$. Figure 2.1 illustrates the direction of the interface normal $\mathbf{n}$ and the sign of the interface curvature κ. Throughout this work, all variables are dimensionless unless they are accented with $\sim$. The jump conditions for $\mathbf{u}$, p and $2\mu\boldsymbol{S}$ at the interface are reviewed in Appendix B.

2.2 Pressure-correction method

In the incompressible flow of two immiscible fluids, the density is discontinuous at the interface, and the density ratio can be of order one thousand (e.g., air-water). Thus, simulating two-fluid flows using a constant density approximation, e.g., the Boussinesq approximation, is not justified. Therefore, the density change between the two fluids must be accounted for directly when solving the governing equations of fluid motion. From a numerical point of view, this introduces additional challenges which are not present when solving incompressible single-fluid flows. These challenges are to obtain a numerical method that is computationally efficient, second-order accurate, and stable for large density ratios.

A common solution technique for the incompressible Navier-Stokes equations is the projection method [18]. In the projection method, a Poisson equation for pressure must be solved numerically at each time step. This operation takes most of the computational time in the projection method. Consequently, much work has gone into developing so-called "fast Poisson solvers", which use a combination of fast Fourier transforms (FFT) and Gauss elimination to solve the Poisson equation directly in Fourier space [e.g., 19, 20, 21, 22]. However, fast Poisson solvers cannot solve the Poisson equation for pressure that arises in two-fluid flows when advancing the solution from time t^n to t^{n+1} ($\Delta t = t^{n+1} - t^n$):

$$\nabla \cdot \left(\frac{1}{\rho^{n+1}} \nabla p^{n+1} \right) = \frac{1}{\Delta t} \nabla \cdot \mathbf{u}^*, \tag{2.4}$$

where ρ is the density, p is the pressure, and $\mathbf{u}^*$ is the approximate velocity field at t^{n+1}. Fast Poisson solvers require a constant coefficient on the left-hand side of the Poisson equation, whereas the coefficient ($1/\rho^{n+1}$) on the left-hand side of Eq. (2.4) varies in space and time. To solve the variable coefficient equation (2.4), a standard practice has been to use iterative methods, e.g., multigrid methods [23, 24, 25], Krylov methods [26, 27] or Krylov methods preconditioned with multigrid [28]. The downside is that iterative methods are often slower than fast Poisson solvers. In fact, they can be up to ten times slower [19]. Additionally, an iterative method's operation count depends on problem parameters (e.g., density ratio) and convergence tolerance, whereas fast Poisson solvers have the advantage of fixed operation counts.

To reduce the computational time in solving variable density incompressible flows, [29] adopted a penalty formulation, whereby only a constant coefficient Poisson equation must be solved at each time step. More recently, for solving the two-fluid coupled Navier-Stokes Cahn-Hilliard (phase-field) equations, [30] developed a velocity-correction method that transforms the Poisson equation (2.4) from a variable to a constant coefficient equation. The underlying idea is to split the variable-coefficient pressure-gradient term into a constant term and a variable term, and then treat the constant term implicitly and the variable term explicitly as

$$\frac{1}{\rho^{n+1}}\nabla p^{n+1} \to \frac{1}{\rho_0}\nabla p^{n+1} + \left(\frac{1}{\rho^{n+1}} - \frac{1}{\rho_0}\right)\nabla \hat{p}, \tag{2.5}$$

where ρ_0 is a constant to be defined in Section 2.2.1 and $\hat{p}$ is an explicit approximation to the pressure at time level $n+1$, specifically,

$$\hat{p} = \begin{cases} p^n & \text{if } J = 1, \\ p^* = 2p^n - p^{n-1} & \text{if } J = 2, \end{cases} \tag{2.6}$$

where the choice of J=1 or 2 indicates, respectively, constant or linear extrapolation of p^{n+1} [1]. Then, applying the substitution (Eq. (2.5)) to the left-hand side of Eq. (2.4), leads to a constant coefficient Poisson equation for pressure,

$$\nabla^2 p^{n+1} = \nabla \cdot \left[\left(1 - \frac{\rho_0}{\rho^{n+1}}\right)\nabla \hat{p}\right] + \frac{\rho_0}{\Delta t}\nabla \cdot \mathbf{u}^* \tag{2.7}$$

that can be solved directly using a fast Poisson solver. Also, in contrast to solving Eq. (2.4), there is no need to assemble variable coefficient matrices at each time step when solving Eq. (2.7). Therefore, by using the splitting technique in Eq. (2.5), there is potential for significant speedup in solving the Navier-Stokes equations for incompressible two-fluid flows.

The remainder of this chapter is organized as follows: in Section 2.2.1 we describe the new pressure-correction method for uniform Cartesian grids and periodic boundary conditions and its coupling to the volume-of-fluid (VoF) method; in Section 2.2.2 we present the spatial discretization of the governing equations. Results for the new two-fluid pressure-correction method are presented in Chap. 2.4.

2.2.1 Time integration

Our two-fluid pressure-correction method is developed starting from that of [18] and [32] for single-phase flows. The solution algorithm proceeds by advecting the volume fraction of the

---

[1] A similar strategy for handling variable coefficients in the advection-diffusion equation was proposed by Gottlieb and Orszag [31, Section 9, p. 114].

droplet fluid, $C(\mathbf{x}, t)$, based on the known velocity field $\mathbf{u}^n$. The VoF advection algorithm [15] that computes $C^{n+1}(\mathbf{x})$ is described in Sec. 2.3. The volume fraction has value $C = 0$ in the carrier fluid, $C = 1$ in the droplet fluid, and $0 < C < 1$ in cells containing the interface separating the two fluids. After computing C^{n+1}, the density and viscosity are computed at time level $n + 1$ as

$$\begin{aligned} \rho^{n+1}(\mathbf{x}) &= \rho_d C^{n+1}(\mathbf{x}) + \rho_c \left[1 - C^{n+1}(\mathbf{x})\right] \\ \mu^{n+1}(\mathbf{x}) &= \mu_d C^{n+1}(\mathbf{x}) + \mu_c \left[1 - C^{n+1}(\mathbf{x})\right]. \end{aligned} \tag{2.8}$$

Next, an approximate velocity is computed by first defining $\mathbf{RU}^n$ as

$$\begin{aligned} \mathbf{RU}^n = &-\nabla \cdot (\mathbf{u}^n \mathbf{u}^n) + \frac{1}{\mathrm{Re}} \left[\frac{1}{\rho^{n+1}} \nabla \cdot \left(\mu^{n+1} (\nabla \mathbf{u}^n + (\nabla \mathbf{u}^n)^T) \right) \right] \\ &+ \frac{1}{\mathrm{We}} \left[\frac{1}{\rho^{n+1}} \kappa^{n+1} \nabla C^{n+1} \right] + \frac{1}{\mathrm{Fr}} \mathbf{g}, \end{aligned} \tag{2.9}$$

which is the right-hand side of the momentum equation (2.1b) without the pressure gradient term. The surface tension force, $\mathbf{f}_\sigma$, is computed as $\mathbf{f}_\sigma = \sigma \kappa \nabla C$ by adopting Brackbill's continuum surface force approach [33]. Next, as recommended in [33], we multiply $\mathbf{f}_\sigma$ in Eq. (2.1b) by $\rho(\mathbf{x}, t)/\langle \rho \rangle$, where $\langle \rho \rangle \equiv \frac{1}{2}(\rho_c + \rho_d)$, such that $\mathbf{f}_\sigma$ is constant across the interface, which reduces the magnitude of the spurious currents at high density ratios (not shown). Thus, Eq. (2.9) becomes

$$\begin{aligned} \mathbf{RU}^n = &-\nabla \cdot (\mathbf{u}^n \mathbf{u}^n) + \frac{1}{\mathrm{Re}} \left[\frac{1}{\rho^{n+1}} \nabla \cdot \left(\mu^{n+1} (\nabla \mathbf{u}^n + (\nabla \mathbf{u}^n)^T) \right) \right] \\ &+ \frac{1}{\mathrm{We}} \left[\frac{\kappa^{n+1} \nabla C^{n+1}}{\langle \rho \rangle} \right] + \frac{1}{\mathrm{Fr}} \mathbf{g}. \end{aligned} \tag{2.10}$$

The interface curvature κ^{n+1} is computed using the height-function method [34] with improvements by [35]. The equations are integrated in time using the Adams-Bashforth scheme:

$$\frac{\mathbf{u}^* - \mathbf{u}^n}{\Delta t} = \frac{3}{2} \mathbf{RU}^n - \frac{1}{2} \mathbf{RU}^{n-1}. \tag{2.11}$$

In the pressure-correction method, to satisfy the divergence-free condition (2.1a), the velocity field is advanced in time by applying the pressure-correction to the approximate velocity, $\mathbf{u}^*$, as

$$\frac{\mathbf{u}^{n+1}-\mathbf{u}^*}{\Delta t} = -\frac{1}{\rho^{n+1}}\nabla p^{n+1}. \tag{2.12}$$

Then, by taking the divergence of Eq. (2.12) and imposing the divergence-free condition on $\mathbf{u}^{n+1}$, we get a Poisson equation for pressure with variable coefficient $(1/\rho^{n+1})$:

$$\nabla\cdot\left(\frac{1}{\rho^{n+1}}\nabla p^{n+1}\right) = \frac{1}{\Delta t}\nabla\cdot\mathbf{u}^*. \tag{2.13}$$

Equations (2.11), (2.12), and (2.13) are solved in a standard, two-fluid pressure-correction method [e.g., 36, 37], which we call the Unsplit method. We solve Eq. (2.13) iteratively using the *hypre* library [38, 39]. Specifically, we use the semicoarsening multigrid (SMG) method for structured grids, which was first introduced in [40].

In our new pressure-correction method, the goal is to obtain a constant-coefficient Poisson equation in place of the variable-coefficient Poisson equation (2.13). To this end, we split the pressure gradient term into a constant part $(1/\rho_0)$ and variable part $(1/\rho^{n+1})$, and then treat the constant part implicitly and the variable part explicitly as

$$\frac{1}{\rho^{n+1}}\nabla p^{n+1} \rightarrow \frac{1}{\rho_0}\nabla p^{n+1} + \left(\frac{1}{\rho^{n+1}}-\frac{1}{\rho_0}\right)\nabla\hat{p}, \tag{2.14}$$

where $\rho_0 = \min(\rho_c, \rho_d)$ for numerical stability [30] and $\hat{p}$ is given by Eq. (2.6). We show in Section 2.4.2 that the choice $J = 1$ (called FastP^n because $\hat{p} = p^n$) reduces the physical accuracy of the solution for flows with finite surface tension. We will show in Section 2.4.2 that, for our pressure-correction method, the choice $J = 2$ (called FastP* because $\hat{p} = p^* = 2p^n - p^{n-1}$), is required to accurately simulate flows with finite surface tension. Substituting (2.14) in Eq. (2.12) gives:

$$\frac{\mathbf{u}^{n+1}-\mathbf{u}^*}{\Delta t} = -\left[\frac{1}{\rho_0}\nabla p^{n+1} + \left(\frac{1}{\rho^{n+1}}-\frac{1}{\rho_0}\right)\nabla\hat{p}\right]. \tag{2.15}$$

Then, by taking the divergence of (2.15) while imposing $\nabla\cdot\mathbf{u}^{n+1} = 0$ yields a constant coefficient Poisson equation,

$$\nabla^2 p^{n+1} = \nabla\cdot\left[\left(1-\frac{\rho_0}{\rho^{n+1}}\right)\nabla\hat{p}\right] + \frac{\rho_0}{\Delta t}\nabla\cdot\mathbf{u}^*, \tag{2.16}$$

which can be solved directly using a fast Poisson solver [e.g., 21, 22]. Finally, using (2.15), we update the velocity field by applying the pressure-correction to $\mathbf{u}^*$ as

$$\mathbf{u}^{n+1} = \mathbf{u}^* - \Delta t \left[\frac{1}{\rho_0} \nabla p^{n+1} + \left(\frac{1}{\rho^{n+1}} - \frac{1}{\rho_0} \right) \nabla \hat{p} \right] . \tag{2.17}$$

In summary, our new pressure-correction algorithm advances the numerical solution in time using the following four steps:

1. Compute C^{n+1} by advecting the C field using the VoF advection algorithm described in Sec. 2.3, or compute C^{n+1} using other methods, e.g., level-set or front-tracking. Then, compute cell-centered values for density and viscosity at time level $n + 1$ using Eq. (2.8).

2. Compute $\mathbf{RU}^n$ using Eq. (2.10), and then compute $\mathbf{u}^*$ using Eq. (2.11).

3. Compute p^{n+1} by solving the constant-coefficient Poisson equation (2.16) using a fast Poisson solver [e.g. 22].

4. Compute $\mathbf{u}^{n+1}$ using Eq. (2.17) in which the pressure correction p^{n+1} is applied to the approximate velocity $\mathbf{u}^*$.

In step 3, we solve the Poisson equation using a combination of one-dimensional FFTs in the x- and y-directions, and Gauss elimination in the z-direction [22]. The three methods are summarized in Table 2.1.

The time step (Δt) must be restricted to ensure numerical stability due to our choice of explicit treatment of the convective, viscous, and surface tension terms. In 3-D, Δt is calculated as

$$\Delta t \leq \frac{1}{2} \min(\Delta t_c, \Delta t_\nu, \Delta t_\sigma), \tag{2.18}$$

where

$$\Delta t_c = \frac{\Delta x}{|U|_{\max}} \tag{2.19}$$

Method	Poisson equation	$\hat{p}$	Poisson solver
FastP*	(2.16)	$2p^n - p^{n-1}$	fast Poisson
FastP^n	(2.16)	p^n	fast Poisson
Unsplit	(2.13)	-	multigrid

Table 2.1: Summary of two-fluid pressure-correction methods.

$$\Delta t_\nu = \frac{\mathrm{Re}\Delta x^2}{6} \tag{2.20}$$

$$\Delta t_\sigma = \sqrt{\frac{\mathrm{We}(\rho_c + \rho_d)\Delta x^3}{4\pi}}. \tag{2.21}$$

For cases of low Re, the viscous stability restriction (2.20) can be eliminated by treating the viscous terms implicitly (see Appendix A), however, in all the simulations presented in this paper, the viscous terms were treated explicitly as in Eq. (2.10) either because: (i) $\Delta t_\nu > \Delta t_\sigma$, (ii) the stability restriction imposed by large density and viscosity gradients was greater than the restriction imposed by Δt_ν, or (iii) switching to implicit time integration would not reduce the number of time steps enough to offset the additional computational cost of solving three Helmholtz equations at each time step. For cases of low We, the capillary time step restriction (2.21) can be lessened by a method outlined in [41] or eliminated by treating the surface tension implicitly [42], however these options were not pursued in this work.

Finally, the numerical methods described in this section have been implemented using Fortran 90, the message passing interface (MPI), OpenMP, and FFTW [43]. To perform parallel multi-core simulations, the domain is decomposed such that the data is distributed in memory in the y-direction and contiguous in memory in the x- and z- directions. The following algorithm is used to solve the Poisson equation for p^{n+1} in parallel.

Algorithm of parallel fast Poisson solver (PFPS)

1. Perform real-to-complex FFT in the x-direction to the right-hand side of Eq. (2.16), which is a three-dimensional (3-D) scalar field;

2. Transpose the 3-D complex data among the computing cores such that the resulting data is distributed in the x-direction and contiguous in the y-direction;

3. Perform complex-to-complex FFT in the y-direction of the 3-D data;

4. Perform Gauss elimination in the z-direction to obtain p^{n+1} in Fourier space [22];

5. Perform complex-to-complex, inverse FFT in the y-direction of the 3-D data;

6. Transpose the 3-D complex data among the computing cores such that it is distributed in the y-direction and contiguous in the x-direction;

7. Perform complex-to-real, inverse FFT in the x-direction of the resulting 3-D data to obtain p^{n+1}.

2.2.2 Spatial discretization

We discretize Eqs. (2.10), (2.16), and (2.17) in 3-D on a uniform staggered Cartesian mesh using central differences. For brevity, we report here the details of the spatial discretization in 2-D. The extension to 3-D follows analogously from the 2-D discretization. The u-component of velocity is located at $x_{i+1/2,j}$, the v-component at $x_{i,j+1/2}$, and all other variables are centered at $x_{i,j}$. Our discretization has the advantage over colocated schemes of not requiring an auxiliary cell-centered velocity field.

We begin discretizing Eq. (2.10) by categorizing the terms as convective fluxes **RCU**, diffusive fluxes **RDU**, and body forces **RBU** (surface tension and gravity):

$$\mathbf{RU} = \mathbf{RCU} + \mathbf{RDU} + \mathbf{RBU} \tag{2.22}$$

with

$$\begin{aligned}\mathbf{RCU} &= -\nabla\cdot(\mathbf{u}^n\mathbf{u}^n)\\ \mathbf{RDU} &= \frac{1}{\mathrm{Re}}\left[\frac{1}{\rho^{n+1}}\nabla\cdot\Big(\mu^{n+1}\big(\nabla\mathbf{u}^n+(\nabla\mathbf{u}^n)^T\big)\Big)\right]\\ \mathbf{RBU} &= \frac{1}{\mathrm{We}}\left[\frac{\kappa^{n+1}\nabla C^{n+1}}{\langle\rho\rangle}\right]+\frac{1}{\mathrm{Fr}}\mathbf{g}.\end{aligned} \tag{2.23}$$

The convective fluxes **RCU** are equivalent to those found in one-fluid flow so we do not include their discretization here [see e.g., 44]. We include the discretization of **RDU** and **RBU** for completeness and because there is no well-established second-order discretization of these terms. The components of the viscous flux vector **RDU** are discretized and computed as follows:

$$RDU_{i+1/2,j} = \frac{1}{\mathrm{Re}}\frac{1}{(\rho_{i+1/2,j})}\left(\frac{DUX_{i+1,j}-DUX_{i,j}}{\Delta x}+\frac{DUY_{i+1/2,j+1/2}-DUY_{i+1/2,j-1/2}}{\Delta y}\right) \tag{2.24}$$

and

$$RDV_{i,j+1/2} = \frac{1}{\mathrm{Re}}\frac{1}{(\rho_{i,j+1/2})}\left(\frac{DUY_{i+1/2,j+1/2}-DUY_{i-1/2,j+1/2}}{\Delta x}+\frac{DVY_{i,j+1}-DVY_{i,j}}{\Delta y}\right), \tag{2.25}$$

where Δx and Δy are the grid sizes in the x- and y-directions, respectively. In Eqs. (2.24) and (2.25), the density at the staggered locations is computed using the arithmetic mean as

$$\rho_{i+1/2,j} = \frac{1}{2}\left(\rho_{i+1,j}+\rho_{i,j}\right) \quad \text{and} \quad \rho_{i,j+1/2} = \frac{1}{2}\left(\rho_{i,j+1}+\rho_{i,j}\right). \tag{2.26}$$

The strain rates in Eqs. (2.24) and (2.25) are calculated as

$$DUX_{i,j} = 2\mu_{i,j}\left(\frac{u_{i+1/2,j}-u_{i-1/2,j}}{\Delta x}\right) \tag{2.27}$$

$$DUY_{i+1/2,j+1/2} = \mu_{i+1/2,j+1/2}\left(\frac{u_{i+1/2,j+1}-u_{i+1/2,j}}{\Delta y}+\frac{v_{i+1,j+1/2}-v_{i,j+1/2}}{\Delta x}\right) \tag{2.28}$$

$$DVY_{i,j} = 2\mu_{i,j}\left(\frac{v_{i,j+1/2}-v_{i,j-1/2}}{\Delta y}\right), \tag{2.29}$$

where the staggered viscosity in Eq. (2.28) is computed using the arithmetic mean

$$\mu_{i+1/2,j+1/2} = \frac{1}{4}(\mu_{i+1,j+1}+\mu_{i+1,j}+\mu_{i,j+1}+\mu_{i,j}). \tag{2.30}$$

Note that in Eq. (2.24), we substituted DUY for DVX because of the symmetry of the rate-of-strain tensor.

Next, we compute the components of the body force vector **RBU** where the non-dimensional gravitational acceleration in Eq. (2.1b) is $g = 1$ and in the negative y-direction ($\mathbf{g} = -\hat{\mathbf{j}}$). Special treatment is required when gravity is oriented in the direction of periodic boundaries to prevent uniform acceleration of both fluids [24, 45]. We explicitly account for the hydrostatic pressure term in the momentum equation (2.1b) by adding $\mathbf{f}_\mathrm{h}/\rho$ to the right-hand side of Eq. (2.1b), where

$$\mathbf{f}_\mathrm{h} = -\frac{\rho_c V_c + \rho_d V_d}{V_c + V_d}\mathbf{g}, \tag{2.31}$$

and V_c and V_d are the total volumes of the carrier fluid and droplet fluid, respectively. The discretized components of **RBU** are

$$RBU_{i+1/2,j} = \frac{1}{\mathrm{We}}\frac{\kappa_{i+1/2,j}}{\langle\rho\rangle}\left(\frac{C_{i+1,j} - C_{i,j}}{\Delta x}\right) \tag{2.32}$$

$$RBV_{i,j+1/2} = \frac{1}{\mathrm{We}}\frac{\kappa_{i,j+1/2}}{\langle\rho\rangle}\left(\frac{C_{i,j+1} - C_{i,j}}{\Delta y}\right) + \frac{1}{\mathrm{Fr}}\left(\frac{f_\mathrm{h}}{\rho_{i,j+1/2}} - 1\right). \tag{2.33}$$

where, as a reminder, $\langle\rho\rangle \equiv \frac{1}{2}(\rho_1 + \rho_2)$.

The surface tension force $\mathbf{f}_\sigma$ must be discretized at the staggered grid locations to be consistent with the location of the pressure gradient term [26]. This discretization produces an exact balance of the pressure gradient and the surface tension if the curvature is exact, which we will show in Sec. 2.4.1. The curvature is computed at the staggered grid point $x_{i+1/2,j}$ as

$$\kappa_{i+1/2,j} = \begin{cases} \kappa_{i+1,j} & \text{if } \kappa_{i,j} = 0 \\ \kappa_{i,j} & \text{if } \kappa_{i+1,j} = 0 \\ \frac{1}{2}(\kappa_{i+1,j} + \kappa_{i,j}) & \text{otherwise.} \end{cases} \tag{2.34}$$

Next, we discretize the right-hand side of Eq. (2.16), which serves as input to the fast Poisson solver:

$$\nabla^2 p_{i,j}^{n+1} = \frac{DPX_{i+1/2,j} - DPX_{i-1/2,j}}{\Delta x} + \frac{DPY_{i,j+1/2} - DPY_{i,j-1/2}}{\Delta y} + DIVU_{i,j} \tag{2.35}$$

where

$$DPX_{i+1/2,j} = \left(1 - \frac{\rho_0}{\rho_{i+1/2,j}}\right)\left(\frac{\hat{p}_{i+1,j} - \hat{p}_{i,j}}{\Delta x}\right), \tag{2.36}$$

$$DPY_{i,j+1/2} = \left(1 - \frac{\rho_0}{\rho_{i,j+1/2}}\right)\left(\frac{\hat{p}_{i,j+1} - \hat{p}_{i,j}}{\Delta y}\right), \tag{2.37}$$

and

$$DIVU_{i,j} = \frac{\rho_0}{\Delta t}\left(\frac{u^*_{i+1/2,j} - u^*_{i-1/2,j}}{\Delta x} + \frac{v^*_{i,j+1/2} - v^*_{i,j-1/2}}{\Delta y}\right). \tag{2.38}$$

Finally, the components of Eq. (2.17) are discretized as

$$u^{n+1}_{i+1/2,j} = u^*_{i+1/2,j} - \Delta t\left[\frac{1}{\rho_0}\left(\frac{p^{n+1}_{i+1,j} - p^{n+1}_{i,j}}{\Delta x}\right) + \left(\frac{1}{\rho_{i+1/2,j}} - \frac{1}{\rho_0}\right)\left(\frac{\hat{p}_{i+1,j} - \hat{p}_{i,j}}{\Delta x}\right)\right] \tag{2.39}$$

and

$$v^{n+1}_{i,j+1/2} = v^*_{i+1/2,j} - \Delta t\left[\frac{1}{\rho_0}\left(\frac{p^{n+1}_{i,j+1} - p^{n+1}_{i,j}}{\Delta y}\right) + \left(\frac{1}{\rho_{i,j+1/2}} - \frac{1}{\rho_0}\right)\left(\frac{\hat{p}_{i,j+1} - \hat{p}_{i,j}}{\Delta y}\right)\right]. \tag{2.40}$$

2.3 Volume-of-fluid method

The computational methods to advect a fluid interface fall into two main categories: 1. interface capturing methods (ICM), such as the volume of fluid (VoF) [46] and the level-set [47] methods; 2. interface tracking methods (ITM), such as the front tracking [48]. Both ICM and ITM are designed to compute (capture or track) sharp interfaces, and can be used on a fixed Cartesian mesh. Mass conservation, the ability to compute strong deformations of the interface, and interface topology changes due to break-up and coalescence are highly desirable features in the simulations of multiphase flows, e.g. gas-liquid and liquid-liquid. Interface topology changes need *ad hoc* modeling in ITM [48], whereas they are directly captured by the ICM [49].

Among the ICM, the level-set is a widely used method where a distance function to the interface is advected with the flow throughout the computational domain in place of the interface itself, thus avoiding the need to advect a discontinuous function. The drawback of the level-set method is that it does not intrinsically conserve mass. In the VoF method, instead, the advection equation of the volume fraction is directly solved for, thus, the VoF method could potentially conserve mass exactly. Limits to this potential may only come from the numerics adopted. A color function representing the volume fraction of the reference phase is advected geometrically and the interface is reconstructed from this function typically with a piecewise linear representation.

VoF advection schemes can be broadly classified as either direction split or unsplit schemes. Split advection schemes consist of a sequence of one-dimensional advection and reconstruction steps in each coordinate direction, thus they are algorithmically straightforward to implement compared to the multidimensional unsplit schemes. On the other hand, unsplit methods have the advantage of only requiring one advection and reconstruction step per time step, however the advection step is often algorithmically complex. This is because unsplit methods require either the computation of a flux polyhedron for each cell face [50] or calculation of polyhedra volumes with non-planar surfaces requiring triangulation [51]. In our experience, these geometric calculations are the computational bottleneck of the VoF advection scheme. Thus, the computational savings of the unsplit versus the split method (if any) are likely to be small. Furthermore, unsplit methods do not necessarily conserve mass to zero machine precision [51]. For these reasons, we chose to adopt a split mass-conserving VoF advection approach.

The three-dimensional VoF advection is performed through the Eulerian implicit - Eulerian algebraic - Lagrangian explicit (EI-EA-LE) algorithm which was originally proposed by Scardovelli *et al.* [52]. We chose EI-EA-LE over the EILE-3D algorithm [53] because EI-EA-LE requires half the number of advection and reconstruction steps and does not require the calculation of three two-dimensional divergence-free velocity fields. Thus, EI-EA-LE is at least two times computationally faster than EILE-3D. The original EI-EA-LE algorithm [52] is globally mass-conserving but generates wisps, and does not conserve the mass of the individual volumes tracked in the flow. We have improved this method with the addition of a redistribution and a wisp suppression algorithm.

Our method is consistent (i.e., the volume of fluid function, C, satisfies the condition

$0 \leq C \leq 1$) and wisps-free and, thus, conserves mass both globally and locally within each volume tracked. We also present and analyze the numerical treatment of the surface tension force within the two-fluid pressure-correction method (Chap. 2.2).

In this chapter we present the VoF interface reconstruction algorithm in Sec. 2.3.1, the interface advection algorithm in Sec. 2.3.2, and the method to compute the interface curvature in Sec. 2.3.3. The redistribution algorithm and wisp suppression algorithm are described in Sec. 2.3.2.

2.3.1 VoF interface reconstruction

The VoF method is characterized by a sharp representation of the interface. In the present VoF method, the interface between the two phases is reconstructed using a piecewise linear interface calculation (PLIC) by [54]. The reconstruction of the interface in each computational cell consists of two steps: the computation of the interface normal, $\mathbf{n} = (n_x, n_y, n_z)$, and the computation of the interface location (Fig. 2.2). The algorithm that we use to evaluate the interface normal is the mixed Young-centered (MYC) method [53] that is a combination of the centered-columns method [55] and the Youngs method [54]. In each cell that contains part of the interface, a set of four different interface normals is computed. Three normals are computed with the centered-columns method, and the fourth normal is computed using the Youngs method. Then, the interface plane normal is chosen among these four normals. Last, the interface plane constant, α, of Eq. (2.46) is computed. We now describe how $\mathbf{n}$ and α are computed.

Centered-columns method

The interface normal is obtained after defining a height function in the $3 \times 3 \times 3$ stencil of cells around each (i, j, k) cell. For each of the three directions, the VoF color function, C, is added column-wise along that direction to give a local height function [55]. In the case of

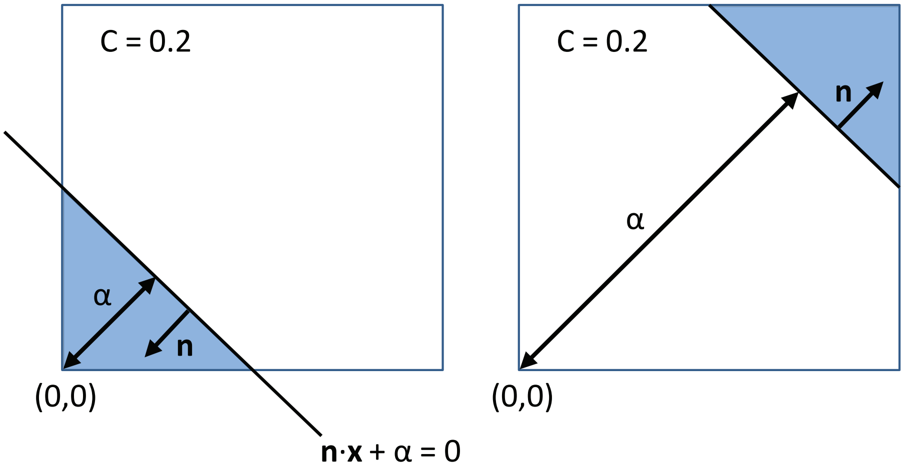

Figure 2.2: Interface normal, **n**, and interface plane constant, α, of Eq. (2.46) for a 2D case with the VoF function $C = 0.2$.

the vertical direction, z, we compute the height function, $z_{i,j,k}$, as

$$z_{i,j,k} = \Delta x \sum_{l=-1}^{1} C_{i,j,k+l}, \tag{2.41}$$

where Δx is the uniform grid spacing. Then, we define the plane equation approximating the interface as

$$\mathrm{sgn}(m_z) z = m_x x + m_y y + a, \tag{2.42}$$

where the sign of the m_z coefficient is computed with a centered finite-difference scheme and stored, and a is a constant. After the height function $z_{i,j,k}$ is computed using (2.41), a centered finite-difference scheme is used to calculate m_x and m_y as derivatives of $z_{i,j,k}$ along the x and y directions, i.e. $m_x = \frac{\partial z_{i,j,k}}{\partial x}$, $m_y = \frac{\partial z_{i,j,k}}{\partial y}$. This scheme approximates a linear interface exactly if the interface intersects only the four vertical faces of the $3 \times 3 \times 3$ stencil cube. If this is not the case, then extra layers of cells should be added in the z direction for the computation of $z_{i,j,k}$ in Eq. (2.41) such to satisfy this condition. For computational efficiency, we avoid the addition of extra layers of cells and show in [15] that combining the centered-column method using Eq. (2.41) with the Youngs method provides second-order accurate approximation of the interface. This was assessed by computing the geometrical error of the PLIC interface reconstruction for a sphere on a uniform mesh.

The height function is calculated for each Cartesian direction, thus giving three different normals to the interface plane. For example, in the z direction, the triplet $\mathrm{sgn}(m_z), m_x, m_y$ is normalized to $m_z^0, m_x^{'}, m_y^{'}$ such that $|m_z^0| + |m_x^{'}| + |m_y^{'}| = 1$. Among the three possible representations of the interface plane, $x = f(y, z)$, $y = g(x, z)$ and $z = h(x, y)$, we choose the one corresponding to the maximum $|m^0|$ coefficient, according to the criterion [53]:

$$|m_{CC}^0| = \max(|m_x^0|, |m_y^0|, |m_z^0|). \tag{2.43}$$

Youngs method

The Youngs interface normal is computed as the gradient of the color function, ∇C, using a second-order centered finite-difference scheme. The normal is first calculated at the eight vertices of the computational cell, then its cell value is computed as the average of these eight normals.

Mixed Youngs-Centered (MYC) method

In the mixed Youngs-centered method (MYC), between the two competing normals computed with the centered column (CC) and the Youngs (Y) methods, the normal having the minimum $|m^0|$ is selected [53],

$$|m^*| = \min(|m_{CC}^0|, |m_Y^0|). \tag{2.44}$$

Then, the unit normal vector $\mathbf{n}$ is computed by normalization of $\mathbf{m}^*$ to unit length,

$$\mathbf{n} = \frac{\mathbf{m}^*}{||\mathbf{m}^*||}. \tag{2.45}$$

Youngs method provides a better estimate at low resolution and for particular alignments of the interface with the grid, while the centered columns method is generally more accurate

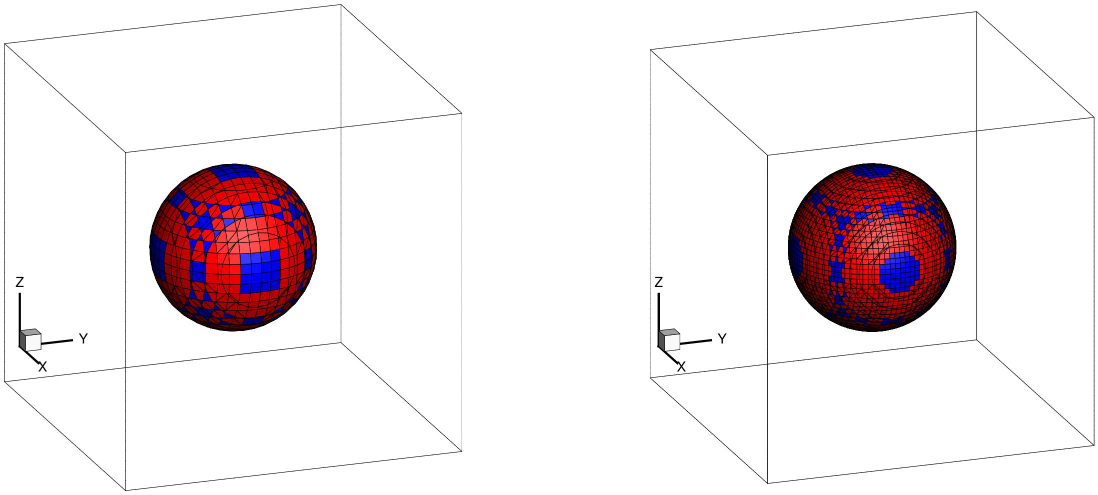

(a) (b)

Figure 2.3: Selection of the interface normal for a sphere placed at the center of a cubic box with 16 (a) and 32 (b) cells across the diameter: Youngs' method (blue) and centered-columns method (red).

at high resolution. The MYC method has the advantage to choose in each cell among the two. We have used the MYC algorithm to reconstruct the interface between a sphere and its surrounding (e.g. liquid droplet in gas) in a uniform Cartesian mesh. Figure 2.3 shows the $C = 0.5$ isosurface for a sphere with a resolution of 16 and 32 mesh points across its diameter, and the cells in which the centered-columns or the Youngs method are selected.

VoF interface plane constant

After computing the interface normal that points towards the reference phase with the MYC method, the plane constant α of the local interface plane equation

$$\mathbf{n} \cdot \mathbf{x} + \alpha = 0, \tag{2.46}$$

has to be computed. α is the distance between the interface plane and the origin of a local coordinate system for each cell (Fig. 2.2). In our flow solver, α is calculated using the analytical tools provided by [56].

2.3.2 Interface advection

We now present the VoF advection with the Eulerian implicit–Eulerian algebraic–Lagrangian explicit (EI-EA-LE) algorithm. We have improved this method, which was originally proposed by Scardovelli *et al.* (2002) [52], with the addition of a redistribution and a wisp suppression algorithm. The redistribution algorithm is needed for ensuring the consistency of the algorithm since small inconsistencies in the VoF function values (i.e., $C < 0$ and $C > 1$) can arise in the Eulerian algebraic (EA) step of the advection. A wisp suppression algorithm has also been developed in Sec. 2.3.2 in order to ensure that small values of C arising in the domain are not neglected and ignored from the computation.

EI-EA-LE advection

Considering a characteristic function χ that has value 1 in the reference phase and 0 in the other, the phase of interest moves obeying the following advection equation:

$$\frac{D\chi}{Dt} \equiv \frac{\partial \chi}{\partial t} + \mathbf{u} \cdot \nabla \chi = 0, \tag{2.47}$$

or equivalently,

$$\frac{\partial \chi}{\partial t} + \nabla \cdot (\mathbf{u}\chi) - \chi \nabla \cdot \mathbf{u} = 0. \tag{2.48}$$

The volume fraction $C_{i,j,k}$ of grid cell (i, j, k) is related to the characteristic function χ by the integral relation

$$C_{i,j,k}(t) = \frac{1}{V_0} \int_{V_0} \chi(\mathbf{x}, t) d\mathbf{x}, \tag{2.49}$$

where V_0 is the volume of the (i, j, k) cell. For 1D advection, integrating Eq. (2.48) in space over the cell and in time with a forward Euler scheme gives:

$$C_i^{n+1} = C_i^n + F_l - F_r + \widetilde{C}_i(\bar{u}_i - \bar{u}_{i-1}), \tag{2.50}$$

where $\bar{u}_i = u_i \Delta t / h$ is a local CFL number, u_i is the velocity component in the x-direction staggered from C for the i-cell, h is the grid cell size, and F_r and F_l denote the right and left fluxes of C.

EI advection If the term $\widetilde{C}_i$ in Eq. (2.50) is evaluated at time step $n+1$ ($\widetilde{C}_i = C_i^{n+1}$), then (2.50) yields an implicit scheme:

$$C_i^{n+1} = \frac{C_i^n + F_l - F_r}{1 - (\bar{u}_i - \bar{u}_{i-1})} \tag{2.51}$$

In terms of material derivative, Eq. (2.51) is equivalent to the following discretization in time of Eq. (2.47):

$$[\chi(\mathbf{x}, t+\Delta t) - \chi(\mathbf{x}, t)] + [\chi(\mathbf{x}, t) - \chi(\mathbf{x} - \mathbf{u}\Delta t, t)] = \chi(\mathbf{x}, t+\Delta t) - \chi(\mathbf{x} - \mathbf{u}\Delta t, t) = 0, \tag{2.52}$$

which defines the Eulerian Implicit (EI) scheme, see Fig. 2.4.

$$\tilde{x} = a(x + \bar{u}_{i-1}), \tag{2.53}$$

where the length $l_x = h + u_{i-1}\Delta t - u_i \Delta t$ is mapped into $l_{\tilde{x}} = h$ with a transformation Jacobian given by $a = l_{\tilde{x}}/l_x = 1/(1 + \bar{u}_{i-1} - \bar{u}_i)$.

LE advection If the term $\widetilde{C}_i$ in Eq. (2.50) is evaluated at time step n ($\widetilde{C}_i = C_i^n$), then (2.50) yields an explicit scheme:

$$C_i^{n+1} = C_i^n(1 + \bar{u}_i - \bar{u}_{i-1}) + F_l - F_r. \tag{2.54}$$

Equation (2.54) is equivalent to the following discretization in time of Eq. (2.47):

$$\chi(\mathbf{x} + \mathbf{u}\Delta t, t + \Delta t) - \chi(\mathbf{x}, t) = 0, \tag{2.55}$$

which defines the Lagrangian Explicit (LE) scheme, see Fig. 2.4.

$$\tilde{y} = by + \bar{v}_{j-1}, \tag{2.56}$$

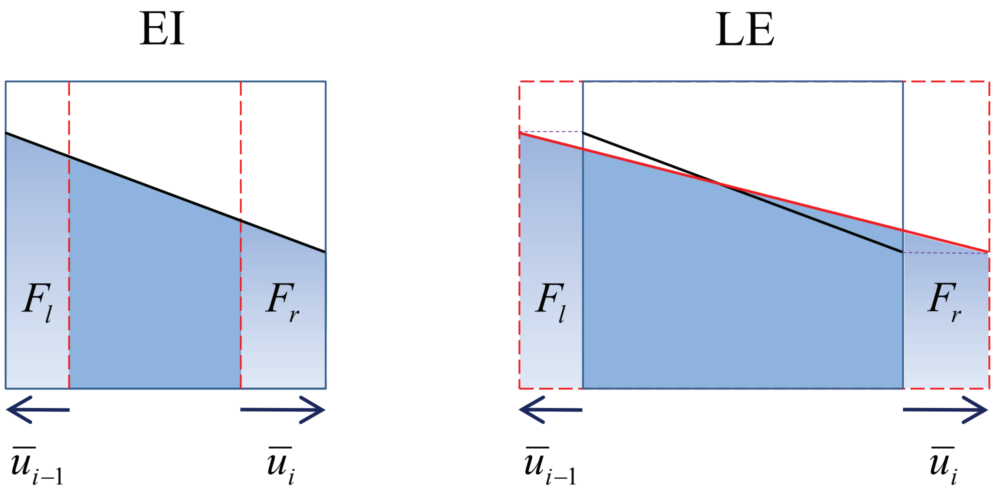

Figure 2.4: Geometrical computation of the fluxes F_l and F_r in the x direction: Eulerian Implicit, Eq. (2.51), (left), and Lagrangian Explicit, Eq. (2.54, (right).

where the length $l_y = h$ is mapped into $l_{\tilde{y}} = h + v_j \Delta t - v_{j-1} \Delta t$ with a transformation Jacobian given by $b = l_{\tilde{y}}/l_y = 1 + \bar{v}_j - \bar{v}_{j-1}$.

In the EI scheme, the fluxes are computed before the mapping, while in the LE scheme the cell and its interface are mapped before computing the fluxes (Fig. 2.4). In both Eqs. (2.51) and (2.54) the fluxes are computed geometrically. This typically requires intersection operations between a polygon and a plane. In our solver, these operations are performed with the analytical tools of [56].

In the case of a 2D flow, the advection equation can be discretized by a two step split scheme where for instance a EI step in the x direction is followed by a LE step in the y direction. The total transformation Jacobian, $J = ab$, is then equal to 1 for a divergence-free 2D velocity field. Thus, the sequence of Eulerian implicit and Lagrangian explicit mappings applied to an incompressible 2D velocity field conserves volume exactly. Since this is a split scheme, an interface reconstruction is performed between the two steps. Also, the EI and LE spatial direction is alternated between successive time steps in order to avoid a preferential direction.

The construction of a 3D mass conserving scheme based on these mappings can be accomplished with the EILE-3D scheme [53] by splitting the 3D velocity field into three sets of 2D incompressible fields $\mathbf{u}_1 = (u_1, v_1, 0)$, $\mathbf{u}_2 = (u_2, 0, w_2)$ and $\mathbf{u}_3 = (0, v_3, w_3)$ such that their sum gives the original 3D field. The computation of these 2D fields is not trivial and a total number of six 1D advection steps and interface reconstructions are needed at each time step. Thus, the mass conservation property of the 2D scheme is extended to 3D. Because the EI and LE schemes can be directly derived from the 1D advection equation, the consistency condition $0 \leq C \leq 1$ is satisfied.

EA advection We followed a different approach as in [52] by designing a third mapping such that the product of its transformation Jacobian with the EI and LE Jacobians gives 1. Therefore, the advection scheme conserves the volume for an incompressible velocity field. Combining these three steps together (e.g. a first EI step along the x direction, a third LE step along z, and an intermediate modified EI step along y) gives:

$$\begin{aligned} \widetilde{x} &= a(x + \bar{u}_{i-1,j,k}) \\ \widetilde{y} &= b(y + \bar{v}_{i,j-1,k}) \\ \widetilde{z} &= cz + \bar{w}_{i,j,k-1} \end{aligned} \tag{2.57}$$

with

$$\begin{aligned} a &= \frac{1}{1 + \bar{u}_{i-1,j,k} - \bar{u}_{i,j,k}} \\ b = \frac{1}{ac} &= \frac{1 + \bar{u}_{i-1,j,k} - \bar{u}_{i,j,k}}{1 + \bar{w}_{i,j,k} - \bar{w}_{i,j-1,k}} \\ c &= 1 + \bar{w}_{i,j,k} - \bar{w}_{i,j,k-1} \end{aligned} \tag{2.58}$$

where the coefficient b is calculated in order to satisfy the condition $J = abc = 1$, and $\bar{u} = u\Delta t/h$, $\bar{v} = v\Delta t/h$, $\bar{w} = w\Delta t/h$, and u, v, w are the velocity components in the x, y

and z directions, respectively. The second step is an algebraic step which does not have a geometric interpretation, therefore the advection algorithm may generate small negative values and small overshoots of C ($C < 0$, and $C > 1$). We call this 3D split algorithm EI-EA-LE. The volume fraction C at time step $n+1$ is computed in three steps, where an interface reconstruction is performed between each of them:

$$\begin{aligned} C^{(1)}_{i,j,k} &= \frac{C^{n}_{i,j,k} + F^{u}_{i-1} - F^{u}_{i}}{1 - \delta_x \bar{u}} \\ C^{(2)}_{i,j,k} &= \frac{C^{(1)}_{i,j,k}(1 - \delta_x \bar{u}) + F^{v}_{j-1} - F^{v}_{j}}{1 + \delta_z \bar{w}} \\ C^{n+1}_{i,j,k} &= C^{(2)}_{i,j,k}(1 + \delta_z \bar{w}) + F^{w}_{k-1} - F^{w}_{k}, \end{aligned} \tag{2.59}$$

where we simplified the notation by introducing the operators $\delta_x \bar{u} = \bar{u}_{i,j,k} - \bar{u}_{i-1,j,k}$ and $\delta_z \bar{w} = \bar{w}_{i,j,k} - \bar{w}_{i,j,k-1}$, and we used F^{u}_{i-1} and F^{u}_{i} to indicate the flux through the left and right face, respectively, for the 1D advection velocity field u, and similarly for F^{v}_{j} and F^{w}_{k}.

The sum of the three steps of Eq. (2.59) simplifies to a balance of fluxes as

$$C^{n+1}_{i,j,k} = C^{n}_{i,j,k} + F^{u}_{i-1} - F^{u}_{i} + F^{v}_{j-1} - F^{v}_{j} + F^{w}_{k-1} - F^{w}_{k}, \tag{2.60}$$

therefore the method conserves volume globally. In Eq. (2.59), the Eulerian fluxes are used in the first and second step, and the Lagrangian fluxes are used in the third step. The EI-EA-LE algorithm requires just three one-dimensional advections and reconstructions per time step, rather than six, and no computation of 2D velocity fields are required as in the EILE-3D algorithm. Thus, the 3D split algorithm EI-EA-LE is 50% computationally less expensive then EILE-3D. The algebraic step (EA) produces small inconsistencies in the values of C ($C < 0, C > 1$) that we remove with the redistribution algorithm described below.

Furthermore, based on the droplet in quiescent flow tests (Sec. 2.4.1), we modified the VoF advection algorithm, trying to reduce the directionality of the 1D advection steps by assigning the first EI sweep to a different direction at each time step. Initially, the EI-EA-LE advection steps were cycled amongst the three spatial directions in a 3-cycle combination: 1. (x, y, z), 2. (y, z, x), and 3. (z, x, y). We then switched the EI-EA-LE advection steps to a 6-cycle combination: 1. (z, y, x), 2. (y, x, z), 3. (x, z, y), 4. (z, x, y), 5. (y, z, x), and 6. (x, y, z). This change was beneficial in delaying the growth of the spurious currents in the static drop case because the VoF advection algorithm becomes more ‘isotropic’.

Redistribution algorithm

The Eulerian algebraic step (EA) may cause small inconsistencies in the volume fraction values ($C < 0$, and $C > 1$). We correct them using a local redistribution algorithm similar to that described by [57]. The redistribution is performed on the C field after the EA advection step only. Since just the undershoots ($C < 0$) are detrimental to the geometrical flux and interface plane constant computation, these are the only inconsistencies treated by the redistribution algorithm. In all our test cases, we observed a minimal presence of $C > 1$ inconsistencies, where the overshoots were limited to values of the order 10^{-7} or less. In the case of a negative value of $C_{i,j,k}$, the following redistribution algorithm is implemented. Among the 26 neighboring cells located in the $3 \times 3 \times 3$ grid around cell (i, j, k):

1. find the cell l, m, n where the sum $C_{i,j,k} + C_{l,m,n}$ is positive and minimized,
2. set $C_{l,m,n} = C_{l,m,n} + C_{i,j,k}$,
3. set $C_{i,j,k} = 0$.

Wisp-suppression algorithm

The calculation of the C fluxes and of the interface plane constant requires intersection operations between a polyhedron and a plane. Because of their finite precision, these operations may cause errors when the plane and one of the faces of the polyhedron are really close. This happens when the volume fraction C is very small or very close to 1, i.e. in nearly-homogeneous cells. In order to avoid these errors, in most VoF methods, the volume fraction in cells where $C > 1 - \epsilon$ or $C < \epsilon$ is set to 1 or 0, respectively, where $\epsilon \sim 10^{-8}$. Thus, these VoF methods do not conserve mass with zero machine accuracy.

Because we want a mass-conserving VoF method, we take a different approach, where we do not reset nearly-homogeneous cells, and skip the advection operations on cells satisfying the condition $C < \epsilon$. Therefore, small values of $0 < C < \epsilon$, also called 'wisps', would detach from the reference phase in the flow field. Leaving the wisps in the domain would still insure global mass conservation but we do not want spurious mass to leave the reference phase. If that was the case, the mass of the individual volumes (local mass) would not be conserved. Moreover, wisps tend to grow unboundedly in time. We, therefore, developed a wisp suppression algorithm that reintroduces the wisps volume fraction in the reference phase. Due to the small magnitude of the wisps ($C < \epsilon$) such treatment has no detrimental effects on the geometrical error of the VoF method as shown by our numerical results presented in [15].

Since the wisps are formed close to the interface when the reference phase retreats from the secondary phase, the wisp suppression algorithm moves the C of the wisps back into the reference phase along the local interface normal computed with the MYC algorithm. If the wisp is not neighboring the reference phase, then it is not re-located: depending on mesh resolution a minimum amount of isolated wisps may linger in the surrounding secondary phase. The wisps suppression algorithm is run at the end of each of the three split advection steps. First, the wisps close to the interface are identified with the criteria:

$$\begin{aligned} 0 \quad < \quad C_{i,j,k} \quad &< \quad \epsilon \qquad \text{AND} \\ \max(C_{i+l,j+m,k+n}) \quad &> \quad \epsilon \qquad l=-1,0,1, \quad m=-1,0,1 \quad n=-1,0,1. \end{aligned} \tag{2.61}$$

Then, the wisps are moved into the reference phase. The destination cell is selected according to the predominant orientation of the local interface normal. Numerical tests have shown that the wisp suppression algorithm limits the total volume fraction of wisps to $\phi_v = 10^{-14}$ in the cases we considered [15].

In summary, our VoF method relies on the MYC interface reconstruction, the EI-EA-LE volume advection scheme, and the redistribution and the wisp suppression algorithms described above. The resulting method conserves mass with machine accuracy, is consistent ($0 \leq C \leq 1$) and free of wisps.

2.3.3 Curvature computation

This section describes the numerical method for computing the curvature of the interface between the two fluids that is needed for calculating the surface tension force, $\mathbf{f}_\sigma$ (Eqs. (2.1b) and (2.3)). In order to compute the interface curvature from the VoF function, C, the height function technique by [34] has been adopted and investigated. A correction based on the local orientation of the interface normal is performed to minimize the error on a spherical interface [58]. The technique is second-order accurate with respect to the mesh size and is computationally efficient. The height function is constructed by integrating the C along the axis direction for which the normal to the interface has the largest component. The method relies solely on the discrete values of C, and is mostly independent from the interface normal computation, which only influences the orientation of the curvature computational stencil, thus, making the method robust. For example, consider the case with the interface normal with the largest component in the z-direction. Then, in the (i, j, k) cell containing the interface (i.e., in the cell where $0 < C_{i,j,k} < 1$), the local height function H is computed along z on a 3×3 computational stencil in the $x - y$ plane for a fixed κ value as

$$H_{r,s} = \sum_{t=t_{down}}^{t_{up}} C^*_{i+r,j+s,k+t} \Delta x \quad \text{with} \quad r = [-1, 0, 1] \quad \text{and} \quad s = [-1, 0, 1] \tag{2.62}$$

where t_{up} and t_{down} are adjusted adaptively based on the local C distribution (t_{up} can vary from 0 to 3, and t_{down} can vary from -3 to 0), and C^* is a modified distribution of the volume fraction C, which is rendered monotonic along the z-direction [58]. The stencil for computing H in the (i, j, k) cell is therefore of variable size and ranges from $3 \times 3 \times 1$ to $3 \times 3 \times 7$. The interface curvature is then computed using the height function H as

$$\kappa = \frac{n_z}{|n_z|} \frac{\left[H_{xx} + H_{yy} + H_{xx}H_y^2 + H_{yy}H_x^2 - 2H_{xy}H_xH_y\right]}{\left[1 + H_x^2 + H_y^2\right]^{3/2}}, \tag{2.63}$$

where the factor $n_z/|n_z|$ gives the sign of n_z to κ, and the partial derivatives of H are computed using the finite difference formula of [58]. These formulas introduce extra staggered terms weighed by a parameter γ which improves the accuracy in three dimensions. The discretized first derivative of H is written as

$$H_x = \frac{[\gamma(H_{1,1} - H_{-1,1}) + H_{1,0} - H_{-1,0} + \gamma(H_{1,-1} - H_{-1,-1})]}{2\Delta x(1+2\gamma)}, \tag{2.64}$$

and the discretized second derivative of H as

$$H_{xx} = \frac{[\gamma(H_{1,1} - 2H_{0,1} + H_{-1,1}) + H_{1,0} - 2H_{0,0} + H_{-1,0} + \gamma(H_{1,-1} - 2H_{0,-1} + H_{-1,-1})]}{\Delta x^2(1+2\gamma)}. \tag{2.65}$$

[58] define the parameter γ as

$$\gamma = 0.2 \quad \text{if} \quad \arccos(\max(|n_x|), \max(|n_y|), \max(|n_z|)) > 0.8 \tag{2.66}$$

$$\gamma = 0 \quad \text{if} \quad \arccos(\max(|n_x|), \max(|n_y|), \max(|n_z|)) \leq 0.8. \tag{2.67}$$

Note that the condition $\arccos(\max(|n_x|), \max(|n_y|), \max(|n_z|)) > 0.8$ occurs when the interface normal is not aligned predominantly to any of the three directions, causing a loss of accuracy in the height function method. The cross-derivative H_{xy} is calculated as

$$H_{xy} = \frac{H_{1,1} - H_{1,-1} - H_{-1,1} + H_{-1,-1}}{4\Delta x^2}. \tag{2.68}$$

The above described method for calculating the curvature is second order accurate, meaning that the error of the curvature decays as $N_{gp/d}^{-2}$ [15].

2.4 Validation and Verification

In this section we test the coupled pressure-correction and VoF flow solver developed in Sec. 2.2 and 2.3 in several applications. Our first objective is to assess the magnitude of the spurious currents for a droplet in quiescent fluid (Sec. 2.4.1), a translating reference frame (Sec. 2.4.1), and Taylor-Green vortex flow (Sec. 2.4.1). We also compute the error between the exact curvature and numerically computed curvature, and show that this error is the source of the spurious currents.

Next, we aim to answer the following questions on applying the splitting technique (Eq. (2.5)) to the two-fluid Navier-Stokes equations:

- Is the split method (Eq. (2.7)) physically less accurate than the unsplit method (Eq. (2.4)) and does the accuracy of the split method depend on the type of extrapolation chosen in Eq. (2.6)?

- What are the computational savings of using the split method? Specifically, how much faster is it to solve Eq. (2.7) directly versus Eq. (2.4) iteratively?

To answer these questions, we first develop a two-fluid pressure-correction method with a constant coefficient Poisson equation, which can be solved directly with a fast Poisson solver. Next, we apply the method to several two-fluid flows to verify and validate the new method, quantify its performance, and evaluate its spatial and temporal accuracy.

Section 2.4.2 compares the numerical solutions obtained when using the standard, unsplit method (i.e., solving Eq. (2.4), called Unsplit), the split method, Eq. (2.5), using J=1 (called FastP^n), and the split method using J=2 (called FastP*). Next, we assess the performance of the unsplit and split formulations by comparing the CPU time when solving Eq. (2.4) using a multigrid solver to the CPU time when solving Eq. (2.7) using a fast Poisson solver. Section 2.4 verifies and validates the new pressure-correction/volume-of-fluid flow solver. This includes two canonical flows: a capillary wave and a falling droplet in quiescent fluid.

The potential computational savings suggest that our method is well-suited for fully-resolved DNS of bubble- and droplet-laden turbulent flows in simple geometries. In addition, because Eq. (2.4) is present regardless of the method used to advect the fluid interface, the pressure-correction method presented in Sec. 2.2 is useful in other interface-capturing (e.g., level-set or phase-field) and front-tracking methods. Furthermore, the splitting technique of the new pressure-correction method could be extended to simulate low-Mach number flows that use the pressure-correction method, e.g., [59].

2.4.1 Coupled droplet/flow cases

In this section, we present the numerical results of the coupled droplet/flow solver for the cases of droplet in a quiescent fluid, droplet in a translating reference frame, and droplet in a

Taylor-Green vortex flow. In all cases, the simulations are three-dimensional and the initial shape of the droplets is spherical. To characterize the droplet-laden flow cases studied, we use two more non-dimensional numbers: the Weber number based on the droplet diameter,

$$\mathrm{We}_D = \frac{\tilde{\rho}\tilde{U}^2\tilde{D}}{\tilde{\sigma}} = \frac{\tilde{D}}{\tilde{L}}\mathrm{We}, \tag{2.69}$$

and the Laplace number,

$$\mathrm{La} = \frac{\tilde{\sigma}\tilde{D}}{\tilde{\rho}\tilde{\nu}^2}. \tag{2.70}$$

Droplet in a quiescent flow

The droplet in a quiescent flow case was performed in order to assess the ability of the flow solver to produce a balance between the pressure gradient and the surface tension force at the interface. The solution should stay constant in time with zero velocity field, however, as reported in previous two-dimensional studies (e.g., Refs. [26] and [25]), spurious currents are generated in the flow field as shown in Fig. 2.5. Figure 2.5 shows the velocity vectors around the droplet in a mid cross-section of the droplet for the case with $\mathrm{We}_D = 0.25$, Re= 31.6 and La= 10^3 at t = 0.1 ($N_{gp/d} = 32$ in a 64^3 mesh). Figure 2.6 shows the r.m.s. of the generated velocity fluctuations for $\mathrm{We}_d = 0.25$, and Re= 31.6 and Re= 316 corresponding to La= 10^3 and 10^5, respectively.

The spurious currents are generated by the imbalance of the pressure gradient and the surface tension force that is computed using Eq. (2.3). In Eq. (2.3), the curvature, κ, is computed numerically using the height-function method Eq. (2.63). To explain if the curvature computed with the height-function method is the source of the numerical imbalance between ∇p and $\mathbf{f}_\sigma$, we also performed the numerical tests using the analytical curvature, $\kappa = \kappa_0$, to compute $\mathbf{f}_\sigma$ through (2.3). Figure 2.6 shows that, at $t = 0$, the r.m.s. of the velocity fluctuations is 10^{-4} for κ computed using (2.63), and is 10^{-16} for $\kappa = \kappa_0$. Later in time, the r.m.s. of the velocity fluctuations is $O(10^{-4}, 10^{-6})$ for κ computed using (2.63), and becomes smaller than $O(10^{-8})$ when using $\kappa = \kappa_0$. This proves that the method is consistent and a balance between pressure gradient and surface tension holds if the curvature is exact.

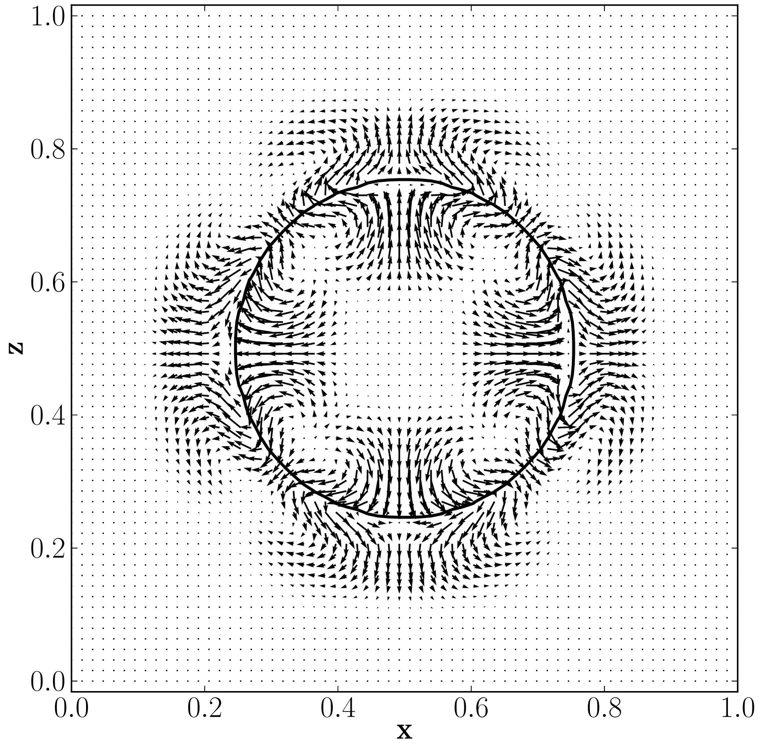

Figure 2.5: Spurious currents for the spherical static droplet with $\mathrm{We}_D = 0.25$ and La= 10^3. Isoline for $C = 0.5$ (solid line), and fluid velocity vectors at $t = 0.1$. The maximum velocity magnitude is 1.4×10^{-4}.

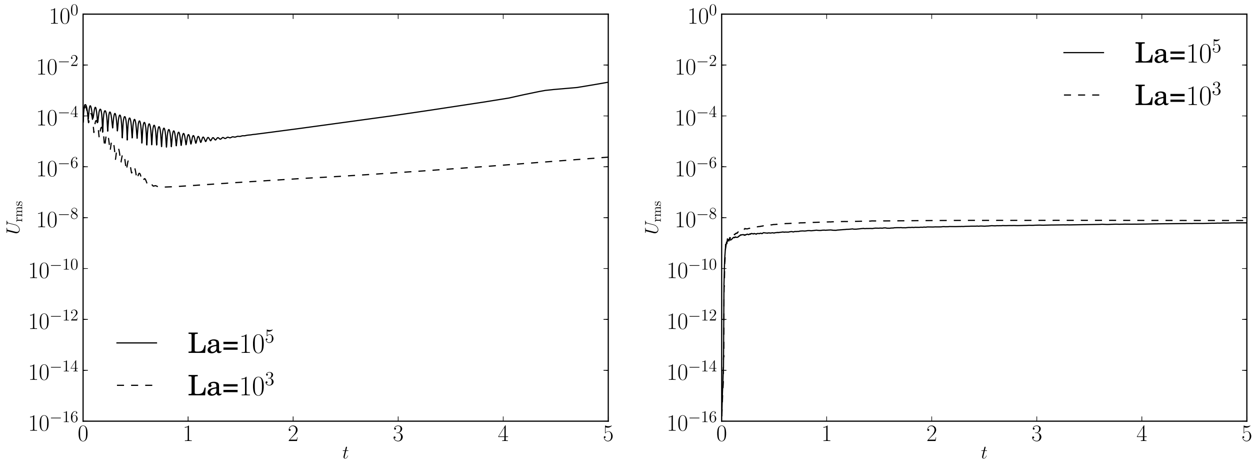

(a)

(b)

Figure 2.6: Time development of the r.m.s. velocity for the static droplet case with $\mathrm{We}_D = 0.25$, and La= 10^3 and La= 10^5. $\mathbf{f}_\sigma$ (Eq. (2.3)) was computed using the curvature, κ, computed using Eq. (2.63) (a), or using the analytical curvature, $\kappa = \kappa_0$ (b).

The error between the exact curvature and numerically computed curvature ($(\kappa - \kappa_0)/\kappa_0$) is shown in Fig. 2.7. There are eight areas where the curvature differs the most from the exact curvature κ_0 where the interface normal is most misaligned from all three spatial axes. These regions are also the regions were spurious currents first occur.

Droplet in a translating reference frame

In this test case, we prescribed a uniform velocity ($u = v = w = 1/(3\sqrt{2})$) throughout the computational domain including the interior of the droplet. Thus, the flow should stay uniform as prescribed by the initial conditions. Figure 2.8 shows the r.m.s. of the generated velocity fluctuations for $\mathrm{We}_D = 0.25$, and Re= 31.6 and Re= 316 corresponding to La= 10^3 and 10^5, respectively. The algorithm proves to be stable, and the r.m.s. of the spurious currents are on the order of 1% of the translating velocity, as shown in Fig. 2.8 (left). Similarly

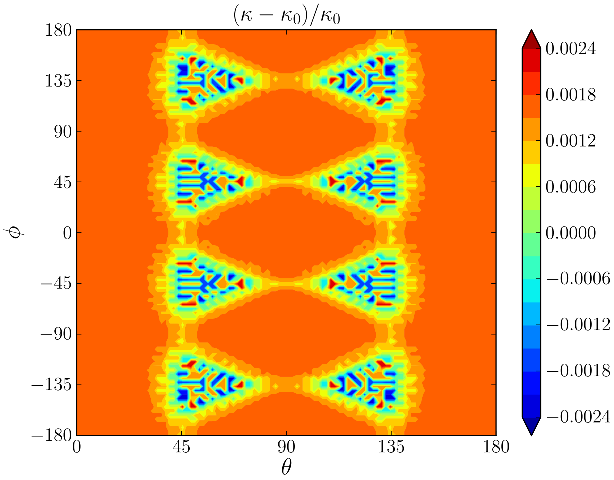

Figure 2.7: Error in curvature, κ, computed with the height-function method, Eq.(2.63), for a spherical droplet with $N_{gp/d} = 32$ as function of spherical coordinates θ and ϕ.

to the case of static droplet, when using $\kappa = \kappa_0$ for computing $\mathbf{f}_\sigma$, the r.m.s. velocity drops to $O(10^{-9})$ as shown in Fig. 2.8 (right).

Droplet in Taylor-Green vortex flow

We then tested the numerical method with a droplet in a Taylor-Green vortex (TGV) flow. Figure 2.9 shows the instantaneous pressure contours, streamlines and droplet/fluid interface ($C = 0.5$ isoline) in the coupled droplet/TGV flow at four different times. This case is for a single spherical droplet with $\mathrm{We}_D = 0.06$, Re= 40 and La=10^3 using $D = 0.15$ and $N_{gp/d} = 20$ in a 128^3 mesh. The initially spherical droplet was released at $t = 0$ with its center at $(x, y, z) = (0.6, 0.5, 0.5)$. The solution is stable after several thousands of time steps, the droplet interface remains smooth in time, and spurious velocities are undetectable in the flow field (Fig. 2.9). In order to quantify if spurious currents affect the mean flow statistics, we have computed the kinetic energy per unit mass, KE, of the single-phase TGV and the droplet-laden TGV at Re= 40, and We_D=0.06 and 0.006, corresponding to La=10^3 and 10^4, respectively. The temporal development of the KE reported in Fig. 2.10 shows that

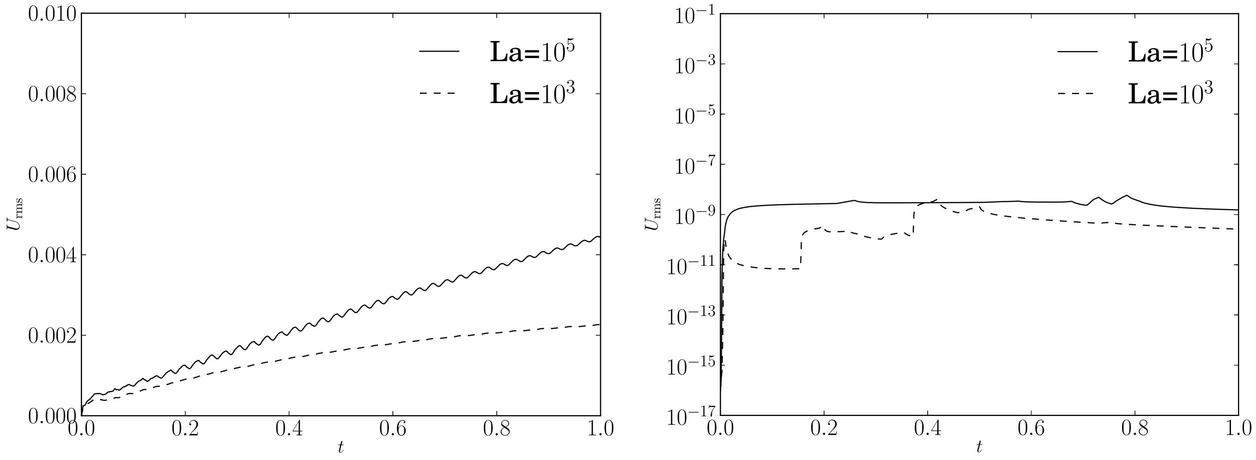

(a) (b)

Figure 2.8: Time development of the spurious r.m.s. velocity for the spherical droplet in a translating reference frame at uniform speed $U = 0.5$ with $\mathrm{We}_D = 0.25$, La= 10^3 and La= 10^5. $\mathbf{f}_\sigma$ (Eq. (2.3)) was computed using the curvature, κ, computed using Eq. (2.63) (left), or using the analytical curvature, $\kappa = \kappa_0$ (right).

the KE of the droplet-laden TGV cases is nearly identical to that of the single-phase TGV, thus, the spurious currents are negligible.

2.4.2 Comparison of FastP, FastP^n, and Unsplit methods*

To determine if the substitution (2.14) is a valid approximation in two-fluid flows for the choices J=1 and J=2, we investigated the agreement of numerical solutions obtained using the FastP^n and FastP* methods with the solution obtained using the Unsplit method, which serves as reference (Table 2.1).

Falling droplet

We simulate a water droplet falling in quiescent air. The dimensional constants for this case are:

$$\begin{aligned}
&\tilde{\rho}_{\mathrm{a}} = 1.204 \text{ kg/m}^3, \quad \tilde{\rho}_{\mathrm{w}} = 998.2 \text{ kg/m}^3, \\
&\tilde{\mu}_{\mathrm{a}} = 1.837 \times 10^{-5} \text{ kg/(m} \cdot \text{s)}, \quad \tilde{\mu}_{\mathrm{w}} = 1.002 \times 10^{-3} \text{ kg/(m} \cdot \text{s)}, \\
&\tilde{\sigma} = 7.28 \times 10^{-2} \text{ kg/s}^2, \\
&\tilde{g} = 9.81 \text{ m/s}^2.
\end{aligned} \tag{2.71}$$

where the subscripts ‘a’ and ‘w’ denote air (fluid 1) and water (fluid 2), respectively. The initial dimensional droplet diameter is $\tilde{D}_0 = 1.4$ mm and the domain is a rectangular box with dimensions $(L_x \times L_y \times L_z) = (2D_0 \times 2D_0 \times 4D_0)$ where $D_0 = 0.5$. The domain is discretized with 64 × 64 × 128 grid points, and the CFL number is $\Delta t/\Delta x = 0.025$ to satisfy Eq. (2.21). The box width $\tilde{L}_x$ and $\sqrt{100\tilde{g}\tilde{L}_x}$ are used as the reference length and velocity scales respectively in Eq. (2.2). The first row of Table 2.2 lists the non-dimensional parameters used in this study.

At time $t = 0$, we released the droplet from rest at $(x, y, z) = (0.5, 0.5, 1.5)$. The flow is integrated from $t = 0$ to $t = 3$ using one of the three different pressure-correction methods described in Sec. 2.2: FastP*, FastP^n, or Unsplit. Figure 2.11 shows the time evolution of the cross-section of the droplet surface in the $y = 0.5$ plane. We find that the FastP* method is in

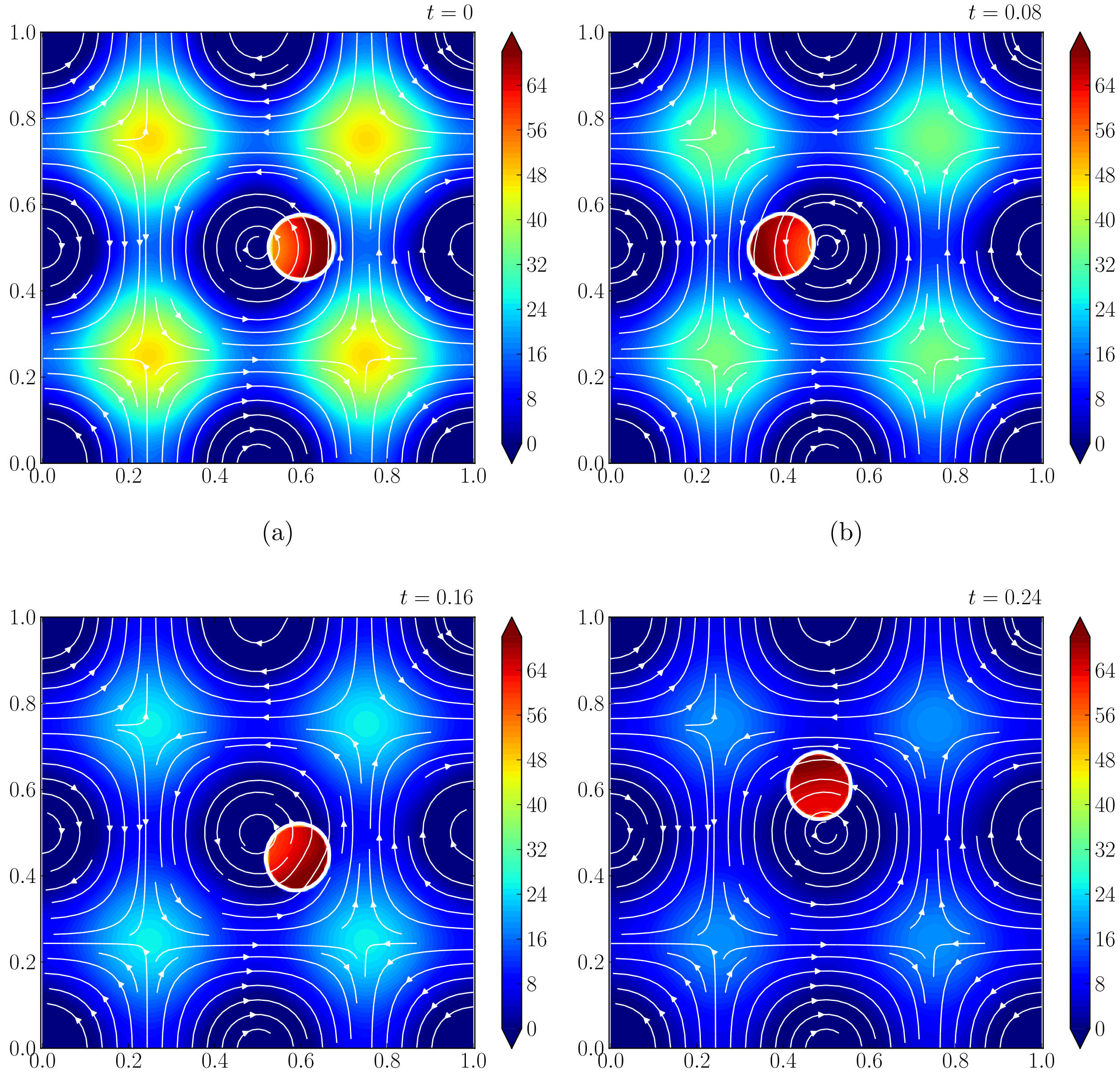

(a)

(b)

(c)

(d)

Figure 2.9: Instantaneous pressure contours and droplet/fluid interface (C=0.5 isoline) for a spherical droplet in the Taylor-Green vortex flow (Re=40, $\mathrm{We}_D = 0.06$, La=10^3, $D = 0.15$, $N_{gp/d} = 20$) at four different times.

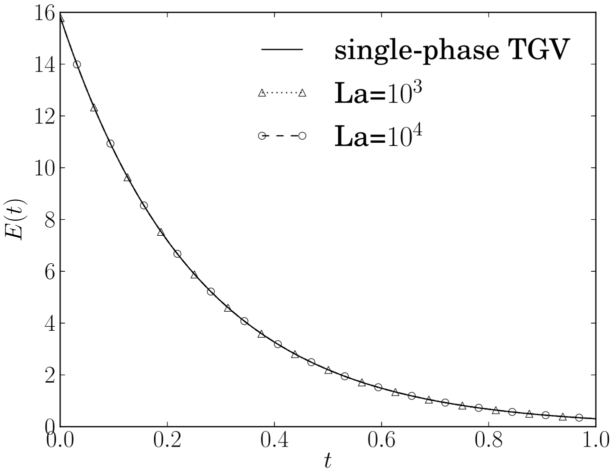

Figure 2.10: Time development of the kinetic energy in the Taylor-Green vortex flow for the single-phase TGV, and the droplet-laden TGV with Re=40, $\mathrm{We}_d = 0.06$ and 0.006 for La=10^3 and 10^4, respectively.

Case	Re	We	Fr	D_0	ρ_2/ρ_1	μ_2/μ_1
Falling droplet	304	0.127	100	0.5	829	54.5
Rising bubble	217	121	1.0	0.5	1.21e-3	2.45e-4

Table 2.2: Non-dimensional parameters used for the rising bubble and falling droplet tests.

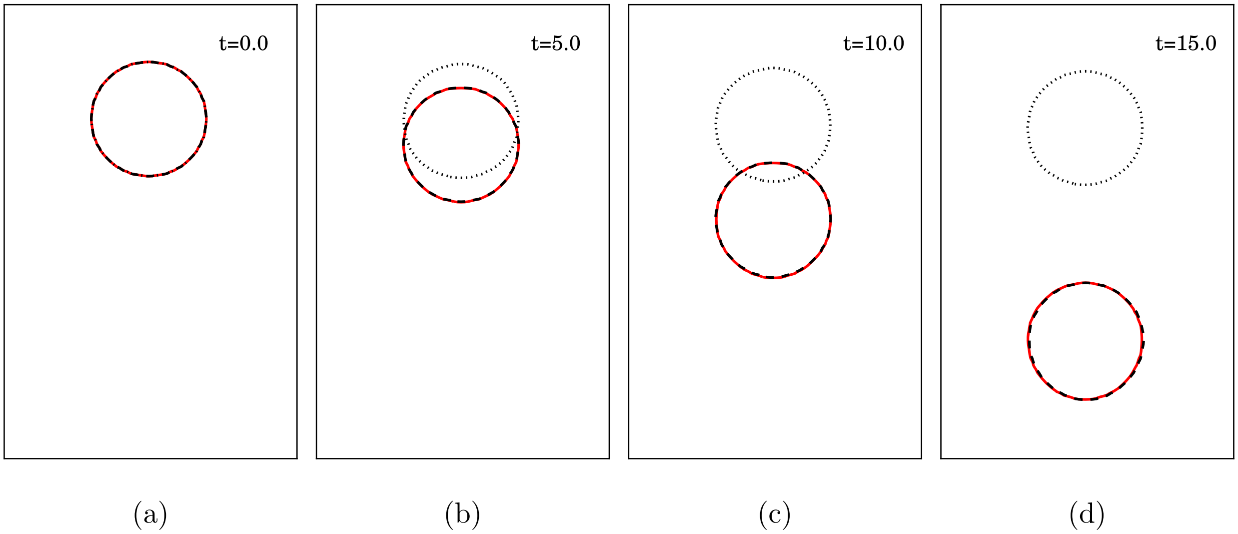

(a) (b) (c) (d)

Figure 2.11: Time development of a water droplet falling in air using the FastP* (dashed black line), FastP^n (dotted black line), and Unsplit (solid red line) methods.

excellent agreement with the Unsplit method, whereas the FastP^n method underpredicts the droplet displacement, in fact, the droplet remains nearly in its initial position. This verifies the FastP* method against the Unsplit method for the falling droplet case. In Section 2.4.6, we validate the FastP* method by comparing our numerical solution for the terminal velocity of a falling droplet to an experimental value.

Rising bubble

Next, we simulate a bubble with initial diameter $\tilde{D}_0 = 1.5$ cm rising in aqueous sugar water due to buoyancy. For this case, fluid 1 is water and fluid 2 is air. The second row of Table 2.2 lists the non-dimensional parameters used for this case. The computational domain and the dimensional parameters are the same as in the falling droplet case (Eq. (2.71)), except the dynamic viscosity of the sugar water is $\tilde{\mu}_{\mathrm{w}} = 7.5 \times 10^{-2}$ kg/(m $\cdot$ s). The domain is discretized with $64 \times 64 \times 128$ grid points, and the CFL number is $\Delta t/\Delta x = 0.005$ to maintain numerical

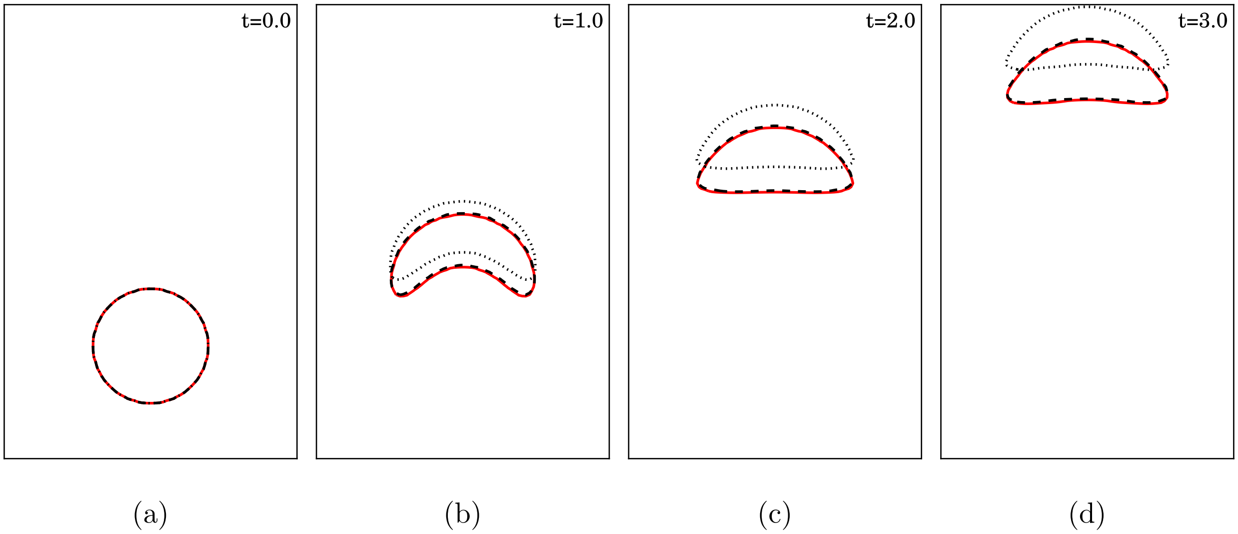

Figure 2.12: Time development of an air bubble (initially spherical) in water using the FastP* (dashed black line), FastP^n (dotted black line), and Unsplit (solid red line) methods.

stability due to the high viscosity ratio ($\mu_1/\mu_2 = 4080$). The box width $\tilde{L}_x$ and $\sqrt{\tilde{g}\tilde{L}_x}$ are used as the reference length and velocity scales, respectively, in Eq. (2.2). At time $t = 0$, we released the bubble from rest at $(x, y, z) = (0.5, 0.5, 0.5)$.

Again, we tested FastP*, FastP^n, and Unsplit for solving this flow. Figure 2.12 shows the time evolution of the bubble surface cross-section in the $y = 0.5$ plane. The results show that the FastP* method is again in excellent agreement with the Unsplit method. In contrast, the FastP^n method is in poor agreement with the Unsplit method. Overall, FastP^n correctly predicts the bubble shape but overpredicts its displacement, whereas FastP* correctly predicts the bubble shape and position. This verifies the FastP* method against the Unsplit method for the rising bubble case as well.

Discussion on the FastP^n and FastP methods*

In this section, we examine the validity of splitting the variable coefficient pressure gradient term as in Eq. (2.5) from a physical viewpoint by considering three positions in a two-fluid flow: (i) in fluid 1, (ii) in fluid 2, and (iii) at the interface separating fluids 1 and 2.

For our example we assume $\rho_2 > \rho_1$, which gives $\rho_0 = \rho_1$. We consider the first position (in fluid 1) and write Eq. (2.5):

$$\frac{1}{\rho_1}\nabla p^{n+1} \rightarrow \frac{1}{\rho_1}\nabla p^{n+1} + \left(\frac{1}{\rho_1} - \frac{1}{\rho_1}\right)\nabla \hat{p} = \frac{1}{\rho_1}\nabla p^{n+1}. \tag{2.72}$$

In (2.72), we observe that the substitution (2.5) applied to fluid 1 is exact. Next, we consider (2.5) in fluid 2 for which the pressure substitution becomes

$$\frac{1}{\rho_2}\nabla p^{n+1} \rightarrow \frac{1}{\rho_1}\nabla p^{n+1} + \left(\frac{1}{\rho_2} - \frac{1}{\rho_1}\right)\nabla \hat{p}. \tag{2.73}$$

This substitution is a good approximation if $\nabla\hat{p} \approx \nabla p^{n+1}$ and exact if $\nabla\hat{p} = \nabla p^{n+1}$. In other words, (2.73) is valid if the local pressure is smooth in time (no shocks, i.e., $\nabla\hat{p} \approx \nabla p^{n+1}$), which holds for incompressible flows. Therefore, we conclude that (2.5) is valid in fluid 2. Last, we consider (2.5) at the interface, which gives

$$\frac{1}{\langle\rho\rangle}\nabla p^{n+1} \rightarrow \frac{1}{\rho_1}\nabla p^{n+1} + \left(\frac{1}{\langle\rho\rangle} - \frac{1}{\rho_1}\right)\nabla \hat{p}. \tag{2.74}$$

Again, this substitution is exact if $\nabla\hat{p} = \nabla p^{n+1}$ and valid if $\nabla\hat{p} \approx \nabla p^{n+1}$. However, at the interface, the local pressure field may not be smooth in time and the pressure jump $\Delta p = p_2 - p_1$ is governed by

$$\Delta p = \sigma\kappa + 2\mu_2 \mathbf{n}\cdot\nabla\mathbf{u}\cdot\mathbf{n} - 2\mu_1 \mathbf{n}\cdot\nabla\mathbf{u}\cdot\mathbf{n} \tag{2.75}$$

where $\mathbf{n}$ is the outward pointing unit normal [33]. We note that because the surface tension force is computed using ∇C, the discrete pressure jump (Δp) will be distributed over a region of thickness $\mathcal{O}(\Delta x)$. The challenge expressed in Eq. (2.74) is to accurately compute $\hat{p}$ using past pressure values (p^n, p^{n-1}, ...) in the sharp transition region such that $\nabla\hat{p} \approx \nabla p^{n+1}$. Our results suggest that a second-order approximation of $\hat{p}$ (FastP*) is significantly more accurate than a first-order approximation of $\hat{p}$ (FastP^n) for predicting the pressure gradient ∇p^{n+1} in the interfacial region. In fact, we found that the first-order approximation is only usable for $\Delta p \approx 0$, i.e., in the limit of zero surface tension ($\sigma = 0$) and inviscid flow ($\mu_2 = \mu_1 = 0$). We also found that using higher-order approximations beyond second-order gave inaccurate results.

While testing the FastP* method, we have found that only in extreme cases of combined high surface tension, curvature, and density ratio, e.g., micron size water droplets in air, the CFL number must be reduced by an amount proportional to the product of σ, κ, and $\max(\rho_2, \rho_1)/\min(\rho_2, \rho_1)$ to preserve numerical accuracy. However, in these extreme cases, the role of surface tension is only to maintain the droplet's spherical shape. Therefore, the surface tension coefficient σ can be reduced as long as the droplet remains spherical, and thus the CFL number can be increased without loss of accuracy. We note that for all the cases presented in this paper, the difference in droplet position and velocity of FastP* relative to Unsplit was less than 1 %.

Performance

The solution of the Poisson equation for pressure is the computational bottleneck in pressure-correction methods, taking more than 50 % of the computational time. In this section, we investigate the computational cost of solving the variable and constant coefficient Poisson equations for pressure in two-fluid flows with the iterative and direct (fast Poisson) solvers, respectively.

To solve the variable coefficient Poisson equation (2.13), we incorporated the *hypre* library [38] into our flow solver. The *hypre* library allows us to benchmark the latest parallel techniques for solving the variable coefficient Poisson equation (2.13) iteratively. We tested different combinations of preconditioners and solvers and found that *hypre* SMG outperformed all others for our test case on a Cartesian uniform grid. Also, we note that *hypre* SMG has good scaling up to 100,000 cores [60] and has been used in other massively parallel incompressible flow solvers [e.g. 61]. Thus, we used *hypre* SMG to solve Eq. (2.13) in our

Unsplit method. Finally, to minimize the number of iterations, we used the previous pressure field (p^n) as an initial guess of the pressure solution (p^{n+1}).

For our test case we simulated a single droplet in decaying isotropic turbulence for 256 time steps. The parameters are:

$$\mathrm{Re} = 107,000,\ \mathrm{We} = 0.25,\ \mathrm{Fr} = \infty,\ D_0 = 0.25,\ \rho_2/\rho_1 = 1000,\ \mu_2/\mu_1 = 1. \tag{2.76}$$

The initial Reynolds number based on the Taylor microscale of turbulence, λ, is $\mathrm{Re}_{\lambda 0} = 190$. The simulations were performed on an Intel Xeon E5-2680 system. We analyzed the weak scaling of the two Poisson solvers by keeping the problem size per core constant at $128^3/2$ grid points and increasing the number of cores from 2 to 1024. For example, when we used 1024 cores we used 1024^3 grid points. For all core counts, *hypre* SMG required 8 multigrid iterations when using a 10^{-6} tolerance. Figure 2.13 shows the average CPU time required to solve the Poisson equations (2.13) and (2.16) using multigrid (*hypre* SMG) and our parallel implementation for multi-core computers of the fast Poisson solver by [62] (see Algorithm of PFPS in Sec. 2.2), respectively. PFPS is about twenty times faster than the multigrid method for all core counts tested. For all cases, the total computational time to solve the two-fluid Navier-Stokes equations ((2.11), (2.16), and (2.17)) for FastP* was ten times lower than that for the Unsplit method.

In addition, the FastP* method satisfies the divergence-free constraint on the velocity field to machine precision at every grid point (i.e., $|\nabla \cdot \mathbf{u}^{n+1}|_{\max} < 10^{-14}$). In contrast, the Unsplit method requires decreasing the convergence tolerance of the multigrid solver to achieve machine precision accuracy. Table 2.3 summarizes the wall clock time and speedup seen when using Multigrid versus PFPS and Unsplit versus FastP* for a tolerance of 10^{-6} and 10^{-14}. These results are for the 1024^3 grid (1024 compute cores). The table shows that for $|\nabla \cdot \mathbf{u}^{n+1}|_{\max} < 10^{-6}$ PFPS is 23 times faster than Multigrid for solving Eq. (2.13) and Eq. (2.16), respectively. If the tolerance is decreased to $|\nabla \cdot \mathbf{u}^{n+1}|_{\max} < 10^{-14}$, the speedup factor increases to 67.52. Table 2.3 shows that for $|\nabla \cdot \mathbf{u}^{n+1}|_{\max} < 10^{-6}$ FastP* is 13.88 times faster than Unsplit for solving Eqs. (2.11)–(2.13) and Eqs. (2.10), (2.16),

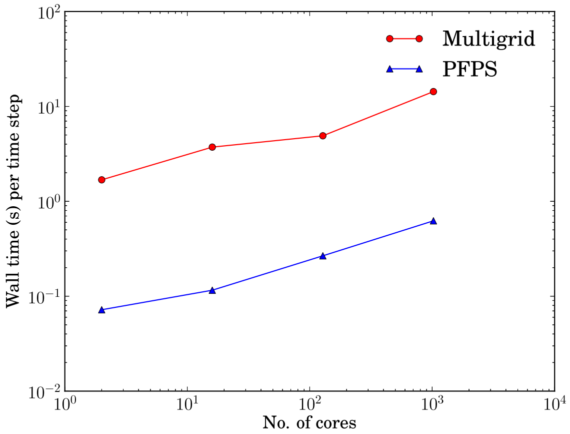

Figure 2.13: Weak scaling of multigrid and fast Poisson solvers on Intel Xeon E5-2680

.

and (2.17), respectively. For the decreased tolerance of $|\nabla \cdot \mathbf{u}^{n+1}|_{\max} < 10^{-14}$, the speedup factor increases to 39.99. As we mentioned, PFPS and FastP* satisfy $|\nabla \cdot \mathbf{u}^{n+1}|_{\max} < 10^{-14}$ by default, whereas for Unsplit, the Multigrid convergence tolerance must be decreased to 10^{-14}. The decreased tolerance increases the number of Multigrid iterations to 34 resulting in greater wall clock time. Table 2.3 also shows that for the Unsplit method the solution of Eq. (2.13) takes greater than 97% of the solution time, and for the FastP* method the solution of Eq. (2.16) takes greater than 58% of the solution time.

Finally, the pressure-splitting (2.14) is also advantageous for iterative methods like *hypre* SMG because it yields only constant coefficient matrices (see left-hand side of Eq. (2.16)), whereas standard Unsplit methods involve variable coefficient matrices (see left-hand side of Eq. (2.13)) that must be setup and computed at each timestep. We found that the setup of the variable coefficient matrix using *hypre* SMG for the Unsplit method costs 25% of the total Poisson solution time. Thus, using Eq. (2.14), saves computational time even when iterative methods are used.

	Poisson solver			Two-fluid Navier-Stokes solver		
Multigrid tolerance	Multigrid (s)	PFPS (s)	Speedup	Unsplit (s)	FastP* (s)	Speedup
$\lvert\nabla \cdot \mathbf{u}^{n+1}\rvert_{\max} < 10^{-6}$	14.32	0.62	23.00	14.74	1.06	13.88
$\lvert\nabla \cdot \mathbf{u}^{n+1}\rvert_{\max} < 10^{-14}$	42.04	0.62	67.52	42.46	1.06	39.99

Table 2.3: Wall clock time per time step (s) and speedup factor for the solution of the Poisson equation (middle column) and the two-fluid Navier-Stokes equations (right column) on a 1024^3 grid using 1024 computing cores on Intel Xeon E5-2680.

2.4.3 Convergence rates

We assess the solver's numerical accuracy by computing its spatial and temporal convergence rates. Special consideration is needed when computing the temporal accuracy of the coupled pressure-correction/VoF flow solver because the VoF advection method uses first-order forward Euler to integrate Eq. (2.47) in time, which is the standard for geometrical VoF methods [45, Chapter 5, p. 108]. In Sec. 2.4.3, we compute the convergence rates independent of the method used to advect the interface by turning the VoF advection off such that $C = C(\mathbf{x})$ for all times. In Sec. 2.4.3 we present the convergence rates with the VoF advection turned on, i.e., $C = C(\mathbf{x}, t)$.

Convergence rates without VoF advection We simulate a fluid cylinder (fluid 2) centered in a two-dimensional Taylor-Green vortex flow (fluid 1) [63]. The non-dimensional parameters for the flow are:

$$\mathrm{Re} = 200,\ \mathrm{We} = \infty,\ \mathrm{Fr} = \infty,\ D = 0.25,\ \rho_2/\rho_1 = 10,\ \mu_2/\mu_1 = 10. \tag{2.77}$$

The fluid velocity in the interior of the cylinder was set equal to the local Taylor-Green vortex velocity at time $t = 0$. In time, the vorticity of both fluids decays owing to viscous diffusion.

	$E_{4\Delta t,2\Delta t}$	$E_{2\Delta t,\Delta t}$	Rate
u	5.94e-8	1.53e-8	1.96
p	3.67e-6	1.84e-6	0.99

Table 2.4: Temporal errors and convergence rate for velocity (u) and pressure (p) in the Taylor-Green vortex flow with a fluid 2 cylinder centered in the domain.

We simulated the flow on a computational mesh of 256^2 points. The smallest time step used was Δt =4.88e-5 and the number of time steps to reach $t_{\text{max}} = 0.05$ was N_t=1024. To evaluate the temporal convergence rate of the solver, the time step was increased to $2\Delta t$ and $4\Delta t$ (N_t=512 and 256) and we computed the error between successive solutions. The L_2 error E for generic flow variable ξ is computed as:

$$E_{2\Delta t,\Delta t} = \sqrt{\frac{1}{N_x N_y}\sum_{i=1}^{N_x}\sum_{j=1}^{N_y}(\xi_{2\Delta t}^{(i,j)} - \xi_{\Delta t}^{(i,j)})^2}. \tag{2.78}$$

Table 2.4 shows the error between successive time steps and the convergence rate. The convergence rate of the u-component of velocity is 1.96, therefore the velocity is second-order in time. The convergence rate of pressure is 0.99, thus it is first-order in time. Second-order pressure convergence in time can be achieved if $\Delta t \gg \text{Re}\Delta x^2$ and periodic boundary conditions are applied [64]. The condition $\Delta t \gg \text{Re}\Delta x^2$ is unlikely to be satisfied in high Reynolds number (Re) turbulent flows. Therefore, the accuracy of the pressure is expected to be first-order for high Re flows and cannot be improved by switching to semi-implicit or implicit time integration, e.g. Adams-Bashforth Crank-Nicolson scheme (see A) when using the pressure-correction method presented. There is a method in which the pressure is 3/2-order accurate in time, but it was developed for single-phase flow [65].

Next, we assess the spatial accuracy of the solver by successively refining the grid and computing the convergence rate of the solution. We again solve the above described Taylor-Green vortex case. We used grids with 32^2, 64^2, and 128^2 points, and we used CFL number

	$E_{4\Delta x,2\Delta x}$	$E_{2\Delta x,\Delta x}$	Rate
u	6.08e-3	1.51e-3	2.01
p	1.04e-1	2.63e-2	1.99

Table 2.5: Spatial errors and convergence rate for velocity (u) and pressure (p) in the Taylor-Green vortex flow with a fluid 2 cylinder centered in the domain.

$\Delta t/\Delta x = 0.001$ such that temporal errors are small. Table 2.5 shows the error between successive grid refinements and the convergence rate. Both velocity and pressure have a second-order convergence rate (2.01 and 1.99, respectively), which is consistent with our central difference discretization in space. In summary, FastP* is first-order in time for the pressure, second-order in time for the velocity, and second-order in space for both pressure and velocity.

Convergence rates with VoF advection

We assess the coupled FastP*/VoF flow solver's numerical accuracy by computing the spatial and temporal convergence rates. The test problem is a two-dimensional capillary wave in a periodic domain. The non-dimensional parameters for the flow are:

$$\mathrm{Re} = 500,\ \mathrm{We} = 1.0,\ \mathrm{Fr} = \infty,\ H_0 = 0.05,\ \rho_2/\rho_1 = 20,\ \mu_2/\mu_1 = 20. \tag{2.79}$$

We do not use Prosperetti's solution [66] for computing the convergence rate of the error because it was derived for fluids of infinite depth and we are using a periodic domain. Instead, we compute the temporal convergence rate by comparing the error in the flow solution computed using successively smaller time steps Δt.

We simulated the flow on a 256^2 grid. The flow was integrated up to $t_{\max} = 0.0625$, and the smallest time step used was Δt =4.88e-5 ($N_t = 1280$). To evaluate the temporal convergence rate of the solver, the time step was increased to $2\Delta t$ and $4\Delta t$ ($N_t = 640$ and

	$E_{4\Delta t,2\Delta t}$	$E_{2\Delta t,\Delta t}$	Rate
u	7.32e-9	3.91e-9	0.90
p	4.67e-7	2.32e-7	1.01
C	7.38e-8	3.58e-8	1.04

Table 2.6: Temporal errors and convergence rate for velocity component (u), pressure (p), and volume fraction (C) in the 2-D capillary wave flow.

320), and we computed the error between successive solutions. The L_2 error E for generic flow variable ξ (u, p, or C) is computed using Eq. (2.78).

Table 2.6 shows the error between successive time step sizes and the convergence rate for u, p, and C. The convergence rate of u is 0.90, which is slightly less than first-order. The convergence rate of pressure and the volume fraction are 1.01 and 1.04 respectively, thus it is first-order. Overall, the coupled flow solver is first-order accurate in time. The cause of the first-order temporal accuracy, despite using second-order Adams-Bashforth in Eq. (2.11), is that the volume fraction is advected by first integrating Eq. (2.47) in each cell and then integrating in time using forward Euler [36, 15]. To overcome this limitation, higher order VoF advection methods have been employed, however they are inadequate for long time simulations [45, Chapter 4, p. 80]. The flow solver could be made fully second-order by using a second-order in time method to advect the interface.

Next, we assess the spatial accuracy of the solver by successively refining the grid and computing the convergence rate of the solution. We solve the above described capillary wave case on 32^2, 64^2, and 128^2 grids. The CFL number is held constant and set to $\Delta t/\Delta x = 0.0025$. Table 2.7 shows the error between successive grid refinements and the convergence rate. The velocity, pressure, and volume fraction all have nearly second-order convergence rates (1.99, 1.89, and 1.87, respectively), which is consistent with our central difference discretization in space (Section 2.2.2) and second-order VoF method [15]. We conclude that

	$E_{4\Delta x,2\Delta x}$	$E_{2\Delta x,\Delta x}$	Rate
u	2.52e-5	6.33e-6	1.99
p	1.68e-3	4.52e-4	1.89
C	1.88e-3	5.14e-4	1.87

Table 2.7: Spatial errors and convergence rate for velocity component (u), pressure (p), and volume fraction (C) in the 2-D capillary wave flow.

the coupled FastP*/VoF method is second-order accurate in space.

2.4.4 Conservation of momentum and kinetic energy

We have checked for discrete linear momentum and kinetic energy conservation in the inviscid limit by simulating a fluid cylinder centered in a two-dimensional Taylor-Green vortex using

$$\mathrm{Re} = \infty,\ \mathrm{We} = \infty,\ \mathrm{Fr} = \infty,\ D = 0.25,\ \rho_2/\rho_1 = 10,\ \mu_2/\mu_1 = 1. \tag{2.80}$$

such that the viscous dissipation of kinetic energy is zero and the interface cannot store energy. We used 128^2 grid points and, at $t = 0$, the fluid velocity in the interior of the cylinder was set equal to the local Taylor-Green vortex velocity. Figure 2.14 shows the time development of the total linear momentum in the x_i direction,

$$\bar{p}_i = \int_V \rho u_i \mathrm{d}V \tag{2.81}$$

normalized by the magnitude of the largest initial momentum vector, $||\mathbf{p}_0||$. Figure 2.14a shows the time development of the kinetic energy

$$K = \int_V \rho u_i u_i \mathrm{d}V \tag{2.82}$$

for for the FastP* versus the Unsplit method. Figure 2.14 shows that the FastP* method and the Unsplit method are in nearly exact agreement. Also, Fig. 2.14 shows that the FastP*

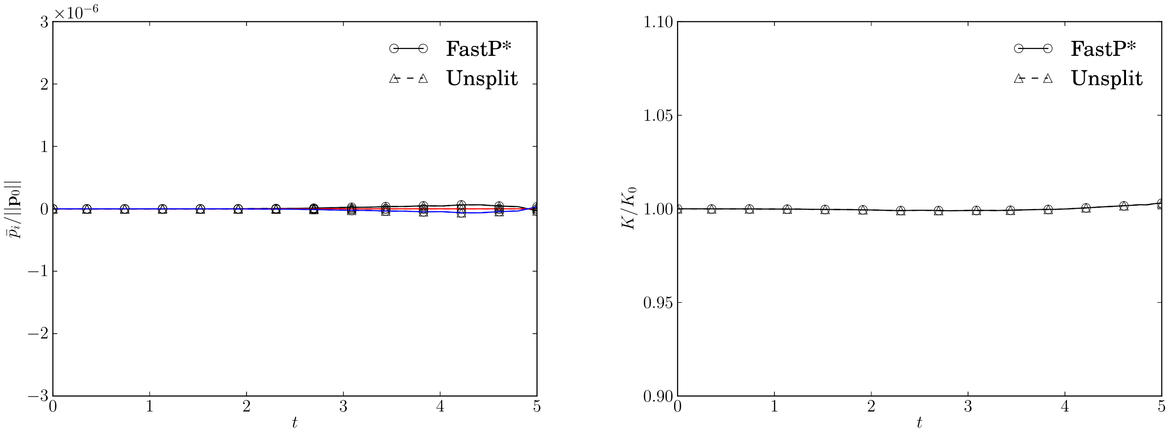

(a) (b)

Figure 2.14: Time development of (a) the x- (black), y- (red), and z-component (blue) of momentum using the FastP* and Unsplit method and (b) the kinetic energy using the FastP* and the Unsplit method.

method conserves momentum and kinetic energy. We associate the slight increase in K seen for $t > 4$ to the increasing deformation of the cylinder interface, and thus decreasing cylinder resolution, $D/\Delta x$. For $t > 4$, parts of the cylinder interface are under resolved ($D/\Delta x < 6$) which decreases the accuracy of the VoF advection algorithm.

2.4.5 Capillary wave

To verify the new pressure-correction method described in Section 2.2, we simulated the capillary wave test case for which there is an analytical solution that was derived by [66]. This test accounts for the effects of surface tension, density ratio, and viscosity ratio. This problem is defined as two immiscible fluids separated by an interface that is initialized with a sinusoidal shape with wavelength λ and small wave amplitude H_0. Prosperetti's analytical solution that we use was derived for two fluids of infinite depth and with equal kinematic viscosities ν.

For our test, we simulated two fluids of equal depth in a periodic domain. The domain has dimensions $0 \le x \le 1$ and $-1.5 \le y \le 1.5$ (64×192 grid points). The volume fraction boundary conditions at the bottom and top boundaries are $C = 1$ for $y = -1.5$ and $C = 0$ for $y = 1.5$. The interface was initialized using a cosine wave with amplitude $H_0 = 0.01$ and wavelength $\lambda = 1.0$ centered at position $y = 0$. The non-dimensional parameters for this case are

$$\mathrm{Re} = 100,\ \mathrm{We} = 1,\ \mathrm{Fr} = \infty,\ \rho_2/\rho_1 = 10 - -10,000,\ \mu_2/\mu_1 = 10 - -10,000, \tag{2.83}$$

Figure 2.15 shows the time development of the wave amplitude H for four cases corresponding to density and viscosity ratios of 10, 100, 1000, and 10,000. For all cases, the numerical simulation is in excellent agreement with Prosperetti's analytical solution, which verifies the pressure-correction method. For the density and viscosity ratio 10 and 100 cases, we used CFL number $\Delta t/\Delta x = 0.01$ so that temporal errors from the VoF advection scheme are negligible [15]. For the 1000 and 10,000 case, we were required to reduce $\Delta t/\Delta x$ to 0.0025 and 0.00025, respectively, to maintain numerical stability. This reduction was required for all the pressure-correction methods tested (i.e., Unsplit, FastP*, and FastP^n). Therefore, we conclude that this numerical stability restriction originates from large density and viscosity gradients produced by the VoF's sharp interface method and not the FastP* method.

2.4.6 Falling droplet in quiescent air

To validate the new pressure-correction method described in Section 2.2, we simulated falling water droplets of varying initial diameter ($\tilde{D}_0 = 0.6$, 1.0, and 1.4 mm) in quiescent air. We determine if the solver can accurately predict the droplet's terminal velocity. We validate our numerical results against Beard's experimental results [67].

The flow is simulated in the droplet reference frame to avoid the extraordinary computational cost required for the fixed reference frame. For example, a 1 mm water droplet released from rest will travel tens of meters before reaching its terminal velocity. The computational domain is a rectangular box with dimensions $(L_x \times L_y \times L_z) = (16D_0 \times 16D_0 \times 32D_0)$ and

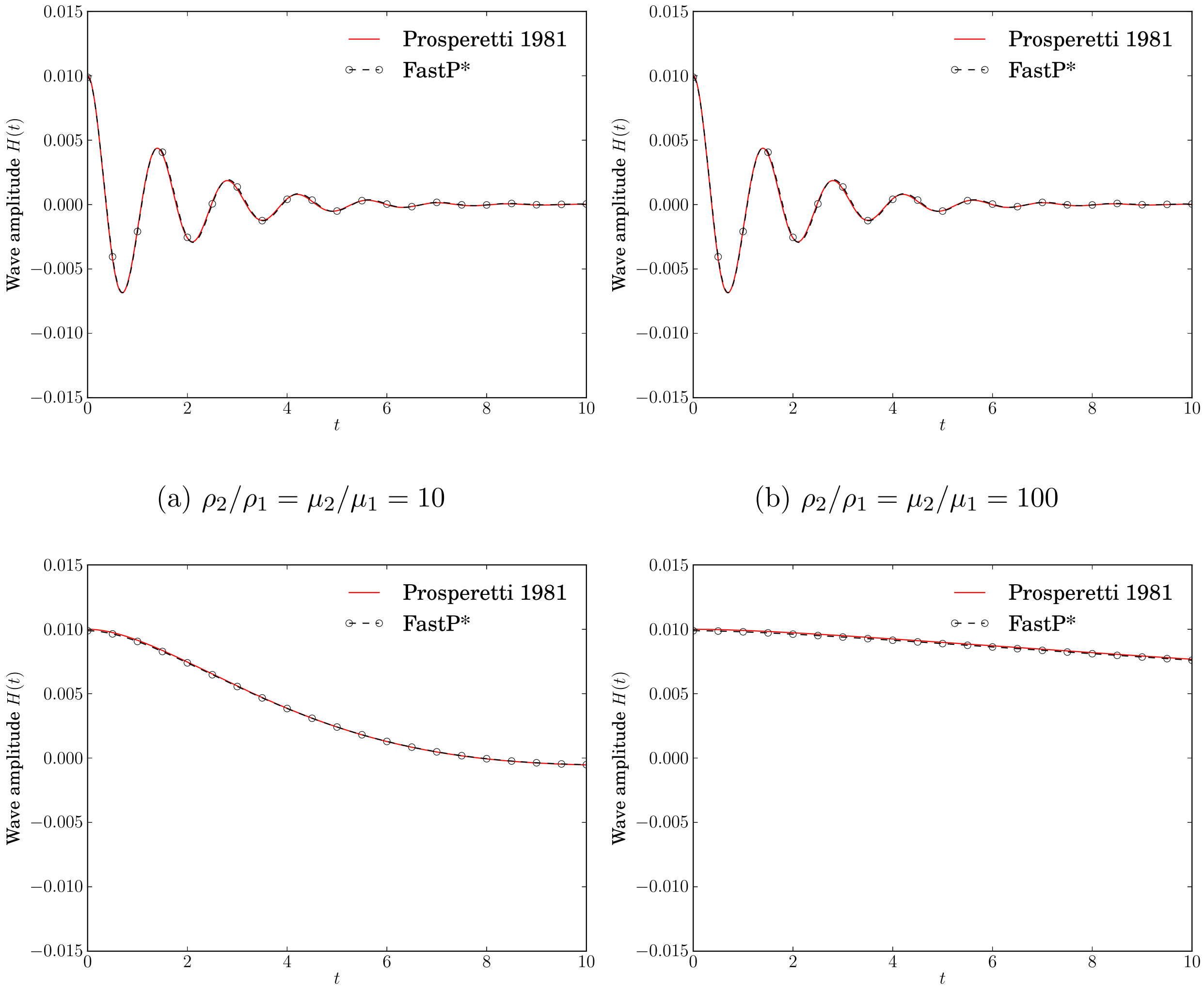

(a) $\rho_2/\rho_1 = \mu_2/\mu_1 = 10$

(b) $\rho_2/\rho_1 = \mu_2/\mu_1 = 100$

(c) $\rho_2/\rho_1 = \mu_2/\mu_1 = 1000$

(d) $\rho_2/\rho_1 = \mu_2/\mu_1 = 10,000$

Figure 2.15: Time development of the capillary wave amplitude for different density and viscosity ratios. Comparison of FastP* numerical solution versus Prosperetti's analytical solution [66].

gravity directed in the negative z-direction. Periodic boundary conditions were imposed in the horizontal x- and y- directions. At the bottom boundary, we imposed a Neumann condition for pressure and a uniform inflow condition for velocity,

$$\frac{\partial p^{n+1}}{\partial z} = 0, \quad u^* = u^{n+1} = 0, \quad v^* = v^{n+1} = 0, \quad w^* = w^{n+1} = V_{\mathrm{t,B}} \ \text{ at } \ z = 0, \tag{2.84}$$

where $V_{\mathrm{t,B}}$ is the droplet's non-dimensional terminal velocity given by Beard's formula [67, Table 1]. At the top boundary, we imposed a Dirichlet condition for pressure and Neumann (stress-free) condition for u, v, and w

$$p^{n+1} = 0, \quad \frac{\partial u^*}{\partial x} = \frac{\partial u^{n+1}}{\partial x} = 0, \quad \frac{\partial v^*}{\partial y} = \frac{\partial v^{n+1}}{\partial y} = 0, \quad \frac{\partial w^*}{\partial z} = \frac{\partial w^{n+1}}{\partial z} = 0 \ \text{ at } \ z = L_z. \tag{2.85}$$

The non-dimensional parameters given by Eq. (2.2) are computed using the box width $\tilde{L}_x$ as the reference length scale, Beard's terminal velocity $\tilde{V}_{\mathrm{t,B}}$ [67] as the reference velocity scale, and the dimensional parameters given in Eq. (2.71). We choose the surrounding fluid (air) as fluid 1 and the droplet (water) as fluid 2. The density ratio $\rho_2/\rho_1 = 829.0$, viscosity ratio $\mu_2/\mu_1 = 54.5$, and initial non-dimensional droplet diameter $D_0 = 0.0625$, were the same for all cases. Table 2.8 shows the non-dimensional parameters for the three cases of different dimensional droplet diameter studied.

Terminal Velocity

The flow is initialized as $(\tilde{u}, \tilde{v}, \tilde{w}) = (0, 0, \tilde{V}_{\mathrm{t,B}})$ except in the (initially spherical) droplet interior, which is set to zero. We simulated the flow on a 512 × 512 × 1024 grid, giving a droplet resolution of 32 grid points per diameter. The simulation is integrated in time from $t = 0$ to $t = 10$, allowing enough time for the droplet to reach equilibrium, i.e., a balance between the drag and gravitational force. This is marked by the droplet's vertical centroid velocity being nearly constant in time (i.e., $\mathrm{d}\tilde{V}_d/\mathrm{d}t \approx 0$). After this condition is met, the numerically determined terminal velocity $\tilde{V}_{\mathrm{t,DNS}}$ can be found from $\tilde{V}_{\mathrm{t,DNS}} = \tilde{V}_{\mathrm{t,B}} + \tilde{V}_d$.

Table 2.8 displays the Reynolds, Weber, and Bond numbers defined, respectively, as

$$\mathrm{Re}_{D_0} = \frac{\tilde{\rho}_a \tilde{V}_{\mathrm{t,B}} \tilde{D}_0}{\tilde{\mu}_a}, \qquad \mathrm{We}_{D_0} = \frac{\tilde{\rho}_a \tilde{V}_{\mathrm{t,B}}^2 \tilde{D}_0}{\tilde{\sigma}}, \ \text{ and } \ \mathrm{Bo}_{D_0} = \frac{(\tilde{\rho}_w - \tilde{\rho}_a)\tilde{g}\tilde{D}_0^2}{\tilde{\sigma}}. \tag{2.86}$$

$\tilde{D}_0$ (mm)	Re_{D_0}	We_{D_0}	Bo_{D_0}	$\tilde{V}_{\mathrm{t,B}}$ (m/s)	$\tilde{V}_{\mathrm{t,DNS}}$ (m/s)	% difference
0.6	95.6	0.06	0.05	2.430	2.441	0.4
1.0	261.8	0.26	0.13	3.994	3.990	-0.1
1.4	472.5	0.61	0.26	5.149	4.957	-3.7

Table 2.8: Falling droplet test parameters. Droplet terminal velocity from Beard's formula [67, Table 1], $\tilde{V}_{\mathrm{t,B}}$, and from DNS result, $\tilde{V}_{\mathrm{t,DNS}}$, and the % difference of the two velocities.

Also shown in Table 2.8 are the dimensional terminal velocities and % difference with the experimental value $(100\times(\tilde{V}_{\mathrm{t,DNS}}-\tilde{V}_{\mathrm{t,B}})/\tilde{V}_{\mathrm{t,B}})$. For all three cases, we show excellent agreement with Beard, which validates our VoF/pressure-correction method.

Droplet wake

For water droplets falling in air with $\mathrm{Bo}_{D_0} < 0.26$ (i.e., D_0=0.6, 1.0, and 1.4 mm), the droplet remains nearly spherical, specifically, there is less than 6 % deviation in height to width ratio from that of a sphere [68, Chapter 7, p. 178]. Therefore, like rigid spheres, these droplets' wakes fall into different regimes depending only on the droplet Reynolds number Re_D. To test the ability of our solver to predict the flow characteristics of these regimes, we have chosen three droplet diameters such to produce wakes that fall into three different regimes. The first regime is for intermediate Reynolds number ($20 \lesssim \mathrm{Re}_D \lesssim 200$), which is characterized by laminar, steady axisymmetric flow, with an attached vortex ring [67]. Figure 2.16(a) shows the instantaneous vorticity contours ω_y for an $x-z$ midplane of the $\tilde{D}_0 = 0.6$ mm droplet with $\mathrm{Re}_{D_0} = 95.6$. The flow solver correctly predicts the laminar and axisymmetric stationary wake. The second regime is for moderate Reynolds number ($200 \lesssim \mathrm{Re}_D \lesssim 450$), which is characterized by asymmetric vorticity in the unsteady wake. Figure 2.16(b) shows

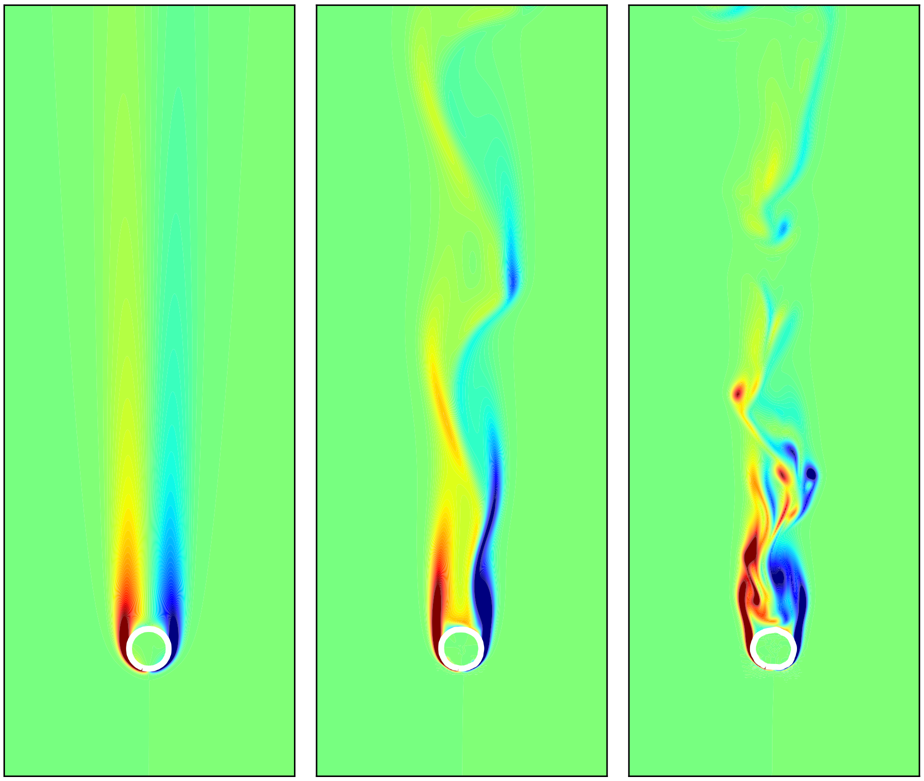

(a) $\tilde{D}_0 = 0.6$ mm (b) $\tilde{D}_0 = 1.0$ mm (c) $\tilde{D}_0 = 1.4$ mm

Figure 2.16: Instantaneous vorticity contours ω_y in a vertical midplane of a water droplet falling in air (Table 2.8). The white line is the droplet interface ($C = 0.5$ isoline).

the vorticity ω_y contours for the $\tilde{D}_0 = 1.0$ mm droplet with $\mathrm{Re}_{D_0} = 261.8$. The third regime is for large Reynolds number ($\mathrm{Re}_D \gtrsim 450$), which is characterized by a chaotic wake. Figure 2.16(c) shows the $\tilde{D}_0 = 1.4$ mm droplet with chaotic wake at $\mathrm{Re}_{D_0} = 472.5$. In conclusion, our flow solver predicts the main flow features of the droplet wake in the range $95.6 \leq \mathrm{Re}_D \leq 472.5$.

To summarize our results for the falling droplet, we found that the coupled pressure-correction/VoF flow solver accurately predicts the terminal velocity of falling water droplets with diameters $\tilde{D}_0 = 0.6$ to $\tilde{D}_0 = 1.4$ mm. Also, the flow solver accurately predicts the droplet wake when the droplet reaches its terminal velocity.

2.5 Summary

We have developed an efficient and second-order accurate pressure-correction method for incompressible two-fluid flows. The method reduces the Poisson equation for pressure from variable to constant coefficient, starting from a splitting idea by Dong and Shen [30]. However, our numerical tests showed that applying this splitting to the pressure gradient term (i.e., using Eq. (2.5) with $\hat{p} = p^n$, called our FastP^n method) is only accurate for vanishingly small surface tension and viscosity. For viscous flows with finite surface tension, we showed that $\hat{p} = p^* = 2p^n - p^{n-1}$ should be used (FastP*). Additionally, we verified FastP* up to a density and viscosity ratio of 10,000, and validated the method for a water droplet falling in air. Finally, we showed that FastP* is capable of fully-resolved DNS of thousands of freely moving droplets in decaying isotropic turbulence on a 1024^3 grid. In summary, we have shown that FastP*:

- reduces the commonly encountered variable coefficient Poisson equation to a constant coefficient equation, which allows for the use of a direct Poisson solver,
- is in excellent agreement with the Unsplit method,
- is about 10–40 times faster than the Unsplit method and our fast Poisson solver is about 20–60 times faster than Multigrid, depending on the tolerance used for Multigrid,
- is second-order in space and time for velocity and second- and first-order in space and time, respectively, for pressure,
- is verified for density and viscosity ratios up to 10,000,
- is validated for a falling water droplet in quiescent air for $95.6 \leq \mathrm{Re} \leq 472.5$, $0.06 \leq \mathrm{We} \leq 0.61$, and $0.05 \leq \mathrm{Bo} \leq 0.26$,

- conserves mass, momentum, and kinetic energy (in the inviscid limit),
- is capable of fully-resolved DNS of thousands of freely moving droplets in decaying isotropic turbulence on a 1024^3 grid in $\mathcal{O}(10)$ hours using 1024 computing cores.

We conclude that FastP* is well-suited for simulating two-fluid flows requiring high spatial and temporal resolution throughout the domain, e.g., droplet- or bubble-laden turbulent flows. Also, because FastP* uses a direct solver, it can be easily adopted in existing incompressible flow codes that rely on a direct solver. Furthermore, FastP* is capable of simulating flows with Dirichlet and Neumann boundary conditions for pressure by using the appropriate modifications to the fast Poisson solver (see, e.g., [21, 22]).

Chapter 3

DNS OF NON-EVAPORATING DROPLETS IN ISOTROPIC TURBULENCE

3.1 Initial conditions and droplet properties

3.1.1 Carrier flow parameters and initial conditions

The initial velocity field was generated by prescribing the TKE spectrum $E(\kappa)$ and ensuring that the initial random velocity field is isotropic, divergence-free with respect to the discretized form of the continuity equation and that the velocity cross-correlation spectra, $R_{ij}(\kappa)$, satisfy the realizability constraint [69].

The initial energy spectrum at time $t = 0$ was prescribed as [70, Sec. 6.5.3]:

$$E(\kappa) = 1.5\left[\varepsilon_0^{2/3}\kappa^{-5/3} f_L(\kappa L) f_\eta(\kappa\eta)\right] \tag{3.1}$$

where κ is the wavenumber, ε_0 is the initial dissipation rate of TKE, $L \equiv k_0^{3/2}/\varepsilon_0$, where k_0 is the initial TKE, f_L is given by

$$f_L(\kappa L) = \left(\frac{\kappa L}{[(\kappa L)^2 + c_L]^{1/2}}\right)^{11/3} \tag{3.2}$$

and f_η is given by

$$f_\eta(\kappa\eta) = \exp\left\{-5.2\left\{\left[(\kappa\eta)^4 + c_\eta^4\right]^{1/4} - c_\eta\right\}\right\}, \tag{3.3}$$

where $c_L = 4.698$ and $c_\eta = 0.416$. The constants c_L and c_η are calculated such that $E(\kappa)$ and $2\mathrm{Re}^{-1}\kappa^2 E(\kappa)$ integrate to k_0 and ε_0, respectively. The values of the dimensionless parameters at $t = 0$ were $k_0 = 3.893 \times 10^{-3}$, $\varepsilon_0 = 1.156 \times 10^{-3}$ and $\mathrm{Re} = 6.42 \times 10^4$. These parameters yield an initial Reynolds number based on the Taylor lengthscale of $\mathrm{Re}_{\lambda 0} = 75$. Figure 3.1 shows the turbulence kinetic energy spectrum at $t = 1$ in case A.

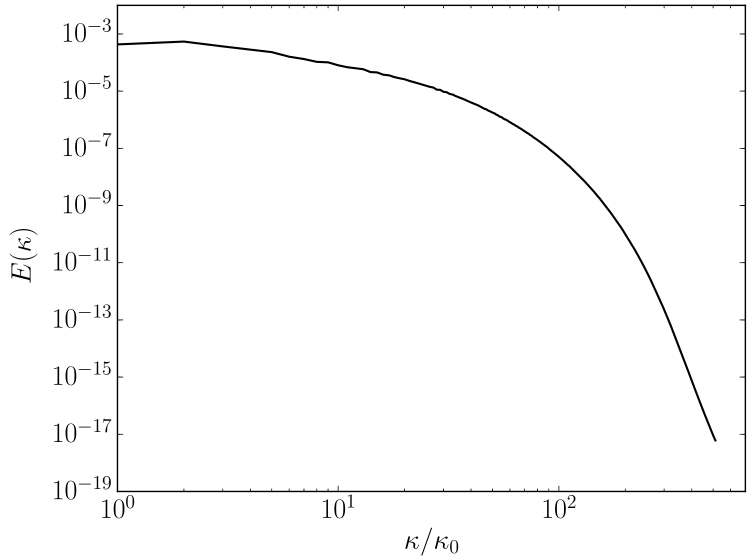

Figure 3.1: Turbulence kinetic energy spectrum at droplet release time, $t = 1$, in case A. The wavenumbers are normalized by the lowest non-zero wavenumber, $\kappa_0 = 2\pi/\mathcal{L}$.

Table 3.1 shows the dimensionless flow parameters at different times t for the droplet-free flow (case A): ℓ and τ_ℓ are the integral length and time scales; Re_ℓ is the Reynolds number based on ℓ; λ is the Taylor lengthscale; η and τ_η are the Kolmogorov length and time scales. The values of the reference length and velocity scales used in normalizing the above quantities were $\tilde{L}_{ref} = 0.032$ m and $\tilde{U}_{ref} = 26.7$ m s^{-1}, which together with the Reynolds number Re, produce the appropriate value of the dimensional kinematic viscosity of the fluid (air at STP) $\tilde{\nu}_{ref} = 1.33 \times 10^{-5}$ m^2 s^{-1}. The smallest scales of turbulence are well resolved as indicated by $\eta\kappa_{\max} \geq 1$ at all times, where $\kappa_{\max} = \pi N$ is the maximum resolved wavenumber and $N = 1024$ is the number of grid points in each direction of our computational grid.

3.1.2 Droplet properties

We perform one simulation (case A) of droplet-free flow and eight simulations (A*–H) of droplet-laden isotropic turbulence (table 3.2). Case A* is a limiting case in which the viscosity

t	U_{rms}	ε	ℓ	λ	η	Re_ℓ	Re_λ	ℓ/η	τ_ℓ	τ_λ	τ_η
0.0	0.0509	$1.15e-3$	0.0965	0.0229	$1.35e-3$	316	75	71.7	1.89	0.45	0.116
1.0	0.0457	$6.10e-4$	0.1038	0.0283	$1.58e-3$	305	83	65.8	2.27	0.62	0.160
6.0	0.0285	$2.18e-4$	0.1082	0.0295	$2.04e-3$	198	54	54.0	3.80	1.05	0.268

Table 3.1: Flow parameters (dimensionless) at initial time ($t = 0$), droplet release time ($t = 1$) and at time $t = 6$ in case A.

and density ratio are unity and the Weber number of the "droplets" is infinity (i.e., the surface tension is null via (2.1b)). We analyze the effects of varying the initial droplet Weber number ($We_{\mathrm{rms}} = D_0 U_{\mathrm{rms}}^2 \rho_c/\sigma$), droplet- to carrier-fluid density ratio ($\varphi = \rho_d/\rho_c$) and droplet- to carrier-fluid viscosity ratio ($\gamma = \mu_d/\mu_c$) in the three sets BCD, CEF, and CGH, respectively, while keeping the other two parameters constant. In cases B, C and D, $\mathrm{We}_{\mathrm{rms}}$ increases from 0.1 to 5.0 by decreasing the non-dimensional surface tension coefficient, $\sigma = 1/\mathrm{We}$, in (2.3). In cases E, C and F, φ increases from 1 to 100 by increasing ρ_d. This in turn increases the mass loading ratio, ϕ_m, from 0.05 to 5.0. In cases G, C and H, γ increases from 1 to 100 by increasing μ_d. The droplet properties were selected for their engineering relevance in spray combustion devices. For all cases, the droplet volume fraction is $\phi_v = 0.05$, the initial number of droplets is $N_d = 3130$, and the initial droplet diameter is $D_0 = 0.03125$ ($\tilde{D}_0 = 1.0$ mm), which is $20\eta_1$ (or $1.1\lambda_1$), where η_1 and λ_1 are the Kolmogorov and Taylor length scales, respectively, at the time the droplets are released in the flow ($t = 1$). In table 3.2 we report the droplet response time, which for the Hadamard–Rybczyński solution [71, 72] of creeping flow over a fluid sphere is

$$\tau_d = \frac{\rho_d}{\rho_c}\frac{D^2}{6\nu}\left(\frac{1+\gamma}{2+3\gamma}\right). \tag{3.4}$$

The prescribed initial velocity field $\mathbf{u}_0$ (see §3.1) evolves free of droplets until $t = 1$, at which time $\mathrm{Re}_{\lambda 1} = 83$ and the skewness of the velocity derivative S_u has reached the value

Case	$\mathrm{We}_{\mathrm{rms}}$	$\varphi \equiv \rho_d/\rho_c$	$\gamma \equiv \mu_d/\mu_c$	τ_d	τ_d/τ_ℓ	τ_d/τ_η	ϕ_m	ϕ_v	We
A	–	–	–	–	–	–	0	0	–
A*	∞	1	1	–	–	–	0.05	0.05	∞
B	0.1	10	10	35.9	15.8	225	0.5	0.05	1.53×10^3
C	1.0	10	10	35.9	15.8	225	0.5	0.05	1.53×10^4
D	5.0	10	10	35.9	15.8	225	0.5	0.05	7.65×10^4
E	1.0	1	10	3.59	1.58	22.5	0.05	0.05	1.53×10^4
F	1.0	100	10	359	158	2250	5.0	0.05	1.53×10^4
G	1.0	10	1	41.8	18.4	261	0.5	0.05	1.53×10^4
H	1.0	10	100	34.9	15.4	219	0.5	0.05	1.53×10^4

Table 3.2: Droplet properties (dimensionless) at release time ($t = 1$).

-0.50, indicating an established nonlinear transfer of TKE across the spectrum. At that time ($t = 1$), the droplets are randomly seeded at rest in the computational domain under the constraint that the distance between their centers must be at least $2.1D_0$, such as to delay droplet-droplet coalescence in cases in which droplets coalesce. In all droplet-laden cases A*–H, the initial positions of the droplets are identical. We also tested different initial random seedings of droplets, and found that the terms in the TKE budget varied by less than 1 % from the mean except Ψ_σ. The power of the surface tension (Ψ_σ) is nearly independent of the droplet seeding for short times. After the onset of coalescence there is slight variation in the power of the surface tension – however, the overall trend is unchanged. Thus, we conclude that the results are essentially statistically independent of the initial positions of the droplets.

The droplets are resolved by 32 grid points per diameter ($D_0/\Delta x = 32$). This resolution provides a good compromise between VoF geometrical accuracy and computational efficiency as shown in [15]. The time step used is $\Delta t = 0.1\Delta x$ and the simulations were stopped after

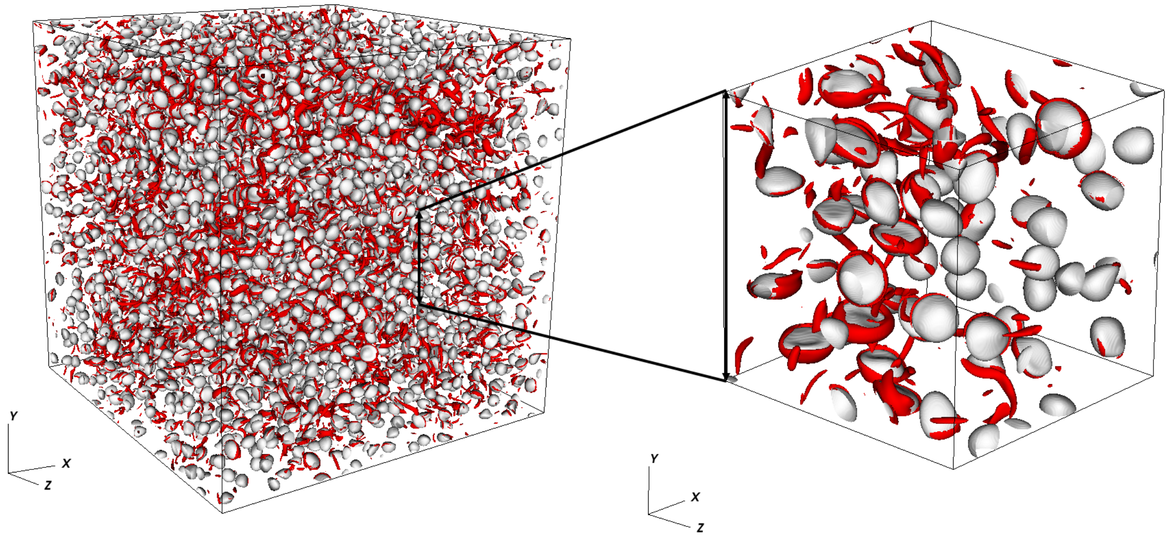

Figure 3.2: Instantaneous droplet interfaces in white ($C = 0.5$ isosurface) and vortical structures in red ($\lambda_2 = -50$ isosurfaces, see [73] for definition of λ_2) in case D at $t = 1.5$. (Left) full domain ($1 \times 1 \times 1$); (right) sub-domain ($0.25 \times 0.25 \times 0.25$).

61,440 time steps at $t = 6$. At this time $\mathrm{Re}_\lambda = 54$ in case A. A snapshot of the computational domain is shown in figure 3.2 which depicts the droplets and vortical structures in case D at $t = 1.5$.

When performing two-fluid flow simulations with surface tension and sharp-interface capturing like VoF, the small errors in the numerical calculation of the interface curvature, κ, generate spurious currents, i.e. unphysical velocity fluctuations near the interface. For droplets at rest or in uniform translation, the magnitude of the spurious currents increases with increasing Laplace number [25, 15],

$$\mathrm{La} = \frac{\sigma \rho D}{\mu^2}; \tag{3.5}$$

therefore, we used the Laplace number to estimate their magnitude in the flow under study. In [15], we showed that, for a droplet in uniform translation and Laplace number of 100,000, the r.m.s. velocity of the spurious currents was less than 0.5% of the translation speed. In cases B–H, the maximum Laplace number is 84,310, and therefore, we expect the magnitude of the spurious currents to be less than 0.5% of U_{rms}. To check if the simulations are tainted by spurious currents, we computed the specific energy spectrum, $E(\kappa)$, by using the entire domain of the velocity field, in cases A–H at $t = 3.5$ (figure 3.3). Spurious currents generate eddies with size of the order of the droplet diameter [see Fig. 17 of 15]. Therefore, evidence of such currents would be marked by a source of energy at wavenumbers near the droplet diameter. Figure 3.3 shows that in the droplet-laden cases (B–H), there is no unphysical bump in the spectra at wavenumbers associated with the droplet diameter. Thus, this shows that any kinetic energy added to the flow artificially by spurious currents is negligible.

Compared to the single-phase spectra (A and A*), the droplet-laden spectra (B–H) show increased energy at high wavenumbers. The increase in energy at high wavenumbers has been explained for finite-size solid particles in decaying isotropic turbulence. [74] showed that the presence of solid particles with $D \sim \lambda$ broke the 'order' of large eddies and creates new eddies of size $D/2 \sim \lambda/2$ on the downstream side of the particle, thus increasing the energy at high wavenumbers. We believe that the presence of the droplet interface also breaks up large eddies, increasing the transfer rate of energy from low to high wavenumbers. Also, notice that $E(\kappa)$ was computed by using the entire domain, therefore the droplet-laden spectra in figure 3.3 includes specific energy from the droplet interiors. Still, the spectra are mostly comprised of the carrier-fluid specific energy (95% by volume). To fully isolate the effects of droplets on the carrier flow would require limiting the FFT analysis to the carrier fluid.

3.2 Turbulence kinetic energy equations

In order to understand and explain the physical mechanisms of droplet and turbulence interactions, we use the evolution equations for the TKE of the two-fluid flow, $k(t)$, the carrier-fluid flow, $k_c(t)$, and the droplet-fluid flow, $k_d(t)$. These equations are derived in Appendix C.

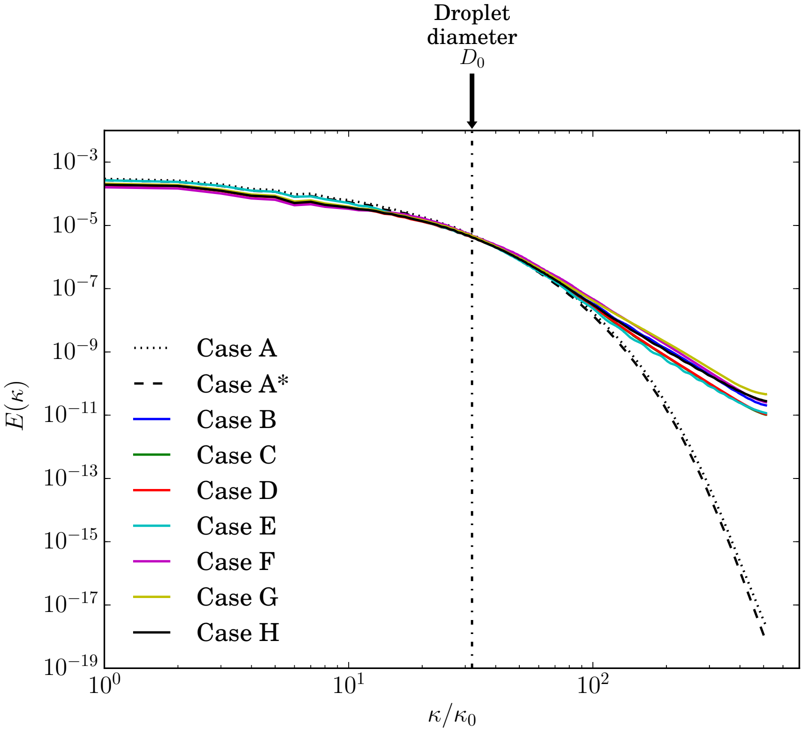

Figure 3.3: Spectra of the specific turbulence kinetic energy at $t = 3.5$ in cases A–H. The wavenumbers are normalized by the lowest non-zero wavenumber, $\kappa_0 = 2\pi/\mathcal{L}$.

The evolution equation for $k(t)$ is

$$\frac{\mathrm{d}k(t)}{\mathrm{d}t} = -\varepsilon(t) + \varPsi_\sigma(t), \tag{3.6}$$

where

$$k(t) \equiv \tfrac{1}{2}\langle \rho u_j u_j \rangle, \quad \varepsilon(t) \equiv \frac{1}{\mathrm{Re}}\langle \mathsf{T}_{ij}\mathsf{S}_{ij}\rangle, \quad \varPsi_\sigma(t) \equiv \frac{1}{\mathrm{We}}\langle u_j f_{\sigma,j}\rangle, \tag{3.7}$$

where $\langle \cdots \rangle$ denotes spatial averaging over the entire domain. T_{ij} is the viscous stress tensor ($\mathsf{T}_{ij} = 2\mu \mathsf{S}_{ij}$) and S_{ij} is the strain-rate tensor, which was defined in §2.1. In (3.7), $\varepsilon(t)$ is the dissipation rate of TKE of the two-fluid flow and $\varPsi_\sigma(t)$ is the power of the surface tension, respectively. By definition, $\varepsilon(t)$ is positive, thus it is a sink of TKE, whereas $\varPsi_\sigma(t)$ is either positive or negative, and thus a source or sink of TKE.

The evolution equation for $k_c(t)$ is

$$\frac{\mathrm{d}k_c(t)}{\mathrm{d}t} = -\varepsilon_c(t) + T_{\nu,c}(t) + T_{p,c}(t), \tag{3.8}$$

and the evolution equation for $k_d(t)$ is

$$\frac{\mathrm{d}k_d(t)}{\mathrm{d}t} = -\varepsilon_d(t) + T_{\nu,d}(t) + T_{p,d}(t). \tag{3.9}$$

The terms in (3.8) and (3.9) are defined as

$$\begin{aligned} k_c(t) &\equiv \tfrac{1}{2}\langle \rho u_j u_j \rangle_c, \quad \varepsilon_c(t) \equiv \frac{1}{\mathrm{Re}}\langle \mathsf{T}_{ij}\mathsf{S}_{ij}\rangle_c, \\ T_{\nu,c}(t) &\equiv \frac{1}{\mathrm{Re}}\frac{\partial\langle \mathsf{T}_{ij}u_j\rangle_c}{\partial x_i}, \quad T_{p,c}(t) \equiv -\frac{\partial\langle u_j p\rangle_c}{\partial x_j}, \end{aligned} \tag{3.10}$$

and

$$\begin{aligned} k_d(t) &\equiv \tfrac{1}{2}\langle \rho u_j u_j \rangle_d, \quad \varepsilon_d(t) \equiv \frac{1}{\mathrm{Re}}\langle \mathsf{T}_{ij}\mathsf{S}_{ij}\rangle_d, \\ T_{\nu,d}(t) &\equiv \frac{1}{\mathrm{Re}}\frac{\partial\langle \mathsf{T}_{ij}u_j\rangle_d}{\partial x_i}, \quad T_{p,d}(t) \equiv -\frac{\partial\langle u_j p\rangle_d}{\partial x_j}, \end{aligned} \tag{3.11}$$

where $\langle \ldots \rangle_c$ and $\langle \ldots \rangle_d$ denote spatial averaging over the carrier fluid and droplet fluid, respectively. In (3.10) and (3.11), $\varepsilon_c(t)$ and $\varepsilon_d(t)$ are the dissipation rates of TKE, $T_{\nu,c}(t)$ and $T_{\nu,d}(t)$ are the viscous powers, and $T_{p,c}(t)$ and $T_{p,d}(t)$ are the pressure powers where, as a reminder, the subscripts c and d denote properties of the carrier- and droplet-fluid flow. For example, $\varepsilon_c(t)$ is the dissipation rate of TKE of the carrier-fluid. By definition, $\varepsilon_c(t)$ and $\varepsilon_d(t)$ are positive, thus they are sinks of TKE, whereas $T_{p,c}(t)$, $T_{p,d}(t)$, $T_{\nu,c}(t)$ and $T_{\nu,d}(t)$ are either positive or negative, and thus sources or sinks of $k_c(t)$ or $k_d(t)$. The power terms in (3.6), (3.8) and (3.9) are related through the identity

$$\mathit{\Psi}_\sigma(t) = (1-\phi_v)\left[T_{\nu,c}(t) + T_{p,c}(t)\right] + \phi_v\left[T_{\nu,d}(t) + T_{p,d}(t)\right], \tag{3.12}$$

which is also derived in Appendix C.

The derived equations, (3.6), (3.8) and (3.9), are summarized schematically in figure 3.4, which depicts the pathways for TKE exchange in droplet-laden isotropic turbulence, and more generally in two-fluid (liquid-liquid or gas-liquid) isotropic turbulence. All terms responsible for the evolution of $k(t)$ (3.6), $k_c(t)$ (3.8) and $k_d(t)$ (3.9) are represented. The middle dashed rectangle encompasses the TKE of the two-fluid flow k, and shows that the dissipation rate, ε, (red arrows) is a sink of TKE and the power of the surface tension, $\mathit{\Psi}_\sigma$, (blue arrow) is either a source or sink of TKE. The power (or transport) terms $T_{\nu,c}(t)$, $T_{p,c}(t)$, $T_{\nu,d}(t)$, $T_{p,d}(t)$ (green arrows) act to redistribute TKE between the carrier fluid and droplet fluid or into interfacial surface energy via three bidirectional pathways: (i) carrier fluid ↔ droplet fluid (ii) carrier fluid ↔ interface and (iii) droplet fluid ↔ interface (white arrow). This relationship is expressed mathematically by (3.12).

3.3 Comparison of TKE budget for droplet-free and droplet-laden turbulence

In this section, we present the effects of the droplets on turbulence relative to the droplet-free flow by analyzing the terms of the TKE budget equation (3.6), and then explain the underlying physical mechanisms.

3.3.1 Two-fluid TKE budget

Figure 3.5 shows the temporal evolution of the turbulence kinetic energy for the two-fluid flow normalized by its initial value, $k(t)/k_0$, in cases A–H. When the droplets are introduced

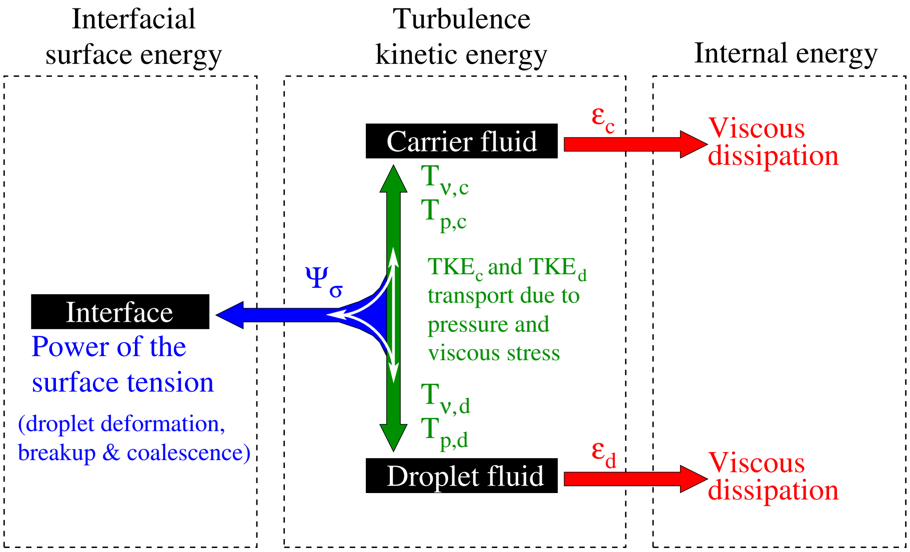

Figure 3.4: Schematic showing the pathways for TKE exchange in droplet-laden, decaying isotropic turbulence. The dashed rectangles from left to right encompass the interfacial surface energy, TKE, and internal energy. The blue arrow represents TKE being exchanged for interfacial surface energy and vice versa by the power of the surface tension. The green arrow denotes transport of TKE between the two fluids and exchange of TKE for surface energy and vice versa. The red arrows represent TKE of the carrier fluid and droplet fluid being transformed into internal energy by viscous dissipation.

($t = 1$), $k(t)$ falls by 5 %, corresponding to the volume fraction of fluid that has been set to zero velocity at this time. In all cases A*–H, $k(t)$ remains lower than that in the droplet-free flow (case A).

Figure 3.6 shows the temporal evolution of the rate of change of the TKE normalized by the initial dissipation rate, $\mathrm{d}(k(t)/\varepsilon_0)/\mathrm{d}t$, in cases A–H. The introduction of the droplets (cases A*–H) increase the initial decay rate of TKE with respect to that of the single-phase flow (case A). For later times ($t > 1 + \tau_\ell$), the decay rate of TKE in cases A*–H stays smaller than that in case A. At early times ($1 < t < 1 + \tau_\ell$), increasing We_{rms} (cases B–D), φ (cases E, C and F), or γ (cases G, C and H) leads to an increase in the decay rate of TKE. At later times $t > 1 + \tau_\ell$, the decay rate of TKE is nearly independent of We_{rms} (figure 3.6a) and γ (figure 3.6c), but decreases monotonically as φ increases (figure 3.6b).

Figure 3.7 and supplementary movie 1 show two-dimensional contours of the local instantaneous kinetic energy ($k' \equiv \frac{1}{2}(\rho u_j u_j)$) and the fluid velocity vectors (u_j) in a sub-region of the computational domain in cases A and C at $t = 1.5$, which corresponds to approximately one Taylor timescale after droplet release ($t \approx 1 + \tau_\lambda$). Comparing figures 3.7(a) and 3.7(b), we note that in 3.7(b) (case C) there are less regions of high k' (red regions), particularly in the droplet wake. Also, inside the droplets, $k' > 0'$, which denotes an increase because the droplets were initially released from rest. This is consistent with k being lower in cases A*–H than it is in case A because $k = \langle k' \rangle$.

To explain why droplets enhance the decay rate of $k(t)$, we analyze the temporal evolution of the terms on the right-hand side of (3.6), that is $\varepsilon(t)$ and $\mathit{\Psi}_\sigma(t)$ (represented by red and blue arrows in figure 3.4). Figure 3.8 shows the temporal evolution of the normalized dissipation rate of TKE for the two-fluid flow, $\varepsilon(t)/\varepsilon_0$. When droplets are introduced into the flow (cases A*–H) at $t = 1$, $\varepsilon(t)$ spikes relative to that of case A. At $t \approx 1 + \tau_\ell$, $\varepsilon(t)$ in cases A*–H crosses over that of case A. The crossover of $\varepsilon(t)$ at $t \approx 1 + \tau_\ell$ (except for in case A*and B) occurs because $k(t)$ in the droplet-laden cases at later times is less than $k(t)$ of the droplet-free case (A), and therefore, the dissipation rate of $k(t)$ is also lower. Furthermore, figures 3.8(a) and 3.8(c) show that, for early times ($1 < t < 1 + \tau_\ell$), $\varepsilon(t)$ is approximately independent of

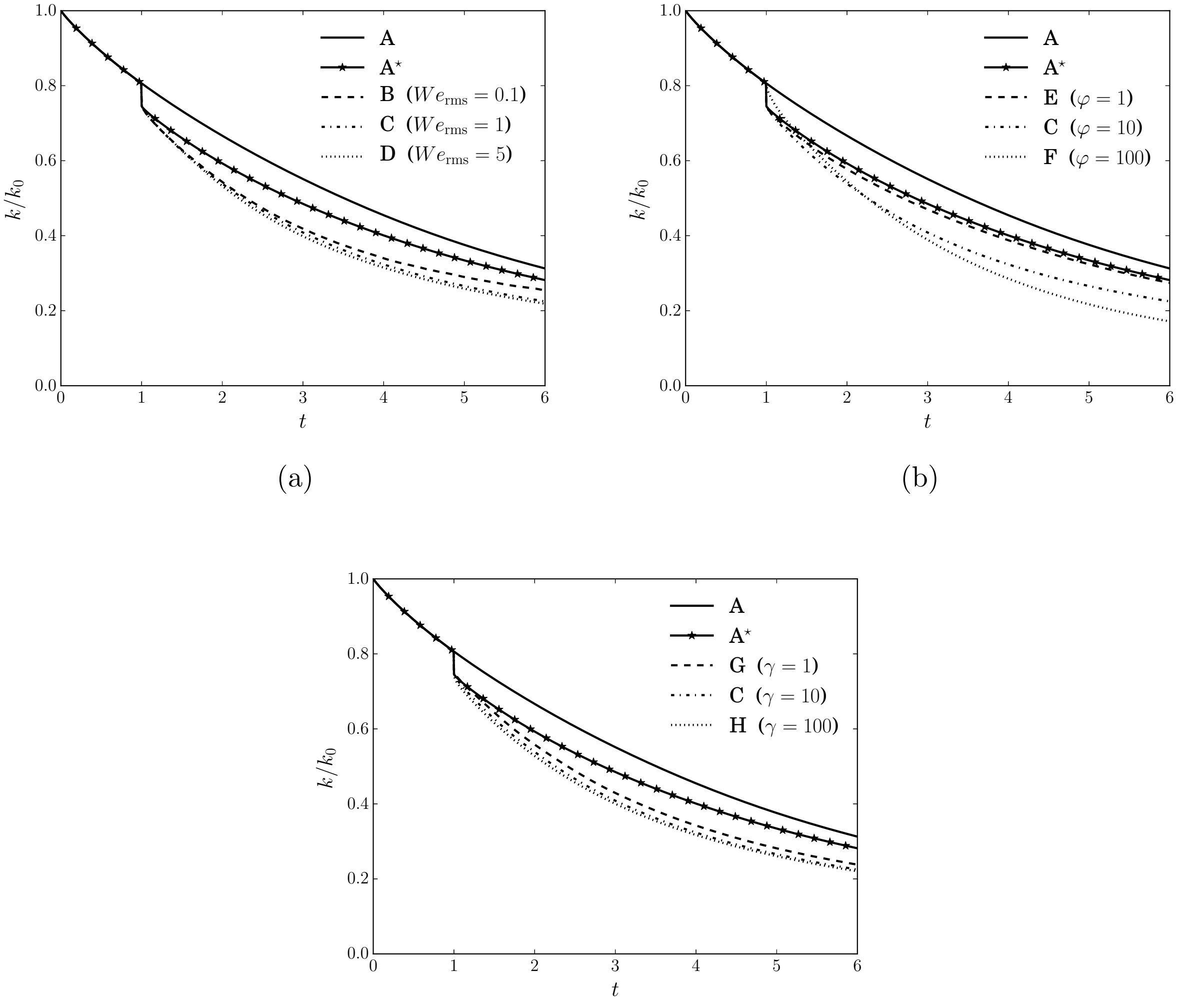

(a)

(b)

(c)

Figure 3.5: Temporal evolution of the turbulence kinetic energy, k, normalized by its initial value, k_0.

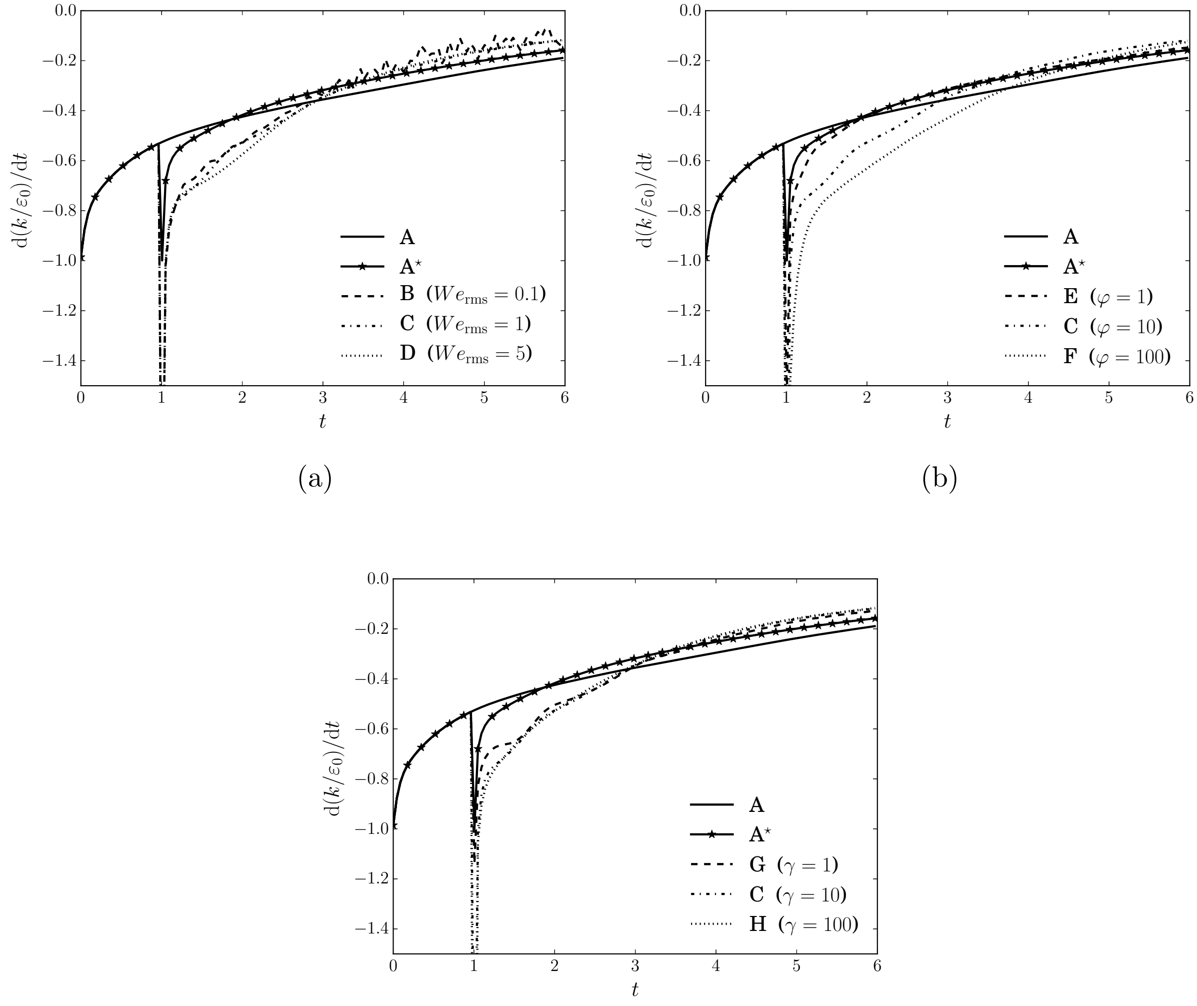

(a)

(b)

(c)

Figure 3.6: Temporal evolution of the rate of change of turbulence kinetic energy, $\mathrm{d}k(t)/\mathrm{d}t$, normalized by the initial value of the dissipation rate, ε_0.

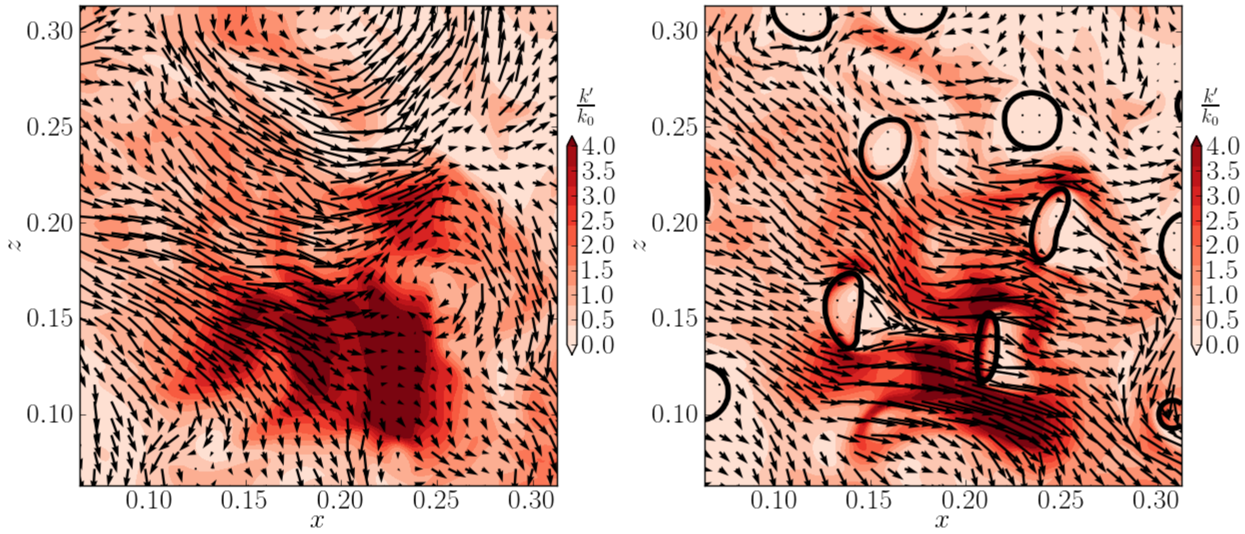

(a)

(b)

Figure 3.7: Instantaneous contours in a subregion of the x–z plane of $k' = \frac{1}{2}(\rho u_j u_j)$ in (a) case A and (b) case C at $t = 1.5$. The black arrows are the instantaneous velocity vectors projected onto the x–z plane.

$\mathrm{We}_{\mathrm{rms}}$ and γ for the range of values tested, whereas figure 3.8(b) shows that $\varepsilon(t)$ increases monotonically with increasing φ. For longer times ($t > 1 + \tau_\ell$), figure 3.8(a) shows that $\varepsilon(t)$ in case B is higher than that in cases C and D, eventually having twice the magnitude at $t = 6$. Figure 3.8(b) shows that $\varepsilon(t)$ in cases C and F crosses over that of E, which is a result of $\mathrm{d}k(t)/\mathrm{d}t$ being higher for ($t < 1 + \tau_\ell$) in cases C and F (see figure 3.6(b)). Figure 3.8(c) shows that $\varepsilon(t)$ remains nearly independent of γ for $1 \leq t \leq 6$.

The power of the surface tension, $\Psi_\sigma(t)$, is zero in cases A and A*($\mathbf{f}_\sigma = 0 \rightarrow \Psi_\sigma = 0$) and positive or negative in droplet-laden cases with finite Weber number (B–H) as shown in figure 3.9. In all cases $\Psi_\sigma(t)$ is initially negative, and the magnitude of the peak increases monotonically for increasing We_{rms} or decreasing γ, whereas it is non-monotonic and nearly independent for increasing φ. In general, $\Psi_\sigma(t)$ tends to oscillate about $\Psi_\sigma(t) = 0$ for early times ($t < 1+\tau_\ell$), which leads to oscillations in the TKE decay rate that are most noticeable in cases B, C and G (figure 3.6). For $t > 1 + \tau_\ell$, $\Psi_\sigma(t)$ is strictly positive, and therefore, the power of the surface tension is a source of TKE. In all cases, $\Psi_\sigma(t)$ is limited to ±5% of ε_0, for $t < 1 + \tau_\ell$, and consequently it plays a neutral role in the time evolution of the TKE for early times. Rather, $\Psi_\sigma(t)$ plays a more important role for $t > 1 + \tau_\ell$, where it behaves as a source of TKE, especially in case B.

Figure 3.9 shows that, for $We_{\mathrm{rms}} = 0.1$ (case B), $\Psi_\sigma(t = 6)$ is roughly 20 % of the initial dissipation rate, ε_0, which corresponds to 50 % of the instantaneous dissipation rate, $\varepsilon(t = 6)$, thus representing a significant source of TKE in (3.6). The enhanced power of the surface tension ($\Psi_\sigma > 0$) is accompanied by enhanced dissipation, $\varepsilon(t)$, relative to case C and D, such that $\mathrm{d}k(t)/\mathrm{d}t$ in case B is nearly equivalent to that in cases C and D, as was seen in figure 3.5(a).

In summary, the results show that, for early times, $1 < t < 1 + \tau_\ell$, the droplets enhance the decay rate of TKE, $\mathrm{d}k(t)/\mathrm{d}t$ (figure 3.6), relative to the droplet free flow, and that this is due almost entirely to the enhanced dissipation rate of TKE, $\varepsilon(t)$ (figure 3.8). The power of the surface tension, $\Psi_\sigma(t)$ (figure 3.9), is limited to ±5% of ε_0, for $t < 2.5$, and consequently it plays a minor role in the early development of $k(t)$. For later times, $t > 1+\tau_\ell$, $\Psi_\sigma(t)$ plays

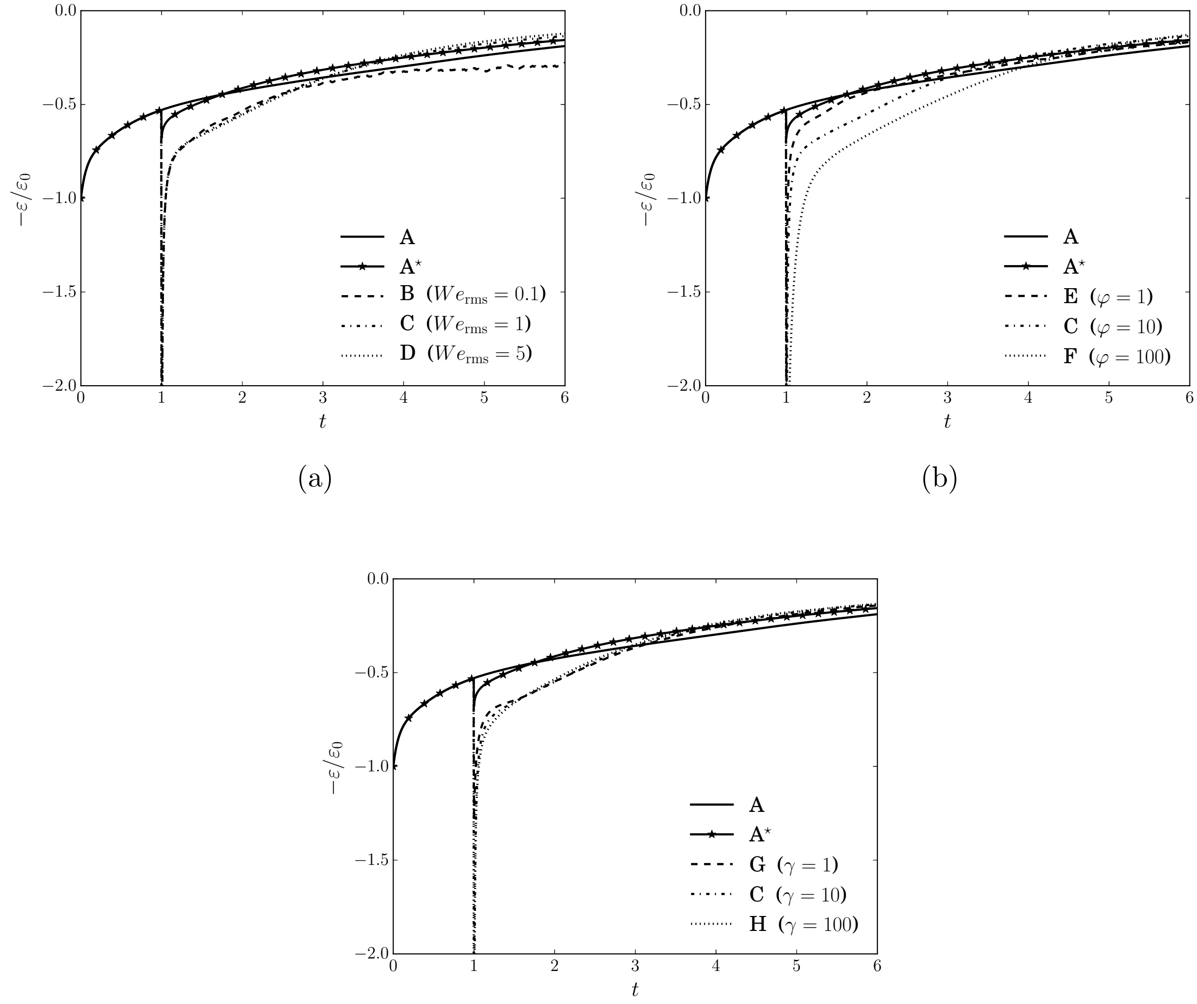

(a) (b)

(c)

Figure 3.8: Temporal evolution of the dissipation rate of turbulence kinetic energy, ε, normalized by its initial value, ε_0.

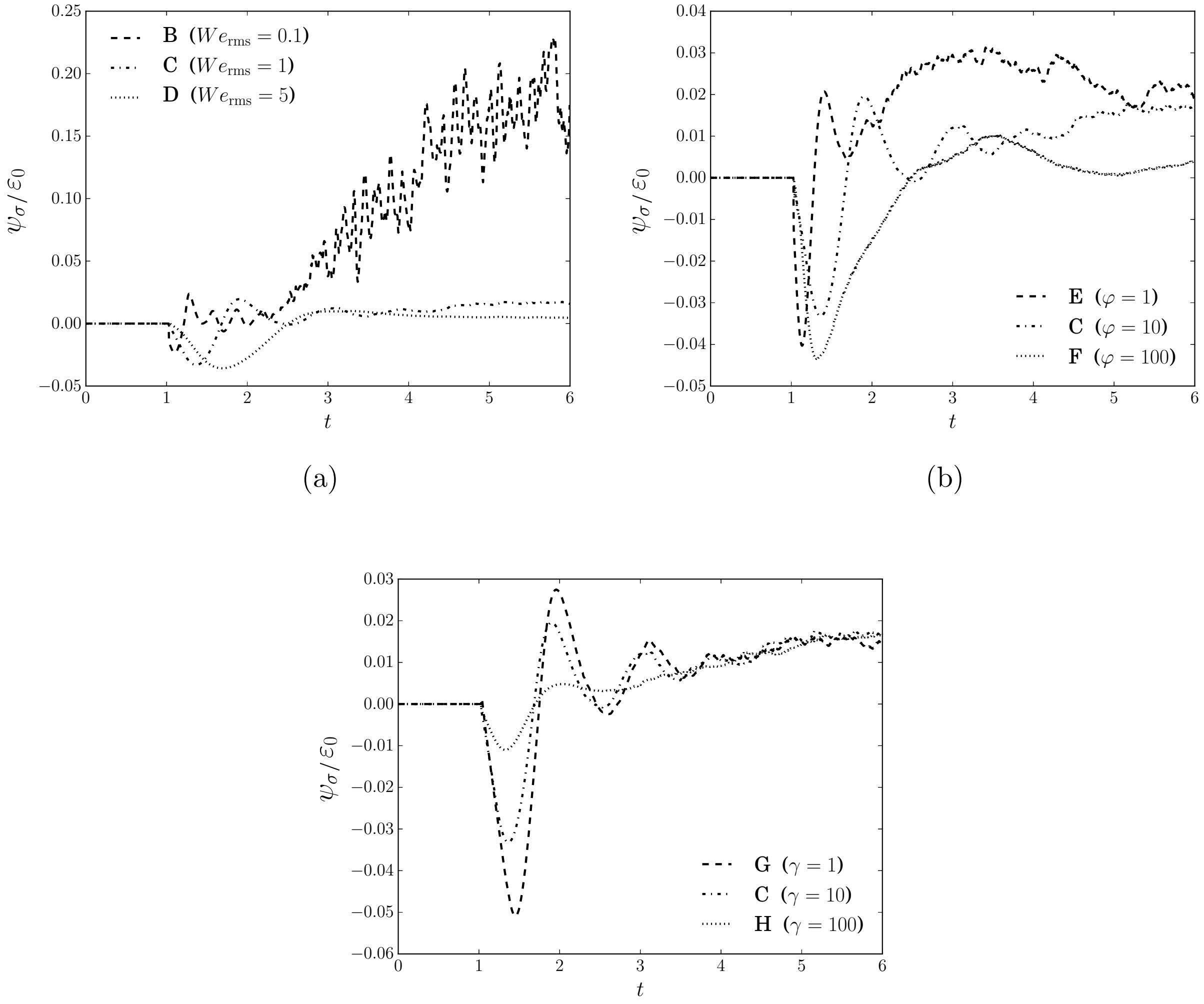

(a)

(b)

(c)

Figure 3.9: Temporal evolution of the power of the surface tension, Ψ_σ, normalized by the initial value of the dissipation rate, ε_0.

a more important role, behaving as a source term with magnitude of up to 50 % of $\varepsilon(t)$ (case B).

3.3.2 Dissipation rate of TKE

To explain why $\varepsilon(t)$ is greater in cases A*–H than in case A, figure 3.10 and supplementary movie 2 show the instantaneous two-dimensional contours of $\varepsilon' \equiv \mathrm{Re}^{-1}(\mathsf{T}_{ij}\mathsf{S}_{ij})$ in a sub-region of the computational domain at $t = 1.5$ in cases A and C. Figure 3.10(b) shows that ε' is enhanced near the droplet surface. The increased ε' near the droplet interface is due to the local increase of S_{ij} which is due to the increase of the velocity gradient $(\partial u_i/\partial x_j)$ near the droplet interface. The increase in $\partial u_i/\partial x_j$ is caused by (i) the velocity being set to zero in the droplet interiors at $t = 1$ (compare $\varepsilon(t)$ case A to cases A*–H), (ii) finite Weber number effects (compare $\varepsilon(t)$ case A*to cases B–H) and (iii) the droplet trajectories deviating from the motion of the carrier fluid in cases in which the droplets are more dense than the carrier fluid (cases B, C, D, F, G and H). The trajectories deviate more because of the higher inertia of the droplets compared to that of the carrier-fluid turbulence eddies (both large and small scales of motion), because the droplet Stokes numbers, based on both the integral time scale and on the Kolmogorov time scale, are much larger than unity, $St_\ell = \tau_d/\tau_\ell = 15.8$ and $St_\eta = \tau_d/\tau_\eta = 225$, respectively. Finally, the local increase of ε' increases $\varepsilon(t)$ because $\varepsilon(t) = \langle \varepsilon' \rangle$.

In §3.3.1 it was shown that for $1 < \tau_\ell < 1 + \tau_\ell$, as We_{rms} and γ are varied, $\varepsilon(t)$ is nearly constant, but as φ increases, $\varepsilon(t)$ increases (figure 3.8b). As φ increases, the droplet inertia increases. For example, the droplet Stokes number (τ_d/τ_ℓ) for $\varphi = 100$ (case F) is 100 times greater than that for $\varphi = 1$ (case E) (table 3.2). As the droplet inertia increases, the trajectories of the droplets compared to those of the surrounding fluid deviate more, which leads to higher velocity gradients $(\partial u_i/\partial x_j)$, and therefore, enhanced ε' near the droplet interface. This can be seen by comparing contours of ε' in cases E $(\tau_d/\tau_\ell = 1.58)$ and F $(\tau_d/\tau_\ell = 158)$, as shown in figure 3.11 at $t = 1.5$ and supplementary movie 3.

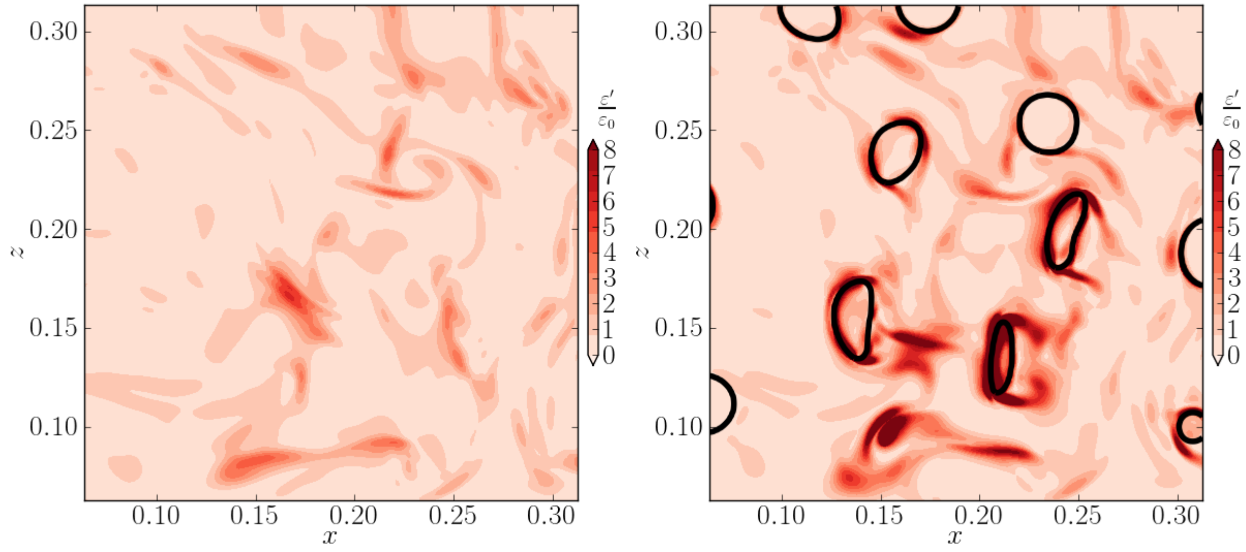

(a) (b)

Figure 3.10: Instantaneous contours in a subregion of the x–z plane of $\varepsilon' = \mathrm{Re}^{-1}(\mathsf{T}_{ij}\mathsf{S}_{ij})$ in (a) case A and (b) case C at $t = 1.5$.

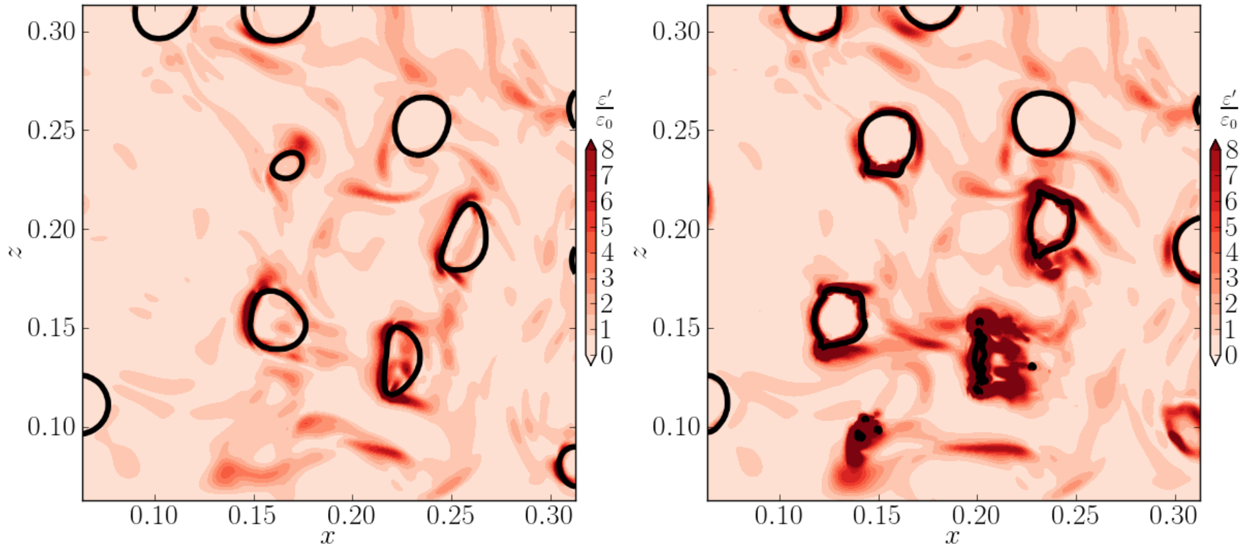

(a)

(b)

Figure 3.11: Instantaneous contours in a subregion of the x–z plane of $\varepsilon' = \mathrm{Re}^{-1}(\mathsf{T}_{ij}\mathsf{S}_{ij})$ in (a) case E and (b) case F at $t = 1.5$.

3.3.3 Power of the surface tension

In §3.3.1, the results have shown that the power of the surface tension can act as a source or sink of TKE. We now explain in more detail the behavior of $\Psi_\sigma(t)$, and why it changes for varying We_{rms}, φ and γ.

Physically, the power of the surface tension, $\Psi_\sigma(t)$, represents the rate of change of the surface energy of the droplet interface. In Appendix D, we derive the following relationship between $\Psi_\sigma(t)$ and the rate of change of the total droplet surface area $\mathrm{d}A(t)/\mathrm{d}t$,

$$\Psi_\sigma(t) = -\frac{1}{\mathrm{We}}\frac{1}{\mathcal{V}}\frac{\mathrm{d}A(t)}{\mathrm{d}t}, \tag{3.13}$$

where $\mathcal{V}$ is the volume of the domain ($\mathcal{V} = 1$) and $A(t)$ is the total droplet surface area defined as

$$A(t) \equiv \sum_{n=1}^{N_d(t)} \iint_{\partial\mathcal{V}_c^{(n)}(t)} \mathrm{d}\mathcal{A} = \sum_{n=1}^{N_d(t)} A^{(n)}(t), \tag{3.14}$$

where $N_d(t)$ is the instantaneous number of droplets, $\partial\mathcal{V}_c^{(n)}(t)$ is the instantaneous control surface that bounds the n-th droplet interface from the carrier-fluid side and $A^{(n)}(t)$ is the instantaneous surface area of the n-th droplet. $\Psi_\sigma(t)$ is directly proportional to the rate of change of droplet surface area (with opposite sign) and the constant of proportionality is the non-dimensional surface tension coefficient We. For example, an increase in droplet surface area in time ($\mathrm{d}A(t)/\mathrm{d}t > 0$), indicates through (3.13) that $\Psi_\sigma(t) < 0$, i.e. the droplets act as a sink of TKE by accumulating energy as droplet interfacial surface energy. We highlight this as a key concept for analyzing the energy budget of turbulent flows laden with deformable droplets (figures 3.4 and 3.12).

At $t = 1$ the droplets are spherical, corresponding to $A(t)$ being minimized, and therefore, immediately after the droplets are released, it must be true that $\mathrm{d}A(t)/\mathrm{d}t \geq 0$ (figure 3.12). Figure 3.13 confirms that A initially grows in time (i.e. $\mathrm{d}A(t)/\mathrm{d}t > 0$), which, from (3.13), corresponds to $\Psi_\sigma(t) < 0$ (figure 3.9). Figure 3.13 shows that, initially, the surface area growth rate, $\mathrm{d}A(t)/\mathrm{d}t$, increases monotonically with increasing We_{rms} or decreasing γ, and is non-monotonic for increasing φ.

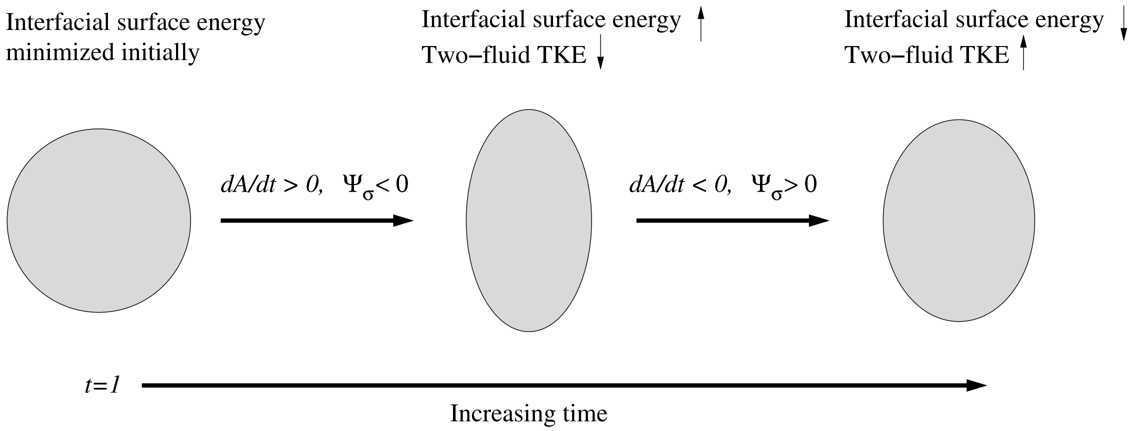

Figure 3.12: Schematic of a droplet oscillating in its fundamental mode that illustrates one of the physical mechanisms of the power of the surface tension ($\mathit{\Psi}_\sigma(t) = \mathrm{We}^{-1}\mathcal{V}^{-1}(\mathrm{d}A(t)/\mathrm{d}t)$). Going from left to right, the surface energy increases (two-fluid TKE decreases) as the droplet surface area increases, and then the surface energy decreases (two-fluid TKE increases) as the droplet surface area decreases (3.13).

In §3.3.3, we saw from figure 3.9 that $\mathit{\Psi}_\sigma(t)$ tends to oscillate for early times ($1 < t < 2.5$). At $t = 1$, the droplets are subjected to immediate aerodynamic forces from the carrier fluid, which leads to the droplets oscillating in unison on average, i.e. periods when $\mathrm{d}A(t)/\mathrm{d}t > 0$ and < 0. Because $\mathit{\Psi}_\sigma(t)$ is directly proportional to $\mathrm{d}A(t)/\mathrm{d}t$ (via (3.13)), oscillations in $\mathrm{d}A(t)/\mathrm{d}t$ lead to oscillations in $\mathit{\Psi}_\sigma(t)$. Figure 3.12 depicts a single droplet system undergoing oscillations. The period of oscillation corresponds to the fundamental vibrational mode of the droplets in the inviscid limit [75], which in non-dimensional form[1] is

$$T_{\mathrm{dvm}} = \frac{\pi}{4}\sqrt{\frac{D^2\, We_{\mathrm{rms}}(3\varphi + 2)}{3U_{\mathrm{rms}}^2}}. \tag{3.15}$$

T_{dvm} is reported in table 3.3 for cases B–H. In case B, the oscillations are a superposition of the fundamental and the second vibrational mode. (3.15) shows that T_{dvm} increases with increasing We_{rms} and φ, and is independent of γ, which is consistent with the behavior of

---

[1] The period of the droplet fundamental vibrational mode in dimensional form is $\tilde{T}_{\mathrm{dvm}} = \frac{\pi}{4}\sqrt{\frac{\tilde{D}^3(3\tilde{\rho}_d + 2\tilde{\rho}_c)}{3\tilde{\sigma}}}$.

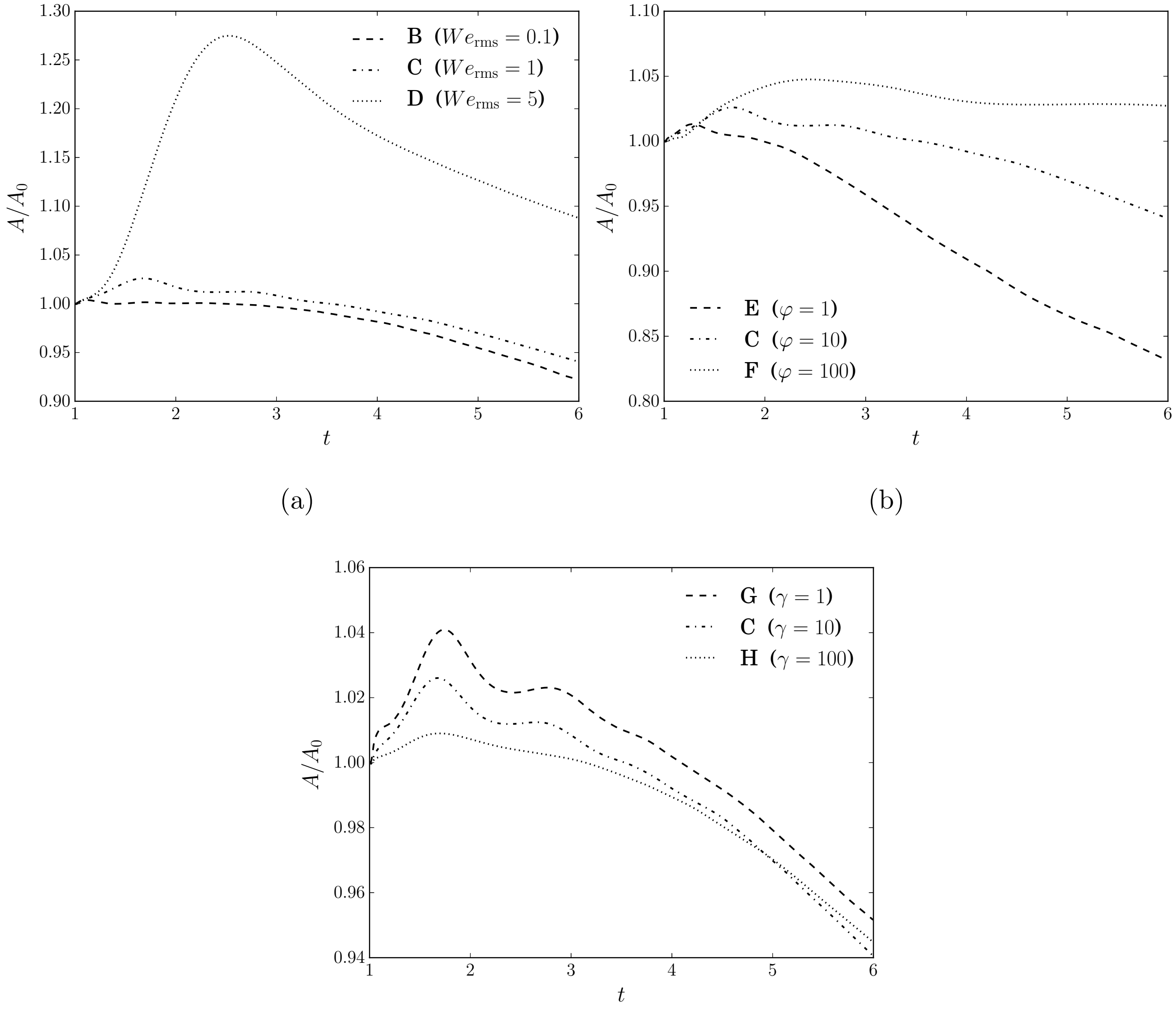

(a) (b)

(c)

Figure 3.13: Temporal evolution of the total surface area of the droplets normalized by its initial value, $A(t)/A_0$.

	B	C	D	E	F	G	H
T_{dvm}	0.55	1.75	3.92	0.69	5.38	1.75	1.75
Oh	0.011	0.034	0.077	0.109	0.011	0.003	0.345

Table 3.3: Oscillation period T_{dvm} of the fundamental droplet vibrational mode (3.15) and Ohnesorge number (3.16) in cases B–H.

$\Psi_\sigma(t)$ seen in figure 3.9.

An additional phenomenon during the droplet oscillations is that TKE is lost irreversibly due to viscous dissipation, which damps $\mathrm{d}A(t)/\mathrm{d}t$ (see figure 3.9). The non-dimensional number which characterizes the degree to which TKE is lost due to viscous dissipation during the droplet oscillations is the Ohnesorge number,

$$Oh = \frac{\tilde{\mu}_d}{\sqrt{\tilde{\rho}_d \tilde{\sigma} \tilde{D}}} = \frac{\gamma \sqrt{We_{\text{rms}}}}{D U_{\text{rms}} \mathrm{Re} \sqrt{\varphi}}, \tag{3.16}$$

which is the ratio of the viscous force to the square root of the product of the inertial and surface tension forces. Table 3.3 shows Oh in all droplet-laden cases B–H. Table 3.3 and (3.16) show that Oh increases with increasing We_{rms}, decreasing φ or increasing γ. As Oh increases, the droplet surface area oscillations in time ($\mathrm{d}A(t)/\mathrm{d}t$) are damped more quickly by viscous forces, and therefore, from (3.13), the oscillations in $\Psi_\sigma(t)$ are also damped more quickly. This explains why the oscillations in $\Psi_\sigma(t)$ are more damped for increasing We_{rms}, decreasing φ or increasing γ as seen in figure 3.9.

We now explain why $\Psi_\sigma(t)$ is strictly positive for longer times. For $t > 1+\tau_\ell$, the droplets surface area, $A(t)$, tends to decrease in time ($\mathrm{d}A(t)/\mathrm{d}t < 0$), which leads to $\Psi_\sigma(t) > 0$ (via (3.13)). It is also interesting to note that at $t = 6$, $A(t)/A_0 < 1$ in cases B, C, E, G and H. The only mechanism that can cause $A(t) < A_0$ in the present flow is droplet coalescence. To demonstrate this, consider the simplified case of two equally sized spherical droplets coalescing to form a larger spherical droplet, as illustrated in figure 3.14. In this case, the

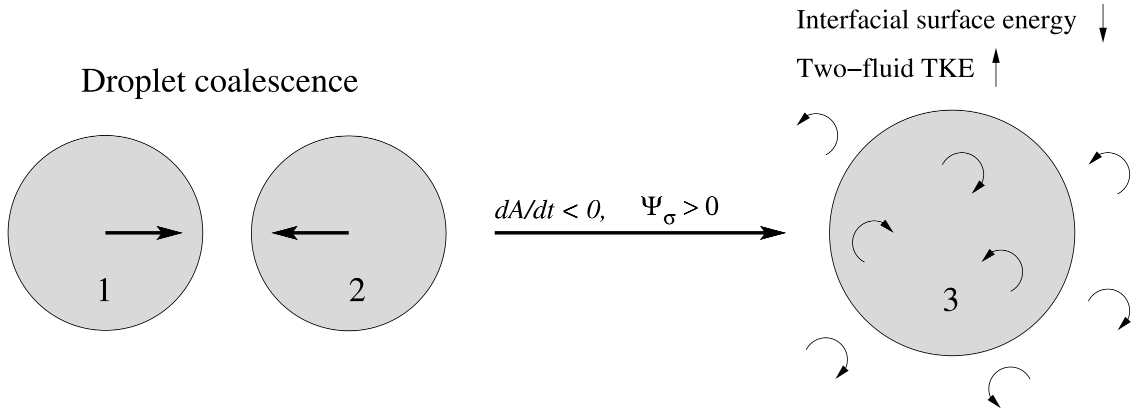

Figure 3.14: Schematic of two spherical droplets with the same diameter and surface area ($A^{(1)} = A^{(2)}$) coalescing to form a larger spherical droplet with surface area $A^{(3)}$. The surface area of the new droplet $A^{(3)}$ is 21 % less than that of the two original droplets $2A^{(1)}$ (i.e., $A^{(3)}/(2A^{(1)}) = 0.79$). More generally, droplet coalescence is associated with $\mathrm{d}A(t)/\mathrm{d}t < 0$, and thus $\Psi_\sigma(t) > 0$ (3.13). This process is reversed during droplet breakup for which $\mathrm{d}A(t)/\mathrm{d}t > 0$ and $\Psi_\sigma(t) < 0$.

total surface area of the droplet fluid decreases by 21 %. Therefore, during coalescence, a fraction of the surface energy stored in the interface is transformed into TKE (blue → green pathway in figure 3.4). This process is reversed during breakup, in which the total droplet surface area increases ($\mathrm{d}A(t)/\mathrm{d}t > 0$), leading to negative power of the surface tension ($\Psi_\sigma(t) < 0$).

To quantify the rate of droplet coalescence we compute the number of droplets in the computational domain as a function of time. Figure 3.15 shows that in cases B, C, E, G and H, the number of droplets decreases in time, indicating that droplets are coalescing. The onset of droplet coalescence, e.g. at $t \approx 2.5$ in case B, leads to fluctuations in $\Psi_\sigma(t)$, as the droplets no longer oscillate in unison with period T_{dvm}, but instead coalesce at different times as they are driven by the turbulent eddies, and will have a period of oscillation greater than T_{dvm}. At $t = 6$ the number of droplets increases with increasing We_{rms}, φ or γ. Figure 3.15

shows that in cases D and F, the number of droplets increases to a value greater than the initial value, which denotes that the number of breakups exceeds the number of coalescences.

To better quantify the number of coalescence and breakup events, the droplet size distribution is computed. We calculate the equivalent spherical diameter of each droplet in the domain as

$$D^{(n)} = (6\mathcal{V}_d^{(n)}/\pi)^{1/3} \tag{3.17}$$

where $\mathcal{V}_d^{(n)}$ is the volume of the n-th droplet. Figure 3.16 shows the probability density function of the equivalent spherical diameter $D^{(n)}$ normalized by its initial value D_0 in cases B–H at $t = 6$. $D^{(n)}/D_0 > 1$ ($D^{(n)}/D_0 < 1$) indicates that the droplet equivalent spherical diameter has increased (decreased), and thus indicates an instance of coalescence (breakup). Figure 3.16 shows that in all cases, except in case F, that some of the droplets have coalesced in groups of two to four, and that as $D^{(n)}/D_0$ increases, the probability density of $D^{(n)}/D_0$ decreases.

We now explain using the probability density of $D^{(n)}/D_0$ why, for $t > 1 + \tau_\ell$, as We_{rms} increases (cases B–D), $\mathit{\Psi}_\sigma(t)$ decreases. Figure 3.16(a) shows that the droplet size distribution at $t = 6$ is roughly equivalent, in cases B and C, indicating that the coalescence rates, and therefore $\mathrm{d}A(t)/\mathrm{d}t$, are roughly equivalent between the two cases for later times, which is confirmed by figure 3.13(a).

The fact that $dA(t)/dt$ is roughly equivalent in cases B and C, combined with the fact that We^{-1} is ten times greater in case B than it is in case C, explains (via (3.13)) why $\mathit{\Psi}_\sigma(t)$ is ten times greater in case B than in case C, as shown in figure 3.9(a). In case D ($We_{\mathrm{rms}} = 5$), figure 3.16(a) shows that, in addition to coalescence ($D^{(n)}/D_0 > 1$), there are values of $D^{(n)}/D_0$ between 0 and 1, which indicates droplet breakup which reduces $\mathrm{d}A/\mathrm{d}t$. From (3.13), both these factors contribute to smaller values of $\mathit{\Psi}_\sigma(t)$ relative to those in cases B and C.

It is interesting to note that the physical mechanisms leading to breakup in cases D and F are different. In case D, supplementary movie 4 shows that the droplets tend to flatten normal to the direction of the flow, forming thin ligaments, which eventually break. This

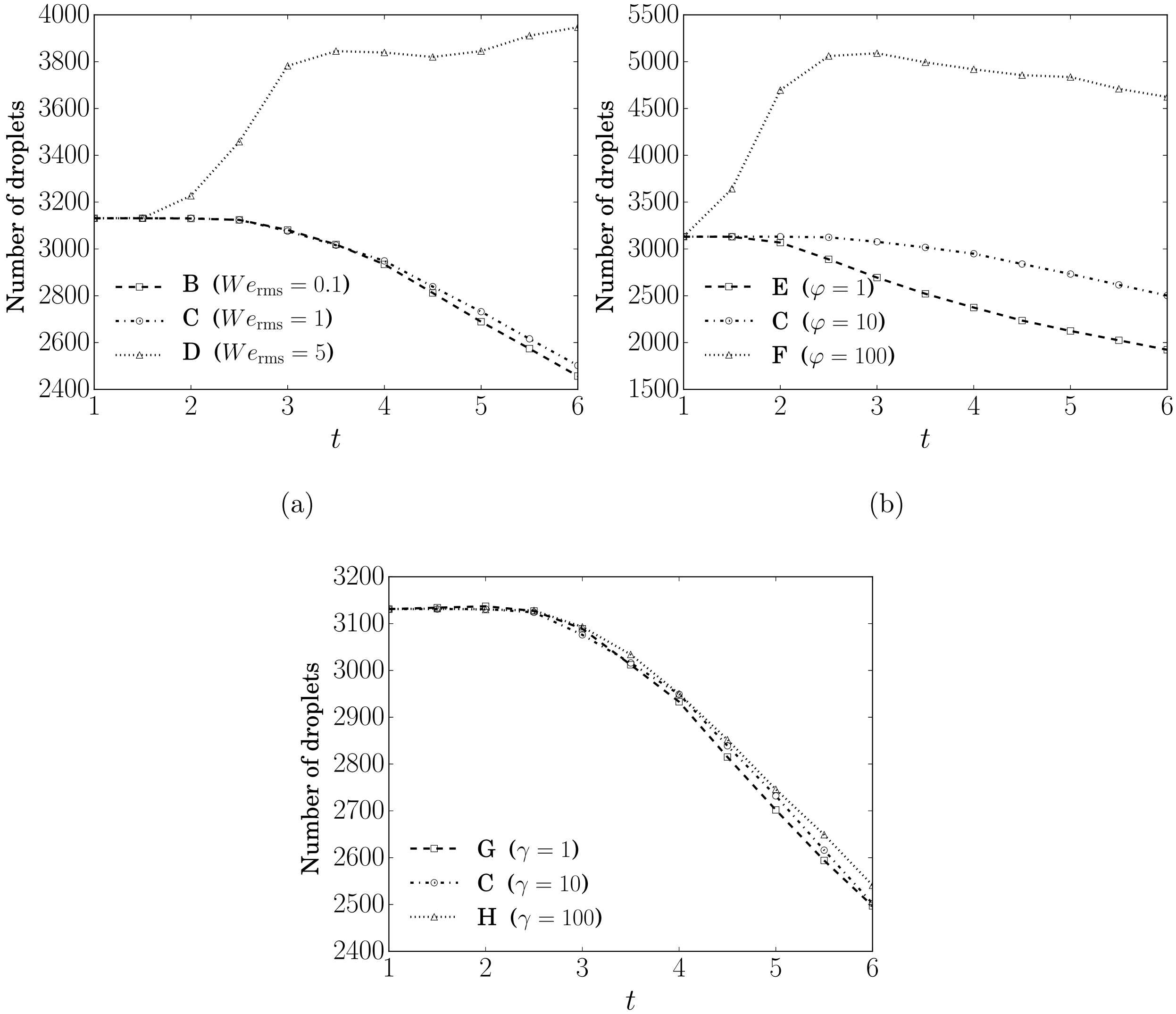

(a) (b)

(c)

Figure 3.15: Number of droplets in the computational domain as a function of time in cases B–H.

type of breakup is characteristic of the Rayleigh-Taylor instability. On the other hand, in case F, supplementary movie 3 shows that the initial velocity difference between the carrier and droplet fluid leads to the formation of waves on the droplet surface. These waves grow and are then stripped from the droplet, which is characteristic of the Kelvin-Helmholtz instability.

Figure 3.16(b) shows that as φ increases, the probability density for $D^{(n)}/D_0 > 1$ decreases. We recall that as φ increases, the droplet Stokes number increases, and therefore, the higher inertia droplets tend to stay near their initial position, whereas the lower inertia droplets tend to collide and then coalesce. The increased coalescence rate contributes to a larger positive $\mathrm{d}A(t)/\mathrm{d}t$, and, from (3.13), increases $\varPsi_\sigma(t)$ as the φ decreases (figure 3.9(b)).

Lastly, figure 3.16(c) shows that varying γ from 1 to 100 has a negligible effect on the droplet size distribution, and thus, the number of coalescence and breakup events is nearly independent of γ. This explains why for $t > 1 + \tau_\ell$, $\varPsi_\sigma(t)$ is nearly equivalent in cases G, C and H as shown figure 3.9(c).

3.4 Droplet fluid, carrier fluid and interface interactions

We have explained how droplets enhance the decay rate of two-fluid TKE ($\mathrm{d}k(t)/\mathrm{d}t$) in §3.3.1 and described the role of surface tension in droplet and turbulence interactions in §3.3.3. In this section, we analyze the time evolution of the TKE budget terms in (3.8) for the carrier fluid and those in (3.9) for the droplet fluid, and explain the underlying physical mechanisms that determine their behavior. We explain how TKE is transferred between the carrier-fluid and droplet-fluid, and how varying We_{rms}, φ and γ modifies this process.

3.4.1 Carrier-fluid TKE budget

Figure 3.17 shows the time evolution of the carrier-fluid TKE normalized by its initial value, $k_c(t)/k_0$, in cases A–H (note that in case A, the droplet-free flow is considered carrier-fluid, i.e. $k(t) = k_c(t)$). In the droplet-laden cases (B–H), $k_c(t)$ increases monotonically with decreasing We_{rms}, φ or γ.

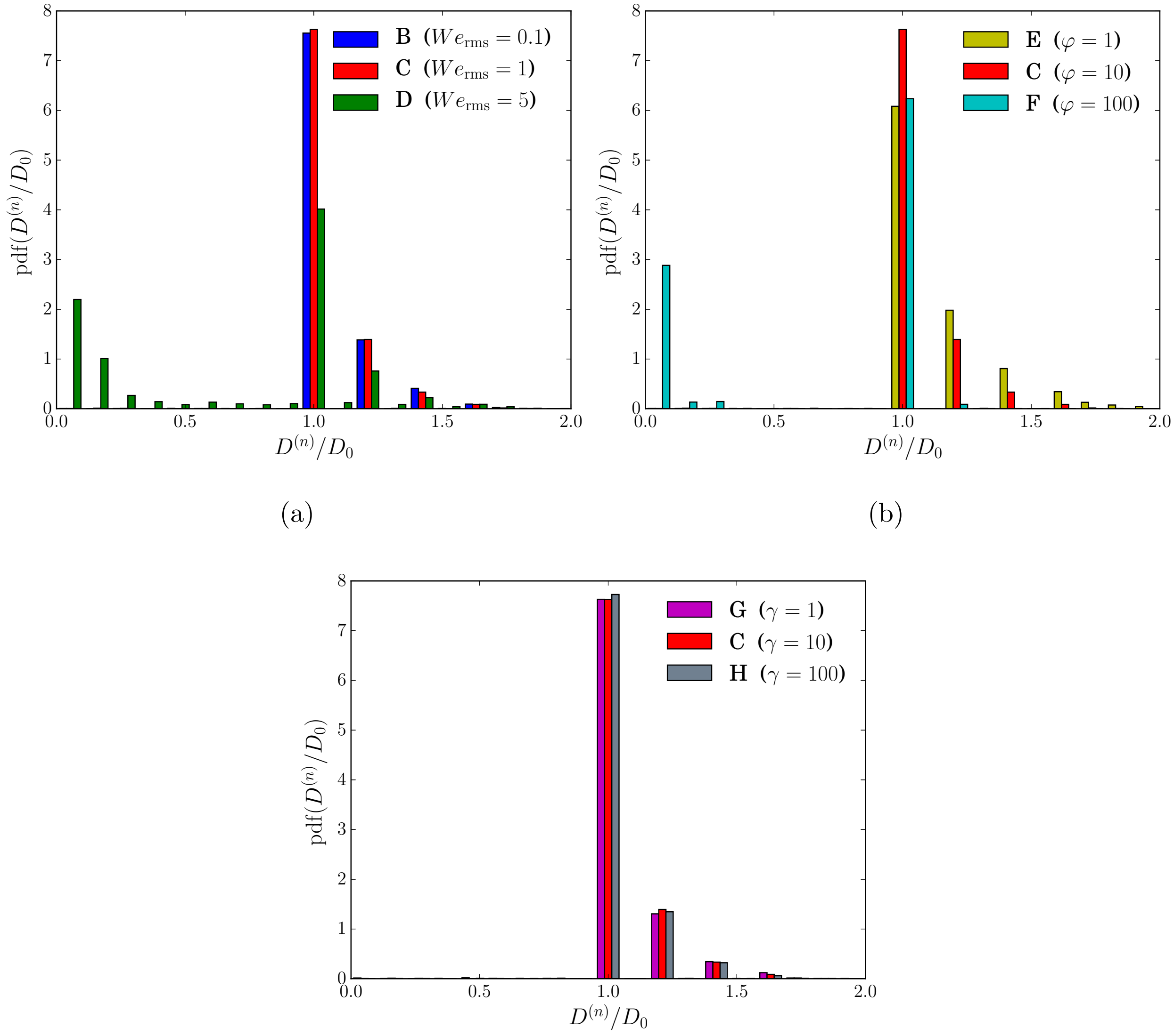

(a)

(b)

(c)

Figure 3.16: Probability density function of droplet size $D^{(n)}/D_0$ at $t = 6$ for varying (a) Weber number, We_{rms}; (b) density ratio, φ; and (c) viscosity ratio, γ.

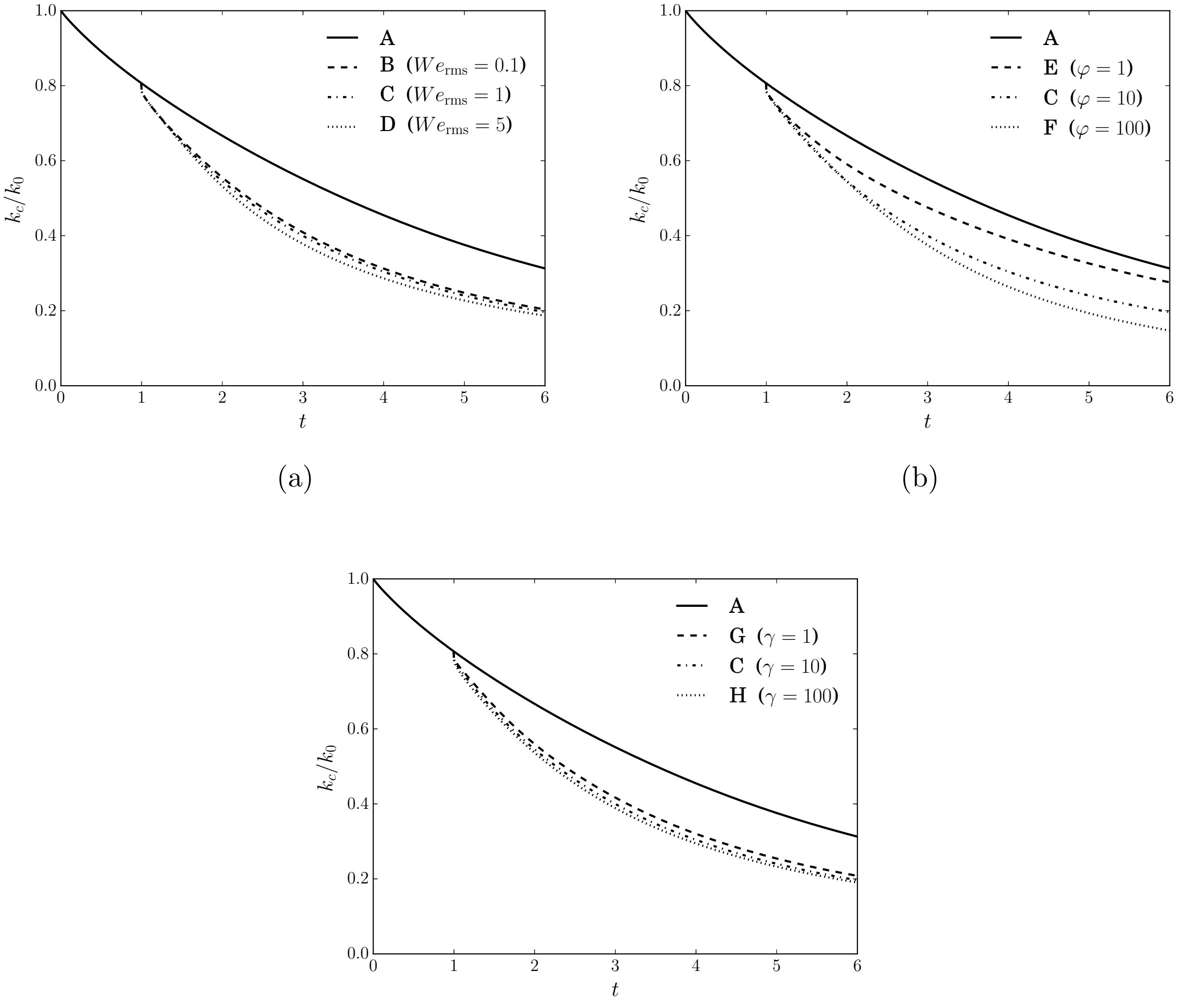

(a)

(b)

(c)

Figure 3.17: Temporal evolution of the carrier-fluid turbulence kinetic energy, k_c, normalized by its initial value, k_0.

Figure 3.18 shows the temporal evolution of the rate of change of the carrier-fluid TKE normalized by the initial dissipation rate, $\mathrm{d}(k_c(t)/\varepsilon_0)/\mathrm{d}t$, in cases A–H. For $1 < t < 1 + \tau_\ell$, $\mathrm{d}(k_c(t)/\varepsilon_0)/\mathrm{d}t$ increases monotonically for increasing We_{rms} (cases B–D), increasing φ (cases E, C and F) or increasing γ (cases G, C and H). At later times $t > 1 + \tau_\ell$, the decay rate of $k_c(t)$ is nearly independent of We_{rms}, φ and γ.

To explain why the droplets (cases B–H) enhance the decay rate of the carrier-fluid TKE, $k_c(t)$, relative to the droplet-free flow (case A), we analyze the time development of the terms on the right-hand side of (3.8): $\varepsilon_c(t)$, $T_{\nu,c}(t)$ and $T_{p,c}(t)$. Figure 3.19 shows the temporal evolution of the carrier-fluid dissipation rate of TKE normalized by its initial value, $\varepsilon_c(t)/\varepsilon_0$, in cases A–H. $\varepsilon_c(t)$ increases when the droplets are released into the flow field ($t = 1$). At early times ($1 < t < 1 + \tau_\ell$), $\varepsilon_c(t)$ is nearly independent of $\mathrm{We}_{\mathrm{rms}}$ (B–D), and it increases with increasing φ (E, C and F) or γ (G, C and H). At time $t \approx 1 + \tau_\ell$ there is a crossover of $\varepsilon_c(t)$ with case A in all droplet-laden cases B–H. The reason for the crossover is the same as the one explained in §3.3.1. The time at which the crossover occurs is independent of We_{rms} and γ but increases with increasing φ.

Figure 3.20 shows the temporal evolution of the normalized power of the viscous stress of the carrier fluid, $T_{\nu,c}(t)/\varepsilon_0$, in cases A–H. In case A, $T_{\nu,c}(t)$ is zero because in spatially homogeneous turbulence, mean quantities (e.g. $\langle \mathsf{T}_{ij} u_j \rangle$ in (3.10)) are invariant with position by definition, and therefore, $\partial \langle \mathsf{T}_{ij} u_j \rangle / \partial x_i = 0$. In contrast, figure 3.20 shows that in the droplet-laden cases (B–H), $T_{\nu,c}(t)$ spikes at $t = 1$ and is negative (a sink of TKE), and then decays, having a magnitude that is roughly 10 % of the initial dissipation rate for $1 < t < 1 + \tau_\ell$. $T_{\nu,c}(t)$ decreases monotonically in time, while asymptotically approaching zero. Figure 3.20 also shows that for $1 < t < 1 + \tau_\ell$, $T_{\nu,c}(t)$ increases for increasing We_{rms} and is non-monotonic for varying φ and γ. In the cases of varying φ (figure 3.20(b)), $T_{\nu,c}(t)$ is roughly equivalent for $\varphi = 10$ (case C) and $\varphi = 100$ (case F), and its value is always greater than that for $\varphi = 1$ (case E). Also, figure 3.20(c) shows that $T_{\nu,c}(t)$ is roughly equivalent for $\gamma = 1$ (case G) and $\gamma = 10$ (case C), and its value is always greater than that for $\gamma = 100$ (case H).

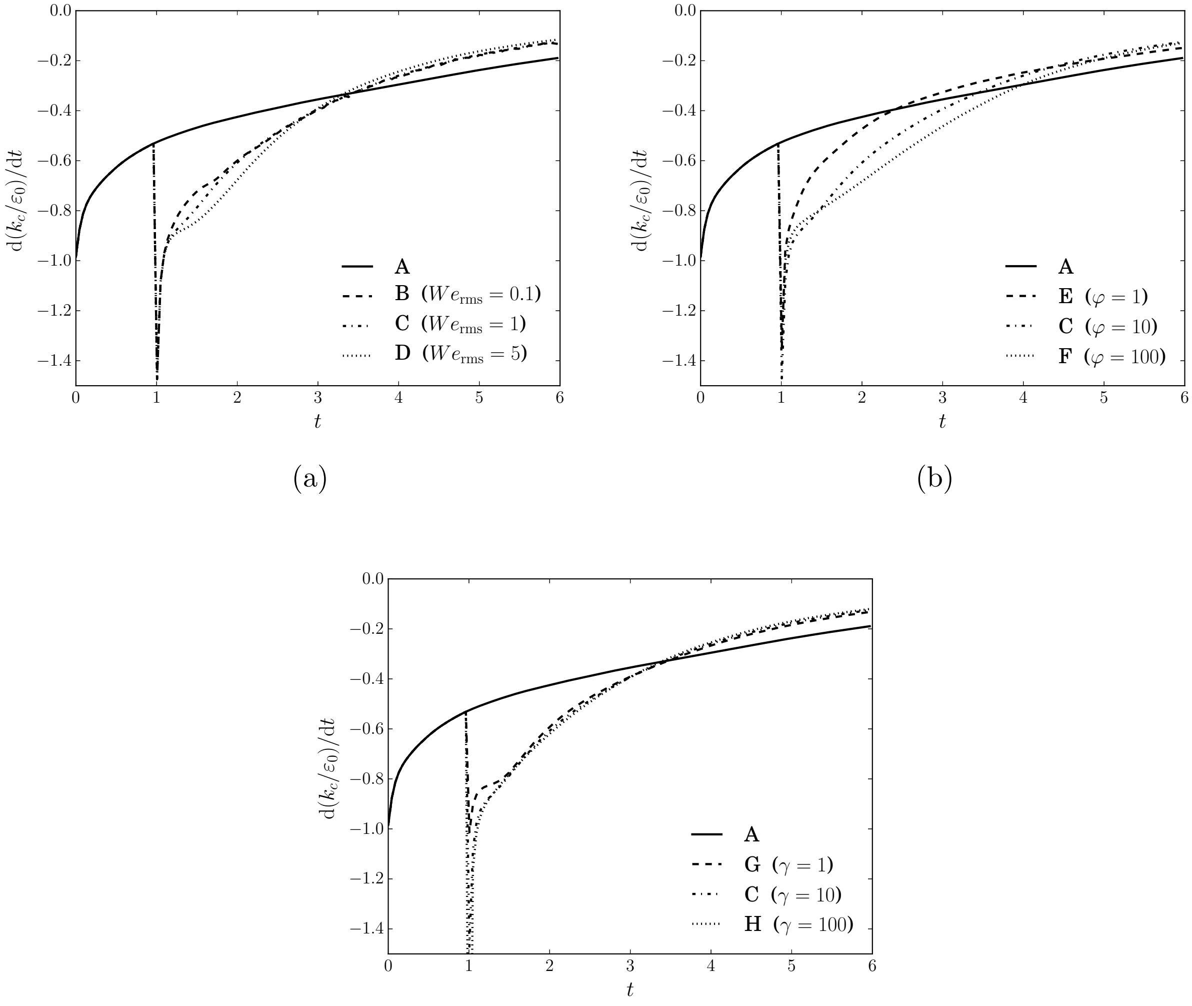

(a)

(b)

(c)

Figure 3.18: Temporal evolution of the rate of change of carrier-fluid turbulence kinetic energy, d$k_c(t)$/dt, normalized by the initial value of the dissipation rate, ε_0.

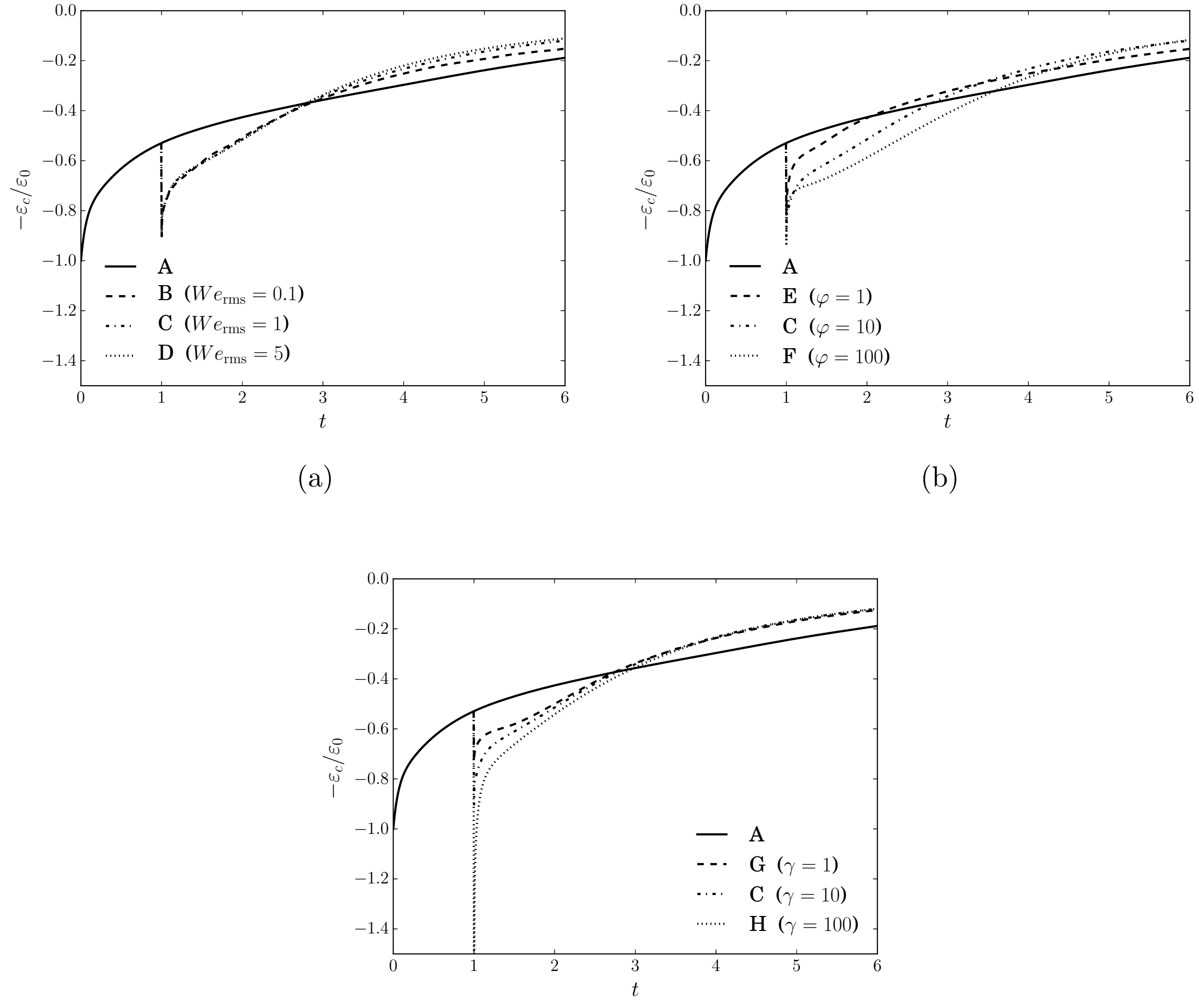

(a)

(b)

(c)

Figure 3.19: Temporal evolution of the carrier-fluid dissipation rate of turbulence kinetic energy, $\varepsilon_c(t)$, normalized by its initial value, ε_0.

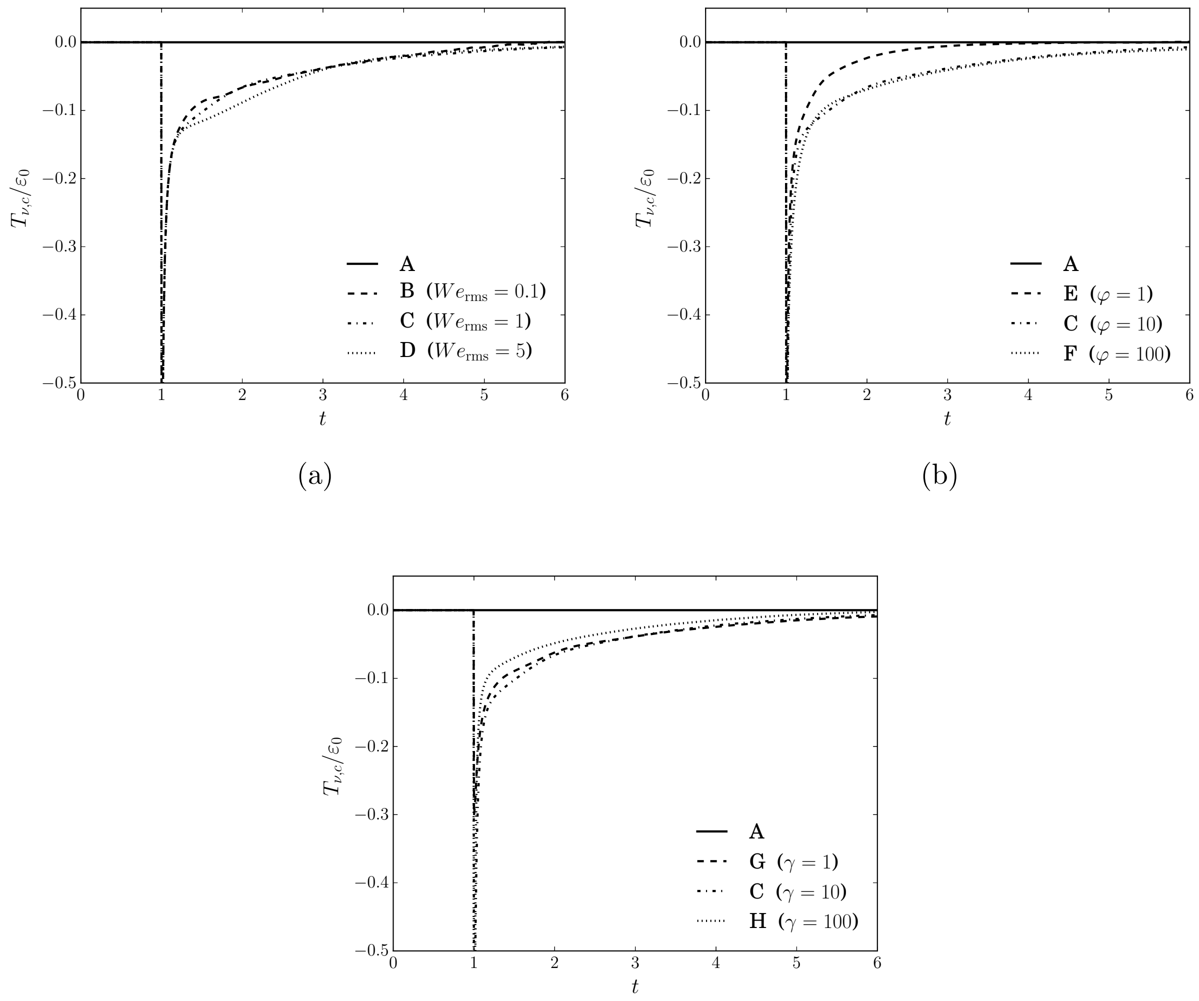

(a)

(b)

(c)

Figure 3.20: Temporal evolution of the carrier-fluid viscous power, $T_{\nu,c}(t)$, normalized by the initial value of the dissipation rate, ε_0.

Figure 3.21 shows that the temporal evolution of the carrier-fluid pressure-power, $T_{p,c}(t)$, normalized by ε_0 in cases A–D. In case A, $T_{p,c}(t)$ is zero as expected for single-phase homogeneous turbulence. In contrast, in cases B–H, $T_{p,c}(t)$ is primarily negative; consequently, it is a sink of $k_c(t)$. For short times after droplet release ($1 < t < 1 + \tau_\ell$), the pressure power acts as a sink of carrier-fluid TKE with its initial magnitude being approximately 10 % of ε_0. As the turbulence decays, $T_{p,c}(t)$ decreases in magnitude towards zero. Figure 3.21 shows that for $1 < t < 2$, $T_{p,c}(t)$ increases monotonically in magnitude for increasing We_{rms} or decreasing γ, and that the behavior is non-monotonic for increasing φ. $T_{p,c}(t)$ decays more slowly for higher φ, which leads to $T_{p,c}(t)$ of the lowest inertia droplets (cases E and C) crossing over that of the highest inertia droplets (cases F).

The results show that for early times, $1 < t < 1 + \tau_\ell$, the droplets enhance the decay rate of carrier-fluid TKE, $\mathrm{d}k_c(t)/\mathrm{d}t$ (figure 3.17), relative to the droplet free flow. The increased decay rate is due to enhanced dissipation, $\varepsilon_c(t)$ (figure 3.19), as well as the presence of viscous power, $T_{\nu,c}(t)$, and pressure power, $T_{p,c}(t)$, both of which are sinks of $k_c(t)$ as shown in figures 3.20 and 3.21, respectively. Most of the carrier-fluid TKE budget $\mathrm{d}k_c(t)/\mathrm{d}t$ is due to $\varepsilon_c(t)$, which makes up roughly 75 % of the budget at $t = 1$, and increases to roughly 90 % of the budget at $t = 6$. The remainder of the budget (approximately 25 % at $t = 1$ and 10 % at $t = 6$) is split between $T_{p,c}(t)$ and $T_{\nu,c}(t)$, which have the same order of magnitude.

The increase in $\mathrm{d}k_c(t)/\mathrm{d}t$ for increasing We_{rms} (figure 3.18(a)) is primarily due to increasing pressure power ($T_{p,c}(t)$) and secondarily to increasing viscous power ($T_{\nu,c}(t)$). The increase in $\mathrm{d}k_c(t)/\mathrm{d}t$ for increasing φ and γ is due primarily to enhanced $\varepsilon_c(t)$.

3.4.2 Droplet-fluid TKE budget

Figure 3.22 shows the time evolution of the droplet-fluid TKE normalized by its initial value, $k_d(t)/k_0$ in cases B–H. As a reminder in cases B–D, We_{rms} increases, in E, C, and F φ increases and in G, C, and H γ increases. In all cases, $k_d(t)$ is initially zero because the droplets are released from rest, and then $k_d(t)$ increases. For $1 < t < 2.5$, $k_d(t)$ increases monotonically with increasing Weber number, but for longer times the behavior is non-

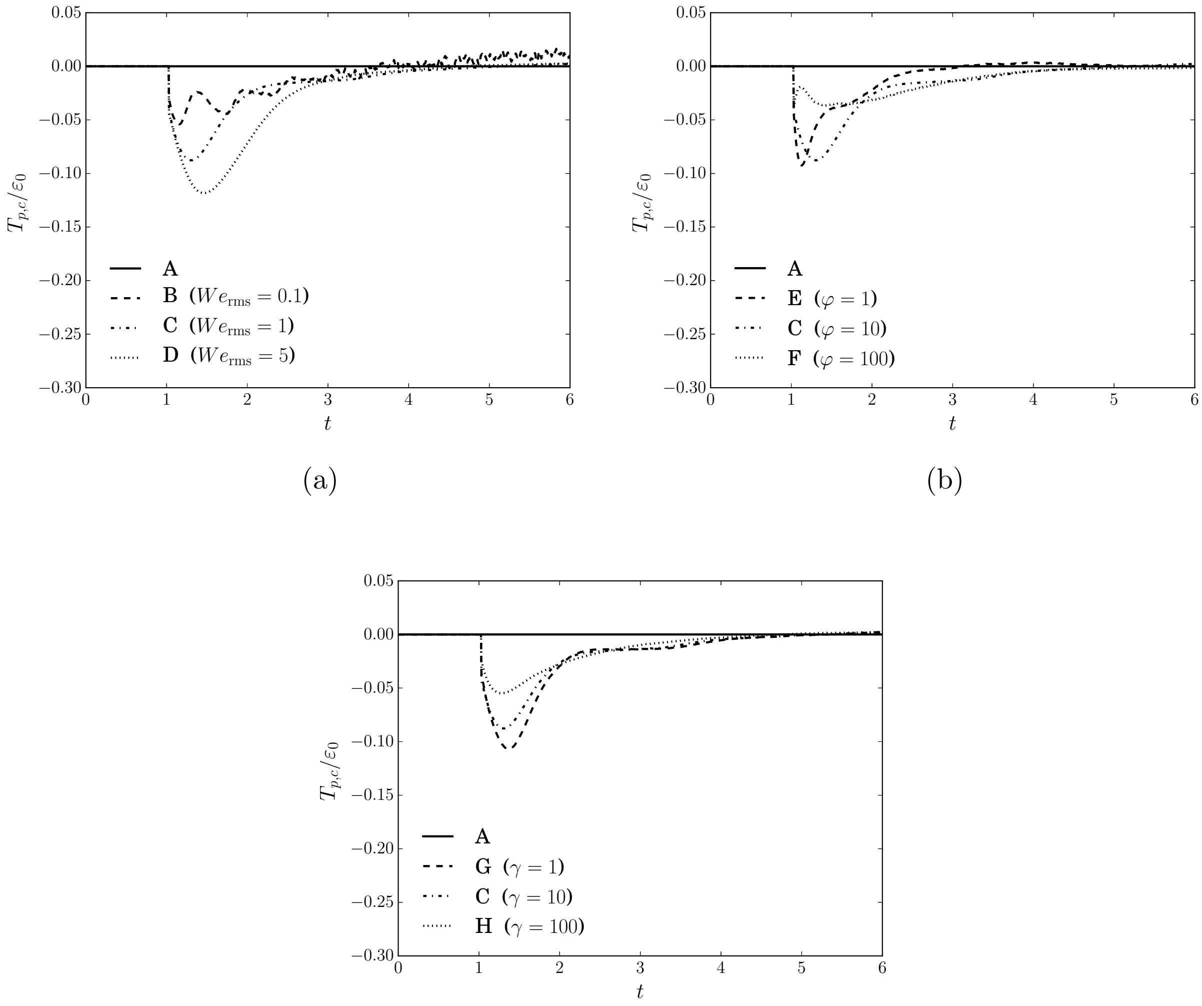

(a)

(b)

(c)

Figure 3.21: Temporal evolution of the carrier-fluid pressure power, $T_{p,c}(t)$, normalized by the initial value of the dissipation rate, ε_0.

monotonic. Figure 3.22(b) shows that $k_d(t)$ is non-monotonic for increasing φ with $k_d(t)$ increasing when φ increases from 1 to 10, but then decreasing when φ increases to 100. Figure 3.22(c) shows that $k_d(t)$ is nearly independent of the viscosity ratio (γ).

Figure 3.23 shows the normalized rate of change of the droplet-fluid TKE, $\mathrm{d}k_d(t)/\mathrm{d}t$ as a function of time. In all droplet-laden cases (B–H), $\mathrm{d}k_d(t)/\mathrm{d}t$ is initially positive, and then decays in time. For early times $1 < t < 1+\tau_\ell$, $\mathrm{d}k_d(t)/\mathrm{d}t$ tends to oscillate, and for later times $t > 1+\tau_\ell$, $\mathrm{d}k_d(t)/\mathrm{d}t$ exhibits fluctuations, especially in case B. $\mathrm{d}k_d(t)/\mathrm{d}t$ is non-monotonic for varying We_{rms}, φ and γ.

To explain the behavior of the droplet-fluid TKE decay rate, $\mathrm{d}k_d(t)/\mathrm{d}t$, we analyze the time development of the terms on the right-hand side of (3.9): $\varepsilon_d(t)$, $T_{\nu,d}(t)$ and $T_{p,d}(t)$. Figure 3.24 shows the time evolution of the normalized droplet-fluid dissipation rate of TKE, $\varepsilon_d(t)/\varepsilon_0$. In all droplet-laden cases (B–H), $\varepsilon_d(t)/\varepsilon_0$ spikes when the droplets are released ($t = 1$). For $1 < t < 2.5$, $\varepsilon_d(t)$ increases monotonically with increasing We_{rms}, increasing φ or decreasing γ. $\varepsilon_d(t)$ tends to decay towards zero, except for in case B, where it grows for later times ($t > 1+\tau_\ell$), and, by $t = 6$, is roughly ten times greater than that in the other six cases (figure 3.24(a).

Figure 3.25 shows the temporal evolution of the normalized, droplet-fluid viscous power, $T_{\nu,d}(t)/\varepsilon_0$. In all droplet-laden cases (B–H), right after droplet release, $T_{\nu,d}(t) > 0$, indicating that the viscous power is a source of TKE for the droplets. The magnitude of $T_{\nu,d}(t)$ decays in time and remains positive, except in case E ($\varphi = 1$, lowest inertia droplets studied). For $1 < t < 2$, as We_{rms} increases, $T_{\nu,d}(t)$ increases. The behavior of $T_{\nu,d}(t)$ with varying φ and γ is non-monotonic.

Figure 3.26 shows the temporal evolution of the normalized, droplet-fluid pressure power, $T_{p,d}(t)/\varepsilon_0$. In cases B–H, right after droplet release, $T_{p,d}(t) > 0$, indicating that $T_{p,d}(t)$ is a source of TKE for the droplets. For early times ($1 < t < 2.5$), $T_{p,d}(t)$ tends to oscillate, and it may oscillate between positive or negative values as in case B. This indicates that $T_{p,d}(t)$ can be a source or sink of TKE in these cases. However, $T_{p,d}(t)$ is mostly a source of $k_d(t)$. For $1 < t < 2$, $T_{p,d}(t)$ increases for increasing We_{rms} or decreasing γ. For longer times

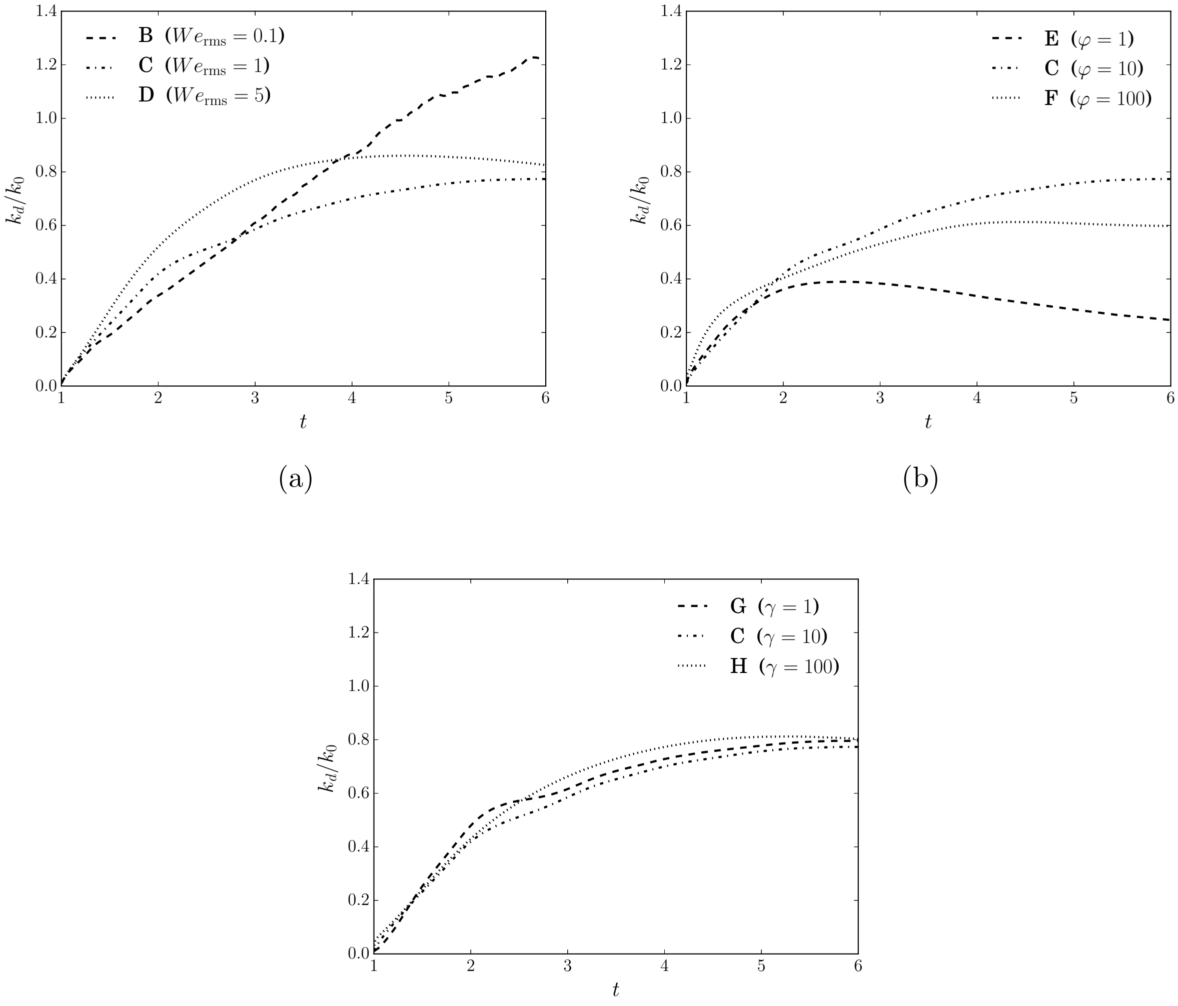

(a)

(b)

(c)

Figure 3.22: Temporal evolution of the droplet-fluid turbulence kinetic energy, $k_d(t)$, normalized by its initial value, k_0.

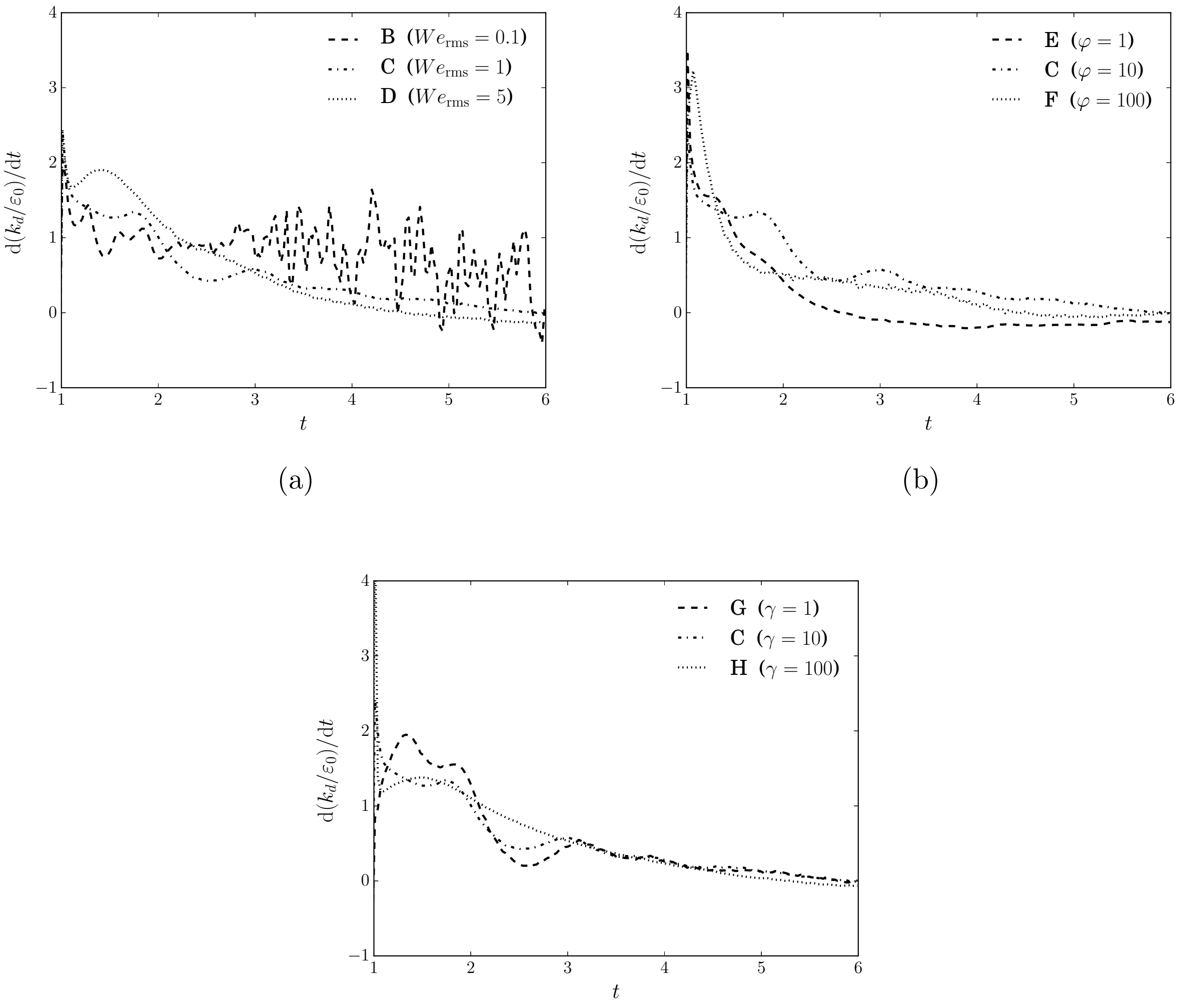

(a)

(b)

(c)

Figure 3.23: Temporal evolution of the rate of change of droplet-fluid turbulence kinetic energy, $\mathrm{d}k_d(t)/\mathrm{d}t$, normalized by the initial value of the dissipation rate, ε_0.

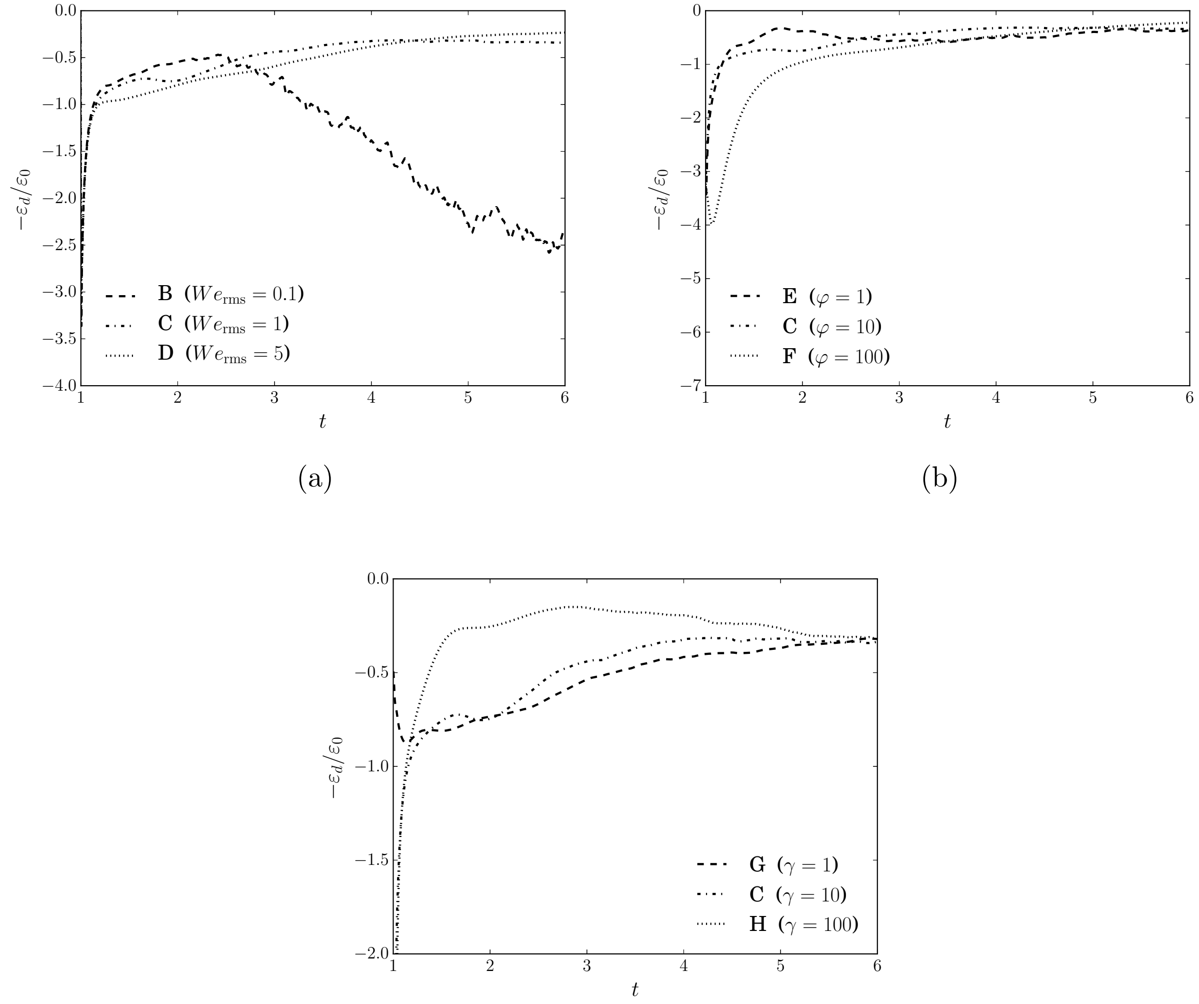

(a)

(b)

(c)

Figure 3.24: Temporal evolution of the droplet-fluid dissipation rate of turbulence kinetic energy, $\varepsilon_d(t)$, normalized by the initial value of the dissipation rate, ε_0.

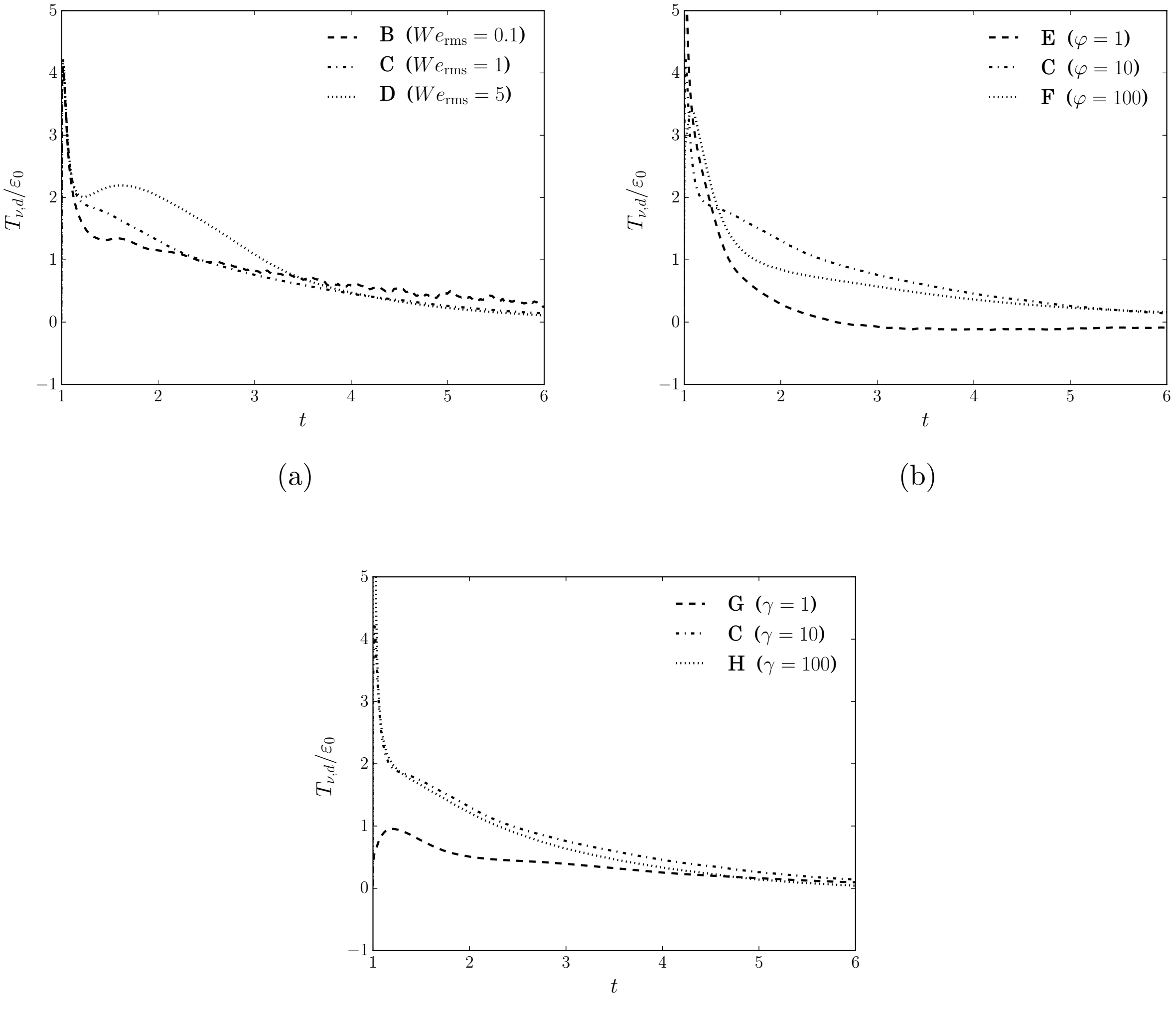

(a)

(b)

(c)

Figure 3.25: Temporal evolution of the droplet-fluid viscous power, $T_{\nu,d}(t)$, normalized by the initial value of the dissipation rate, ε_0.

$(t > 1 + \tau_\ell)$, $T_{p,d}(t)$ increases for decreasing $We_{\rm rms}$ or decreasing φ.

To summarize, for $1 < t < 2$, $k_d(t)$ grows in time because $T_{\nu,d}(t)$ and $T_{p,d}(t)$ are both sources of $k_d(t)$, and their sum is greater than the droplet-fluid dissipation rate ($\varepsilon_d(t)$), and therefore, via (3.9), $\mathrm{d}k_d(t)/\mathrm{d}t > 0$. For $t > 1 + \tau_\ell$, the decay in $\mathrm{d}k_d(t)/\mathrm{d}t$ is caused by $T_{\nu,d}(t) + T_{p,d}(t)$ decaying more quickly than $\varepsilon_d(t)$; consequently, $-\varepsilon_d(t) + T_{\nu,d}(t) + T_{p,d}(t)$ approaches zero, and even becomes negative in cases D, E, F and H. Case B is an exception to this trend, as figure 3.22(a) shows $k_d(t)$ continues to grow, which is due to enhanced $T_{p,d}(t)$ (figure 3.26(a)) relative to the other six cases. Finally, the oscillations in $\mathrm{d}k_d(t)/\mathrm{d}t$ (figure 3.23) are caused by oscillations in $T_{p,d}(t)$ (figure 3.26).

3.4.3 Interfacial energy balance

In figure 3.4, we have shown that $k_c(t)$ can be transferred to the droplet-fluid (green arrow) or to the interface (blue arrow). This raises the question: how much of $k_c(t)$ is transferred to $k_d(t)$ and how much is transferred to $\varPsi_\sigma(t)$? Using (3.12), we quantify how much of $k_c(t)$ goes into $k_d(t)$ and how much goes into $\varPsi_\sigma(t)$. Figure 3.27 shows the time evolution of the terms in (3.12) in cases B–H. In all cases $\phi_v(T_{\nu,d}(t) + T_{p,d}(t)) > \varPsi_\sigma(t)$, indicating that of the $k_c(t)$ lost via $T_{\nu,c}(t) + T_{p,c}(t)$, $k_d(t)$ gains more of that energy than the interface. Also, figure 3.27 shows that, in the majority of cases, $(1 - \phi_v)T_{p,c}(t) + \phi_v T_{p,d}(t)$ is greater than $(1 - \phi_v)T_{\nu,c}(t) + \phi_v T_{\nu,d}(t)$. Therefore, of the $k_c(t)$ that gets converted to surface energy via $\varPsi_\sigma(t)$, most of it comes from $T_{p,c}(t)$.

3.4.4 Dissipation rate of TKE in the carrier and droplet fluid

In §3.4.1, the results showed that $\varepsilon_c(t)$ increases for increasing density ratio, φ (figure 3.19(b)) and in §3.4.2, the same trend was shown for $\varepsilon_d(t)$. We now explain why $\varepsilon_c(t)$ and $\varepsilon_d(t)$ increase with φ. Figure 3.11 shows that as φ increases (cases E and F), ε' increases at the carrier- and droplet-fluid side of the interface (the physical mechanism for the increase is explained in §3.3.2). The local increase of ε' in the carrier and droplet fluid increases both $\varepsilon_c(t)$ and $\varepsilon_d(t)$ because $\varepsilon_c(t) = \langle \varepsilon' \rangle_c$ and $\varepsilon_d(t) = \langle \varepsilon' \rangle_d$, respectively.

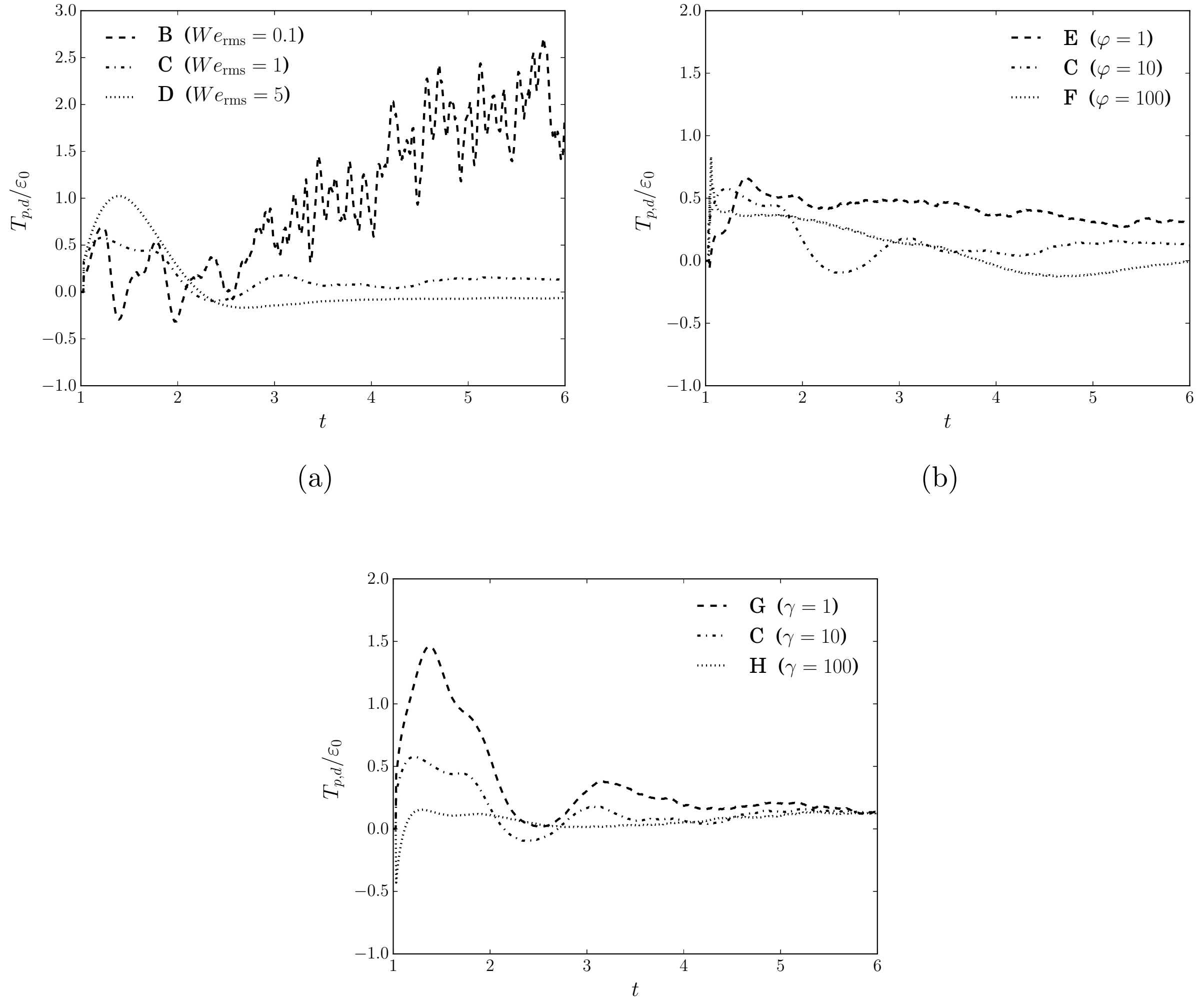

(a)

(b)

(c)

Figure 3.26: Temporal evolution of the droplet-fluid pressure power, $T_{p,d}$, normalized by the initial value of the dissipation rate, ε_0.

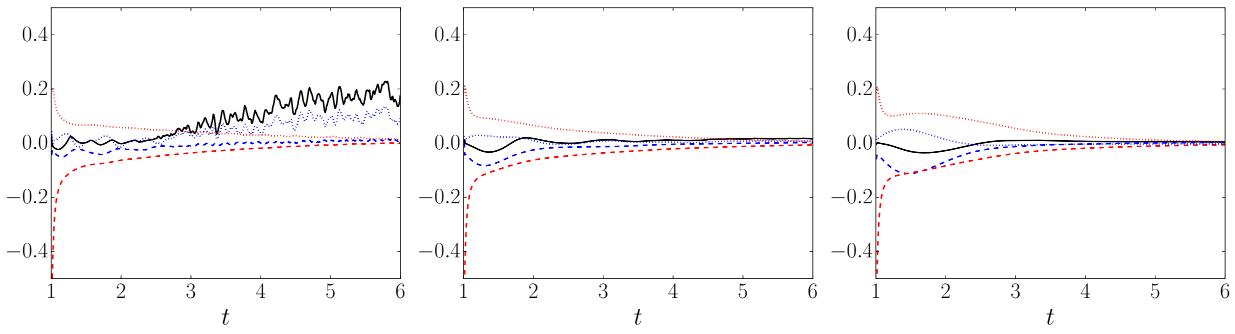

(a) case B

(b) case C

(c) case D

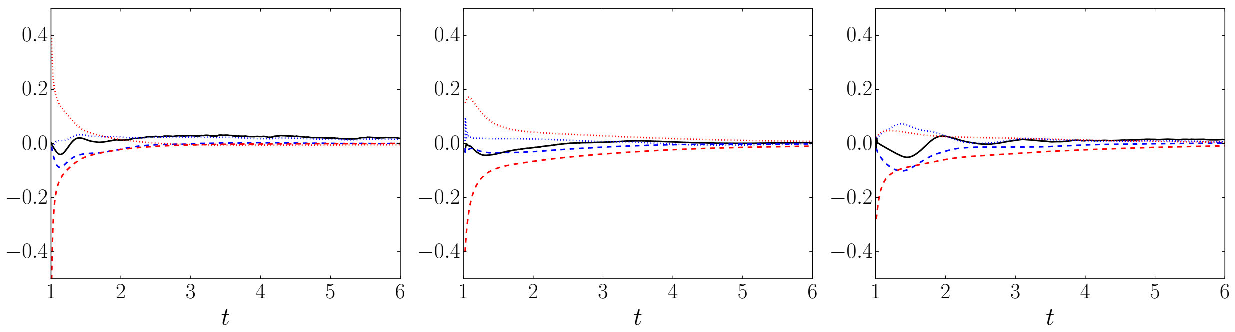

(d) case E

(e) case F

(f) case G

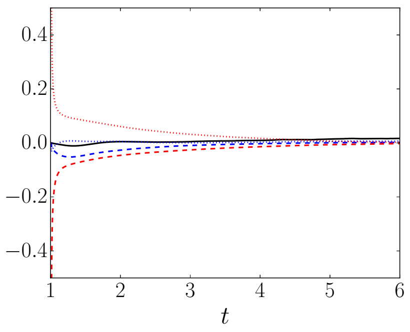

(g) case H

Figure 3.27: Time evolution of the normalized terms in the interfacial energy balance equation (3.12), $\Psi_\sigma(t) = (1-\phi_v)\,[T_{\nu,c}(t) + T_{p,c}(t)] + \phi_v\,[T_{\nu,d}(t) + T_{p,d}(t)]$ in cases B–H. $\Psi_\sigma/\varepsilon_0$ (solid black line); $(1-\phi_v)T_{p,c}/\varepsilon_0$ (dashed blue line); $(1-\phi_v)T_{\nu,c}/\varepsilon_0$ (dashed red line); $\phi_v T_{p,d}/\varepsilon_0$ (dotted blue line); $\phi_v T_{\nu,d}/\varepsilon_0$ (dotted red line).

It was also shown in §3.4.1 that, for increasing viscosity ratio, γ, $\varepsilon_c(t)$ increases (figure 3.19(c)) and $\varepsilon_d(t)$ decreases (figure 3.24(c)). To explain this behavior, we analyze how varying γ modulates the velocity field at the droplet interface. Figure 3.28 shows the velocity profiles in an x-y plane, $u(y)$, through the midsection of a droplet in cases G ($\gamma = 1$) and H ($\gamma = 100$). The figure shows that (i) $\partial u/\partial y$ at the interface is continuous for $\gamma = 1$ and discontinuous for $\gamma = 100$ and (ii) the magnitude of the velocity gradient in the carrier fluid ($\partial u_c/\partial y$) increases as γ increases from 1 to 100. To explain this, consider two cases of the flow near the interface of a droplet initially released from rest in two uniform flows with the same Re, We_{rms} and φ, but different γ (figure 3.29). The boundary conditions at the droplet interface (Appendix B) stipulate that: (i) the velocity is continuous

$$u_c = u_d, \tag{3.18}$$

and (ii) the tangential stress is continuous

$$\mu_c \frac{\partial u_c}{\partial y} = \mu_d \frac{\partial u_d}{\partial y} \rightarrow \frac{\partial u_c}{\partial y} = \gamma \frac{\partial u_d}{\partial y}. \tag{3.19}$$

Figure 3.29 shows that as γ increases, $\partial u_c/\partial y$ increases and $\partial u_d/\partial y$ decreases near the interface, consequently, because ε' is proportional to $\mu(\partial u/\partial y)^2$, ε' near the interface increases in the carrier fluid and decreases in the droplet-fluid. This mechanism can also be seen in droplet-laden isotropic turbulence by comparing contours of ε' in cases G ($\gamma = 1$) and H ($\gamma = 100$), which are shown in figure 3.30 at $t = 1.5$ and supplementary movie 5.

3.4.5 Viscous power

In §3.4.1 and §3.4.2, the results have shown that the viscous power is a sink of TKE for the carrier-fluid ($T_{\nu,c}(t) < 0$) and a source of TKE for the droplet fluid ($T_{\nu,d}(t) > 0$). We now explain why $T_{\nu,c}(t) < 0$ and $T_{\nu,d}(t) > 0$ and how varying We_{rms}, φ and γ changes their magnitude.

Figure 3.31 shows the instantaneous two-dimensional contours of $T'_\nu \equiv \text{Re}^{-1}\partial(\mathcal{T}_{ij}u_j)/\partial x_i$ in a sub-region of the computational domain at $t = 1.1$ (supplementary movie 6 shows the

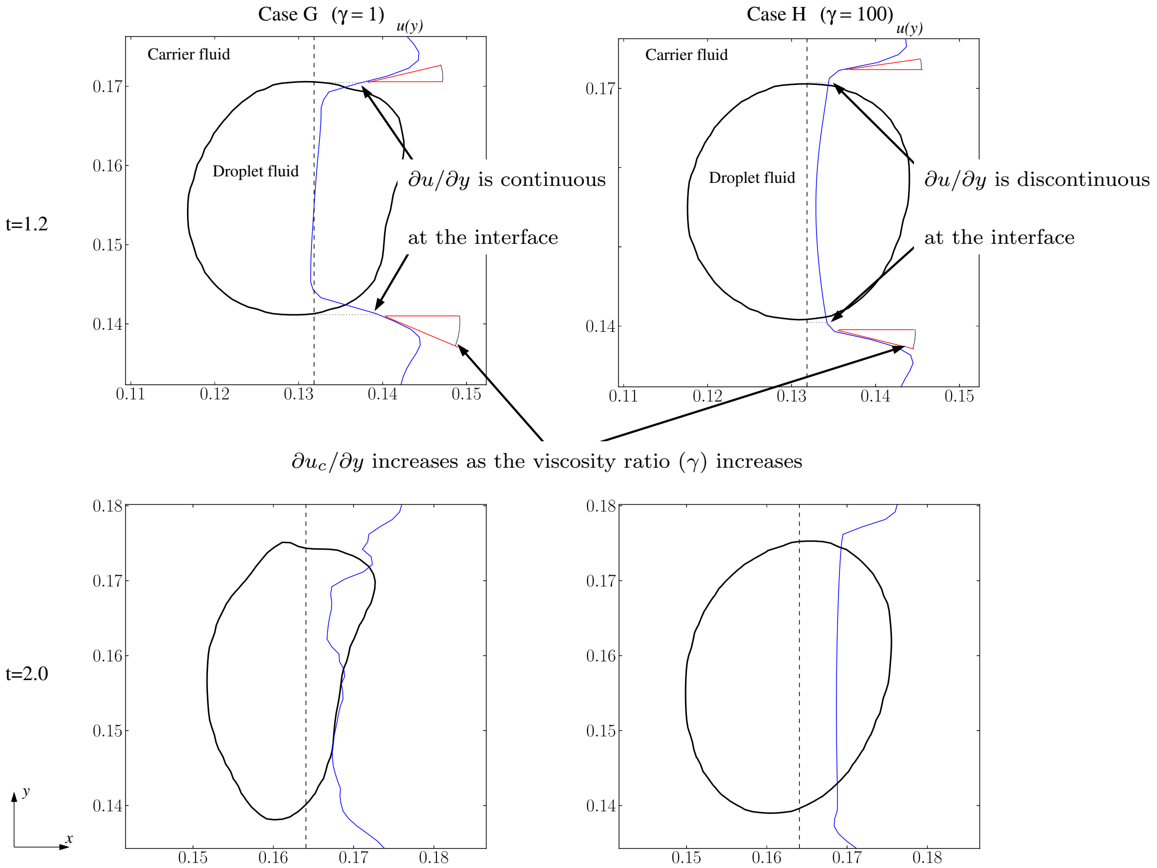

Figure 3.28: Cross sections of a droplet (black line; $C = 0.5$ isoline) showing the u-velocity profile, $u(y)$, (blue line) taken at the dashed line in cases G (left column) and H (right column) at $t = 1.2$ (top row) and $t = 2$ (bottom row). Contrasting $u(y)$ in both figures, we see that $\partial u/\partial y$ is discontinuous in case H ($\gamma = 100$) and that $\partial u/\partial y$ in the carrier fluid is greater in case H than it is in case G.

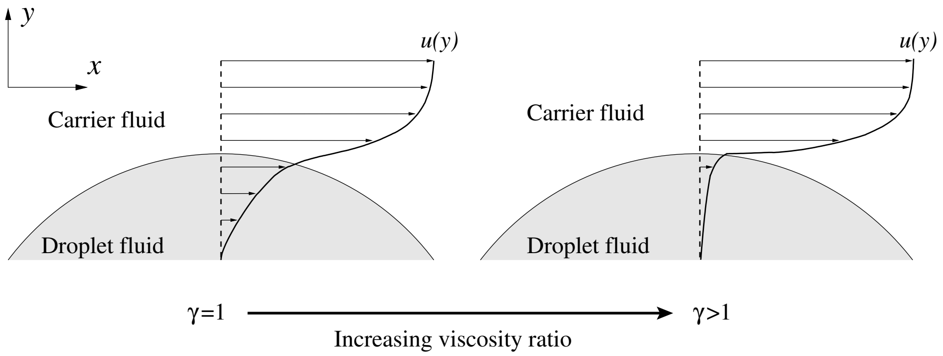

Figure 3.29: Illustration of the velocity profile, $u(y)$, at the interface of a droplet released from rest in uniform flow. The illustration depicts the effects of varying the viscosity ratio, γ. Unity viscosity ratio $\gamma = 1$ (left figure); viscosity ratio greater than unity $\gamma > 1$ (right figure).

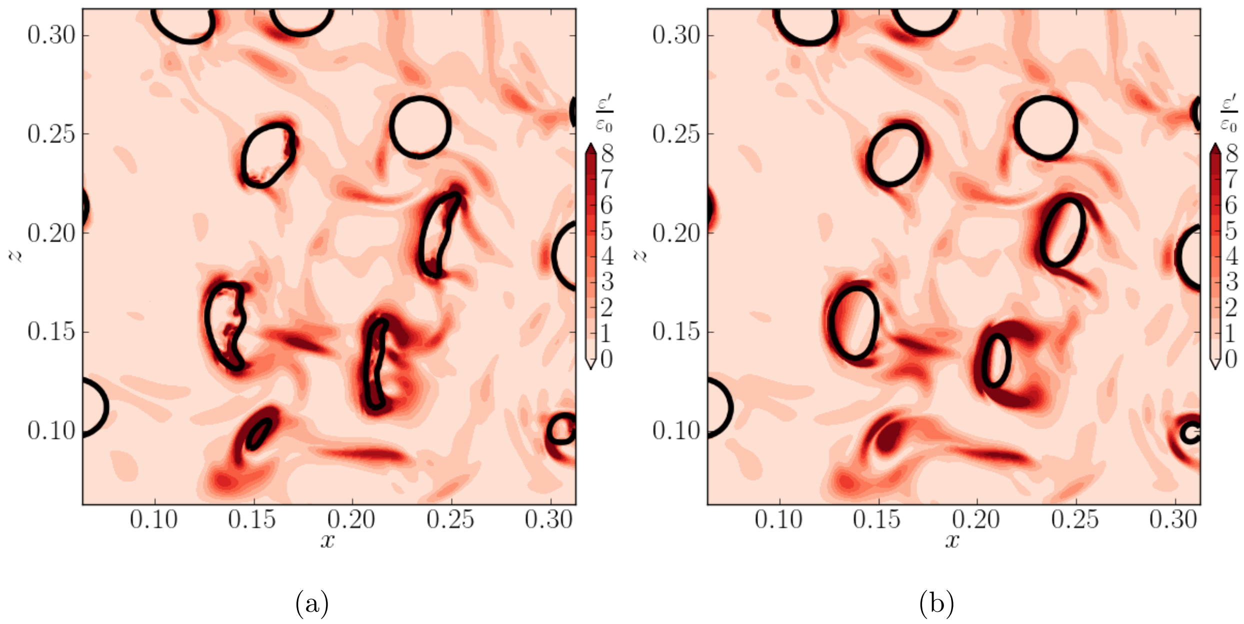

(a)

(b)

Figure 3.30: Instantaneous contours in a subregion of the x–z plane of $\varepsilon' = \mathrm{Re}^{-1}(T_{ij}S_{ij})$ in (a) case G and (b) case H at $t = 1.5$.

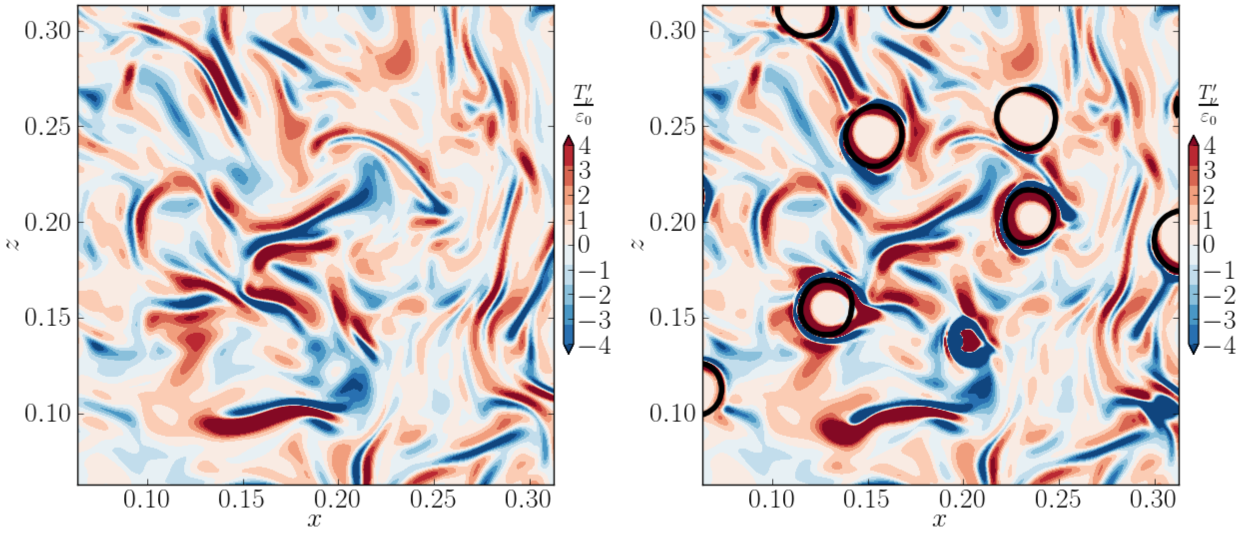

(a) (b)

Figure 3.31: Instantaneous contours in a subregion of the x–z plane of $T'_\nu = \mathrm{Re}^{-1}\partial(u_j \mathsf{T}_{ij})/\partial x_i$ in (a) case A and (b) case C at $t = 1.1$.

animated contours for $1 < t < 3.5$). For single-phase flow $T_{\nu,c}(t) = 0$, figure 3.31(a) shows regions of $T'_\nu > 0$ and < 0. In contrast, in the droplet-laden flow (case C), figure 3.31(b) shows that T'_ν is preferentially negative in the carrier fluid and positive in the droplet fluid. Such modulation of T'_ν by the droplets induces $T_{\nu,c}(t) < 0$ and $T_{\nu,d}(t) > 0$ because $T_{\nu,c}(t) = \langle T'_\nu \rangle_c$ and $T_{\nu,d}(t) = \langle T'_\nu \rangle_d$. Finally, $T_{\nu,c}(t) < 0$ and $T_{\nu,d}(t) > 0$ indicates that there is a net flux of TKE from the carrier fluid to the droplet fluid.

In §3.4.1, the results showed that, for early times $1 < t < 1 + \tau_\ell$, $T_{\nu,c}(t)$ increases in magnitude with increasing Weber number. The reason for the behavior is unclear from analyzing two-dimensional contours of T'_ν in cases B and D (not shown), because they are qualitatively similar. Therefore, to explain the behavior, we begin be rewriting $T_{\nu,c}(t)$ (3.10) as a volume integral, and then by transforming it to a surface integral using the divergence theorem as

$$T_{\nu,c}(t) = \frac{1}{\mathcal{V}_c}\sum_{n=1}^{N_d}\frac{1}{\mathrm{Re}}\iint_{\partial\mathcal{V}_c^{(n)}(t)}\left(\mathcal{T}\mathbf{u}\cdot\mathbf{n}\right)\mathrm{d}\mathcal{A}. \tag{3.20}$$

Equation (3.20) can be interpreted as the rate of work on the carrier fluid due to the viscous stress acting on $\partial\mathcal{V}_c^{(n)}$. We note that the contributions from the boundaries of the computational domain sum to zero due to periodicity, and therefore, the power in (3.20) is due entirely to viscous forces exerted on the carrier-fluid by the droplets. Therefore, $T_{\nu,c}(t)$ can be interpreted as the work on the carrier-fluid due to viscous drag from the droplets.

Equation (3.20) shows that $T_{\nu,c}(t)$ depends on both the magnitude of the integrand and the amount of droplet surface area over which the integration is performed. This dependence is expressed as

$$T_{\nu,c}(t) = \frac{1}{\mathcal{V}_c}G_\nu(t)A(t), \tag{3.21}$$

where $A(t)$ is the instantaneous total surface area of the droplets (3.14) and $G_\nu(t)$ is the mean value of the integrand in (3.20), which is defined as

$$G_\nu(t) = \frac{1}{A(t)}\frac{1}{\mathrm{Re}}\sum_{n=1}^{N_d(t)}\iint_{\partial\mathcal{V}_c^{(n)}(t)}\Big(|\mathbf{u}||\mathcal{T}\mathbf{n}|\cos\left(\theta_\nu\right)\Big)\mathrm{d}\mathcal{A}, \tag{3.22}$$

Compared to that in (3.20), we have rewritten the integrand in (3.22) in terms of the magnitude of the velocity vector, $|\mathbf{u}|$, the magnitude of the traction vector, $|\mathcal{T}\mathbf{n}|$, and the angle, θ_ν, formed between $\mathbf{u}$ and $\mathcal{T}\mathbf{n}$. Table 3.4 shows the normalized values of $G_\nu(t)$ and $A(t)$ at $t = 1.5$.

Table 3.4 shows that as We_{rms} increases from 0.1 to 5, $G_\nu(t)$ increases in magnitude by 25 % and $A(t)$ increases by 6 %, and therefore, both contribute to an increase in the magnitude of $T_{\nu,c}(t)$. To explain the increase in magnitude of $G_\nu(t)$, we analyze the ensemble average $(\overline{\cdots})$ of the following terms from the right-hand side of (3.22): $|\mathbf{u}|$, $\mathrm{Re}^{-1}|\mathcal{T}\mathbf{n}|$, and $\cos(\theta_\nu)$. Table 3.4 shows that as We_{rms} increases from 0.1 to 5, $\overline{\cos(\theta_\nu)}$ is roughly constant, and thus, it is not responsible for the increase in $G_\nu(t)$. Table 3.4 also shows that as We_{rms} increases from 0.1 to 5, $\overline{|\mathbf{u}|}$ increases by 12 % and $\mathrm{Re}^{-1}|\mathcal{T}\mathbf{n}|$ stays nearly constant. Figures 3.33(a–c) shows the scatter plot of $|\mathbf{u}|$ and $\mathrm{Re}^{-1}|\mathcal{T}\mathbf{n}|$ for 4000 randomly selected

Case	G_ν^*	G_p^*	A/A_0	$\overline{\lvert\mathbf{u}\rvert}^*$	$\mathrm{Re}^{-1}\overline{\lvert\mathcal{T}\mathbf{n}\rvert}^*$	$\overline{\lvert-p\mathbf{n}\rvert}^*$	$\overline{\cos(\theta_\nu)}$	$\overline{\cos(\theta_p)}$
B	-0.220	-0.077	1.00	0.57	0.193	3.49	-0.784	-0.055
C	-0.252	-0.183	1.02	0.62	0.194	1.26	-0.772	-0.135
D	-0.275	-0.280	1.06	0.65	0.189	1.27	-0.822	-0.162
E	-0.129	-0.099	1.01	1.21	0.144	1.17	-0.353	-0.047
F	-0.233	-0.087	1.02	0.31	0.240	1.33	-0.794	-0.102
G	-0.218	-0.236	1.03	0.92	0.206	1.40	-0.694	-0.096
H	-0.175	-0.119	1.01	0.36	0.152	1.20	-0.555	-0.150

Table 3.4: Droplet surface statistics in the carrier fluid at $t = 1.5$. The quantities denoted with the superscript * are normalized as follows: G_ν and G_p are normalized by $\frac{1}{2}\rho U_{\mathrm{rms},1}^3$, $\overline{|\mathbf{u}|}$ is normalized by $U_{\mathrm{rms},1}$, and $\mathrm{Re}^{-1}\overline{|\mathcal{T}\mathbf{n}|}$ and $\overline{|-p\mathbf{n}|}$ are normalized by $\frac{1}{2}\rho U_{\mathrm{rms},1}^2$.

samples, and that $|\mathbf{u}|$ and $\mathrm{Re}^{-1}|\mathcal{T}\mathbf{n}|$ are positively correlated. Consequently, as $\overline{|\mathbf{u}|}$ increases with We_{rms}, $\mathrm{Re}^{-1}\overline{|\mathbf{u}||\mathcal{T}\mathbf{n}|}$ also increases, such as to increase the right-hand side of (3.22), i.e. increases $G_\nu(t)$.

To explain the increase in $\overline{|\mathbf{u}|}$ with increasing We_{rms}, we analyze the pressure distribution on the droplet. Flow separation in cases B–D leads to fore-aft asymmetry in the pressure distribution, in which the pressure is higher on the windward side of the droplet than it is on the leeward side as shown in figure 3.32. In case B, because $We_{\mathrm{rms}} = 0.1$, the surface tension forces dominate pressure forces, consequently, the droplets remain spherical. As We_{rms} increases to 1 (case C) and 5 (case D), the pressure forces increasingly overcome surface tension forces, leading to droplet deformation. Because the pressure on the windward side of the droplet is greater than that on the leeward side (figure 3.32), the droplets tend to flatten with the largest dimension perpendicular to the direction of the flow. Such deformation makes the droplet less streamlined and increases the droplet frontal area. The consequences of the deformation can be quantified by computing the pressure force acting on the carrier

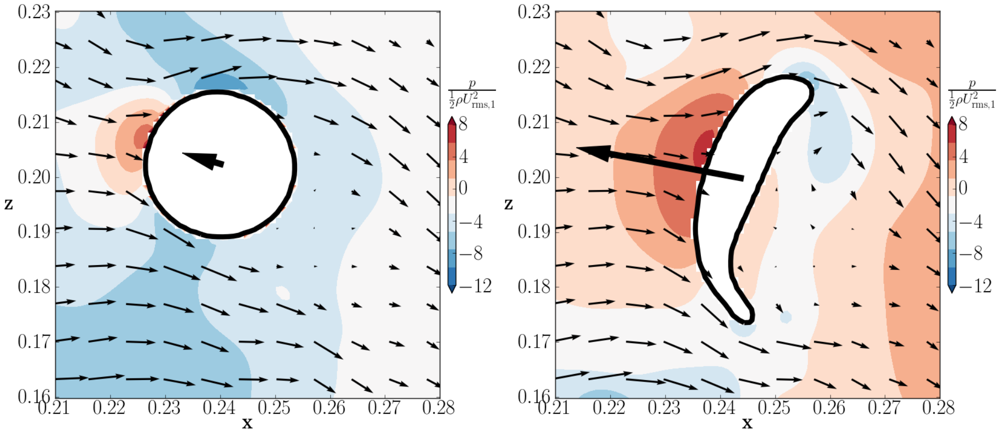

(a) $We_{\mathrm{rms}} = 0.1$ (b) $We_{\mathrm{rms}} = 5$

Figure 3.32: Instantaneous contours of normalized pressure in a subregion of the $x - z$ plane at $t = 1.5$ in (a) case B and (b) case D. Small black arrows are fluid velocity vectors projected on the $x - z$ plane, and the large black arrow is the resultant pressure force acting on the carrier fluid from the droplet, $\mathbf{F}_p$ (3.23). The droplet fluid is masked for clarity.

fluid due to the n-th droplet as

$$\mathbf{F}_p^{(n)}(t) = \iint_{\partial \mathcal{V}_c^{(n)}(t)} (-p\mathbf{n})\,\mathrm{d}\mathcal{A}. \tag{3.23}$$

Figure 3.32 shows $\mathbf{F}_p^{(n)}(t)$ for a selected droplet in cases B and D. Comparing figures 3.32(a) and (b) reveals that $\mathbf{F}_p(t)$ increases with increasing We_{rms}. The force on the droplet is $-\mathbf{F}_p(t)$, and therefore, as We_{rms} increases, the pressure force on the droplet increases, consequently the droplet acceleration increases, and thus the droplet surface velocity $|\mathbf{u}|$ increases. This is proved by the increase in the size of the the tails of the $|\mathbf{u}|$ distribution (i.e. ($|\mathbf{u}| > 0.6$)), as shown in figure 3.33, and by the increase of $\overline{|\mathbf{u}|}$ with We_{rms}, as shown in table 3.4.

In §3.4.1, figure 3.20(b) shows that for increasing φ from 1 to 100, $T_{\nu,c}(t)$ is lowest in magnitude for $\varphi = 1$ (case E), whereas $T_{\nu,c}(t)$ for $\varphi = 10$ and 100 (cases C and F) was roughly equal. Table 3.4 shows that, in cases C and F, $G_\nu(t)$ increases in magnitude by 95 % and 81 %, respectively, with respect to case E. The droplet surface area, $A(t)$, varies

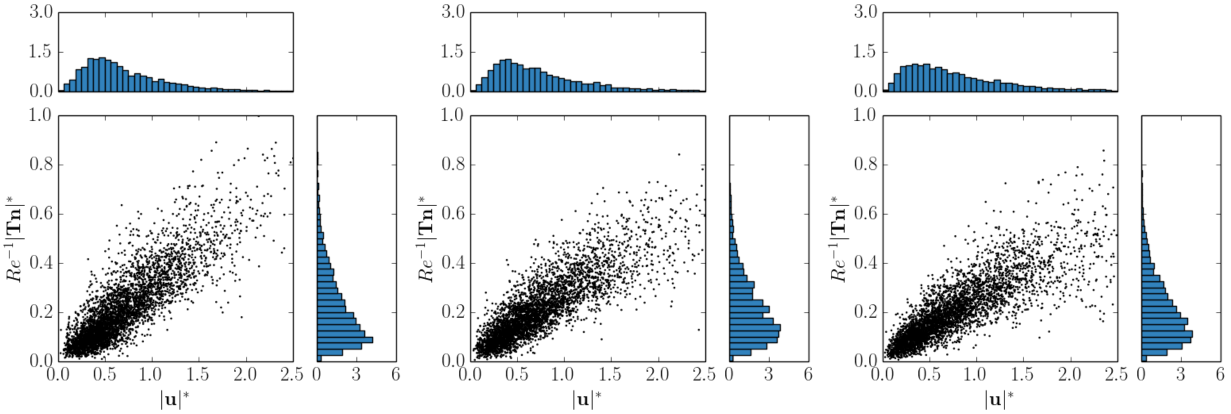

(a) $\mathrm{We}_{\mathrm{rms}} = 0.1$ (b) $\mathrm{We}_{\mathrm{rms}} = 1$ (c) $\mathrm{We}_{\mathrm{rms}} = 5$

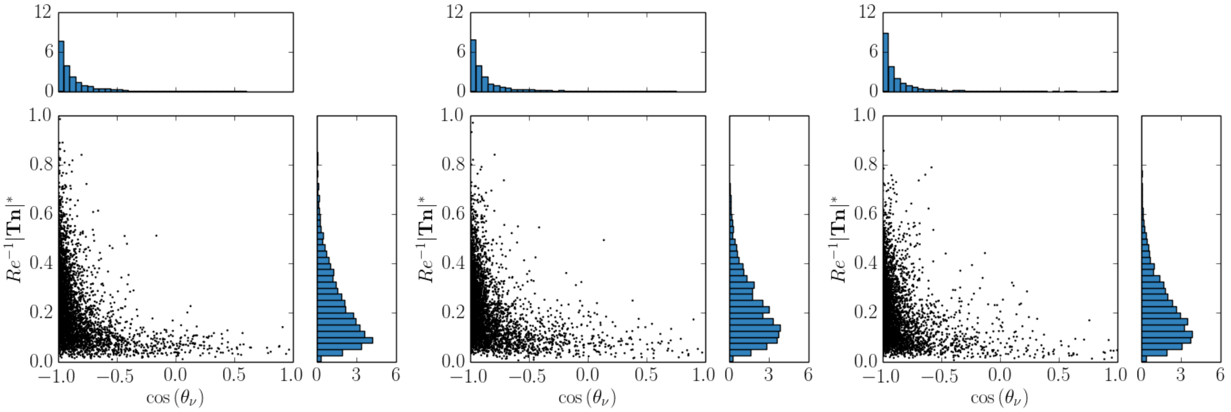

(d) $\mathrm{We}_{\mathrm{rms}} = 0.1$ (e) $\mathrm{We}_{\mathrm{rms}} = 1$ (f) $\mathrm{We}_{\mathrm{rms}} = 5$

Figure 3.33: Scatter plots of $|\mathbf{u}|$ vs. $\mathrm{Re}^{-1}|\mathcal{T}\mathbf{n}|$ (a–c) and $\cos(\theta_\nu)$ vs. $\mathrm{Re}^{-1}|\mathcal{T}\mathbf{n}|$ (d–f) in cases B–D for 4000 randomly selected samples at $t = 1.5$. One-dimensional probability density functions of the corresponding variables are shown in the margins of each scatter plot.

by 1 % between the three cases. Therefore, via (3.21), the increase of $T_{\nu,c}(t)$ in cases C and F relative to case E is primarily due to increasing $G_\nu(t)$. To explain the increase in magnitude of $G_\nu(t)$, figure 3.34(d)–(f) show that when $\varphi = 1$ (case E), $\cos\theta_\nu$ is nearly uniformly distributed between -1 and 0.4, whereas when $\varphi = 10$ and 100 (case C and F), $\cos\theta_\nu$ has values primarily at -1. Also, table 3.4 shows that $\overline{\cos(\theta_\nu)}$ in case E is approximately half of that in cases C and F. At the same time, table 3.4 shows that as φ increases, $\overline{|\mathbf{u}|}$ decreases, $\mathrm{Re}^{-1}\overline{|\mathbf{u}||\mathcal{T}\mathbf{n}|}$ increases and $\overline{\cos(\theta_\nu)}$ increases. Figure 3.34(a)–(c) shows that the increase in $\overline{|\mathbf{u}||\mathcal{T}\mathbf{n}|}$ is balanced by the decrease in $\overline{|\mathbf{u}|}$, and thus, the increase in $\overline{\cos(\theta_\nu)}$ from case E to C is responsible for the increase in the magnitude of $G_\nu(t)$, and therefore, $T_{\nu,c}(t)$. Furthermore, the increase in $\cos\theta_\nu$ with increasing φ is explained as follows. We recall from §3.3.2 that as φ increases the droplet inertia increases, leading to the droplet trajectories deviating more from the surrounding fluid trajectories. As a consequence, as φ increases, the viscous force on the carrier fluid, $\mathcal{T}\mathbf{n}$, becomes increasingly misaligned with the local velocity $\mathbf{u}$, thus increasing θ_ν.

Finally, we analyze in more detail the effects of γ on $T_{\nu,c}(t)$. Figure 3.20(c) shows that $T_{\nu,c}(t)$ is roughly equivalent for $\gamma = 1$ (case G) and $\gamma = 10$ (case C), and its value is always greater than that for $\gamma = 100$ (case H). Table 3.4 shows that $A(t)$ decreases monotonically by 2 % from case G to case F, and that in cases C and G, $G_\nu(t)$ increases in magnitude by 44 % and 25 %, respectively, with respect to case H. Therefore, via (3.21), the increase of $T_{\nu,c}(t)$ in cases C and G relative to case H is mainly due to increasing $G_\nu(t)$. To explain the increase in magnitude of $G_\nu(t)$, table 3.4 and figures 3.35(d)–(f) show that $\overline{|\mathbf{u}|}$, $\mathrm{Re}^{-1}\overline{|\mathbf{u}||\mathcal{T}\mathbf{n}|}$ and $\overline{\cos(\theta_\nu)}$ are higher in cases C and G than they are in case H. Thus, it is the combination of these factors that leads to the increase in $G_\nu(t)$ from case H to C, and therefore, $T_{\nu,c}(t)$. However, among the three terms, $\overline{|\mathbf{u}|}$ shows the greatest increase in cases C and G relative to case H, with an increase by a factor of 1.7 and 2.6, respectively. The increase in $\overline{|\mathbf{u}|}$ with decreasing γ is explained by figure 3.29. Note that in the limit $\gamma \to \infty$, which corresponds to $\mu_d \to \infty$, momentum diffuses instantaneously in the droplet, and thus, the droplet behaves as a rigid body, whereas in the limit $\gamma \to 0$, which corresponds to $\mu_d \to 0$, the droplet surface

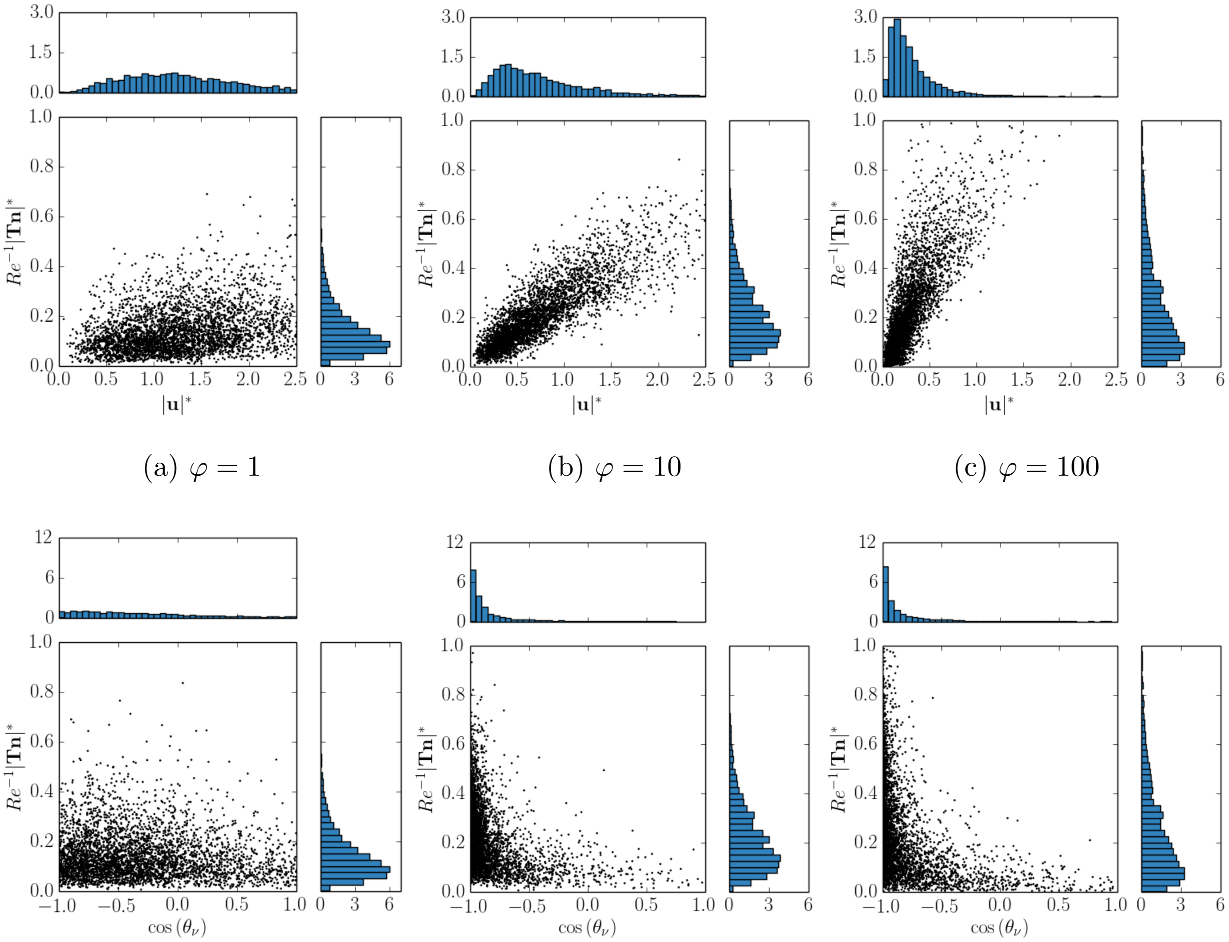

(a) $\varphi = 1$ (b) $\varphi = 10$ (c) $\varphi = 100$

(d) $\varphi = 1$ (e) $\varphi = 10$ (f) $\varphi = 100$

Figure 3.34: Scatter plots of $|\mathbf{u}|$ vs. $\mathrm{Re}^{-1}|\mathcal{T}\mathbf{n}|$ (a–c) and $\cos(\theta_\nu)$ vs. $\mathrm{Re}^{-1}|\mathcal{T}\mathbf{n}|$ (d–f) in cases E, C and F for 4000 randomly selected samples at $t = 1.5$. One-dimensional probability density functions of the corresponding variables are shown in the margins of each scatter plot.

Case	$\overline{\lvert\mathbf{V}_d\rvert}/U_{\text{rms},1}$	$k_d/k_{c,1}$	$k_{d,\text{trans}}(\%)$	$k_{d,\text{rot}}(\%)$	$k_{d,\text{int}}(\%)$
B	0.209	0.235	74.9	2.4	22.7
C	0.223	0.289	72.0	3.0	25.0
D	0.231	0.355	63.6	4.3	32.1
E	0.852	0.286	81.4	3.3	15.3
F	0.074	0.285	71.2	5.4	23.4
G	0.187	0.316	49.4	3.5	47.1
H	0.263	0.300	94.6	1.8	3.6

Table 3.5: Droplet statistics at $t = 1.5$ in cases B–H. $\overline{\lvert\mathbf{V}_d\rvert}$ is the ensemble average of the mean droplet velocity magnitude and $k_d(t)$ is the droplet velocity ($U_{\text{rms},1}$ and $k_{c,1}$ are the r.m.s. velocity and TKE at $t = 1$.). Columns 4–6 are the percentage of droplet TKE associated with droplet translation ($k_{d,\text{trans}}(t)$), rotation ($k_{d,\text{rot}}(t)$), and internal circulation ($k_{d,\text{int}}(t)$).

behaves as a free-shear (slip) boundary.

Table 3.4 shows that, at $t = 1.5$, as γ increases from 1 to 100, the mean droplet surface velocity $\overline{\lvert\mathbf{u}\rvert}$ decreases by 61 %. At the same time, table 3.5 shows that the mean droplet velocity, $\overline{\lvert\mathbf{V}_d\rvert}$, increases by a factor of 3.6. Figure 3.22(c) shows that the decrease in $\overline{\lvert\mathbf{u}\rvert}$ and the increase in $\overline{\lvert\mathbf{V}_d\rvert}$ balance in such a way that the droplet kinetic energy, $k_d(t)$, is nearly independent of γ. This suggests that as γ increases, the $k_d(t)$ associated with internal circulation decreases and the $k_d(t)$ associated with mean droplet translation increases.

To prove this statement from the DNS data, in Appendix E, we decompose $k_d(t)$ as

$$k_d(t) = k_{d,\text{trans}}(t) + k_{d,\text{rot}}(t) + k_{d,\text{int}}(t), \qquad (3.24)$$

where $k_{d,\text{trans}}(t)$ is translational TKE, $k_{d,\text{rot}}(t)$ is the rotational TKE, and $k_{d,\text{int}}(t)$ is the TKE associated with internal circulation, and compute the three forms of droplet kinetic energy using the derived formulas of (E.10). Table 3.5 shows that as γ increases (cases G, C and H),

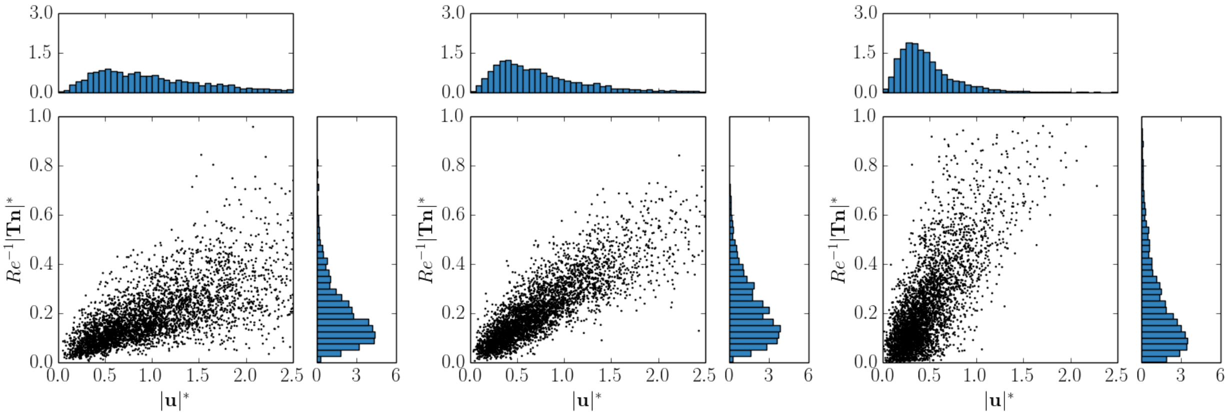

(a) $\gamma = 1$

(b) $\gamma = 10$

(c) $\gamma = 100$

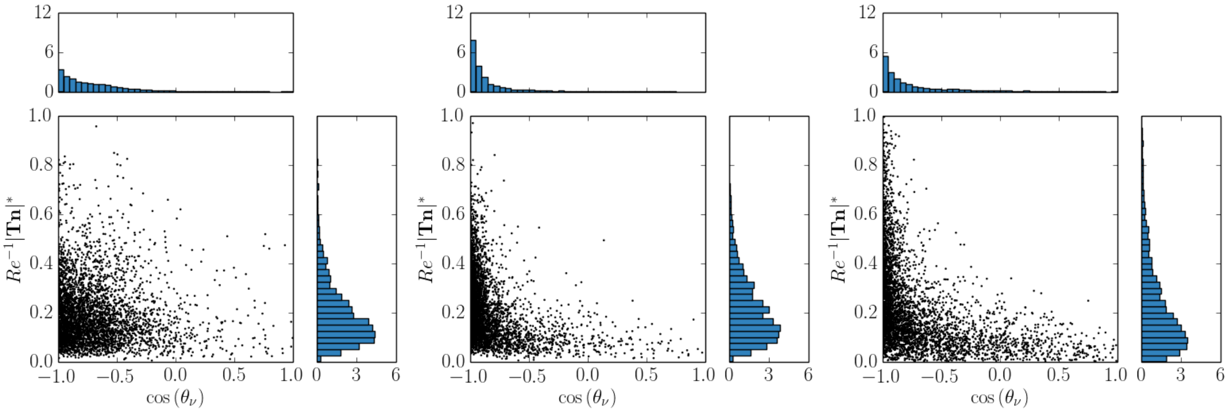

(d) $\gamma = 1$

(e) $\gamma = 10$

(f) $\gamma = 100$

Figure 3.35: Scatter plots of $|\mathbf{u}|$ vs. $\mathrm{Re}^{-1}|\mathcal{T}\mathbf{n}|$ (a–c) and $\cos(\theta_\nu)$ vs. $\mathrm{Re}^{-1}|\mathcal{T}\mathbf{n}|$ (d–f) in cases G, C and H for 4000 randomly selected samples at $t = 1.5$. One-dimensional probability density functions of the corresponding variables are shown in the margins of each scatter plot.

$k_{d,\mathrm{trans}}(t)$ increases from 49 % to 95 %, $k_{d,\mathrm{int}}(t)$ decreases from 47 % to 3.6 %, and $k_{d,\mathrm{rot}}(t)$ is 5 % or less in all cases. This proves quantitatively that, as γ increases, the fraction of carrier-fluid TKE ($k_c(t)$) that goes into droplet translational TKE ($k_{d,\mathrm{trans}}(t)$) increases, and that going into TKE associated with droplet internal circulation ($k_{d,\mathrm{int}}(t)$) decreases.

3.4.6 Pressure power

In §3.4.1 and §3.4.2, the results in figures 3.21 and 3.26 have shown that the pressure power is mostly a sink of TKE for the carrier-fluid ($T_{p,c}(t) < 0$) and a source of TKE for the droplet fluid ($T_{p,d}(t) > 0$). We now explain why $T_{p,c}(t) < 0$ and $T_{p,d}(t) > 0$ and how varying We_{rms}, φ and γ modifies their magnitude.

By using the same procedure that leads to (3.20), the role of $T_{p,c}(t)$ is clarified if we write it in integral form

$$T_{p,c}(t) = \frac{1}{\mathcal{V}_c} \sum_{n=1}^{N_d(t)} \iint_{\partial \mathcal{V}_c^{(n)}(t)} (-p\mathbf{u} \cdot \mathbf{n}) \, \mathrm{d}\mathcal{A}. \tag{3.25}$$

(3.25) is the rate of work on the carrier fluid due to pressure forces acting on $\partial \mathcal{V}_c^{(n)}$. As stated in §3.4.5, the rate of work in (3.25) is entirely due to forces exerted on the carrier-fluid by the droplets. Therefore, $T_{p,c}(t)$ can be interpreted as the work on the carrier-fluid due to pressure drag from the droplets.

As in §3.4.5, $T_{p,c}(t)$ can be expressed in terms of the mean value of the integrand and the droplets surface area:

$$T_{p,c}(t) = \frac{1}{\mathcal{V}_c} G_p(t) A(t). \tag{3.26}$$

where $A(t)$ is the instantaneous total surface area of the droplets and $G_p(t)$ is the mean value of the integrand in (3.25), which is defined as

$$G_p(t) = \frac{1}{A(t)} \sum_{n=1}^{N_d(t)} \iint_{\partial \mathcal{V}_c^{(n)}(t)} \Big(|\mathbf{u}| |-p\mathbf{n}| \cos\left(\theta_p\right) \Big) \mathrm{d}\mathcal{A}. \tag{3.27}$$

The integrand in $G_p(t)$ is rewritten in terms of $|\mathbf{u}|$, the magnitude of the pressure vector $|-p\mathbf{n}|$, and the angle, θ_p, between $\mathbf{u}$ and $-p\mathbf{n}$.

Now, we explain why $T_{p,c}(t)$ increases with increasing We_{rms} for $1 < t < 2$. Table 3.4 shows that as We_{rms} increases from 0.1 to 5, $G_p(t)$ increases in magnitude by a factor of 3.6 and $A(t)$ increases by 6 %; consequently, both contribute to an increase in the magnitude of $T_{p,c}(t)$ via (3.26), with $G_p(t)$ playing a more dominant role. To explain why $G_p(t)$ increases in magnitude with increasing We_{rms}, table 3.4 shows that as We_{rms} increases, $\overline{|\mathbf{u}|}$ increases by 12 % and $\overline{\cos(\theta_p)}$ increases in magnitude by a factor of nearly three. Both of these increases contribute to increased $G_p(t)$ via (3.27). We also note that case B has a mean pressure magnitude, $\overline{-p\mathbf{n}}$, that is 2.8 times larger than in case C and D. However, figure 3.36(d) shows that most of the $-p\mathbf{n}$ samples are clustered near $\cos(\theta_p) \approx 0.1$, and thus, contribute to reducing the magnitude of $G_p(t)$, whereas in cases C and D, the $-p\mathbf{n}$ samples are increasingly skewed towards $\cos(\theta_p) < 0$, and therefore, contribute to increasing the magnitude of $G_p(t)$. In summary, the increase in magnitude of $G_p(t)$, and consequently of $T_{p,c}(t)$, is due primarily to an increase in magnitude of $\overline{\cos(\theta_p)}$.

§3.4.1 showed that, at $t = 1.5$, $T_{p,c}(t)$ is non-monotonic for increasing φ. Table 3.4 shows that as φ increases (cases E, C and F), $A(t)$ is nearly constant and $G_p(t)$ is non-monotonic, increasing in magnitude from case E to case C and then decreasing from case C to case F. Therefore, from (3.26), the non-monotonic behavior in $G_p(t)$, explains the non-monotonic behavior in $T_{p,c}(t)$. Table 3.4 also shows that as φ increases, $\overline{|\mathbf{u}|}$ decreases, $\overline{|-p\mathbf{n}|}$ increases, and $\overline{\cos(\theta_p)}$ is non-monotonic. Figure 3.37 shows that as φ increases, the variance in $|\mathbf{u}|$ decreases and that its mean decreases, which is confirmed by table 3.4. The figure also shows that the probability density function of $|-p\mathbf{n}|$ appears nearly independent of φ, and that the variance in $\cos(\theta_p)$ decreases with increasing φ. The distribution of $\cos(\theta_p)$ is skewed more towards $\cos(\theta_p) < 0$ in case C than it is in cases E and F, which, via (3.27), explains why $G_p(t)$ is highest in case C.

To explain why $T_{p,c}(t)$ decreases in magnitude with increasing γ (cases G, C and H), table 3.4 shows that $A(t)$ decreases by 3 % and $G_p(t)$ decreases in magnitude by 50 % with increasing γ, consequently, via (3.26), both contribute to decreasing the magnitude of $T_{p,c}(t)$. Table 3.4 also shows that as γ increases from 1 to 100, $\overline{|\mathbf{u}|}$ decreases by 60 %, $\overline{|-p\mathbf{n}|}$

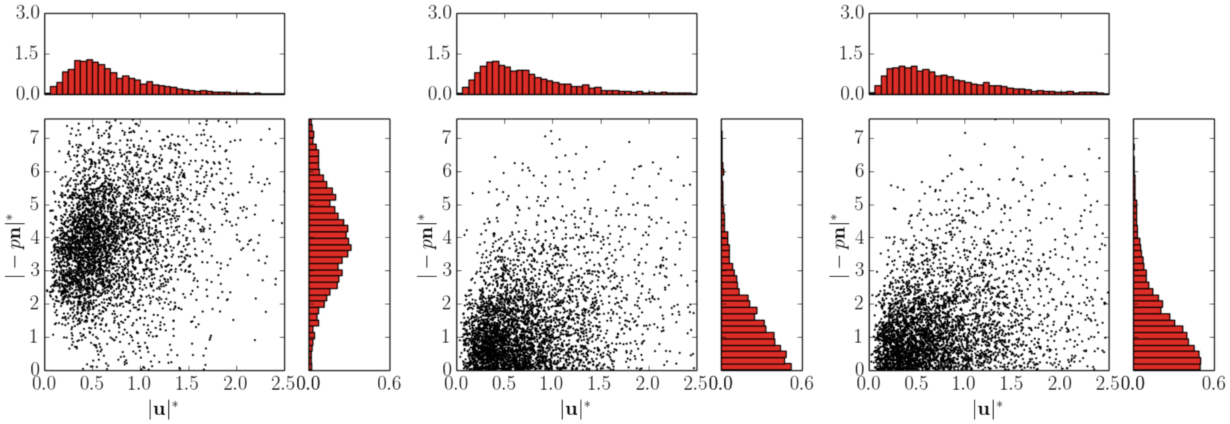

(a) $\mathrm{We}_{\mathrm{rms}} = 0.1$ (b) $\mathrm{We}_{\mathrm{rms}} = 1$ (c) $\mathrm{We}_{\mathrm{rms}} = 5$

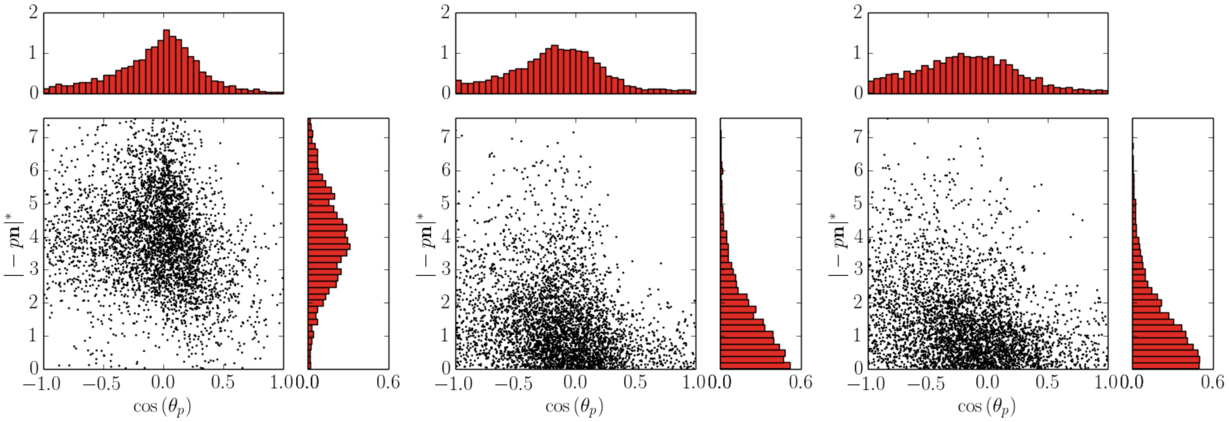

(d) $\mathrm{We}_{\mathrm{rms}} = 0.1$ (e) $\mathrm{We}_{\mathrm{rms}} = 1$ (f) $\mathrm{We}_{\mathrm{rms}} = 5$

Figure 3.36: Scatter plots of $|\mathbf{u}|$ vs. $|-p\mathbf{n}|$ (a–c) and $\cos(\theta_p)$ vs. $|-p\mathbf{n}|$ (d–f) in cases B–D for 4000 randomly selected samples at $t = 1.5$. One-dimensional probability density functions of the corresponding variables are shown in the margins of each scatter plot.

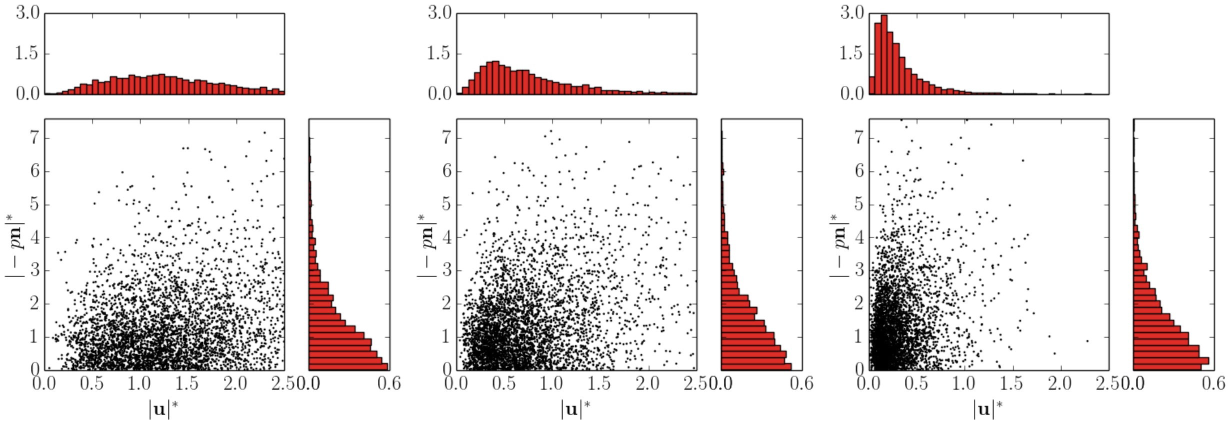

(a) $\varphi = 1$ (b) $\varphi = 10$ (c) $\varphi = 100$

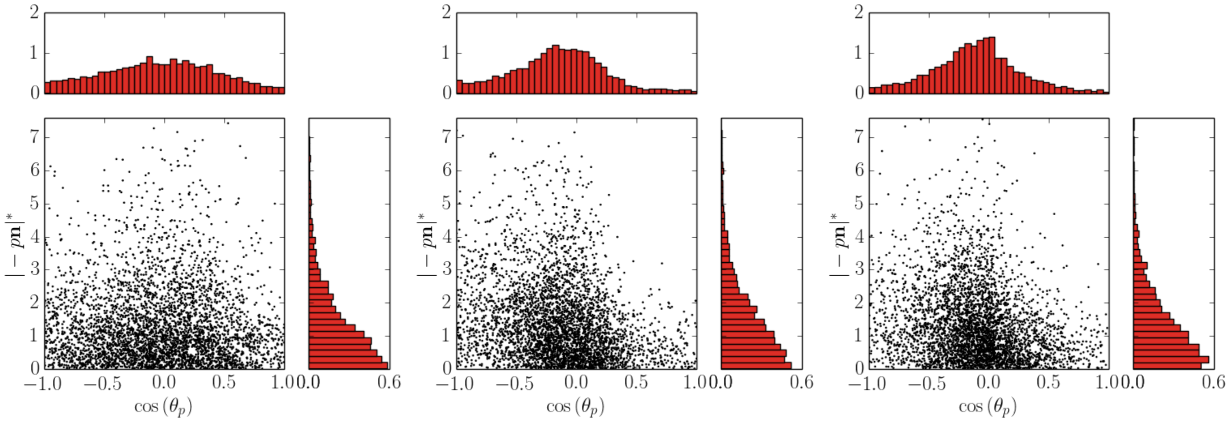

(d) $\varphi = 1$ (e) $\varphi = 10$ (f) $\varphi = 100$

Figure 3.37: Scatter plots of $|\mathbf{u}|$ vs. $|-p\mathbf{n}|$ (a–c) and $\cos(\theta_p)$ vs. $|-p\mathbf{n}|$ (d–f) in cases E, C and F for 4000 randomly selected samples at $t = 1.5$. One-dimensional probability density functions of the corresponding variables are shown in the margins of each scatter plot.

decreases by 14 %, and $\overline{\cos(\theta_p)}$ increases in magnitude by 56 %. As γ increases, because the combined decrease in $\overline{|\mathbf{u}|}$ and $\overline{|-p\mathbf{n}|}$ is greater than the increase in magnitude of $\overline{\cos(\theta_p)}$, $G_p(t)$ decreases in magnitude via (3.27). Figures 3.38(a–c) show that as γ increases, the variance of $|\mathbf{u}|$ decreases and the probability density function is centered at lower values of $|\mathbf{u}|$, which is confirmed by table 3.4. As mentioned, this behavior contributes to decreased $T_{p,c}(t)$ with increasing γ. Figures 3.38(d–f) show that as γ increases, the variance in $\cos(\theta_p)$ increases, such that the distribution is nearly uniform from -1 to 1. As a consequence, the correlation between $\cos(\theta_p)$ and $|-p\mathbf{n}|$ is less than that in cases E and C, and therefore, lessens the influence of the increase in magnitude of $\overline{\cos(\theta_p)}$ with increasing γ. Consequently via (3.26), as γ increases, $T_{p,c}(t)$ decreases in magnitude mostly because of the reduction in $G_p(t)$ and secondarily because of the reduction in $A(t)$.

3.5 Summary

We have performed direct numerical simulations (DNS) of decaying isotropic turbulence laden with deformable droplets, whose diameter is approximately equal to the Taylor lengthscale at the time of droplet release. The goal of the study was to explain the physical mechanisms of droplet-turbulence interaction. Understanding these mechanisms is a prerequisite for developing predictive, physics-based turbulence models. We simulated eight cases in which we released 3130 droplets from rest in decaying isotropic turbulence at an initial Reynolds number based on the Taylor lengthscale of $Re_\lambda = 83$. In each case we varied the Weber number ($0.1 \leq We_{\mathrm{rms}} \leq 5$), the density ratio between the droplet fluid and the carrier fluid ($1 \leq \rho_d/\rho_c \leq 100$) and the dynamic viscosity ratio between the droplet fluid and the carrier fluid ($1 \leq \mu_d/\mu_c \leq 100$). The governing equations were discretized and solved in a cubic domain using 1024^3 grid points, and each droplet was resolved by 32 grid points across its diameter. The droplets were captured in time using the volume-of-fluid method by [15] and the equations governing the incompressible flow of fluid outside and inside the droplets were solved using the fast pressure-correction method of [16]. The findings of this study are summarized as follows:

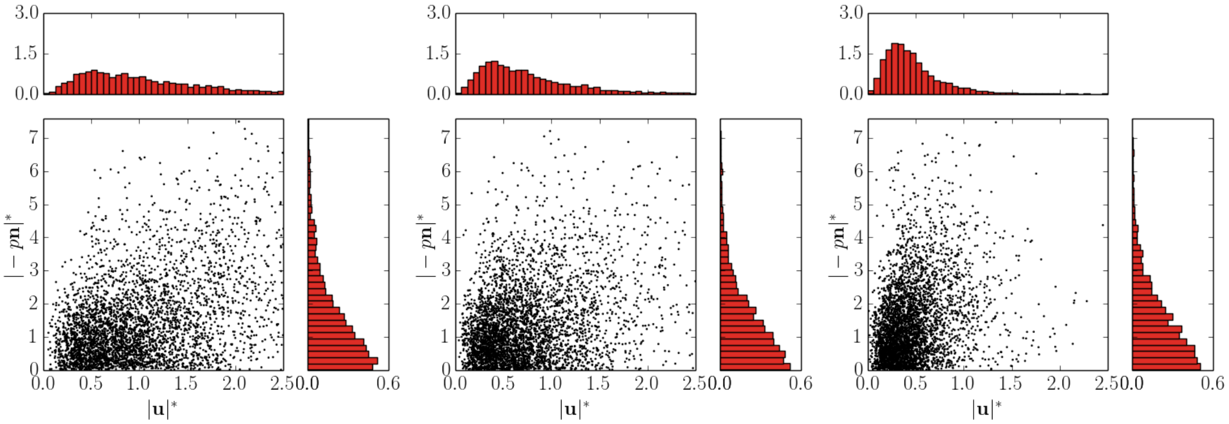

(a) $\gamma = 1$ (b) $\gamma = 10$ (c) $\gamma = 100$

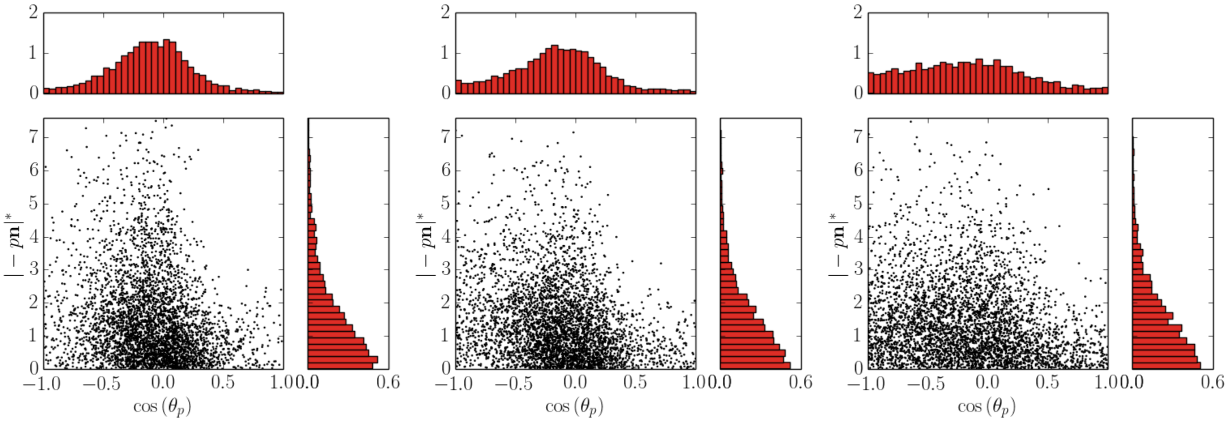

(d) $\gamma = 1$ (e) $\gamma = 10$ (f) $\gamma = 100$

Figure 3.38: Scatter plots of $|\mathbf{u}|$ vs. $|-p\mathbf{n}|$ (a–c) and $\cos(\theta_p)$ vs. $|-p\mathbf{n}|$ (d–f) in cases G, C and H for 4000 randomly selected samples at $t = 1.5$. One-dimensional probability density functions of the corresponding variables are shown in the margins of each scatter plot.

(a) We derived the turbulence kinetic energy (TKE) budget equations of droplet-laden decaying isotropic turbulence for the two fluids, the carrier fluid and the droplet fluid (Appendix C). Compared to the single-phase TKE equation, the two-fluid TKE equation has an additional term, the power of the surface tension, $\Psi_\sigma(t)$. The carrier-fluid and droplet-fluid TKE equations have two extra terms respectively in addition to the viscous dissipation rate: the power of the viscous stress ($T_{\nu,c}$ and $T_{\nu,d}$) and the power of the pressure ($T_{p,c}$ and $T_{p,d}$). Also, an equation relating the power of the surface tension to the rate of change of the droplet surface area (3.13) is derived in Appendix D. These TKE equations allowed us to summarize all the possible all the pathways of TKE exchange in droplet-laden decaying isotropic turbulence (figure 3.4).

(b) When the droplets are released into the flow from rest, the velocity gradient normal to the droplet interface increases rapidly, and consequently the local dissipation rate of TKE increases. The enhanced local dissipation increases the overall dissipation rate of TKE, and therefore, increases the decay rate of TKE compared to that of the droplet-free flow.

(c) The power of the surface tension, $\Psi_\sigma(t)$, represents exchange of TKE and surface energy, and therefore, can be a source or sink of TKE. $\Psi_\sigma(t)$ is initially a sink of TKE, owing to the fact that the droplets are initially spherical (minimum surface energy), and thus, for non-zero We_{rms}, their surface area (energy) can only increase. Before droplet coalescence, $\Psi_\sigma(t)$ is limited to $\pm$ 5 % of the dissipation rate, and hence, $\Psi_\sigma(t)$ plays a minor role in the overall TKE budget. The droplets tend to oscillate in unison with a period equal to the fundamental vibrational mode of the droplets in the inviscid limit. Because $\Psi_\sigma(t)$ is directly proportional (with opposite sign) to the rate of change of the droplets surface area ($\Psi_\sigma(t) = -\mathrm{We}^{-1}\mathcal{V}^{-1}(\mathrm{d}A(t)/\mathrm{d}t)$), droplet oscillations lead to oscillations in $\Psi_\sigma(t)$. For later times, $\Psi_\sigma(t)$ tends to be a source of TKE due to coalescence of droplets. In the case of $We_{\mathrm{rms}} = 0.1$, $\Psi_\sigma(t)$ can be up to 50 % in magnitude of the instantaneous dissipation rate, and therefore, should be accounted for in turbulence models.

(d) For short times ($1 < t < 1 + \tau_\ell$), as the Weber number, $\mathit{We}_{\mathrm{rms}}$, increases from 0.1 to 5

$\hookrightarrow$ the droplets shape deviates more and more from spherical, thus the total droplet surface area, $A(t)$, increases

$\hookrightarrow$ the rate of increase of the surface area, $\mathrm{d}A(t)/\mathrm{d}t$, is greater than the decrease in We^{-1}, such that the magnitude of $\mathrm{We}^{-1}\mathcal{V}^{-1}(\mathrm{d}A(t)/\mathrm{d}t)$ increases

$\hookrightarrow$ the negative peak in $\Psi_\sigma(t)$ increases ($\Psi_\sigma(t) = -\mathrm{We}^{-1}\mathcal{V}^{-1}(\mathrm{d}A(t)/\mathrm{d}t)$), i.e. the rate at which the droplet interface "absorbs" TKE, $k(t)$, increases with $\mathit{We}_{\mathrm{rms}}$

$\hookrightarrow$ the decay rate of two-fluid TKE, $\mathrm{d}k(t)/\mathrm{d}t$ increases.

$\hookrightarrow$ Fore-aft pressure asymmetry develops on the droplet surface causing the droplets to flatten with the largest dimension perpendicular to the direction of the local mean flow, i.e. the droplet frontal area increases and the droplets become less streamlined

$\hookrightarrow$ the net pressure force on the droplets increases, and so does the feedback force on the carrier-fluid, $\mathbf{F}_p$, which opposes the carrier-fluid motion

$\hookrightarrow$ the ensemble average of the mean droplet velocity magnitude, $\overline{|\mathbf{V}_d|}$, increases

$\hookrightarrow$ the droplets follow the motion of the surrounding fluid more closely

$\hookrightarrow$ the strain rate at the droplet interface decreases

$\hookrightarrow$ the decreased strain rate and increased droplet surface area combine in such a way that the two-fluid dissipation rate of TKE, $\varepsilon(t)$, and the carrier-fluid dissipation rate, $\varepsilon_c(t)$, are independent of $\mathit{We}_{\mathrm{rms}}$.

(e) For long times ($t > 1 + \tau_\ell$), the droplets coalesce or break up depending on $\mathit{We}_{\mathrm{rms}}$.

- For $\mathit{We}_{\mathrm{rms}} = 0.1$ and $\mathit{We}_{\mathrm{rms}} = 1$ the droplets only coalesce, which reduces the total surface area of the droplets, i.e. $\mathrm{d}A(t)/\mathrm{d}t < 0$. The coalescence rate is roughly equivalent in both cases such that

$\hookrightarrow$ the rate of decrease of total droplet surface area, $\mathrm{d}A(t)/\mathrm{d}t$, is also roughly equivalent in both cases

$\hookrightarrow$ $\Psi_\sigma(t)$ is ten times greater for $We_{\mathrm{rms}} = 0.1$ than for $We_{\mathrm{rms}} = 1$ because the non-dimensional surface tension coefficient, We^{-1}, is ten times greater. Thus, for $We_{\mathrm{rms}} = 0.1$, the droplets can act as a significant source of TKE, e.g., at $t = 6$, $\Psi_\sigma(t)$ is 50 % that of the dissipation rate of TKE, $\varepsilon(t)$.

$\hookrightarrow$ the addition of TKE to the two-fluid flow by $\Psi_\sigma(t)$ leads to an increase in $\varepsilon(t)$ that is proportional to the increase in $\Psi_\sigma(t)$, such that the decay rate of two-fluid TKE, $\mathrm{d}k(t)/\mathrm{d}t$, is equivalent in both cases.

- For $We_{\mathrm{rms}} = 5$ the droplets coalesce and break up, which has the following consequences relative to the cases in which there is only coalescence ($We_{\mathrm{rms}} = 0.1$ and 1):

$\hookrightarrow$ the decay rate of the total droplet surface area, $\mathrm{d}A/\mathrm{d}t$, is reduced

$\hookrightarrow$ the power of the surface tension, $\Psi_\sigma(t)$, is reduced

$\hookrightarrow$ the decay rate of $k(t)$ is increased.

(f) As the density ratio, φ, increases from 1 to 100, the droplets inertia increases.

$\hookrightarrow$ the droplet trajectories deviate more from those of the surrounding fluid

$\hookrightarrow$ the velocity gradient, $\partial u_i/\partial x_j$, at the droplet interface (both in the carrier fluid and droplet fluid) increases

$\hookrightarrow$ the local dissipation rate of TKE, $\mathrm{Re}^{-1}(\mathsf{T}_{ij}\mathsf{S}_{ij})$, increases in the vicinity of the droplet interface

$\hookrightarrow$ the dissipation rate of TKE, $\varepsilon(t)$, increases (***i***)

$\hookrightarrow$ the tendency of droplets to stay at their initial positions increases

$\hookrightarrow$ the ensemble average of the mean droplet velocity magnitude, $\overline{|\mathbf{V}_d|}$, decreases

$\hookrightarrow$ the coalescence rate of the droplets decreases

$\hookrightarrow$ the decay rate of the total droplet surface area, $\mathrm{d}A(t)/\mathrm{d}t$ decreases

$\hookrightarrow$ the power of the surface tension, $\Psi_\sigma(t)$, decreases (***ii***)

$\hookrightarrow$ as a result of (***i***) and (***ii***), the decay rate of TKE, $\mathrm{d}k(t)/\mathrm{d}t$ increases.

(g) As the viscosity ratio, γ, increases from 1 to 100, the droplets increasingly behave more similarly to rigid, no-slip bodies (i.e. solid particles).

- $\hookrightarrow$ the velocity gradient at the droplet interface increases in the carrier fluid and decreases in the droplet fluid
  - $\hookrightarrow$ the local dissipation rate of TKE increases in the carrier fluid and decreases in the droplet fluid
    - $\hookrightarrow$ the carrier-fluid dissipation rate of TKE, $\varepsilon_c(t)$, increases, and the droplet-fluid dissipation rate of TKE, $\varepsilon_d(t)$, decreases
      - $\hookrightarrow$ the increase in $\varepsilon_c(t)$ and the decrease in $\varepsilon_d(t)$ are balanced such that, the two-fluid dissipation rate, $\varepsilon(t)$, is independent of γ (***iii***).
- $\hookrightarrow$ the droplet deformation rate decreases
  - $\hookrightarrow$ the rate of change of droplet surface area, $\mathrm{d}A(t)/\mathrm{d}t$, decreases
    - $\hookrightarrow$ the magnitude of power of the surface tension $\Psi_\sigma(t)$ decreases (***iv***).
      - $\hookrightarrow$ as a result of (***iii***) and (***iv***), the decay rate of TKE, $\mathrm{d}k(t)/\mathrm{d}t$ increases.

(h) The droplet fluid TKE, $k_d(t)$, initially increases in time due to the transfer of TKE from the carrier-fluid to the droplet fluid via viscous power, $T_{\nu,c}$, and pressure power, $T_{p,c}$. As γ increases from 1 to 100 the droplet-fluid TKE associated with internal circulation, $k_{d,\mathrm{int}}(t)$, decreases from 47 % to 4 %, the translational droplet-fluid TKE, $k_{d,\mathrm{trans}}(t)$, increases from 49 % to 95 %, the rotational droplet-fluid TKE, $k_{d,\mathrm{rot}}(t)$, decreases from 4 % to 2 %, and the total droplet-fluid TKE, $k_d(t)$, is independent of γ. In other words, as γ increases, the ensemble average of the mean droplet velocity magnitude, $\overline{|\mathbf{V}_d|}$, decreases and the internal circulation increases, while $k_d(t)$ is nearly independent. Therefore, as γ increases and $k_{d,\mathrm{trans}}(t)$ increases, it is incorrect to think that $k_d(t)$ will also increase, because the $k_{d,\mathrm{int}}(t)$ decreases, and the net effect is that $k_d(t)$ will stay invariant with γ.

(i) Before the onset of coalescence, the droplets tend to oscillate in unison with a period of oscillation corresponding to the fundamental vibrational mode of the droplet in the inviscid limit. The droplet oscillations lead to oscillations in $\mathrm{d}A(t)/\mathrm{d}t$, and thus $\Psi_\sigma(t)$. As We_rms

increases and φ increases, the period of the droplets fundamental vibrational mode, T_{dvm}, increases, and consequently so does the period of oscillations in $\Psi_{\sigma}(t)$. Also, the droplet oscillations are damped by viscous effects, and the degree of damping is characterized by the Ohnesorge number, Oh. As Oh increases, the oscillations in $\mathrm{d}A(t)/\mathrm{d}t$ and $\Psi_{\sigma}(t)$ are increasingly damped. Oh increases for increasing We_{rms}, decreasing φ or increasing γ.

Chapter 4

MATHEMATICAL FORMULATION FOR EVAPORATING DROPLETS: INCOMPRESSIBLE FORMULATION

4.1 Governing equations

Under the following assumptions:

- The liquid phase and gas phase are incompressible
- The liquid phase is mono-component; the gas-phase is bi-component, consisting of an inert gas and liquid vapor
- The gas is insoluble in the liquid
- The production of thermal energy by viscous dissipation is negligible

the dimensionless governing equations for gas-liquid flow with phase change are:
Continuity equation:

$$\nabla \cdot \mathbf{u} = \frac{1}{\mathrm{Re\ Sc}} \dot{m} \left(\frac{1}{\rho_g} - \frac{1}{\rho_l} \right) \tag{4.1}$$

where the non-dimensional mass flux rate per unit volume due to phase change is

$$\dot{m} = \frac{\rho}{1 - Y_v} \nabla Y_v \cdot \mathbf{n} \delta(n). \tag{4.2}$$

which is positive ($\dot{m} > 0$) during evaporation and negative ($\dot{m} < 0$) during condensation.
Momentum equation:

$$\rho \left(\frac{\partial \mathbf{u}}{\partial t} + (\mathbf{u} \cdot \nabla) \mathbf{u} \right) = -\nabla p + \frac{1}{\mathrm{Re}} \nabla \cdot \left(\mu (\nabla \mathbf{u} + \nabla \mathbf{u}^T) \right) + \frac{1}{\mathrm{We}} \mathbf{f}_\sigma \tag{4.3}$$

where the non-dimensional force due to surface tension is

$$\mathbf{f}_\sigma = \kappa \mathbf{n} \delta(n). \tag{4.4}$$

Energy equation:

$$\rho c_p \left(\frac{\partial T}{\partial t} + (\mathbf{u} \cdot \nabla) T \right) = \frac{1}{\text{Re Pr}} \left[\nabla \cdot (k \nabla T) \right] - \frac{1}{\text{Re Sc Ste}} \dot{m} \tag{4.5}$$

Vapor mass conservation equation:

$$\frac{\partial Y_v}{\partial t} + (\mathbf{u} \cdot \nabla) Y_v = \frac{1}{\text{Re Sc}} \nabla^2 Y_v \tag{4.6}$$

where $\mathbf{u}$ is the velocity (mass-averaged), ρ is the density, μ is the dynamic viscosity, p is the pressure, T is the temperature, c_p is the specific heat at constant pressure, k is the thermal conductivity, and Y_v is the vapor mass fraction. All these variables are functions of space and time. The fluid properties, ρ, μ, c_p, and k are piecewise constant. We use the sign convention that $\dot{m} > 0$ denotes evaporation. In Eqs. (4.1), (4.3), (4.5), and (4.6) Re, Sc, We, Pr, and Ste are, respectively, the Reynolds, Schmidt, Weber, Prandtl, and Stefan numbers defined as:

$$\text{Re} = \frac{\tilde{U} \tilde{L} \tilde{\rho}_g}{\tilde{\mu}_g}, \qquad \text{Sc} = \frac{\tilde{\mu}_g}{\tilde{D}_{gv} \tilde{\rho}_g}, \qquad \text{We} = \frac{\tilde{\rho}_g \tilde{U}^2 \tilde{L}}{\tilde{\sigma}}, \qquad \text{Pr} = \frac{\tilde{\mu}_g \tilde{c}_{p,g}}{\tilde{k}_g}, \qquad \text{Ste} = \frac{\tilde{c}_{p,g} \tilde{T}_g}{\Delta \tilde{h}_v}, \tag{4.7}$$

where $\tilde{U}$, $\tilde{L}$, $\tilde{\rho}_g$, $\tilde{\mu}_g$, $\tilde{\sigma}$, $\tilde{c}_{p,g}$, $\tilde{k}_g$, $\tilde{T}_g$, $\Delta \tilde{h}_v$, and $\tilde{D}_{gv}$ denote, in order, the reference dimensional velocity, length, density, dynamic viscosity, surface tension coefficient, specific heat at constant pressure, thermal conductivity, temperature, latent heat of vaporization, and mass diffusivity of vapor in the gas phase used to non-dimensionalize the governing equations. The reference density, viscosity, specific heat, and thermal conductivity are chosen to be that of the ambient gas, making their values unity in the gas phase. The reference temperature is chosen to be the initial ambient gas temperature, therefore the non-dimensional temperature of the gas phase is initially unity. Throughout the paper, all variables are dimensionless unless they are accented with $\sim$.

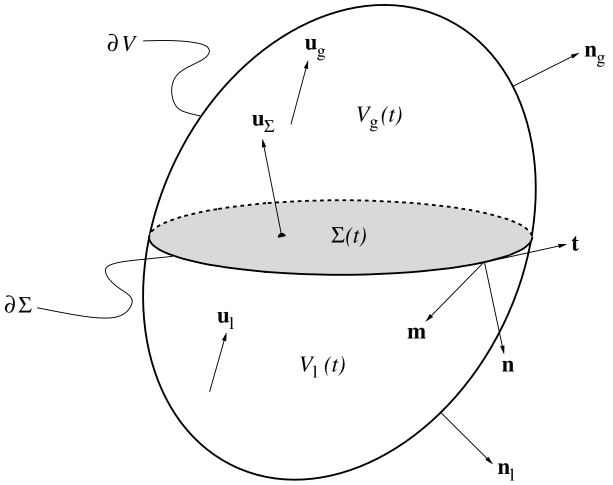

Figure 4.1: Control volume $\mathcal{V}(t)$ containing an interface $\Sigma(t)$ separating the liquid and gas phases, $\mathcal{V}_l(t)$ and $\mathcal{V}_g(t)$, respectively.

4.2 Numerical methods

In this section we describe the numerical methods used. The equations are discretized on a staggered grid in three dimensions with the u-component of velocity located at $x_{i+1/2,j,k}$, the v-component at $x_{i,j+1/2,k}$, the w-component at $x_{i,j,k+1/2}$, and all other variables are centered at $x_{i,j,k}$. All spatial derivatives are discretized using the second-order central difference scheme, with the exception of the normal gradient of the vapor mass fraction and the fluxes of vapor species near the interface, which will be discussed in Sections 4.2.2 and 4.2.3, respectively.

4.2.1 VoF advection in the presence of phase change

To update the volume fraction field from C^n to C^{n+1}, we take the approach of computing the interface velocity ($\mathbf{u}_\Sigma$) directly, and use this velocity field to advect C. This type of approach has been used in front-tracking methods, e.g. [76].

Starting from the jump conditions for the normal velocity across the interface

$$\rho_g(\mathbf{u}_\Sigma - \mathbf{u}_g)\cdot\mathbf{n} = \rho_l(\mathbf{u}_\Sigma - \mathbf{u}_l)\cdot\mathbf{n} = \frac{1}{\text{Re Sc}}\dot{m}'', \tag{4.8}$$

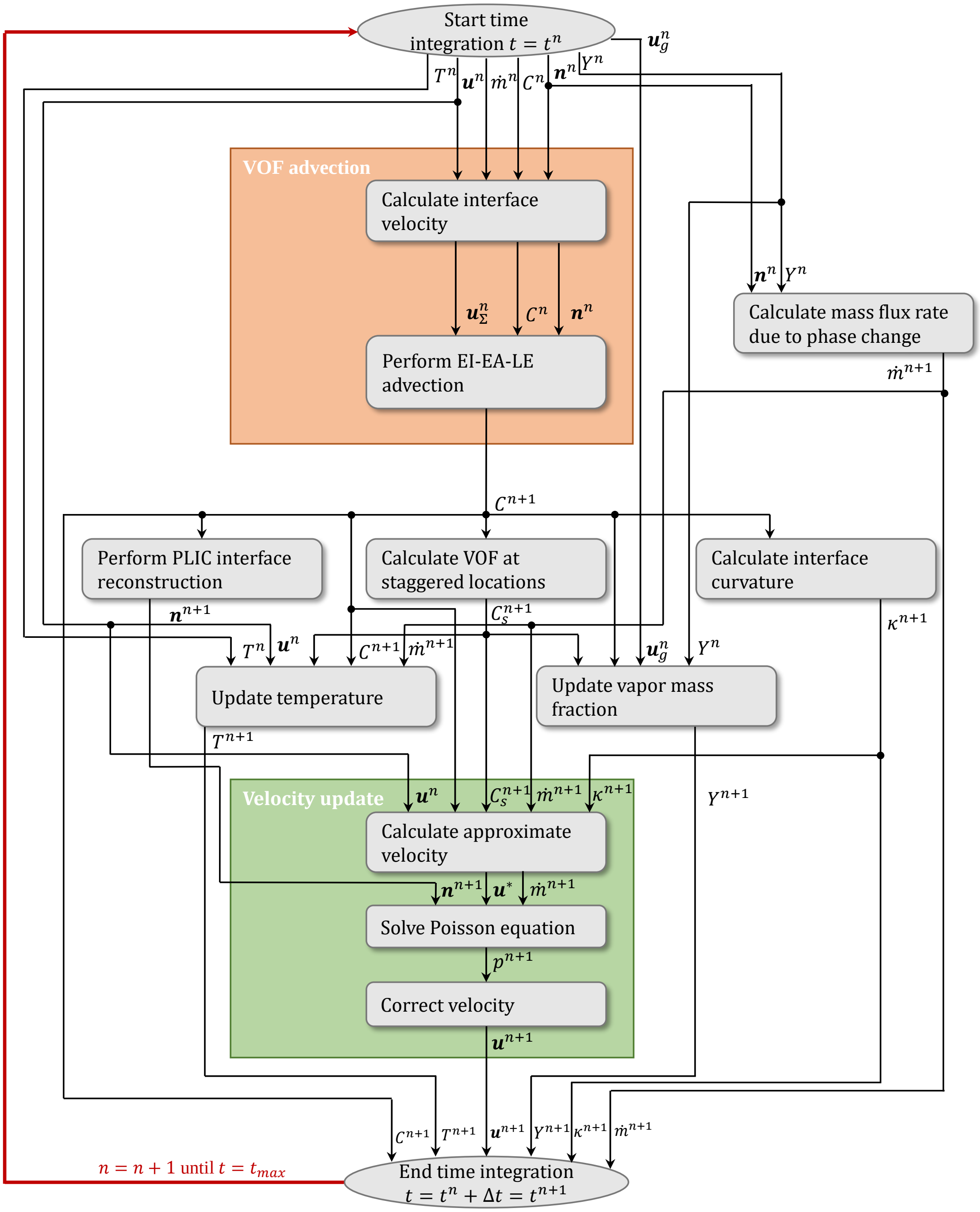

Figure 4.2: Flowchart of flow solver for simulating incompressible gas-liquid flows with phase change using the volume-of-fluid method and pressure-correction method.

one can obtain the following expression for the normal component of the interface velocity

$$\mathbf{u}_\Sigma \cdot \mathbf{n} = \frac{1}{\text{Re Sc}} \frac{\dot{m}''}{2} \left(\frac{1}{\rho_l} + \frac{1}{\rho_g} \right) + \frac{1}{2} \left(\mathbf{u}_l + \mathbf{u}_g \right) \mathbf{n}. \tag{4.9}$$

We compute the interface velocity, $\mathbf{u}_\Sigma$, at the centroid of the PLIC interface. Because the velocity field in the one-fluid formulation is defined as

$$\mathbf{u} = \mathbf{u}_l C + \mathbf{u}_g (1 - C), \tag{4.10}$$

we notice that setting $C = 0.5$ would give the second term in Eq. (4.9). Therefore, because the interface location is defined as the collection of points where $C = 0.5$, we use the PLIC interface to approximate this location. We compute the centroid location of the PLIC interface, then use trilinear interpolation of the velocity field at the centroid to find an approximation of $(\mathbf{u}_l + \mathbf{u}_g)/2$ which is then used in Eq. (4.9) to calculate $\mathbf{u}_\Sigma$. The interface velocity is then computed as

$$\mathbf{u}_\Sigma = (\mathbf{u}_\Sigma \cdot \mathbf{n})\mathbf{n} + (\mathbf{u} \cdot \mathbf{t})\mathbf{t}, \tag{4.11}$$

where the unit tangent vector, $\mathbf{t}$, is found using the Gram-Schmidt process such that one of the vectors in the orthonormal set is $\mathbf{n}$, i.e. $\mathbf{n} \cdot \mathbf{t} = 0$. In Eq. (4.11), we have made use of the fact that the tangential velocity of the interface is equal to that of the surrounding fluid, i.e.,

$$\mathbf{u}_\Sigma \cdot \mathbf{t} = \mathbf{u}_l \cdot \mathbf{t} = \mathbf{u}_g \cdot \mathbf{t}. \tag{4.12}$$

The interface velocity $\mathbf{u}_\Sigma$ is stored at cell centers ($x_{i,j}$), therefore the interface velocity must be distributed to cell faces before the VoF advection can take place. To distribute the interface velocity we use an averaging procedure that is identical to how the interface curvature κ is calculated at cell faces. For example, the u-component of the interface velocity at position $x_{i+1/2,j}$ ($u_{i+1/2,j,\Sigma}$) is computed as

$$u_{i+1/2,j,\Sigma} = \begin{cases} u_{i+1,j,\Sigma} & \text{if } u_{i,j,\Sigma} = 0 \\ u_{i,j,\Sigma} & \text{if } u_{i+1,j,\Sigma} = 0 \\ \frac{1}{2}(u_{i+1,j,\Sigma} + u_{i,j,\Sigma}) & \text{otherwise.} \end{cases} \tag{4.13}$$

The staggered interface velocity field is then used to advance the C field from time level n to $n+1$ as

$$C^{n+1} = C^n + \mathcal{L}(u_\Sigma^n) \tag{4.14}$$

where the operator $\mathcal{L}$ symbolizes the geometric flux calculation of the EI-EA-LE VoF advection scheme [15]. In principle, this approach could be used with any VoF advection scheme.

4.2.2 Computation of mass flux rate due to phase change

Our task is to calculate the mass flux rate due to phase change in cells containing the interface $(0 < C < 1)$ starting from Eq. (4.2). Instead of computing the gradient of Y_v and taking the normal projection as in Eq. (4.2), we compute the normal derivative directly as

$$\dot{m}'' = \frac{\rho}{1 - Y_v} \frac{\partial Y_v}{\partial n} \tag{4.15}$$

using the normal probe approach similar to that of [77] (note that we focus on computing the mass flux per unit area, $\dot{m}''$, and return to discretizing the δ function in Eq. (4.2) later). Consider Fig. 4.3 in which we have illustrated a typical computation cell in which $\dot{m}''$ must be computed. The first point is located at the centroid of the PLIC interface, $Y_{v,sat}$. From the $Y_{v,sat}$ location, two virtual probes, $Y_{v,p1}$ and $Y_{v,p2}$, are extended into the gas phase in the direction normal to the interface a distance equal to h and $2h$, respectively. Using the normal probe values, Eq. (4.15) is discretized using a one-sided second-order finite difference scheme

$$\dot{m}''^{n+1}_{i,j} = \frac{\rho^{n+1}}{1 - Y^n_{v,sat}} \frac{3Y^n_{v,sat} - 4Y^n_{v,p1} + Y^n_{v,p2}}{2h}. \tag{4.16}$$

The vapor mass fraction at the probe locations is computed using bilinear (or trilinear) interpolation based on the values of Y_v in the neighboring four (or eight) grid nodes.

As mentioned previously, saturation conditions are assumed at the interface. Therefore, $Y_{v,sat}$ is a function of the saturation pressure, p_{sat}, which is found using the Clausius-Clapeyron relation

$$\tilde{p}_{\text{sat}} = \tilde{p}_{\text{boil}} \exp\left[-\frac{\Delta\tilde{h}_v \tilde{M}_v}{\tilde{R}_u}\left(\frac{1}{\tilde{T}_{\text{sat}}} - \frac{1}{\tilde{T}_{\text{boil}}}\right)\right], \tag{4.17}$$

where $\tilde{p}_{\text{boil}}$ is the vapor pressure at $\tilde{T}_{\text{boil}}$ (note that the normal boiling point is commonly chosen as the reference state), and $\tilde{M}_v$ is the molar mass of the vapor. $\tilde{T}_{\text{sat}}$ is the saturation temperature. The non-dimensional form of Eq. (4.17) is

$$p_{\text{sat}} = \exp\left[-\frac{1}{\text{Ste}_{\text{c}}}\left(\frac{1}{T_{\text{sat}}} - \frac{1}{T_{\text{boil}}}\right)\right], \tag{4.18}$$

where $\tilde{p}_{\text{boil}}$ and the initial ambient gas temperature, $\tilde{T}_g$, have been used as reference values and where we have introduced a pseudo Stefan number

$$\text{Ste}_{\text{c}} = \frac{\tilde{R}_u \tilde{T}_g}{\Delta\tilde{h}_v \tilde{M}_v}. \tag{4.19}$$

Note that the saturation temperature T_{sat} is calculated at the PLIC centroid in each cell. Because the PLIC centroid is off-grid, we use linear interpolation to approximate T_{sat} from the neighboring cell centered values of T. The mass fraction of saturated vapor at the gas-liquid interface is

$$Y_{v,\text{sat}} = \frac{p_{\text{sat}} \frac{M_v}{M_a}}{p_{\text{sat}} \frac{M_v}{M_a} + (1 - p_{\text{sat}})}, \tag{4.20}$$

where M_v/M_a is the molar mass ratio of the liquid vapor and ambient gas.

The final step is calculate the mass flux per unit area. This is done by using the relation $\delta(n) = |\nabla C|$ in Eq. (4.2), such that $\dot{m} = \dot{m}''|\nabla C|$, where

$$|\nabla C|_{i,j} = \sqrt{\left(\frac{C_{i+1} - C_{i-1}}{2h}\right)^2 + \left(\frac{C_{j+1} - C_{j-1}}{2h}\right)^2}. \tag{4.21}$$

Because $|\nabla C|_{i,j}$ is non-zero in a region of width about $2h$ about the interface, we must populate cells adjacent to the interface with an estimate of $\dot{m}''$. This is done by taking the arithmetic mean of the non-zero values of $\dot{m}''$ in the eight (twenty six) neighboring cells in 2D (3D).

4.2.3 Computation of the vapor mass fraction

The vapor mass fraction at the new time step, Y_v^{n+1}, is found by integrating Eq. (4.6) in time using the first-order Euler scheme

$$\frac{Y_v^{n+1} - Y_v^n}{\Delta t} = RY^n, \tag{4.22}$$

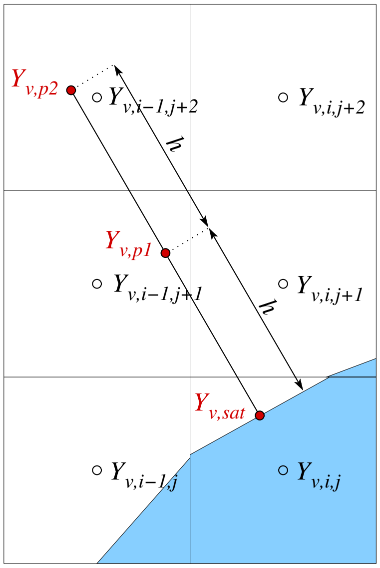

Figure 4.3: Computational stencil for obtaining the normal gradient of Y_v, $\partial Y_v/\partial n$, in cells containing the gas-liquid interface. The first point is located at the PLIC centroid and is at saturation conditions ($Y_{v,sat}$) and the two other points, $Y_{v,p1}$ and $Y_{v,p2}$, are located in the gas phase a distance h and $2h$, respectively, from the interface in the normal direction. $Y_{v,pi}$ is calculated using multidimensional linear interpolation.

where

$$RY^n = -(\mathbf{u}^n \cdot \nabla)Y_v + \frac{1}{\text{Re Sc}}\nabla^2 Y_v^n. \tag{4.23}$$

A first-order explicit scheme is chosen in Eq. (4.22) for two reasons: (i) the time integration of the VoF field is first-order, and therefore using a higher-order time integration for Y_v would not increase the global accuracy of the solution and (ii) the interface will, in general, cross into new computational cells, which, if second-order Adams-Bashforth time integration is being used, requires that the method switch to first-order for a timestep because the fluxes of Y_v at $t = t^{n-1}$ are unavailable in the new cell. Note that in Eq. (4.23) we do not include a source term for vapor, but rather we prescribe a Dirichlet boundary condition on Y_v at the interface. When the second-order finite difference stencil crosses into the liquid phase, i.e. requires values of $Y_{v,i,j}$ in cells where $C_{i,j} > 0.5$, we switch to a one-sided finite difference stencil that is directed into the gas phase.

The Dirichlet boundary condition $Y_v(x = \Sigma) = Y_{v,sat}$ requires that the spatial derivatives in Eq. (4.23) be calculated on a non-uniform grid because generally the interface does not coincide with the grid. Consider, for example, a one-dimensional case in which the interface is located between $x_i - 1$ and x_i as depicted in Fig. 4.4. The interface is located a distance θh from x_i and $(1-\theta)h$ from x_{i-1}, where θ is the distance from the interface to x_i normalized to the range [0,1]. The m-th derivative of Y_v at x_i is then calculated as

$$\left.\frac{\partial^m Y_v}{\partial x^m}\right|_{x=x_i} = \gamma_0 Y_{v,sat} + \gamma_1 Y_{v,i} + \gamma_2 Y_{v,i+1} + \gamma_3 Y_{v,i+2} + \gamma_4 Y_{v,i+3} \tag{4.24}$$

on the stencil $x = [-\theta h, 0, h, 2h, 3h]$, with the derivative being calculated at $x = 0$. The finite difference weights γ_i are calculated using the method found in [78]. In general, this scheme is expected to be at least fourth-order accurate for the first derivative and third-order accurate for the second derivative. Special care must be taken when $\theta << 1$ since as $\theta \to 0$ some $\gamma_i \to \infty$. Therefore, we limit use of Eq. (4.24) to $\theta \geq 1/4$. If $\theta < 1/4$, we omit Y_i and the derivatives are calculated as

$$\left.\frac{\partial^m Y_v}{\partial x^m}\right|_{x=x_i} = \gamma_0 Y_{v,sat} + \gamma_1 Y_{v,i+1} + \gamma_2 Y_{v,i+2} + \gamma_3 Y_{v,i+3}. \tag{4.25}$$

on the stencil $x = [-\theta h, h, 2h, 3h]$, and, again, the derivative is calculated at $x = 0$. In general, Eq (4.25) is expected to be at least third-order accurate for the first derivative and second-order accurate for the second derivative.

The above described method can be generalized to multidimensions in a straightforward manner. The most difficult task is calculating θ, which we address now. Unlike level-set methods where a signed distance function to the interface is tracked, VoF methods do not inherently contain this information. One possible solution is to use the height-function technique, e.g. [79]. However, we propose an alternative, and perhaps simpler solution for this problem. The idea is to compute the volume of liquid in control volumes centered at staggered locations (e.g. $x_{i+1/2,j}$). From this staggered volume fraction field, one can estimate the distance to the interface from cell-centered locations $x_{i,j}$. We denote this staggered volume fraction field as C_s. Then, for the example in which the interface is located between x_{i-1} and x_i, θ is related to C_s by

$$\theta = 1 - C_{s,i-1/2}. \tag{4.26}$$

Figure 4.5 depicts how C_s is defined and calculated. To calculate $C_{s,i-1/2,j}$ (see Fig. 4.5(a)), we define a control volume of side length h (denoted by the dashed line), centered at $x_{i-1/2,j}$. We then calculate the volume cut by the PLIC interface in the left half and the right half (denoted by hatches), and sum these contributions to get $C_{s,i-1/2,j}$. An analogous procedure is used to calculate $C_{s,i,j+1/2}$. In Fig. 4.5(a), the interface is located between $x_{i-1,j}$ and $x_{i,j}$, therefore, to calculate an x-derivative of Y_v at $x_{i-1,j}$, one would use

$$\theta_x = 1 - C_{s,i-1/2,j}, \tag{4.27}$$

where θ_x is the distance between the interface and $x_{i-1,j}$, and the resulting finite-difference stencil would be $x = [\theta_x h, 0, -h, \ldots]$ (assuming $\theta_x \geq 1/4$). In Fig. 4.5(b), the interface is located between $x_{i,j}$ and $x_{i,j+1}$, therefore, to calculate a y-derivative of Y_v at $x_{i,j+1}$, one would use

$$\theta_y = 1 - C_{s,i,j+1/2}, \tag{4.28}$$

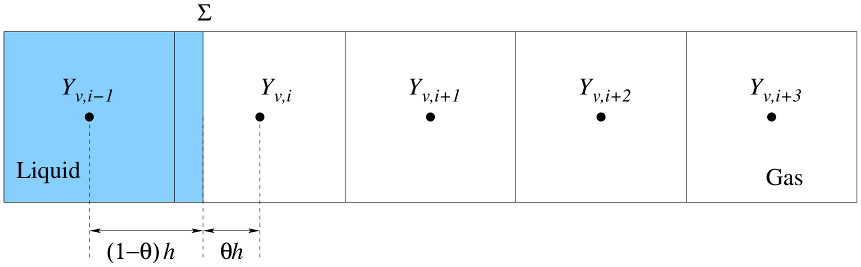

Figure 4.4: Computation of Y_v derivatives at the interface with Dirichlet boundary condition $Y_{v,sat}$.

where θ_y is the distance between the interface and $x_{i,j+1}$, and the resulting finite-difference stencil would be $y = [-\theta_y h, 0, h, \ldots]$ (assuming $\theta_y \geq 1/4$).

4.2.4 Computation of the temperature

The temperature at the new time step, T^{n+1}, is found by integrating Eq. (4.5) in time using the 2nd-order Adams-Bashforth scheme

$$\frac{T^{n+1} - T^n}{\Delta t} = \frac{3}{2} RT^n - \frac{1}{2} RT^{n-1}, \tag{4.29}$$

where

$$RT^n = RCT^n + RDT^n + RST^n. \tag{4.30}$$

where RCT, RDT, and RST are, respectively, the convective, diffusive, and source terms on the right-hand side of Eq. (4.5). They are defined as

$$\begin{aligned} RCT^n &= -\mathbf{u}^n \cdot \nabla T^n \\ RDT^n &= \frac{1}{\rho^n c_p^n} \frac{1}{\mathrm{RePr}} \left[\nabla \cdot (k^n \nabla T^n) \right] \\ RST^n &= -\frac{1}{\rho^n c_p^n} \frac{1}{\mathrm{Ste}} \dot{m}^n \left| \nabla C^n \right| . \end{aligned} \tag{4.31}$$

We discretize the terms in Eq. (4.31) using second-order central differences. Here we present a novel discretization of RDT^n and RST^n in 2D. The discretization of RCT^n is standard

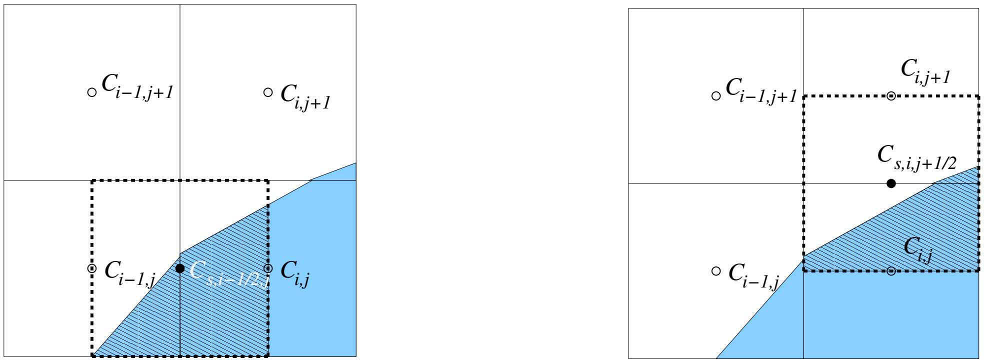

(a) Control volume for calculating $C_{s,i-1/2,j}$ (b) Control volume for calculating $C_{s,i,j+1/2}$

Figure 4.5: Illustration of how to calculate the liquid volume at staggered grid locations. The control volumes for the volume calculation are indicated by the dashed lines. Volume that is included in calculating $C_{s,i-1/2,j}$ and $C_{s,i,j+1/2}$ is indicated by the hatched regions.

and equivalent to what would be found in single-phase flow. RDT^n is discretized as follows

$$RDT_{i,j} = \frac{1}{\rho_{i,j} c_{p,i,j}} \frac{1}{\text{RePr}} \left[\frac{k_{i+1/2,j}(T_{i+1,j} - T_{i,j}) - k_{i-1/2,j}(T_{i,j} - T_{i-1,j})}{h^2} + \frac{k_{i,j+1/2}(T_{i,j+1} - T_{i,j}) - k_{i,j-1/2}(T_{i,j} - T_{i,j-1})}{h^2} \right]. \tag{4.32}$$

where $\rho_{i,j} c_{p,i,j}$ is calculated using the harmonic mean

$$\rho_{i,j} c_{p,i,j} = \left(\frac{C_{i,j}}{\rho_l c_{p,l}} + \frac{1 - C_{i,j}}{\rho_g c_{p,g}} \right)^{-1} \tag{4.33}$$

It is important to note that using the arithmetic mean $\rho_{i,j} c_{p,i,j} = \rho_l c_{p,l} C_{i,j} + \rho_g c_{p,g}(1 - C_{i,j})$, can lead to unphysical values of ρc_p and therefore should not be used. To calculate the staggered thermal conductivities in Eq. (4.32), we use a novel method that leverages the staggered volume fraction field

$$\begin{aligned} k_{i+1/2,j} &= k_l C_{s,i+1/2,j} + k_g(1 - C_{s,i+1/2,j}) \\ k_{i,j+1/2} &= k_l C_{s,i,j+1/2} + k_g(1 - C_{s,i,j+1/2}). \end{aligned} \tag{4.34}$$

Compared to using the standard approach, $k_{i+1/2,j} = \frac{1}{2}(k_{i+1,j} + k_{i,j})$, where $k_{i+1,j}$ and $k_{i,j}$ are calculated using the cell-centered volume fractions $C_{i+1,j}$ and $C_{i,j}$, Eq. (4.34) leads to a sharper representation of the temperature field near the interface.

RST^n is discretized as follows

$$RST_{i,j} = -\frac{1}{\rho_{i,j} c_{p,i,j}} \frac{1}{\mathrm{Ste}} \dot{m}^n_{i,j} \sqrt{\left(\frac{C_{s,i+1/2,j} - C_{s,i-1/2,j}}{h}\right)^2 + \left(\frac{C_{s,i,j+1/2} - C_{s,i,j-1/2}}{h}\right)^2}. \tag{4.35}$$

Note that we have used the staggered volume fractions to discretize $|\nabla C|$. This leads to a sharper representation of the Dirac delta function, and therefore leads to less smearing of the source term in Eq. (4.5).

4.2.5 Fast pressure-correction method

To advance the momentum equation in time, we use the pressure-correction method. The pressure correction method we use is based on our FastP* method [16]. The main advantage of this approach is that it reduces the Poisson equation that must be solved at each time step from variable- to constant-coefficient. Therefore, a direct, FFT-based Poisson solver can be used.

Eq. 4.3 is recast in a more compact form as

$$\frac{\partial \mathbf{u}}{\partial t} = -\frac{1}{\rho} \nabla p + \mathbf{RU} \tag{4.36}$$

where

$$\mathbf{RU}^n = -\mathbf{u}^n \cdot \nabla \mathbf{u}^n + \frac{1}{\mathrm{Re}} \frac{1}{\rho^{n+1}} \nabla \cdot \left[\mu^{n+1} \left(\nabla \mathbf{u}^n + (\nabla \mathbf{u}^n)^T\right)\right] + \frac{1}{\mathrm{We}} \frac{1}{\bar{\rho}} \kappa^{n+1} \nabla C^{n+1}, \tag{4.37}$$

and where we have multiplied $\mathbf{f}_\sigma$ by $\rho/\bar{\rho}$, where $\bar{\rho} = (\rho_l + \rho_g)/2$. We compute an approximate velocity field, $\mathbf{u}^*$, by neglecting the pressure gradient in Eq. (4.36) and integrating in time using the second-order Adams-Bashforth scheme

$$\frac{\mathbf{u}^* - \mathbf{u}^n}{\Delta t} = \frac{3}{2} \mathbf{RU}^n - \frac{1}{2} \mathbf{RU}^{n-1}. \tag{4.38}$$

Next, the final velocity at the new time step, $\mathbf{u}^{n+1}$, is obtained in the pressure-correction (projection) step

$$\frac{\mathbf{u}^{n+1}-\mathbf{u}^{*}}{\Delta t}=-\left[\frac{1}{\rho_0}\nabla p^{n+1}+\left(\frac{1}{\rho^{n+1}}-\frac{1}{\rho_0}\right)\nabla\hat{p}\right], \tag{4.39}$$

where, as in [16], the pressure gradient is split into a constant-coefficient part ($1/\rho_0$) and variable-coefficient part ($1/\rho^{n+1}$), and then treat the constant-coefficient part implicitly and the variable-coefficient part explicitly as

$$\frac{1}{\rho^{n+1}}\nabla p^{n+1}\rightarrow\frac{1}{\rho_0}\nabla p^{n+1}+\left(\frac{1}{\rho^{n+1}}-\frac{1}{\rho_0}\right)\nabla\hat{p}, \tag{4.40}$$

where $\rho_0=\min(\rho^{n+1})$ for numerical stability and $\hat{p}$ is a second-order explicit approximation of p^{n+1}, i.e. $\hat{p}=2p^{n}-p^{n-1}$. The pressure at the new time step, p^{n+1}, is obtained by solving the Poisson equation for pressure

$$\nabla^2 p^{n+1}=\nabla\cdot\left[\left(1-\frac{\rho_0}{\rho^{n+1}}\right)\nabla\hat{p}\right]+\frac{\rho_0}{\Delta t}\left[\nabla\cdot\mathbf{u}^{*}-\nabla\cdot\mathbf{u}^{n+1}\right], \tag{4.41}$$

where $\nabla\cdot\mathbf{u}^{n+1}$ is given by

$$\nabla\cdot\mathbf{u}^{n+1}=\frac{1}{\mathrm{Re\ Sc}}\dot{m}^{n+1}\left(\frac{1}{\rho_g^{n+1}}-\frac{1}{\rho_l^{n+1}}\right). \tag{4.42}$$

4.3 Results

4.3.1 Verification of VoF advection with constant mass flux

The objective of this section is to verify the accuracy of the method described in Section 4.2.1. We select test cases in which $\dot{m}''$ is set to a constant and the geometry of the gas-liquid interface is known exactly, allowing us to derive an analytical expression for the total VoF volume as a function of time.

Evaporation of a 1D pool

We consider a one-dimensional domain that contains one half gas and one half liquid separated by an interface as shown in Fig. 4.6. The lower boundary is a wall and the upper

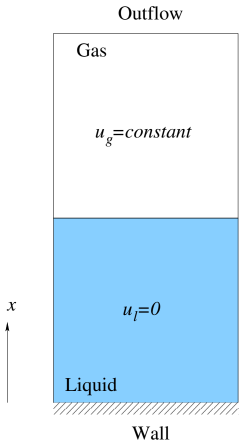

Figure 4.6: Domain for 1D pool evaporation with constant $\dot{m}''$.

boundary is an outflow plane. The liquid remains at rest ($u_l = 0$) as the interface moves towards the wall. Using Eq. (4.8), the gas velocity is

$$u_g = \frac{1}{\text{Re Sc}} \dot{m}'' \left(\frac{1}{\rho_g} - \frac{1}{\rho_l} \right). \tag{4.43}$$

By integrating the interface velocity, u_Σ, in time, one can show that the height of the interface evolves as

$$h(t) = h_0 - \frac{1}{\text{Re Sc}} \frac{\dot{m}''}{\rho_l} t, \tag{4.44}$$

where h_0 is the initial height.

For our test, we use a domain of length $L = 1$ discretized using 32 points, and the interface initialized at $h_0 = 0.5$. The non-dimensional parameters are Re$= 200$, Sc$= 1$, $\dot{m}'' = 30$, and $\rho_g/\rho_l = 4$. The fluids are initially at rest.

Figure 4.7 shows the time development of the interface height, $h(t)$, and the gas-phase velocity, $u_g(t)$. In both cases, there is excellent agreement between the exact and numerical solution. In fact, the solutions agree to machine zero. Something to notice is that $u_g(t)$ remains constant even as the interface crosses grid nodes. This demonstrates that imposing the velocity jump by discretizing the δ-function as Eq. (4.21) yields an exact balance of mass

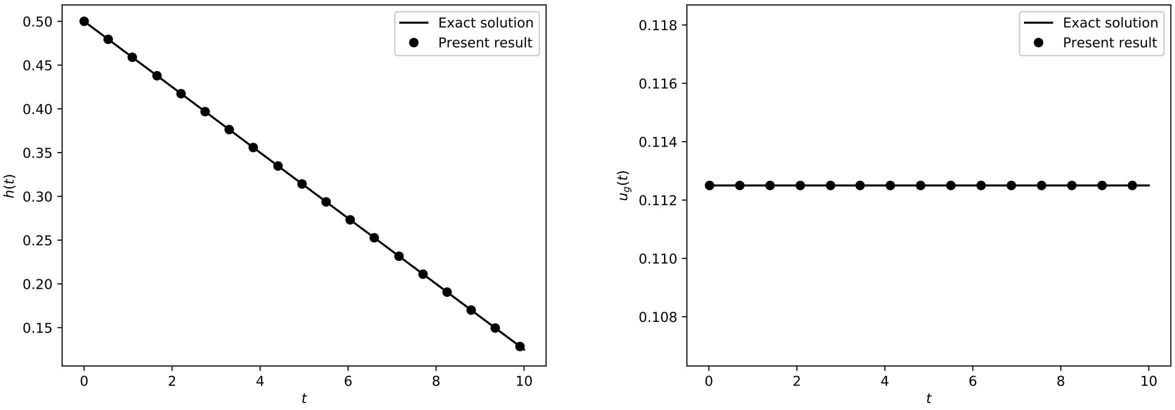

(a) (b)

Figure 4.7: Time evolution of (a) the interface height and (b) the gas-phase velocity.

flux across the interface. We have tested other grid sizes and density ratios up to 10,000 and found that the solution agrees to machine zero for all cases.

Evaporation and condensation of a 2D droplet

We consider a two-dimensional square domain with a wall on the bottom boundary, an outflow on top, and periodic boundary conditions in the horizontal direction. We initialize a circular droplet in the center of the domain and release it from rest in quiescent fluid. We impose a constant evaporative mass flux, $\dot{m}''$ such that Stefan flow is generated around the droplet. The Stefan flow propels the droplet away from the wall. If the droplet remains circular (i.e. the Weber number is sufficiently less than unity) then the normalized droplet diameter squared evolves as

$$\left(\frac{D(t)}{D_0}\right)^2 = \left(1 - \frac{1}{\text{Re Sc}}\frac{2}{D_0}\frac{\dot{m}''}{\rho_l}t\right)^2 . \tag{4.45}$$

For our test, we use a domain of length $L = 1$ discretized using 256^2 points. The initial droplet diameter is $D_0 = 0.25$. The non-dimensional parameters are Re= 250, Sc= 1,

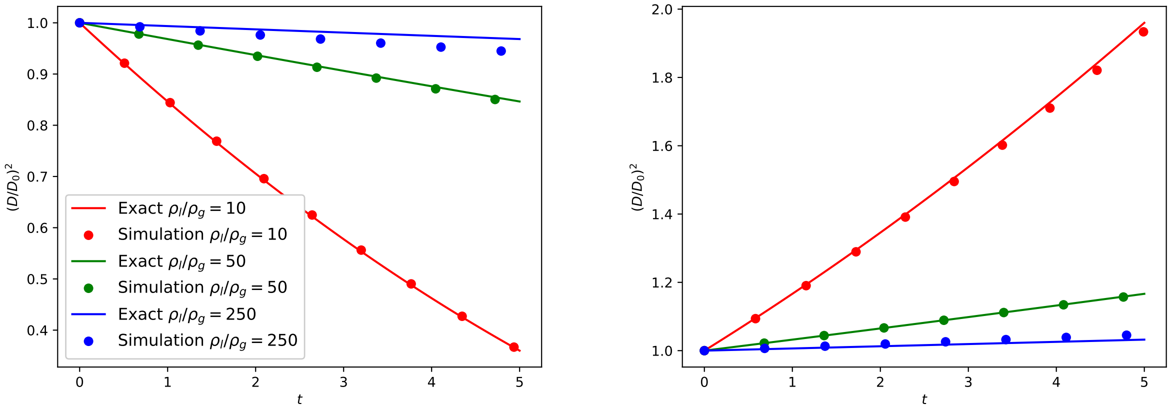

(a) Evaporating droplet

(b) Condensing droplet

Figure 4.8: Time evolution of the normalized droplet diameter squared for (a) an evaporating droplet and (b) condensing droplet. The exact solutions and numerical solutions are shown for density ratios of 10, 50, and 250.

We= 10, $\dot{m}'' = 25$ for the evaporating droplet and $\dot{m}'' = -25$ for the condensing droplet, and ρ_g/ρ_l =10, 50 and 250.

Figure 4.8 shows the time development of $(D/D_0)^2$ for the evaporating and condensing droplets at the various density ratios. In general, there is good agreement between the exact solution and the simulation, and the agreement improves as ρ_l/ρ_g decreases. In the case with worst agreement (evaporating droplet with $\rho_l/\rho_g = 250$) the relative error in $(D/D_0)^2$ at $t = 5$ is 2.6%.

Figures 4.9 and 4.10 show the velocity vectors for the $\rho_l/\rho_g = 10$ cases at three different times (t=0, 2.5, and 5). The figures show that our implementation of the $\nabla \cdot \mathbf{u}$ source/sink term in Eq. (4.1) leads to a sharp jump in the normal velocity at the interface as one would like. Also, the Stefan flow generated by the evaporation and condensation processes, causes the droplet to be propelled away from and towards the wall, respectively. The droplet maintains a circular shape as it travels away from or towards the wall and while shrinking

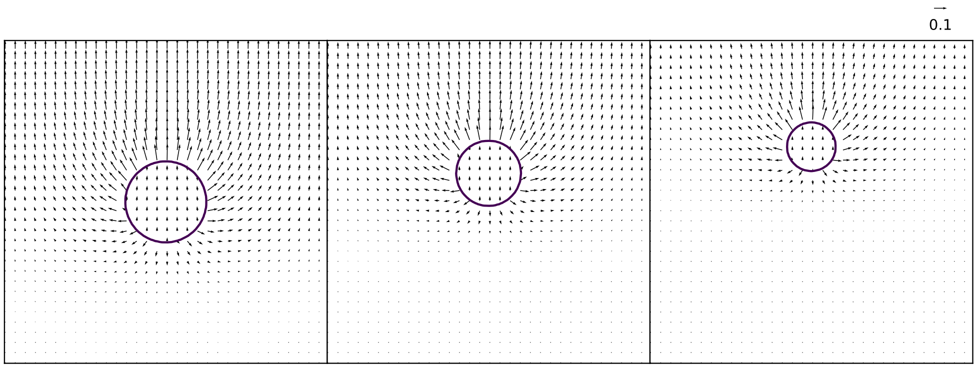

Figure 4.9: Velocity vectors around the evaporating droplet with $\rho_l/\rho_g = 10$ at t= 0, 2.5, and 5. The black line is a $C = 0.5$ isocontour representing the gas-liquid interface.

or growing in size. These figures demonstrate the ability of the VoF advection algorithm described in Section 4.2.1 to capture evaporating and condensing droplets that are in motion.

Our tests in Section 4.3.1 have shown that the VoF advection algorithm yields the exact volume in 1D, independent of the grid resolution. We now assess the spatial convergence rate in 2D. For this, we select the case of an evaporating droplet with $\rho_l/\rho_g = 250$ and vary the number of grid points per droplet diameter as $N_{gp,d}$= 16, 32, and 64. The time step is selected as $\Delta t/\Delta x^2 = 5$. The remaining parameters are the same as reported earlier in the section.

Figure 4.11 shows the time evolution of the normalized droplet diameter squared for varying $N_{gp,d}$. The figure shows that as $N_{gp,d}$ increases, the normalized droplet diameter converges to the exact solution. To quantify the convergence rate, we compute the error, E_D, between the computed and exact values of $(D/D_0)^2$. Table 4.1 report E_D and the convergence rate. The table shows that the method is slightly higher than first-order accurate.

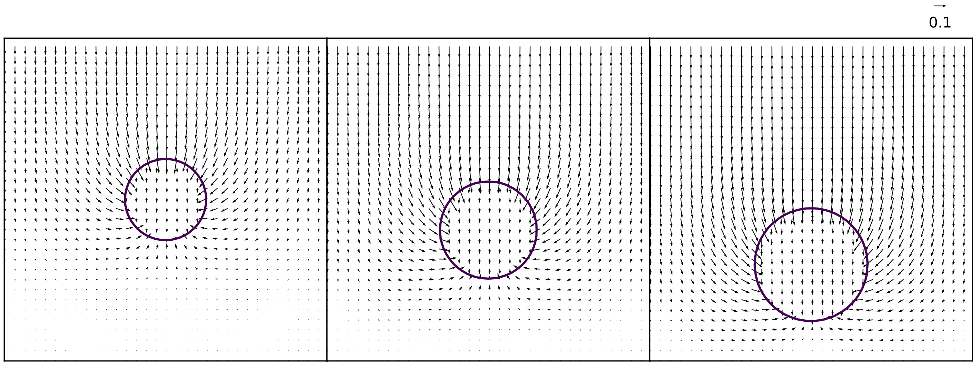

Figure 4.10: Velocity vectors around the condensing droplet with $\rho_l/\rho_g = 10$ at t= 0, 2.5, and 5. The black line is a $C = 0.5$ isocontour representing the gas-liquid interface.

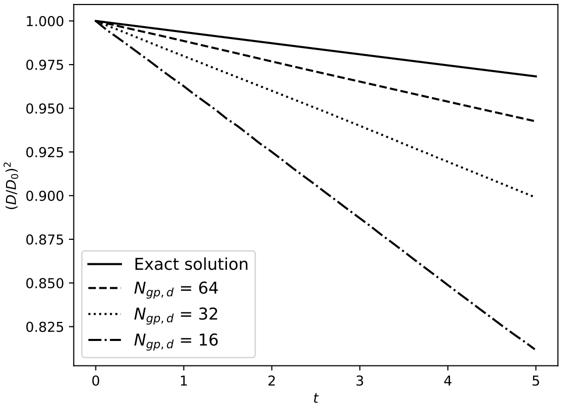

Figure 4.11: Time evolution of the normalized droplet diameter squared for an evaporating droplet compared to the exact solution and for varying number of grid points per diameter, $N_{gp,d}$

$N_{gp,d}$	E_D	Rate
16	1.57e-1	–
32	6.93e-2	1.18
64	2.58e-2	1.43

Table 4.1: Error in the normalized droplet diameter squared $(D/D_0)^2$ as a function of the number of grid points per diameter $N_{gp,d}$ for a 2D evaporating droplet with constant mass flux rate.

4.3.2 Verification of mass flux rate computation

To verify the accuracy of the mass flux rate computation that was described in Section 4.2.2, we consider a 1D Stefan flow in the domain depicted in Fig. 4.6. We assume isothermal conditions and infinite Stefan number such that the energy equation can be neglected for this case. The vapor mass fraction field has Dirichlet boundary conditions applied at the gas-liquid interface and the outflow plane. We assume that $\rho_l/\rho_g = \infty$ such that the interface remains stationary ($\mathbf{u}_\Sigma = 0$) as the liquid evaporates. Under these assumptions, there are analytical solutions for $Y_v(x)$ and $\dot{m}''$. In this section we only focus on $\dot{m}''$, and will return to verifying $Y_v(x)$ in the next section. The exact mass flux rate per unit area is

$$\dot{m}''_{\text{exact}} = \frac{1}{\text{Re Sc}} \frac{\rho_g}{L_g} \ln\left(\frac{1 - Y_{v,L}}{1 - Y_{v,sat}}\right), \tag{4.46}$$

where L_g is the distance from the interface to the outflow plane and $Y_{v,L}$ and $Y_{v,sat}$ are the vapor mass fractions at the outflow plane and the interface, respectively.

The conditions for the test are $L_g = 0.5$, Re=200, Sc=1, $Y_{v,L} = 0$, $Y_{v,sat} = 0.5$, and $\rho_l/\rho_g = \infty$. We initialize $Y_v = 0$ in the gas phase and then integrate in time until $Y_v(x)$ reaches the steady-state solution. When $Y_v(x)$ reaches steady-state, we compute $\dot{m}$. We test on three different grids, N=16, 32, and 64. Table 4.2 shows the error in the mass flux ($E_{\dot{m}''} = |\dot{m}''_{\text{sim}} - \dot{m}''_{\text{exact}}|$) as function of the grid spacing Δx. The table shows that the mass

Δx	$E_{\dot{m}''}$	Rate
1/16	2.91e-3	–
1/32	7.06e-4	2.04
1/64	1.74e-4	2.02

Table 4.2: Error in the vaporization rate per unit area $E_{\dot{m}''}$ as a function of the grid spacing Δx for 1D Stefan problem.

flux calculation (Eq. (4.16)) is second-order accurate.

4.3.3 Verification of the temperature and vapor mass fraction fields

In this section we verify the accuracy of the methods for solving the vapor mass fraction and temperature fields as described in Sections 4.2.3 and 4.2.4. We consider the 1D Stefan flow problem illustrated in Figure 4.6. Dirichlet conditions for vapor mass fraction and temperature are applied at the outflow boundary. At the lower wall, a Dirichlet boundary conditions is applied for temperature. At the interface, a Dirichlet boundary condition is applied for the saturated vapor mass fraction. Under these assumptions the analytical solution for the vapor mass fraction field is

$$Y_v(x) = 1 - (1 - Y_{v,sat}) \left(\frac{1 - Y_{v,L}}{1 - Y_{v,sat}} \right)^{(2x-1)/L}, \tag{4.47}$$

where L is the length of the gas-liquid domain and the interface is located at $x = L/2$.

The solution for the temperature at the interface ($x = L/2$) is

$$T_\Sigma = \frac{L T_L \dot{m}'' + L \frac{\dot{m}''}{\mathrm{Ste}} \left(1 - e^{K(3L/2)}\right) + 2\mathrm{Le} T_0 \frac{k_l}{k_g} \left(e^{K(3L/2)} - 1\right)}{L c_{p,1} \dot{m}'' + 2\mathrm{Le} \frac{k_l}{k_g} (e^{K(3L/2)} - 1)}, \tag{4.48}$$

where K is a function given by

$$K(x) = \frac{\dot{m}''(x - L)}{\mathrm{Le}}, \tag{4.49}$$

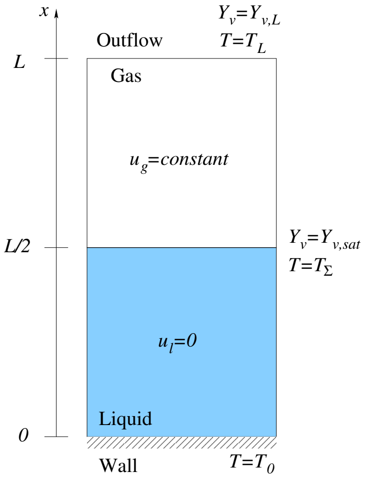

Figure 4.12: Domain for 1D Stefan flow.

and where Le is the Lewis number,

$$\mathrm{Le} = \frac{\tilde{k}_{\mathrm{ref}}}{\tilde{\rho}_{\mathrm{ref}}\tilde{D}_{gv}\tilde{c}_{p,\mathrm{ref}}} = \frac{\mathrm{Sc}}{\mathrm{Pr}}. \tag{4.50}$$

The solution to the temperature field in the liquid phase ($0 < x \leq L/2$) is

$$T(x) = \frac{2(T_\Sigma - T_0)}{L}x + T_0 \tag{4.51}$$

and in the gas phase ($L/2 < x < L$) the solution is

$$\begin{aligned} T(x) = T_L e^{K(x)} + T_\Sigma(1 - e^{K(x)}) + \frac{1}{\mathrm{Ste}}(e^{K(x)} - 1) \\ + \frac{2\ \mathrm{Le}}{L\ \dot{m}''}\frac{k_l}{k_g}\left[T_0(1 - e^{K(x)}) + T_\Sigma(e^{K(x)} - 1)\right]. \end{aligned} \tag{4.52}$$

The conditions for the test are $L = 1$, Re=200, Sc=1, Pr=0.5, Ste=0.5, $Y_{v,L} = 0$, $Y_{v,sat} = 0.5$, $T_0 = 0.7$, $T_L = 0.8$, $\rho_l/\rho_g = 10^{10}$, $c_{p,l}/c_{p,g} = 10^{-9}$, and $k_l/k_g = 4$. Note that ρ_l/ρ_g is made sufficiently large such that the interface is practically stationary and $c_{p,l}/c_{p,g}$ is made sufficiently small such that the heat capacities of the liquid and gas phase are of the same order of magnitude. To test the convergence properties of the schemes, we tested three grids $N = 16$, 32, and 64.

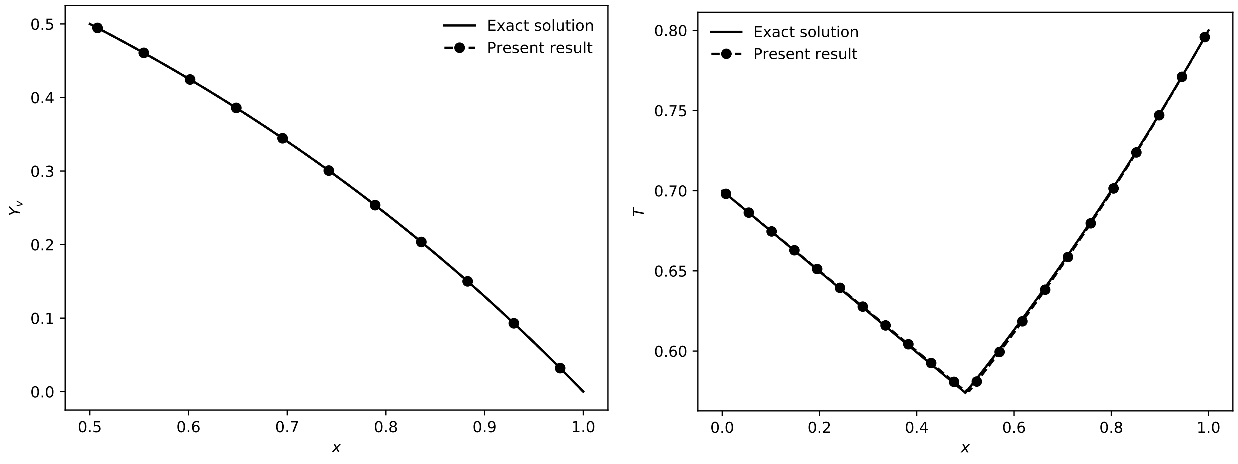

(a) (b)

Figure 4.13: Profiles of (a) the vapor mass fraction and (b) the temperature for 1D Stefan flow. The numerical result was obtained on 64 point grid and is plotted against the exact solution.

Figure 4.13 shows the profiles of the vapor mass fraction and temperature compared to the analytical solution on the finest grid ($N = 64$). We see that both $Y_v(x)$ and $T(x)$ are in excellent agreement with the analytical solution. Figure 4.13(a) shows that the exponential Y_v profile (Eq. (4.47)) is captured for the the 1D Stefan flow. We see that in Fig. 4.13(b) that the correct temperature profile is verified in both the liquid ($x < L/2$) and gas ($x \geq L/2$). At the interface, the scheme accurately captures the jump in $\partial T/\partial x$ due to $k_l/k_g \neq 0$. Furthermore the singular source/sink term (last term in Eq. (4.5)) is captured sharply by the discretization presented in Eq. (4.35).

Table 4.3 shows the L1 error of the vapor mass fraction (E_{Y_v}) and temperature (E_T) profiles as function of the grid spacing Δx. The table shows that the vapor mass fraction $Y_v(x)$ is between first- and second-order accurate. The temperature $T(x)$ is first-order accurate.

Δx	E_{Y_v}	Rate	E_T	Rate
1/16	5.84e-4	–	7.74e-3	–
1/32	1.86e-4	1.65	3.91e-3	0.98
1/64	6.41e-5	1.54	1.97e-3	0.99

Table 4.3: L1 error norm of the vapor mass fraction and temperature as a function of the grid spacing Δx.

4.3.4 Verification of fully coupled solver: 3D evaporating droplet at rest

In this section we verify the fully-coupled solver (as illustrated in Fig. 4.2) by solving the momentum, temperature, and vapor mass fraction fields while also computing the mass flux rate using Eq. (4.15) and the saturated vapor mass fraction using Eq. (4.20). We compare the numerical results to known solutions.

We consider a spherical droplet in a cubic domain. Periodic boundary conditions are applied in the two horizontal directions and outflow boundaries are applied in the vertical direction. Initially, the gas and liquid velocities are zero, the temperature field is uniform, and the gas phase is devoid of vapor. In our simulation, the domain has length $L = 1$ on all sides, the initial droplet diameter is $D_0 = 0.25$, and we use a 442^3 grid. The parameters and initial conditions are Re=200, Sc=1, Pr=1, Ste=1, Ste_c=7.506e-2, $T_{\text{boil}} = 1.14$, $\rho_l/\rho_g = 40$, $\mu_l/\mu_g = 10$, $c_{p,l}/c_{p,g} = 2.5$, $k_l/k_g = 3$, and $M_v/M_a = 1$.

To verify the accuracy of the simulation we compute the mean Sherwood number of the droplet as a function of time, and compare it to the exact, steady-state solution for a static 3D sphere. The Sherwood number is calculated as

$$\text{Sh} = \text{Re Sc } D \; h_{\text{mass}}, \tag{4.53}$$

where, we recall, Re Sc is the non-dimensional mass diffusivity, D is the droplet diameter,

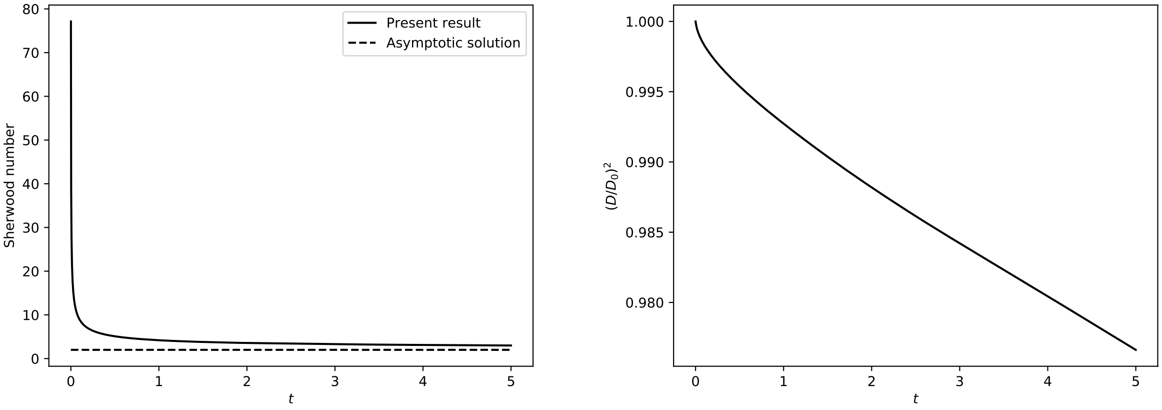

(a)

(b)

Figure 4.14: Time evolution of (a) the Sherwood number (b) the normalized droplet diameter squared.

and h_{mass} is the average mass transfer coefficient calculated as

$$h_{\text{mass}} = \frac{\dot{M}}{A\ \rho_g (Y_{v,sat} - Y_{v,\infty})}, \tag{4.54}$$

where $\dot{M}$ is the rate of change of droplet mass, A is the droplet surface area, and $Y_{v,\infty}$ is the vapor mass fraction in the far field.

Figure 4.14 shows the time evolution of the Sherwood number (Sh) and the normalized droplet diameter squared $(D/D_0)^2$. Figure 4.14(a) shows that the Sherwood number approaches the correct asymptotic solution of Sh=2. Figure 4.14(b) shows that after an initial transient period, $(D/D_0)^2$ decays linearly in time, which verifies that our simulation follows the D^2-law for the isolated static droplet.

4.4 Summary

We have developed a volume-of-fluid based flow solver for incompressible gas-liquid flows with phase change. In particular the method addresses flows in which the liquid is monocomponent and the gas phase is bicomponent, consisting of an inert gas and a liquid vapor. We have proposed a novel method for capturing the gas-liquid interface in the presence of heat and mass transfer within the VoF framework. The main advantage of this method is that it does not require a costly projection step of the liquid velocity to divergence-free space. We have demonstrated that this method is accurate up to density ratios of 250 for evaporating and condensing droplets. Using a normal probe approach, we have verified that the mass flux rate is computed to second-order accuracy. The method was shown to be between first and second-order accurate for computing the vapor mass fraction field and first-order for computing the temperature. We also tested a 3D evaporating droplet at rest and showed that the Sherwood number approached the correct asymptotic value and that the droplet diameter followed the D^2-law.

Chapter 5

MATHEMATICAL FORMULATION FOR EVAPORATING DROPLETS: LOW MACH NUMBER FORMULATION

5.1 Governing equations

We consider the gas-liquid system depicted in Fig. 5.1. The gas volume ($\mathcal{V}_g$) and the liquid volume ($\mathcal{V}_l$) are separated by an interface Σ. Under the following assumptions:

- The liquid phase is incompressible and the gas phase is compressible
- The Mach number of the gas phase is sufficiently small such that acoustic phenomena can be neglected, while retaining compressibility
- The liquid phase is mono-component; the gas-phase is bi-component, consisting of an inert gas and liquid vapor

the dimensionless governing equations are (see F for derivation):

Continuity equation:

$$\frac{\partial \rho}{\partial t} + \nabla \cdot (\rho \mathbf{u}) = 0 \tag{5.1}$$

Momentum equation:

$$\rho \left(\frac{\partial \mathbf{u}}{\partial t} + (\mathbf{u} \cdot \nabla)\mathbf{u} \right) = -\nabla p + \frac{1}{\mathrm{Re}} \nabla \cdot \left[\mu \left(\nabla \mathbf{u} + \nabla \mathbf{u}^T - \frac{2}{3}(\nabla \cdot \mathbf{u})\mathbf{I} \right) \right] + \frac{1}{\mathrm{We}} \mathbf{f}_\sigma \tag{5.2}$$

where the non-dimensional force due to surface tension is

$$\mathbf{f}_\sigma = \kappa \mathbf{n} \delta(n). \tag{5.3}$$

Energy equation:

$$\rho c_p \left(\frac{\partial T}{\partial t} + (\mathbf{u} \cdot \nabla) T \right) = \frac{\gamma - 1}{\gamma} \frac{\mathrm{d}p_0}{\mathrm{d}t} + \frac{1}{\mathrm{Re\ Pr}} \nabla \cdot (k \nabla T) - \frac{1}{\mathrm{Re\ Sc\ Ste}} \dot{m} \tag{5.4}$$

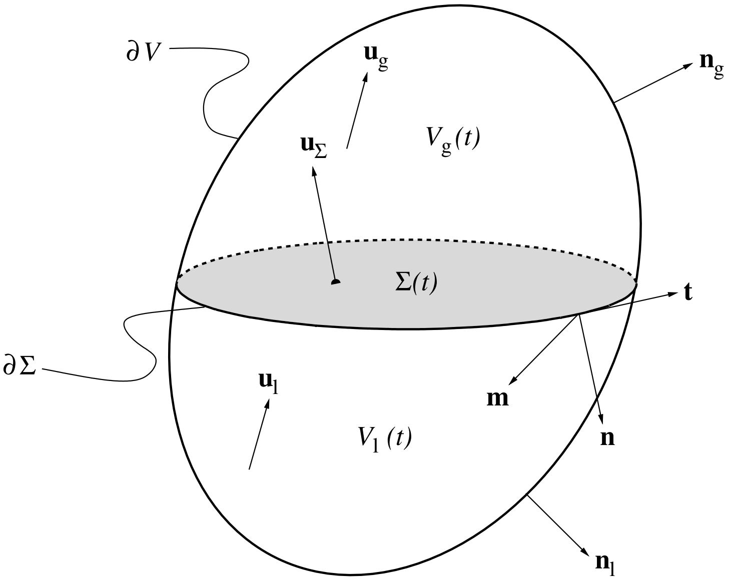

Figure 5.1: Control volume $\mathcal{V}(t)$ containing an interface $\Sigma(t)$ separating the liquid and gas phases, $\mathcal{V}_l(t)$ and $\mathcal{V}_g(t)$, respectively.

Vapor mass conservation equation:

$$\rho\left(\frac{\partial Y_v}{\partial t} + (\mathbf{u}\cdot\nabla)Y_v\right) = \frac{1}{\text{Re Sc}}\left[\nabla\cdot(\rho\nabla Y_v)\right] \tag{5.5}$$

where $\mathbf{u} = \mathbf{u}(\mathbf{x}, t)$ is the velocity (mass-averaged), $\rho = \rho(\mathbf{x}, t)$ is the density, $\mu = \mu(\mathbf{x}, t)$ is the dynamic viscosity, $p = p(\mathbf{x}, t)$ is the dynamic pressure, $T = T(\mathbf{x}, t)$ is the temperature, $c_p = c_p(\mathbf{x}, t)$ is the specific heat at constant pressure, $\gamma = c_p/c_v$ is the ratio of specific heats ($\gamma = 1$ for $\mathbf{x} \in \mathcal{V}_l$), $p_0 = p_0(t)$ is the thermodynamic pressure, $k = k(\mathbf{x}, t)$ is the thermal conductivity, and $Y_v = Y_v(\mathbf{x}, t)$ is the vapor mass fraction. The fluid properties μ, c_p, and k are piecewise constant and are computed as

$$\phi = (1 - H)\phi_g + H\phi_l, \tag{5.6}$$

where ϕ_g and ϕ_l are constant properties (i.e. μ, c_p, and k) and H is a Heaviside function which has value zero in the gas phase and one in the liquid phase. The density field is computed as

$$\rho = (1 - H)\rho_g + H\rho_l, \tag{5.7}$$

where the density of the liquid phase (ρ_l) is assumed constant, while the density of the gas phase (ρ_g) can vary in space in time and is taken to be a calorically perfect gas that obeys the equation of state

$$p_0 = \rho T \frac{R_u}{\overline{M}}, \tag{5.8}$$

where $\overline{M}$ is the average molar mass of the mixture,

$$\overline{M} = \left(\frac{Y_v}{M_v} + \frac{1 - Y_v}{M_a} \right)^{-1}, \tag{5.9}$$

where M_v is the molar mass of the vapor phase and M_a is the molar mass of the ambient gas.

In Eqs. (5.1), (5.2), (5.4), and (5.5) Re, Sc, We, Pr, Ste, and Sc are, respectively, the Reynolds, Weber, Prandtl, Stefan, and Schmidt numbers defined as:

$$\mathrm{Re} = \frac{\tilde{U}\tilde{L}\tilde{\rho}_g}{\tilde{\mu}_g}, \quad \mathrm{Sc} = \frac{\tilde{\mu}_g}{\tilde{D}_{gv}\tilde{\rho}_g}, \quad \mathrm{We} = \frac{\tilde{\rho}_g\tilde{U}^2\tilde{L}}{\tilde{\sigma}}, \quad \mathrm{Pr} = \frac{\tilde{\mu}_g\tilde{c}_{p,g}}{\tilde{k}_g}, \quad \mathrm{Ste} = \frac{\tilde{c}_{p,g}\tilde{T}_g}{\Delta\tilde{h}_v}, \tag{5.10}$$

where $\tilde{U}$, $\tilde{L}$, $\tilde{\rho}_g$, $\tilde{\mu}_g$, $\tilde{\sigma}$, $\tilde{c}_{p,g}$, $\tilde{k}_g$, $\tilde{T}_g$, $\Delta\tilde{h}_v$, and $\tilde{D}_{gv}$ denote, in order, the reference dimensional velocity, length, density, dynamic viscosity, surface tension coefficient, specific heat at constant pressure, thermal conductivity, temperature, latent heat of vaporization, and mass diffusivity of vapor in the gas phase used to non-dimensionalize the governing equations. The reference density, viscosity, specific heat, and thermal conductivity are chosen to be that of the ambient gas, making their values unity in the gas phase. The reference temperature is chosen to be the initial ambient gas temperature, therefore the non-dimensional temperature of the gas phase is initially unity. Throughout the paper, all variables are dimensionless unless they are accented with $\sim$.

The continuity equation (Eq. (5.1)) can be re-expressed as a divergence constraint on the velocity field (see F for derivation),

$$\nabla \cdot \mathbf{u} = \begin{cases} -\dfrac{1}{p_0}\dfrac{dp_0}{dt} + \dfrac{1}{T}\dfrac{DT}{Dt} + \overline{M}\left(\dfrac{1}{M_v} - \dfrac{1}{M_a}\right)\dfrac{DY_v}{Dt} & \text{for } \mathbf{x} \in \mathcal{V}_g \\ \dfrac{1}{\text{Re Sc}}\dot{m}\left(\dfrac{1}{\rho_g} - \dfrac{1}{\rho_l}\right) & \text{for } \mathbf{x} \in \Sigma \\ 0 & \text{for } \mathbf{x} \in \mathcal{V}_l, \end{cases} \tag{5.11}$$

where in the gas phase there is expansion or contraction due to the low Mach number formulation, at the interface there is expansion due to evaporation or compression due to condensation, and in the liquid phase the velocity field is divergence-free due to incompressibility. Equation (5.11), as opposed to Eq. (5.1), will be used to close the set of governing equations.

Finally, to close the set of equations, an equation for p_0 is required. Under the assumption that the domain is constant volume and there is no net inflow/outflow of mass, the thermodynamic pressure, p_0, obeys the following ordinary differential equation (see G for derivation)

$$\begin{aligned} \frac{\mathrm{d}p_0}{\mathrm{d}t} = \frac{p_0}{\mathcal{V}_g}\Bigg\{ &\int_{\mathcal{V}}\left(\frac{1}{\rho_g} - \frac{1}{\rho_l}\right)\dot{m}\,\mathrm{d}\mathcal{V} \\ &+ \int_{\mathcal{V}_g}\left[\frac{1}{T}\frac{DT}{Dt} + \overline{M}\left(\frac{1}{M_v} - \frac{1}{M_a}\right)\frac{DY_v}{Dt}\right]\mathrm{d}\mathcal{V}\Bigg\}, \end{aligned} \tag{5.12}$$

where DT/Dt and DY_v/Dt are the material derivatives of the temperature and vapor mass fraction, respectively.

5.2 Numerical methods

In this section we describe the numerical methods used. The equations are discretized on a staggered grid and, unless otherwise specified, all spatial derivatives are discretized using the second-order central difference scheme.

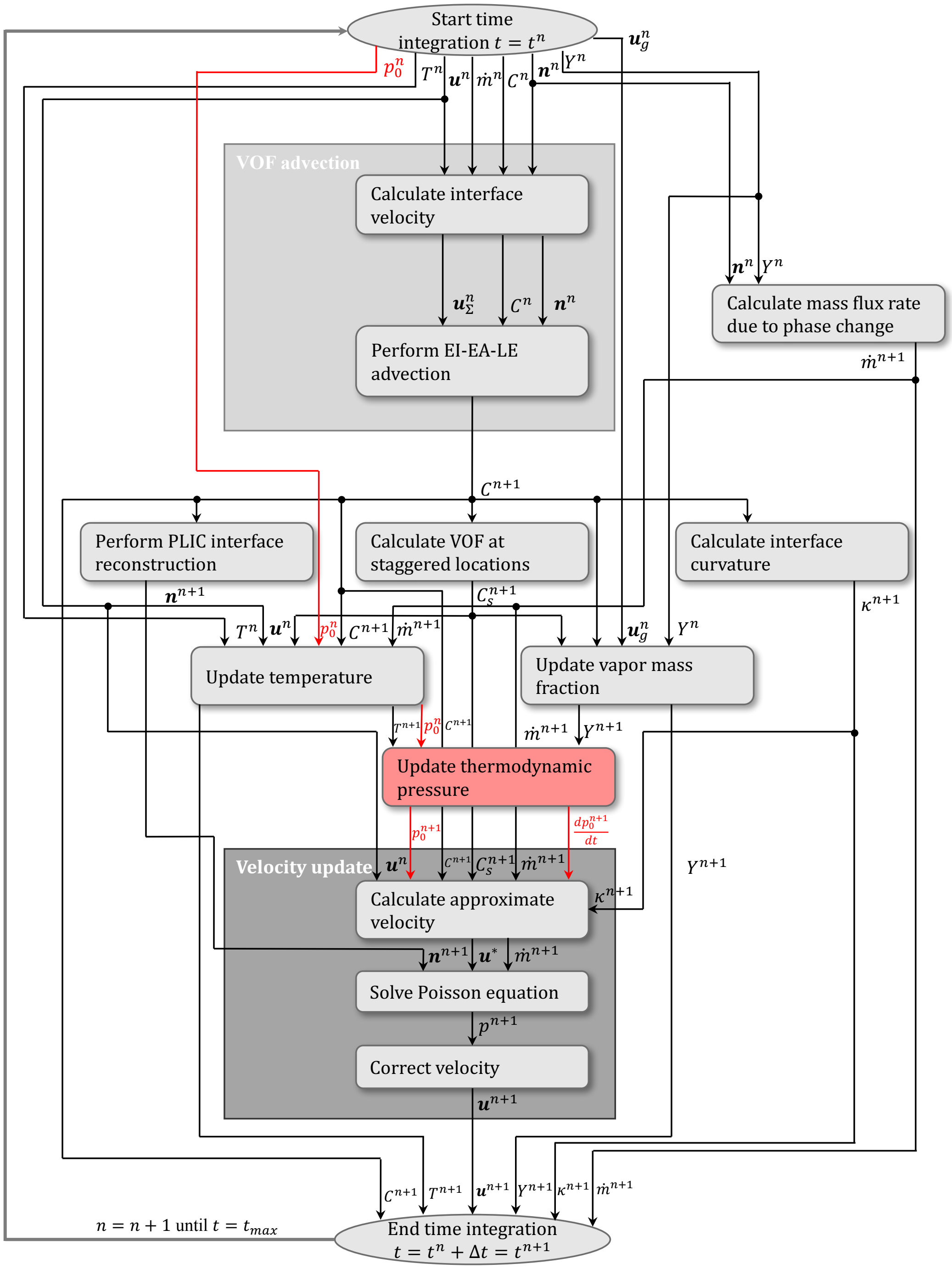

Figure 5.2: Flowchart of flow solver for simulating gas-liquid flows with phase change using the low Mach number formulation. Additions to the flow solver relative to the incompressible solver presented in Part 1 [80] are in red.

5.2.1 Computation of the vapor mass fraction

In Part 1 [81] we solved the incompressible form of the vapor mass conservation equation. In that equation, the density drops out because it is constant. In the present flow, the gas-phase density varies in space and time, which must be accounted for. This adds additional complexity to the spatial discretization of the diffusive term, especially near the interface. In this section we present our approach for handling this.

The vapor mass fraction at the new time step, Y_v^{n+1}, is found by integrating Eq. (5.5) in time using the first-order Euler scheme

$$\frac{Y_v^{n+1} - Y_v^n}{\Delta t} = RY^n, \tag{5.13}$$

where

$$RY^n = -(\mathbf{u}^n \cdot \nabla)Y_v^n + \frac{1}{\text{Re Sc}} \frac{1}{\rho^{n+1}} \left[\nabla \cdot \left(\rho^{n+1} \nabla Y_v^n\right)\right]. \tag{5.14}$$

To calculate the variable density diffusive term, we use the same second-order central difference scheme that is used to discretize the diffusive term in the momentum equation [16]. Like in Part 1 [81], when the second-order central difference stencil contains a point that is in the liquid ($C_{ij} > 0.5$), we switch to a one-sided finite difference approach on a non-uniform mesh.

Again, we consider a one-dimensional example in which the interface is located between x_{i-1} and x_i and the interface normal is directed in the negative x direction. We compute the diffusive flux as

$$\left.\frac{\partial}{\partial x}\left(\rho \frac{\partial Y_v}{\partial x}\right)\right|_{x=x_i} = \gamma_0 RDY_\Sigma + \gamma_1 RDY_{i+1} + \gamma_2 RDY_{i+2} + \gamma_3 RDY_{i+3}, \tag{5.15}$$

on the stencil $x = [-\theta h, h, 2h, 3h, 4h]$, with the derivative being calculated at $x = 0$. The finite difference weights γ_i are calculated using the method found in [78]. The RDY terms correspond to $\rho^{n+1}(\partial Y_v^n)/(\partial x)$. Using RDY_Σ as an example, these terms are computed as

$$\left.\rho \frac{\partial Y_v}{\partial x}\right|_{x=x_\Sigma} = RDY_\Sigma = \rho_\Sigma \left(\alpha_0 Y_{v,sat} + \alpha_1 Y_{v,i} + \alpha_2 Y_{v,i+1} + \alpha_3 Y_{v,i+2} + \alpha_4 Y_{v,i+3}\right) \tag{5.16}$$

on the stencil $x = [-\theta h, 0, h, 2h, 3h, 4h]$. The finite difference weights α_i are calculated using the method found in [78]. We repeat this procedure for the remaining three terms (RDY_{i+1}, ...). Note that the same five values of Y_v are used in all calculations of RDY, but we vary the location at which $(\partial Y_v)/(\partial x)$ is evaluated, which modifies the α_i coefficients. The RDY computation (Eq. (5.16)) is fourth-order accurate and the diffusive flux (Eq. (5.15)) is third-order accurate. As we described in Part 1, if $\theta < 0.25$, we eliminate $Y_{v,i}$ from the calculation of the derivatives. This reduces the accuracy of Eq. (5.16) and Eq. (5.15) to third and second order, respectively.

5.2.2 Computation of thermodynamic pressure

The thermodynamic pressure at the new time step, p_0^{n+1}, is found by integrating Eq. (5.4) in time using the 2nd-order Adams-Bashforth scheme

$$\frac{p_0^{n+1} - p_0^n}{\Delta t} = \frac{3}{2} RP^n - \frac{1}{2} RP^{n-1}, \tag{5.17}$$

where

$$\begin{aligned} RP^n = \frac{p_0^n}{\mathcal{V}_g} \Bigg\{ & \int_{\mathcal{V}} \left(\frac{1}{\rho_g^{n+1}} - \frac{1}{\rho_l^{n+1}} \right) \dot{m}^{n+1} \, \mathrm{d}\mathcal{V} \\ & + \int_{\mathcal{V}_g} \left[\frac{1}{T^{n+1}} \frac{DT}{Dt}^{n+1} + \overline{M} \left(\frac{1}{M_v} - \frac{1}{M_a} \right) \frac{DY_v}{Dt}^{n+1} \right] \mathrm{d}\mathcal{V} \Bigg\}. \end{aligned} \tag{5.18}$$

The integrals over the gas phase are computed in 3D as

$$\int_{\mathcal{V}_g} \phi \, \mathrm{d}\mathcal{V} = \sum_{C_{i,j,k} < \epsilon} \phi \Delta x^3, \tag{5.19}$$

where the summation is performed over all cells in which the volume fraction $C_{i,j,k}$ is less than ϵ, where we have chosen ϵ =1e-8 (note that we use double precision floating-point numbers throughout the code).

5.2.3 Fast pressure-correction method

The pressure-correction method presented in Part 1 [81] requires only a slight modification, which we will describe here. Like in Part 1, we use the FastP* method [16] in order to avoid having to solve a variable-coefficient Poisson equation for pressure. The Poisson equation, has the same form as that found in the incompressible formulation, and we repeat it here

$$\nabla^2 p^{n+1} = \nabla \cdot \left[\left(1 - \frac{\rho_0}{\rho^{n+1}} \right) \nabla \hat{p} \right] + \frac{\rho_0}{\Delta t} \left[\nabla \cdot \mathbf{u}^* - \nabla \cdot \mathbf{u}^{n+1} \right]. \tag{5.20}$$

The right-hand side term, $\nabla \cdot \mathbf{u}^{n+1}$, is given by

$$\nabla \cdot \mathbf{u}^{n+1} = \frac{1}{\text{Re Sc}} \dot{m}^{n+1} \left(\frac{1}{\rho_g^{n+1}} - \frac{1}{\rho_l^{n+1}} \right). \tag{5.21}$$

$$\nabla \cdot \mathbf{u}^{n+1} = \begin{cases} -\frac{1}{p_0^n} RP^n + \frac{1}{T^{n+1}} \frac{DT^{n+1}}{Dt} + \overline{M}^{n+1} \left(\frac{1}{M_v} - \frac{1}{M_a} \right) \frac{DY_v^{n+1}}{Dt} & \text{if } \left| \nabla C^{n+1} \right| = 0 \text{ and } C^{n+1} < \epsilon \\ \frac{1}{\text{Re Sc}} \dot{m}^{n+1} \left(\frac{1}{\rho_g^{n+1}} - \frac{1}{\rho_l^{n+1}} \right) & \text{if } \left| \nabla C^{n+1} \right| \neq 0 \\ 0 & \text{if } \left| \nabla C^{n+1} \right| = 0 \text{ and } C^{n+1} > \epsilon. \end{cases} \tag{5.22}$$

5.3 Results

5.3.1 Verification of low Mach number formulation: 2D droplet at rest with constant $\dot{m}$

In this section we assess the ability of the low Mach number formulation to simulate flows with phase change in periodic domains. In particular we check that the condition

$$\int_{\mathcal{V}} \nabla \cdot \mathbf{u} \, \mathrm{d}\mathcal{V} = 0 \tag{5.23}$$

is satisfied and that the total mass contained in the domain is conserved, i.e.

$$\frac{\mathrm{d}m}{\mathrm{d}t} = \frac{\mathrm{d}}{\mathrm{d}t} \int_{\mathcal{V}} \rho \, \mathrm{d}\mathcal{V} = 0. \tag{5.24}$$

To better understand the difference between the incompressible formulation presented in Part 1 [81] and the low Mach number formulation presented here, we simulate an evaporating and condensing droplet at rest in both an open domain and a closed domain.

For our test, we use a domain of length $L = 1$ discretized using 128^2 points. In one of the simulations the upper and lower boundary are outflow/inflow planes and periodic boundary conditions are applied in the horizontal direction. In the other simulation, periodic boundary conditions are applied in all four directions. The initial droplet diameter is $D_0 = 0.25$. The non-dimensional parameters are Re= 250, Sc= 1, We= 10, Ste= ∞, $M_v/M_a = 1$, $\gamma = 1$, $\dot{m}'' = 25$ for the evaporating droplet and $\dot{m}'' = -25$ for the condensing droplet, and ρ_g/ρ_l =40. The fluids are initially at rest.

Figure 5.3 shows the velocity vectors and contours of $\nabla \cdot \mathbf{u}$ for an evaporating droplet in a domain with outflow boundaries at the upper and lower plane (Figs. 5.3(a) and 5.3(c)) and for an evaporating droplet a domain with periodic boundaries in all directions (Figs. 5.3(b) and 5.3(d)). Comparing Figs. 5.3(a) and 5.3(b) clearly shows the effect the low Mach number has on the velocity field. When the low Mach number formulation is active, outflow from the domain is stopped, while expansion at the interface due to phase change still occurs. Figure 5.3(c) shows that for the incompressible formulation $\nabla \cdot \mathbf{u} > 0$ at the interface and $\nabla \cdot \mathbf{u} = 0$ everywhere else as expected. Figure 5.3(d) again shows that $\nabla \cdot \mathbf{u} > 0$ due to evaporation, $\nabla \cdot \mathbf{u} = 0$ inside the droplet, but $\nabla \cdot \mathbf{u} < 0$ in the gas phase, such that Eq. (5.23) is satisfied.

Figure 5.4 shows the same series as in Fig. 5.3, but for the case of a condensing droplet ($\dot{m} = -25$). Comparing Figs. 5.3(a) and 5.3(b) shows that the low Mach number formulation prevents inflow as one would expect. Figure 5.4(d) shows that $\nabla \cdot \mathbf{u} < 0$ at the interface due to condensation, $\nabla \cdot \mathbf{u} = 0$ inside the droplet, and that $\nabla \cdot \mathbf{u} > 0$ in the gas phase. In fact, in all cases which the low Mach number formulation is applied, Eq. (5.23) is satisfied to machine precision. This is guaranteed by solving the Poisson equation for pressure (Eq. (5.22)) to machine precision.

Next we assess the mass conservation properties of the low Mach number formulation and compare it the incompressible case where mass is allowed to flow in and out of the upper and lower boundary. Figure 5.5 shows the time evolution of the total mass in the domain for the four cases considered. For the incompressible cases, the figure shows that the total mass of the domain decreases for an evaporating droplet and increases for a condensing droplet. For the low Mach number cases, the exact solution is $m/m_0 = 1$ because $dm/dt = 0$ (see in

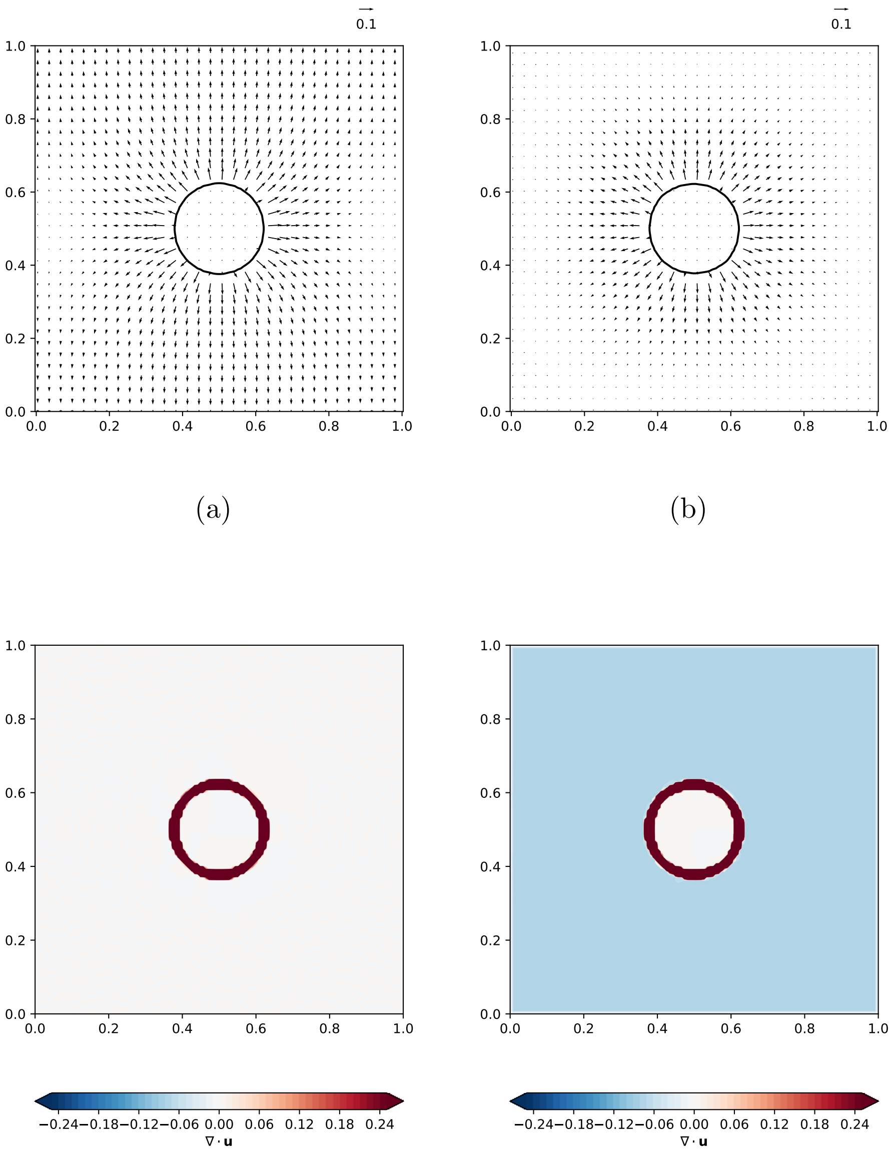

(a) (b)

(c) (d)

Figure 5.3: Top row: Velocity vectors around a condensing droplet at $t = 1$ using the (a) incompressible formulation and (b) the low Mach number formulation. Bottom row: Contours of $\nabla \cdot \mathbf{u}$ that correspond to the velocity field shown above.

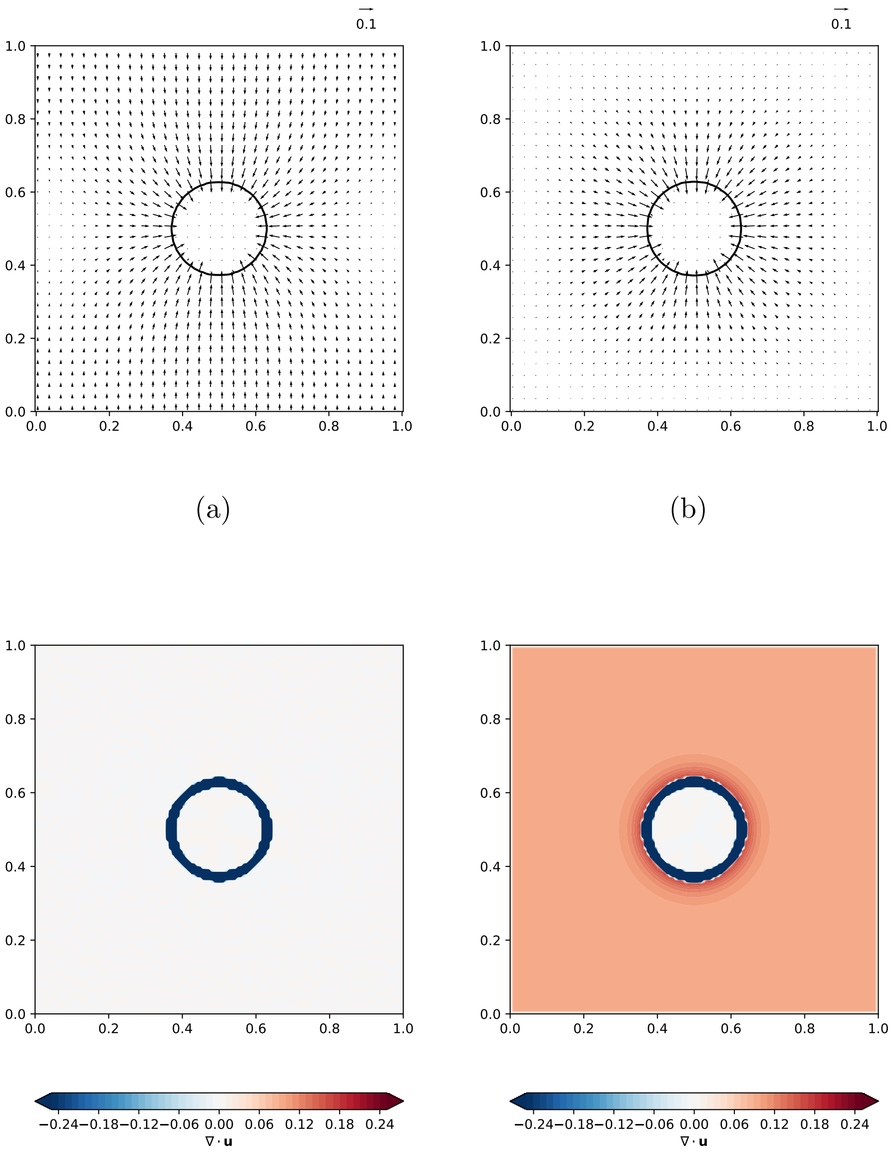

(a) (b)

(c) (d)

Figure 5.4: Top row: Velocity vectors around an evaporating droplet at $t = 1$ using the (a) incompressible formulation and (b) the low Mach number formulation. Bottom row: Contours of $\nabla \cdot \mathbf{u}$ that correspond to the velocity field shown above.

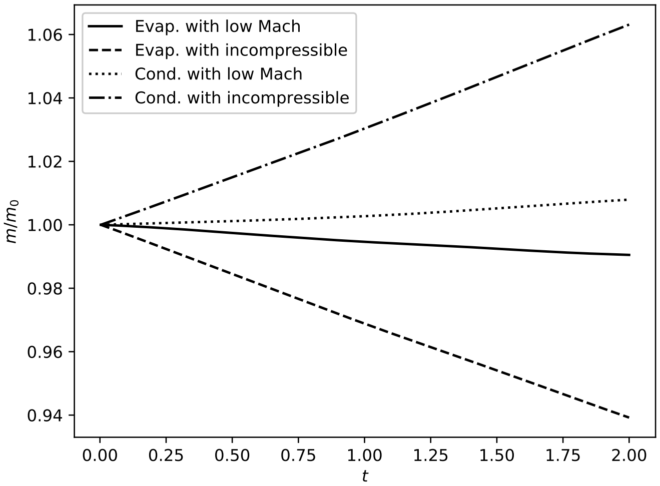

Figure 5.5: Time evolution of the normalized mass in the domain for an evaporating and condensing droplet and with and without the low Mach number formulation.

Eq. (5.24)). We see that for the evaporating droplet, the total mass decreases slightly and for the condensing droplet, the total mass increases slightly. We note that the mass error at $t = 2$ is less than 1%. We remind the reader that the important kinetmatic constraint in Eq. (5.23) is satisfied to machine zero.

The final task is to asses the convergence properties of the low Mach number scheme. We consider the case of the evaporating droplet in a domain with four periodic boundary conditions, and with the non-dimensional properties mentioned earlier in the section. We know that because the domain is fully periodic, Eq (5.24) expresses global mass conservation. However due to numerical error, this condition will only be satisfied approximately. The exact solution to the problem is $m(t)/m_0 = 1$, where m is the instantaneous mass in the domain and m_0 is the initial mass of the domain.

Figure 5.6 shows the time evolution of m/m_0 for varying $N_{gp,d}$ as 8, 16, and 32. The figure shows that, generally, mass is lost from the domain for the case of an evaporating droplet. We see that m/m_0 converges towards the exact solution $m/m_0 = 1$ as we increase $N_{gp,d}$.

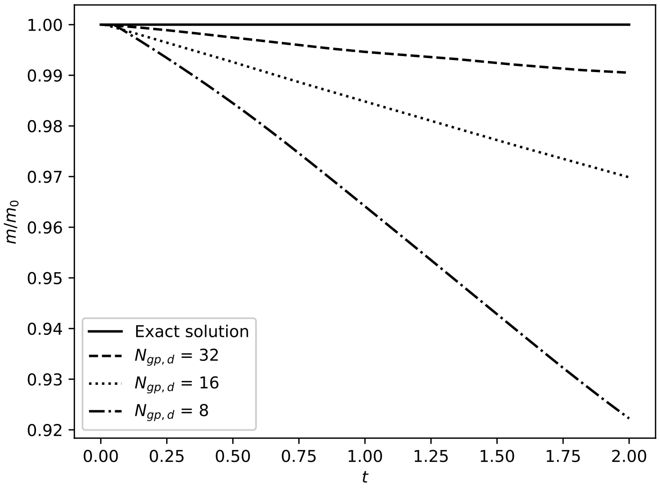

Figure 5.6: Time evolution of the normalized mass in the domain for an evaporating and condensing droplet and with and without the low Mach number formulation.

We observed a similar convergence trend in Part I [81] (Fig. 11) for the droplet volume in incompressible flow. Therefore, we believe that the error is due to the VoF advection scheme not being perfectly mass conservative in the presence of chase change as was demonstrated in Part I [81].

Table 5.1 shows the mass error $E_m = 1 - m/m_0$, at $t = 2$, and as a function of the number of grid points per droplet diameter ($N_{gp,d}$). The table shows that the mass conservation is between first and second-order accurate.

5.4 Summary

In this section we extended the method presented in the previous section of in order to simulate gas-liquid flows in closed and periodic domains using the low Mach number formulation. We derived the equations governing gas-liquid flows with phase change in which the liquid phase is incompressible and the gas phase is compressible, but assumed to be at low Mach number.

$N_{gp,d}$	E_m	Rate
8	7.78e-2	–
16	3.01e-2	1.37
32	9.49e-3	1.67

Table 5.1: Mass error as a function of the number of grid points per diameter $N_{gp,d}$ for a 2D evaporating droplet with constant mass flux rate.

Chapter 6

DNS OF AN EVAPORATING DROPLET OF IN FORCED ISOTROPIC TURBULENCE

In this section we demonstrate the ability of the coupled volume-of-fluid and pressure-correction method to perform DNS of an evaporating droplet in forced isotropic turbulence. We use the forcing scheme by [82] which uses a feedback control method to quickly converge to a constant value of the turbulence kinetic energy (TKE). The method is based on the forcing scheme originall proposed by Lundgren [83], in which a linear source term is added to the momentum equation as

$$\rho\left(\frac{\partial \mathbf{u}}{\partial t}+(\mathbf{u}\cdot\nabla)\mathbf{u}\right)=-\nabla p+\frac{1}{\mathrm{Re}}\nabla\cdot\left[\mu\left(\nabla\mathbf{u}+\nabla\mathbf{u}^T-\frac{2}{3}(\nabla\cdot\mathbf{u})\mathbf{I}\right)\right]+\frac{1}{\mathrm{We}}\mathbf{f}_\sigma+A(1-C)\mathbf{u}, \tag{6.1}$$

where the A is the forcing coefficient which is computed as

$$A(t)=\frac{\varepsilon(t)-G[k(t)-k_\infty]2k_\infty/3\varepsilon_\infty}{2k(t)}, \tag{6.2}$$

where $\varepsilon(t)$ is the instantaneous dissipation rate of TKE, $k(t)$ is the instantaneous TKE, G is a dimensionless constant that acts as a proportional gain ($G = 67$ is used here as recommended in [82]) and k_∞ and ε_∞ are the steady-state values of the dissipation and TKE, respectively. Note that in Eq. (6.1), we multiply the forcing term by $(1-C)$, such that the forcing is only active in the gas phase where $C = 0$.

The initial velocity field was generated by prescribing the TKE spectrum $E(\kappa)$ and ensuring that the initial random velocity field is isotropic, divergence-free with respect to the discretized form of the continuity equation and that the velocity cross-correlation spectra, $R_{ij}(\kappa)$, satisfy the realizability constraint [69].

The initial energy spectrum at time $t = 0$ was prescribed according to the model spectrum

[84]

$$E(\kappa) = 16\sqrt{\frac{2}{\pi}} u_0^2 \frac{\kappa^4}{\kappa_{\text{peak}}^5} \exp -2\left(\frac{\kappa}{\kappa_{\text{peak}}}\right)^2, \tag{6.3}$$

where κ is the wavenumber, κ_{peak} is the wave number of peak energy, and u_0 is the initial r.m.s. velocity. The wave number of peak energy is $\kappa_{\text{peak}} = 1$ and the non-dimensional kinematic viscosity, Re, is chosen to yield an an initial Taylor scale Reynolds number of $\text{Re}_{\lambda 0}$=25 in conjunction with the initial turbulence kinetic energy and dissipation rate.

The DNS was performed on a 256^3 mesh with triply periodic boundary conditions. The droplet was resolved by 32 grid points across its diameter. In the simulation we use the following parameters

$$\begin{aligned}
&\text{Re} = 3820,\ \text{Sc} = 2.7,\ \text{We} = 3082,\ \text{Pr} = 0.7,\ \text{Ste} = 1,\ \text{Ste}_c = 0.146,\\
&D_0 = 0.125,\ \frac{\rho_l}{\rho_g} = 40,\ \frac{\mu_l}{\mu_g} = 25,\ \frac{c_{p,l}}{c_{p,g}} = 2.5,\ \frac{k_l}{k_g} = 3.2,\ \frac{M_v}{M_a} = 1,\\
&\frac{T_l}{T_g} = 0.403,\ \frac{T_{\text{boil}}}{T_g} = 0.4968.
\end{aligned} \tag{6.4}$$

These non-dimensional parameters correspond roughly to a decane droplet evaporating in isotropic turbulence with an initial gas temperature of $\tilde{T}_g = 900\text{K}$ and initial liquid temperature of $\tilde{T}_l = 363\text{K}$.

The initial velocity field inside the droplet is zeroed out, and than projected onto a divergence-free space to satisfy $\nabla \cdot \mathbf{u}$. The initial temperature field is set as $T = CT_l + (1 - C)T_g$. To obtain more physical initial conditions for T and Y_v, we allow the initial fields to diffuse for a time of $t = 5$. To do this we solve Eqs. (5.4) and (5.5) while neglecting the convective term.

Figure 6.1 shows a 3D volume rendering of the vapor mass fraction field Y_v at three instances in time ($t = 0.2$, 5, and 10). The figure shows that as the vapor diffuses from the droplet surface, it is transported away from the droplet surface by the surrounding turbulent eddies.

Figure 6.2 shows 2D cross sections of T, Y_v and $\dot{m}$, taken at a midplane in the domain at $t = 5$. We see that the structure of the temperature field and vapor mass fraction

(a) $t = 0.2$ (b) $t = 5$ (c) $t = 10$

Figure 6.1: Volume rendering of the vapor mass fraction Y_v at three instances in time $t = 0.2$, 5 and, 10.

field are nearly identical, which is to be expected as they are both governed by convection-diffusion equations. We notice that the temperature field appears to be more diffuse. This is explained by the Lewis number being greater than unity (Le=3.86), which indicates that thermal diffusion proceeds at a faster rate than mass diffusion. Figure 6.2(c) shows the local evaporation rate $\dot{m}$ on the surface of the droplet. It is interesting to note the variations of $\dot{m}$ along the droplet surface. The figure also shows that the highest evaporation rate (at roughly 11 o'clock) corresponds to the location on the droplet surface where the vapor mass boundary layer is thinnest. This is in agreement with our expectations because $\dot{m}$ is proportional to the normal gradient of the vapor mass fraction [81].

Finally, we compute the mean Sherwood number of the droplet as a function of time. The method to calculate Sh is presented in Chapter 4, so we do not repeat it here. Figure 6.3 shows the time evolution of the mean Sherwood number. After an initial transient period, the Sherwood number approaches a steady-state value of approximately 15.5. We note that this value is nearly eight times higher than that for a droplet in quiescent gas. This quantifies the effectiveness of turbulence in enhancing droplet vaporization.

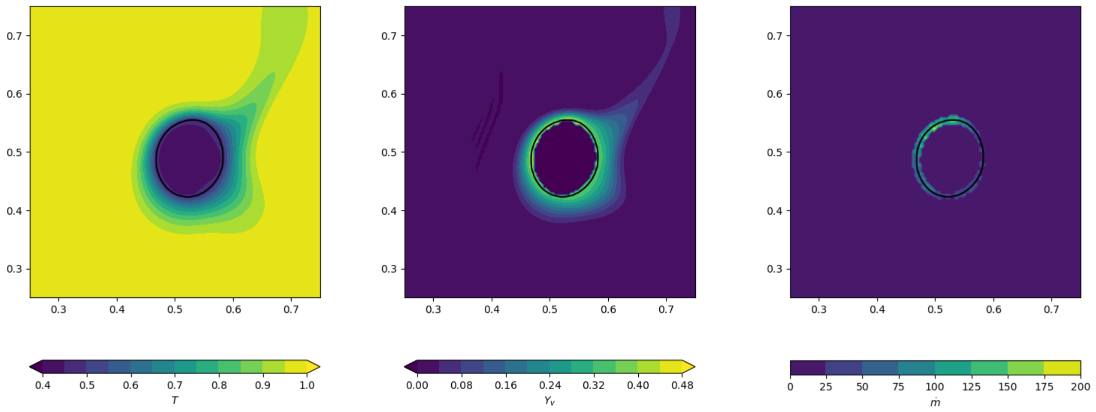

(a) (b) (c)

Figure 6.2: Contours of (a) temperature (b) vapor mass fraction and (c) mass flux rate due to phase change at $t = 5$.

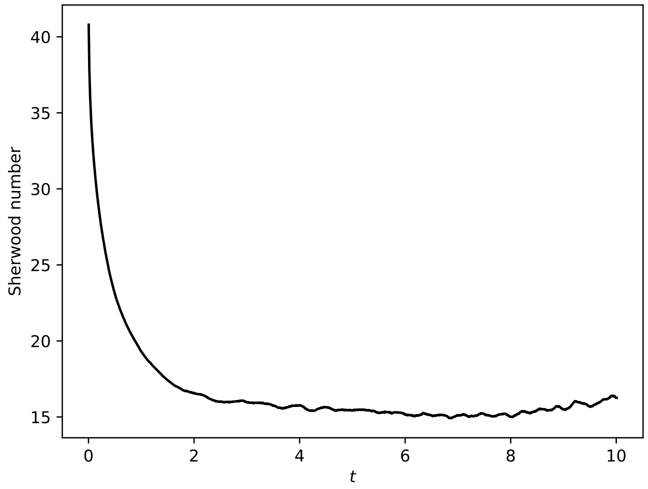

Figure 6.3: Time evolution of the mean Sherwood number for an evaporating droplet in forced isotropic turbulence at $Re_{\lambda 0} = 23.5$.

Chapter 7

CONCLUSIONS

In this work, we have made advances in direct numerical simulation of droplet-laden turbulent flows. These advances have taken place on two main fronts: (i) improved computational methods for multiphase flows and (ii) improved understanding of the physical mechanisms of droplet-laden isotropic turbulence.

In Chapter 2 a new pressure-correction method has been developed for simulating incompressible two-fluid flows with large density and viscosity ratios. The method's main advantage is that the variable coefficient Poisson equation that arises in solving the incompressible NavierStokes equations for two-fluid flows is reduced to a constant coefficient equation, which can be solved using an FFT-based, fast Poisson solver. This reduction is achieved by splitting the variable-density pressure gradient in the governing equations. The validity of this splitting is demonstrated in numerical tests up to density and viscosity ratios of 10,000. Because the scheme can use a direct, FFT-based fast Poisson solver as opposed to an iterative method, the overall solution time of the Navier-Stokes equations is reduced by a factor of 10-40, and the resulting velocity field is divergence-free to machine epsilon.

In Chapter 3 we have performed direct numerical simulations of droplets in decaying isotropic turbulence while resolving the flow inside and outside the droplets and accounting for surface tension. We have conducted a parametric study, varying one of three parameters: the density ratio between the droplet and the carrier fluid, the ratio of dynamic viscosities between the droplet and carrier fluid, and the surface tension coefficient. The turbulence kinetic energy budgets equations for droplet-laden decaying isotropic turbulence are derived and presented for the first time. Additionally, we establish a relationship between the rate of work due to surface tension and the rate of change of the total droplet surface area. This link, coupled with the simulations, shows how droplet deformation, breakup, and coalescence influences the overall kinetic energy budget of droplet-laden turbulent flows. Such knowledge can be used to improve the predictive capabilities of computational models used in engineering design.

In Chapters 4 and 5 we developed a flow solver capable of simulating gas-liquid flows that are undergoing either evaporation or condensation or both. The main novelty of the approach presented in Chapter 4 is that the VOF algorithm captures the motion of the gas-liquid interface in the presence of phase change without requiring a projection step for the liquid velocity as in existing methods. The method is verified against an analytical solution for a Stefan flow problem, and the D^2 law is verified for a single droplet in quiescent gas. We then extend this method in Chapter 5 to be able to simulate gas-liquid flows with phase change in domains that are closed or have periodic boundary conditions in all directions. Here we demonstrate that the flow solver satisfies the kinematic constraint that all sources and sinks of $\nabla \cdot \mathbf{u}$ must sum to zero. We also show that the solver conserved the total mass of the domain to less than 1% for an evaporating and condensing droplet.

Finally, in Chapter 6 we have performed DNS of an evaporating droplet in forced isotropic turbulence. The DNS results showed that turbulence leads to non-uniform mass flux rate along the droplet surface, which is caused by varying thickness of the vapor mass boundary layer surrounding the droplet. We also saw that turbulence lead to a significant (nearly 8 times) increase in the Sherwood number, compared to a droplet in quiescent conditions.

This work has advanced both the numerical methods and physical understanding of droplet-laden turbulent flows. However, there remain many open questions and avenues for further research. We suggest a few here:

- In performing direct numerical simulation (DNS) of finite-size droplets in turbulence, one of the outstanding challenges is to resolve droplet collisions fully. The problem stems from the fact that the thickness of the film between colliding drops is almost always several orders of magnitude smaller than the smallest lengthscales of the surrounding flow. This separation of scales makes fully resolving the film prohibitively expensive from a computational standpoint. Therefore, in all present DNS studies of finite-size droplets in turbulence, droplet collisions are not fully resolved. One approach towards overcoming this is to use a subgrid-scale model to determine whether approaching droplets will separate or coalesce. However, present methods are strongly dependent on the underlying film drainage model employed, and thus their predictive capabilities are uncertain. Another approach is to attempt to fully resolve the thin film by refining the mesh only in these small regions using adaptive mesh refinement.

- Computing and establishing a theory for the turbulence kinetic energy spectrum in two-fluid flows remains an open question. The challenge in computing the spectrum stems from the density discontinuity at the interface. The jump leads to Gibbs phenomena when one tries to compute the spectrum of $\rho\mathbf{u}$ for example. Also, one may want to compute the energy spectrum of only the carrier phase such to isolate the effects of the dispersed phase on the carrier phase. One possible approach would be to introduce a filtering operation to remove the contribution of the droplets to the energy spectrum.

- A parametric study of DNS of evaporating or condensing droplets in isotropic turbulence is needed to quantify the effects of varying key non-dimensional parameters on the rate of phase change and the flow. Some of these key parameters are the Schmidt number, Prandtl number, Lewis number, Stefan number, and the ratio of the droplet diameter to the Kolmogorov lengthscale. This will aid in developing more sophisticated and accurate models that can be used in complex flows.

BIBLIOGRAPHY

[1] J. Towns et al. “XSEDE: Accelerating Scientific Discovery”. *Computing in Science & Engineering* 16.5 (2014), pp. 62–74.

[2] N. Wilkins-Diehr et al. “An Overview of the XSEDE Extended Collaborative Support Program”. *High Performance Computer Applications: 6th International Conference, ISUM 2015, Mexico City, Mexico, March 9-13, 2015, Revised Selected Papers.* Cham: Springer International Publishing, 2016, pp. 3–13.

[3] R. A. Shaw. “Particle-turbulence interactions in atmospheric clouds”. *Annu. Rev. Fluid Mech.* 35.1 (2003), pp. 183–227.

[4] L. Bourouiba, E. Dehandschoewercker, and J. W. M. Bush. “Violent expiratory events: on coughing and sneezing”. *Journal of Fluid Mechanics* 745 (2014), pp. 537–563.

[5] P. D. Berkman and R. V. Calabrese. “Dispersion of viscous liquids by turbulent flow in a static mixer”. *AIChE J.* 34.4 (1988), pp. 602–609.

[6] C. Qin et al. “Spray-cooling concept for wind-based compressed air energy storage”. *J. Renew. Sustain. Energy* 6.4 (2014), p. 043125.

[7] W. A. Sirignano. “Fuel droplet vaporization and spray combustion theory”. *Prog. Energy and Combust. Sci.* 9.4 (1983), pp. 291–322.

[8] G. M. Faeth, L. P. Hsiang, and P. K. Wu. “Structure and breakup properties of sprays”. *Int. J. Multiphase Flow* 21 (1995), pp. 99–127.

[9] S. Elghobashi. “On predicting particle-laden turbulent flows”. *Appl. Sci. Res.* 52 (1994), pp. 309–329.

[10] S. Balachandar and J. K. Eaton. “Turbulent dispersed multiphase flow”. *Annu. Rev. Fluid Mech.* 42 (2010), pp. 111–133.

[11] A. Ferrante and S. Elghobashi. "On the physical mechanism of two-way coupling in particle-laden isotropic turbulence". *Phys. Fluids* 15.2 (2003), pp. 315–329.

[12] T. S. Yang and S. S. Shy. "Two-way interaction between solid particles and homogeneous air turbulence: particle settling rate and turbulence modification measurements". *J. Fluid Mech.* 526 (2005), pp. 171–216.

[13] F. Lucci, A. Ferrante, and S. Elghobashi. "Is Stokes number an appropriate indicator for turbulence modulation by particles of Taylor-length-scale size?" *Phys. Fluids* 23 (2011), pp. 1–7.

[14] W. A. Sirignano. *Fluid dynamics and transport of droplets and sprays.* Cambridge University Press, 1999.

[15] A. Baraldi, M. S. Dodd, and A. Ferrante. "A mass-conserving volume-of-fluid method: Volume tracking and droplet surface-tension in incompressible isotropic turbulence." *Comput. Fluids* 96 (2014), pp. 322–337.

[16] M. S. Dodd and A. Ferrante. "A fast pressure-correction method for incompressible two-fluid flows". *J. Comput. Phys.* 273 (2014), pp. 416–434.

[17] M. S. Dodd and A Ferrante. "On the interaction of Taylor lengthscale size droplets and isotropic turbulence". *J. Fluid Mech.* 806 (2016), pp. 356–412.

[18] A. J. Chorin. "Numerical solution of the Navier-Stokes equations". *Math. Comput.* 22.104 (1968), pp. 745–762.

[19] R. W. Hockney. "A fast direct solution of Poisson's equation using Fourier analysis". *J. Assoc. Comput. Mach.* 12.1 (1965), pp. 95–113.

[20] B. L. Buzbee, G. H. Golub, and C. W. Nielson. "On direct methods for solving Poisson's equations". *SIAM J. Num. Anal.* 7.4 (1970), pp. 627–656.

[21] P. N. Swarztrauber. "The methods of cyclic reduction, Fourier analysis and the FACR algorithm for the discrete solution of Poisson's equation on a rectangle". *SIAM Review* 19.3 (1977), pp. 490–501.

[22] H. Schmidt, U. Schumann, and H. Volkert. *Three dimensional, direct and vectorized elliptic solvers for various boundary conditions.* Rep. 84-15. DFVLR-Mitt, 1984.

[23] S. O. Unverdi and G. Tryggvason. "A front-tracking method for viscous, incompressible, multi-fluid flows". *J. Comput. Phys.* 100.1 (1992), pp. 25–37.

[24] D. Gueyffier et al. "Volume-of-fluid interface tracking with smoothed surface stress methods for three-dimensional flows". *J. Comput. Phys.* 152.2 (1999), pp. 423–456.

[25] Stéphane Popinet. "An accurate adaptive solver for surface-tension-driven interfacial flows." *J. Comput. Phys.* 228.16 (2009), pp. 5838–5866.

[26] M.M. Francois et al. "A balanced-force algorithm for continuous and sharp interfacial surface tension models within a volume tracking framework". *J. Comput. Phys.* 213.1 (2006), pp. 141–173.

[27] G. D. Weymouth and D. K-P Yue. "Conservative volume-of-fluid method for free-surface simulations on Cartesian-grids". *J. Comput. Phys.* 229.8 (2010), pp. 2853–2865.

[28] M. Sussman and E. G. Puckett. "A coupled level set and volume-of-fluid method for computing 3D and axisymmetric incompressible two-phase flows". *Journal of Computational Physics* 162.2 (2000), pp. 301–337.

[29] J-L Guermond and A. Salgado. "A splitting method for incompressible flows with variable density based on a pressure Poisson equation". *J. Comput. Phys.* 228.8 (2009), pp. 2834–2846.

[30] S. Dong and J. Shen. "A time-stepping scheme involving constant coefficient matrices for phase-field simulations of two-phase incompressible flows with large density ratios". *J. Comput. Phys.* 231.17 (2012), pp. 5788–5804.

[31] D. Gottlieb and S. A. Orszag. *Numerical analysis of spectral methods: theory and applications.* SIAM, 1977.

[32] R. Temam. “Sur l’approximation de la solution des équations de Navier-Stokes par la méthode des pas fractionnaires (II)”. *Archive for Rational Mechanics and Analysis* 33.5 (1969), pp. 377–385.

[33] J.U. Brackbill, D.B. Kothe, and C. Zemach. “A continuum method for modeling surface tension”. *J. Comput. Phys.* 100.2 (1992), pp. 335–354. ISSN: 0021-9991.

[34] S.J. Cummins, M.M. Francois, and D.B. Kothe. “Estimating curvature from volume fractions”. *Comput. Struct.* 83.6-7 (2005), pp. 425–434.

[35] J. López et al. “An improved height function technique for computing interface curvature from volume fractions”. *Comput. Methods Appl. Mech. Engrg.* 198.33 (2009), pp. 2555–2564.

[36] E. G. Puckett et al. “A high-order projection method for tracking fluid interfaces in variable density incompressible flows”. *J. Comput. Phys.* 130.2 (1997), pp. 269–282.

[37] V. Le Chenadec and H. Pitsch. “A monotonicity preserving conservative sharp interface flow solver for high density ratio two-phase flows”. *J. Comput. Phys.* 249 (2013), pp. 185–203.

[38] R. D. Falgout and U. M. Yang. “hypre: A library of high performance preconditioners”. *Computational Science–ICCS 2002*. Springer, 2002, pp. 632–641.

[39] R. D. Falgout, J. E. Jones, and U. M. Yang. “The design and implementation of hypre, a library of parallel high performance preconditioners”. *Numerical solution of partial differential equations on parallel computers*. Springer, 2006, pp. 267–294.

[40] S. Schaffer. “A semicoarsening multigrid method for elliptic partial differential equations with highly discontinuous and anisotropic coefficients”. *SIAM J. Sci. Comput.* 20.1 (1998), pp. 228–242.

[41] M. Sussman and M. Ohta. “A stable and efficient method for treating surface tension in incompressible two-phase flow”. *SIAM Journal on Scientific Computing* 31.4 (2009), pp. 2447–2471.

[42] S. Hysing. “A new implicit surface tension implementation for interfacial flows”. *Int. J. Numer. Methods Fluids* 51.6 (2006), pp. 659–672.

[43] M. Frigo and S. G. Johnson. “The design and implementation of FFTW3”. *Proc. of the IEEE* 93.2 (2005), pp. 216–231.

[44] F. H. Harlow and J. E. Welch. “Numerical calculation of time-dependent viscous incompressible flow of fluid with free surface”. *Phys. Fluids* 8 (1965), pp. 2182–2189.

[45] G. Tryggvason, R. Scardovelli, and S. Zaleski. *Direct numerical simulations of gas-liquid multiphase flows.* Cambridge University Press, 2011.

[46] B. Lafaurie et al. “Modelling merging and fragmentation in multiphase flows with SURFER”. *J. Comput. Phys.* 113.1 (1994), pp. 134–147.

[47] S. Osher and J.A. Sethian. “Fronts propagating with curvature-dependent speed: algorithms based on Hamilton-Jacobi formulations”. *J. Comput. Phys.* 79.1 (1988), pp. 12–49.

[48] S.O. Unverdi and G. Tryggvason. “A front-tracking method for viscous, incompressible, multi-fluid flows”. *J. Comput. Phys.* 100.1 (1992), pp. 25–37.

[49] J. Schlottke and B. Weigand. “Direct numerical simulation of evaporating droplets”. *J. Comput. Phys.* 227.10 (2008), pp. 5215–5237.

[50] J Hernández et al. “A new volume of fluid method in three dimensions–Part I: Multidimensional advection method with face-matched flux polyhedra”. *Int. J. Numer. Methods Fluids* 58.8 (2008), pp. 897–921.

[51] V. Le Chenadec and H. Pitsch. “Combination of 3D unsplit forward and backward volume-of-fluid transport and coupling to the level set method”. *J. Comput. Phys.* 233 (2013), pp. 10–33.

[52] R. Scardovelli et al. “A marker-VOF algorithm for incompressible flows with interfaces”. *Advances in Free Surface and Interface Fluid Dynamics.* Vol. 1. ASME Conf. Proc., Joint U.S.-European Fluids Engineering Division Conference. 2002, pp. 905–910.

[53] E. Aulisa et al. “Interface reconstruction with least-squares fit and split advection in three-dimensional Cartesian geometry”. *J. Comput. Phys.* 225.2 (2007), pp. 2301–2319.

[54] D. L. Youngs. “Time-dependent multi-material flow with large fluid distortion”. *Numer. Methods Fluid Dyn.* 1.1 (1982), pp. 41–51.

[55] R. Scardovelli and S. Zaleski. “Interface reconstruction with least-square fit and split Eulerian–Lagrangian advection”. *Int. J. Numer. Methods Fluids* 41.3 (2003), pp. 251–274.

[56] J. López and J. Hernández. “Analytical and geometrical tools for 3D volume of fluid methods in general grids”. *J. Comput. Phys.* 227.12 (2008), pp. 5939–5948.

[57] D.J.E. Harvie and D.F. Fletcher. “A new volume of fluid advection algorithm: the stream scheme”. *J. Comput. Phys.* 162.1 (2000), pp. 1–32. ISSN: 0021-9991.

[58] J. López and J. Hernández. “On reducing interface curvature computation errors in the height function technique”. *J. Comput. Phys.* 229 (2010), pp. 4855–4868.

[59] F. Nicoud. “Conservative high-order finite-difference schemes for low-Mach number flows”. *J. Comput. Phys.* 158.1 (2000), pp. 71–97.

[60] A. H. Baker et al. “Scaling hypre’s multigrid solvers to 100,000 cores”. *High-Performance Scientific Computing.* Springer, 2012, pp. 261–279.

[61] J. Schmidt et al. *Large scale parallel solution of incompressible flow problems using uintah and hypre.* Tech. rep. Technical Report UUSCI-2012-002, Scientific Computing and Imaging Institute, 2012.

[62] H. Schmidt, U. Schumann, and H. Volkert. *Three dimensional, direct and vectorized elliptic solvers for various boundary conditions.* Rep. 84-15. DFVLR-Mitt, 1984.

[63] G. I. Taylor. “On the decay of vortices in a viscous fluid”. *Philos. Mag.* XLVI (1923), pp. 671–674.

[64] D. L. Brown, R. Cortez, and M. L. Minion. “Accurate projection methods for the incompressible Navier–Stokes equations”. *J. Comput. Phys.* 168.2 (2001), pp. 464–499.

[65] L. J. P. Timmermans, P. D. Minev, and F. N. Van De Vosse. “An approximate projection scheme for incompressible flow using spectral elements”. *Int. J. Numer. Methods Fluids* 22.7 (1996), pp. 673–688.

[66] A. Prosperetti. “Motion of two superposed viscous fluids.” *Phys. Fluids* 24 (1981), p. 1217.

[67] K. V. Beard. “Terminal velocity and shape of cloud and precipitation drops aloft”. *J. Atmos. Sci.* 33.5 (1976), pp. 851–864.

[68] R. Clift, J. R. Grace, and M. E. Weber. *Bubbles, Drops and Particles*. Dover, 2005.

[69] U. Schumann. “Realizability of Reynolds-stress turbulence models”. *Phys. Fluids* 20 (1977), p. 721.

[70] S. B. Pope. *Turbulent Flows*. Cambridge Univ. Press, 2000.

[71] J. S. Hadamard. “Mouvement permanent lent d’une sphère liquide et visqueuse dans un liquide visqueux”. *CR Acad. Sci* 152.25 (1911), pp. 1735–1738.

[72] W. Rybczyński. “Über die fortschreitende Bewegung einer flüssigen Kugel in einen zähen Medium”. *Bull. Acad. Sci. Cracovie* A (1911), pp. 40–46.

[73] J. Jeong and F. Hussain. “On the identification of a vortex”. *J. Fluid Mech.* 285 (1995), pp. 69–94.

[74] F. Lucci, A. Ferrante, and S. Elghobashi. “Modulation of isotropic turbulence by particles of Taylor length-scale size”. *J. Fluid Mech.* 650 (2010), pp. 1–51.

[75] A. Frohn and N. Roth. *Dynamics of droplets*. Springer, 2000.

[76] A. Esmaeeli and G. Tryggvason. “Computations of film boiling. Part I: numerical method”. *Int. J. of Heat and Mass Transfer* 47.25 (2004), pp. 5451–5461.

[77] H. S. Udaykumar, R. Mittal, and W. Shyy. “Computation of solid–liquid phase fronts in the sharp interface limit on fixed grids”. *J. Comput. Phys.* 153.2 (1999), pp. 535–574.

[78] B. Fornberg. “Generation of finite difference formulas on arbitrarily spaced grids”. *Mathematics of Computation* 51.184 (1988), pp. 699–706.

[79] M. Sussman. “A second order coupled level set and volume-of-fluid method for computing growth and collapse of vapor bubbles”. *J. Comput. Phys.* 187.1 (2003), pp. 110–136.

[80] M. S. Dodd and A. Ferrante. “A coupled volume-of-fluid and pressure-correction method for gas-liquid flows with phase change: II. Low Mach number formulation”. *J. Comput. Phys.* (), in preparation.

[81] M. S. Dodd and A. Ferrante. “A coupled volume-of-fluid and pressure-correction method for gas-liquid flows with phase change: I. Incompressible formulation”. *J. Comput. Phys.* (), in preparation.

[82] M. Bassenne et al. “Constant-energetics physical-space forcing methods for improved convergence to homogeneous-isotropic turbulence with application to particle-laden flows”. *Physics of Fluids* 28.3 (2016), p. 035114.

[83] T. S. Lundgren. “Linearly forced isotropic turbulence”. *Annual Research Briefs*. Center for Turbulence Research, Stanford, 2003, pp. 461–473.

[84] U. Schumann and J. R. Herring. “Axisymmetric homogeneous turbulence: a comparison of direct spectral simulations with the direct-interaction approximation”. *J. Fluid Mech.* 76.4 (1976), pp. 755–782.

[85] Daniel D Joseph. *Stability of Fluid Motions: Vol.: 2.* Springer-Verlag, 1976.

[86] R. Aris. *Vectors, Tensors and the Basic Equations of Fluid Mechanics.* Dover, 1989.

[87] D. D. Joseph and Y. Y. Renardy. *Fundamentals of two-fluid dynamics. Pt. I: Mathematical theory and applications.* Springer-Verlag, 1993.

Appendix A

IMPLICIT TIME INTEGRATION OF VISCOUS TERMS

In solving the Navier-Stokes equations, the viscous numerical stability restriction ($\Delta t \leq (1/2)\Delta t_\nu$) can be eliminated by treating the viscous terms implicitly using Crank-Nicolson time integration. This allows for a greater time step in low Reynolds number simulations, which allows $\Delta t \gg \mathrm{Re}\Delta x^2$, a requirement for second-order temporal accuracy to be realized on the pressure [64]. The implicit treatment introduces a variable coefficient Helmholtz equation which has been most efficiently solved iteratively in other two-fluid pressure-correction methods (e.g., in [25]). Instead, we reduce the variable coefficient Helmholtz equations to constant coefficient equations (similarly to the pressure splitting in Eq. (2.5)) by using the basic splitting idea [31, 30]. The constant coefficient Helmholtz equation can then be solved directly using a fast FFT-based elliptic solver [e.g. 21, 22]. For time integration, we use second-order Adams-Bashforth for the convective and force terms and second-order Crank-Nicolson for the diffusive terms which gives:

$$\begin{aligned} \frac{\mathbf{u}^* - \mathbf{u}^n}{\Delta t} &= \frac{1}{2}(3\mathbf{H}^n - \mathbf{H}^{n-1}) \\ &+ \frac{1}{2}\frac{1}{\mathrm{Re}}\frac{1}{\rho^{n+1}}\left[\nabla\cdot\left(\mu^{n+1}\mathbf{D}(\mathbf{u}^n)\right) + \nabla\cdot\left(\mu^{n+1}\mathbf{D}(\mathbf{u}^*)\right)\right] \end{aligned} \tag{A.1}$$

with

$$\begin{aligned} \mathbf{H}^k &= -\nabla\cdot(\mathbf{u}^k\mathbf{u}^k) + \frac{1}{\rho^{k+1}}\frac{1}{\mathrm{We}}\mathbf{f}_\sigma^{k+1} \\ \mathbf{D}(\mathbf{u}^k) &= (\nabla\mathbf{u}^k + (\nabla\mathbf{u}^k)^T). \end{aligned} \tag{A.2}$$

The last viscous term in Eq. (A.1) with variable coefficients is split into a constant part and a variable part, and the constant part is treated implicitly and the variable part explicitly [30], i.e.,

$$\frac{1}{\rho^{n+1}}\nabla\cdot\left(\mu^{n+1}\mathbf{D}(\mathbf{u}^*)\right) \rightarrow \nu_0\nabla^2\mathbf{u}^* + \frac{1}{\rho^{n+1}}\nabla\cdot\left(\mu^{n+1}\mathbf{D}(\mathbf{u}^n)\right) - \nu_0\nabla^2\mathbf{u}^n \tag{A.3}$$

where $\nu_0 = \frac{1}{2}\left(\frac{\mu_c}{\rho_c} + \frac{\mu_d}{\rho_d}\right)$. Unlike the pressure field, the velocity field is continuous across the interface, thus, we do not need to linearly extrapolate $\mathbf{u}^n$ in time as we did for the pressure in (2.14) (see Section 2.4.2). The substitution in (A.3) is consistent because we recover the constant-property Navier-Stokes equations if we set $\mu_c = \rho_c = \mu_d = \rho_d = 1$. Substituting Eq. (A.3) into Eq. (A.1) gives:

$$\begin{aligned}\frac{\mathbf{u}^* - \mathbf{u}^n}{\Delta t} &= \frac{1}{2}(3\mathbf{H}^n - \mathbf{H}^{n-1}) \\ &\quad + \frac{1}{\mathrm{Re}}\frac{1}{\rho^{n+1}}\left[\nabla \cdot \left(\mu^{n+1}\mathbf{D}(\mathbf{u}^n)\right)\right] + \frac{1}{2}\frac{1}{\mathrm{Re}}\left(\nu_0\nabla^2\mathbf{u}^* - \nu_0\nabla^2\mathbf{u}^n\right).\end{aligned} \tag{A.4}$$

Multiplying Eq. (A.4) by $(-2\mathrm{Re}/\nu_0)$ and rearranging terms gives the Helmholtz equation for $\mathbf{u}^*$:

$$\nabla^2\mathbf{u}^* - \frac{2\mathrm{Re}}{\nu_0\Delta t}\mathbf{u}^* = -\frac{2\mathrm{Re}}{\nu_0\Delta t}\mathbf{u}^n - \frac{\mathrm{Re}}{\nu_0}\left(3\mathbf{H}^n - \mathbf{H}^{n-1}\right) - \frac{2}{\nu_0}\frac{1}{\rho^{n+1}}\left[\nabla \cdot \left(\mu^{n+1}\mathbf{D}(\mathbf{u}^n)\right)\right] + \nabla^2\mathbf{u}^n. \tag{A.5}$$

Equation (A.5) can be solved using a fast elliptic solver [e.g. 21, 22]. Once $\mathbf{u}^*$ is known, the solution algorithm proceeds as described in Sec. 2.2.1 by next computing p^{n+1} from Eq. (2.16) and then $\mathbf{u}^{n+1}$ from Eq. (2.17). We have tested the method solving Eq. (A.5) for the capillary wave case and found excellent agreement with Prosperetti's analytical solution up to density and viscosity ratios 10,000.

Appendix B

JUMP CONDITIONS AT THE DROPLET INTERFACE AND INTEGRAL FORM OF THE KINETIC ENERGY EQUATION FOR A TWO-FLUID FLOW

We consider the incompressible flow of two immiscible fluids separated by a common interface in the absence of any body forces and without phase change. The geometry of the control volume we consider, which is adapted from [85, p. 242], is illustrated in figure B.1. The control volume, $\mathcal{V}(t)$ is a material volume, i.e., fluid elements can not cross its boundaries. $\mathcal{V}(t)$ consists of two volumes of fluid, $\mathcal{V}_c(t)$ and $\mathcal{V}_d(t)$ (e.g. the carrier and droplet fluid), separated by an interface $\Sigma(t)$, such that $\mathcal{V} = \mathcal{V}_c \cup \mathcal{V}_d$. The volumes $\mathcal{V}_c$ and $\mathcal{V}_d$ are bounded by $\partial\mathcal{V}_c(t)$ and $\partial\mathcal{V}_d(t)$, respectively, the boundary of $\mathcal{V}(t)$ is $\partial\mathcal{V} = \partial\mathcal{V}_c \cup \partial\mathcal{V}_d - \Sigma$ and the interface satisfies $\Sigma = \partial\mathcal{V}_c \cap \partial\mathcal{V}_d$. The unit normals to $\partial\mathcal{V}_c$ and $\partial\mathcal{V}_d$ are $\mathbf{n}_c$ and $\mathbf{n}_d$, respectively. $\mathbf{n}$ is a unit vector normal to Σ that is directed from the carrier fluid to the droplet fluid, and consequently $\mathbf{n} = \mathbf{n}_c$ for $\mathbf{x} \in \Sigma$. $\partial\Sigma$ is a contact line satisfying $\partial\Sigma = \Sigma \cap \partial\mathcal{V}$. $\mathbf{t}_S$ is a unit vector tangent to $\partial\Sigma$, and $\mathbf{m}$ is a unit vector perpendicular to $\partial\Sigma$ and pointing out of Σ. $\mathbf{n}$, $\mathbf{t}_S$, and $\mathbf{m}$ are defined such that they form an orthonormal set (e.g., $\mathbf{m} = \mathbf{n} \times \mathbf{t}_S$).

Note, in the following subsections we refer to quantities with '*d*' subscript as droplet quantities; however, we have made no assumptions about the density ratio and viscosity ratio, and therefore, the following equations not only hold for droplet-laden flows but also for bubble-laden flows, and, in general, for the incompressible flow of two immiscible fluids separated by an interface.

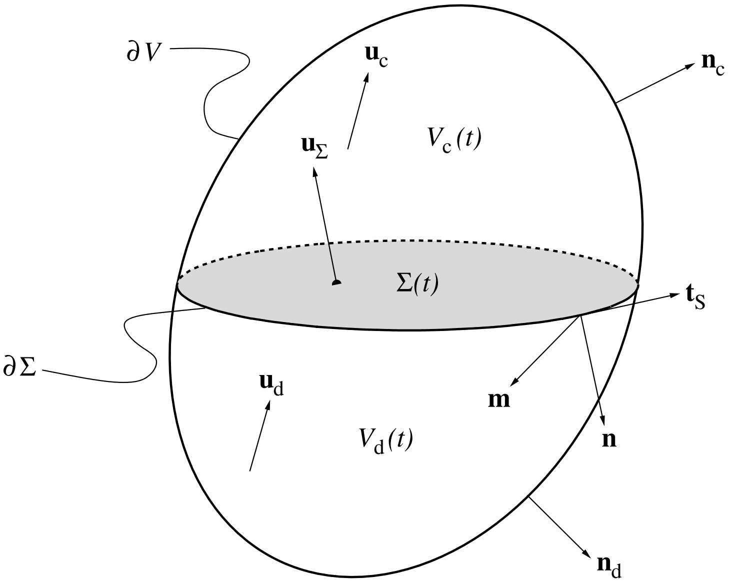

Figure B.1: Control volume $\mathcal{V}(t)$ containing an interface $\Sigma(t)$ separating two immiscible volumes of fluid, $\mathcal{V}_c(t)$ and $\mathcal{V}_d(t)$.

B.1 Conservation of mass

The principle of conservation of mass states that the mass of a material volume does not change

$$\frac{\mathrm{d}}{\mathrm{d}t}\int_{\mathcal{V}} \rho \mathrm{d}\mathcal{V} = 0. \tag{B.1}$$

By taking the limit $\partial\mathcal{V} \to \Sigma$, and assuming that there is no mass flux across the interface, one obtains that the normal components of velocity are equal [86, p. 236]

$$\mathbf{u}_d \cdot \mathbf{n} = \mathbf{u}_c \cdot \mathbf{n} = \mathbf{u}_\Sigma \cdot \mathbf{n}, \quad \mathbf{x} \in \Sigma. \tag{B.2}$$

Also for viscous fluids under standard operating conditions, it is an experimentally observed fact that the two fluids do not slip, and therefore, the velocity is continuous across the interface

$$\mathbf{u}_d = \mathbf{u}_c = \mathbf{u}_\Sigma, \quad \mathbf{x} \in \Sigma, \tag{B.3}$$

which we rewrite using jump notation (i.e. $[\![\phi]\!] = \phi_c - \phi_d$),

$$[\![\mathbf{u}]\!] = 0. \tag{B.4}$$

B.2 Conservation of momentum

The conservation equation for the linear momentum of $\mathcal{V}$ is [87, p. 22]

$$\frac{\mathrm{d}}{\mathrm{d}t}\int_{\mathcal{V}} \rho\mathbf{u}\ \mathrm{d}\mathcal{V} = \int_{\partial\mathcal{V}} \boldsymbol{\tau}\mathbf{n}\ \mathrm{d}\mathcal{A} + \int_{\partial\Sigma} \sigma\mathbf{m}\ \mathrm{d}\ell, \tag{B.5}$$

where $\boldsymbol{\tau}$ is the fluid stress tensor, which for an incompressible Newtonian fluid is

$$\begin{aligned} \boldsymbol{\tau} &= -p\mathsf{I} + \mu\left(\nabla\mathbf{u} + (\nabla\mathbf{u})^T\right) \\ &= -p\mathsf{I} + 2\mu\mathsf{S}, \end{aligned} \tag{B.6}$$

where I is the identity tensor, $\mathsf{S} \equiv \frac{1}{2}\left(\nabla\mathbf{u} + (\nabla\mathbf{u})^T\right)$ is the strain-rate tensor and $\mathrm{d}\ell$ is an infinitesimal arc length (not to be confused with the integral lengthscale of turbulence, ℓ). On the left hand side of (B.5) is the rate of change of momentum, and on the right hand side, the two terms represent, respectively, the force acting on the boundary due to fluid stress and the force due to surface tension. We note that the last term in (B.5) is a line integral along the contact line $\partial\Sigma$. This term can be converted from a line integral to a surface integral by using the divergence theorem for curved surfaces, i.e.

$$\int_{\partial\Sigma} \sigma\mathbf{m}\ \mathrm{d}\ell = \int_{\Sigma} \nabla_s\sigma\ \mathrm{d}\mathcal{A} + \int_{\Sigma} \kappa\sigma\mathbf{n}\ \mathrm{d}\mathcal{A}, \tag{B.7}$$

where ∇_s is the surface gradient defined as

$$\nabla_s = \nabla - \mathbf{n}(\mathbf{n}\cdot\nabla). \tag{B.8}$$

Combining (B.5) and (B.7), using the divergence theorem, and accounting for a discontinuity in $\boldsymbol{\tau}$ yields

$$\begin{aligned} 0 = &\int_{\mathcal{V}} \left(\rho\frac{\mathrm{d}\mathbf{u}}{\mathrm{d}t} - \nabla\cdot\boldsymbol{\tau}\right)\ \mathrm{d}\mathcal{V} \\ &+ \int_{\Sigma} \left([\![\boldsymbol{\tau}]\!]\mathbf{n} - \nabla_s\sigma - \kappa\sigma\mathbf{n}\right)\mathrm{d}\mathcal{A}. \end{aligned} \tag{B.9}$$

By taking the limit $\partial\mathcal{V} \to \Sigma$, and noting that Σ was chosen arbitrarily we obtain the jump condition for momentum at Σ

$$[\![\boldsymbol{\tau}]\!]\mathbf{n} = \nabla_s\sigma + \kappa\sigma\mathbf{n}, \quad \mathbf{x} \in \Sigma. \tag{B.10}$$

Using (B.6), the normal stress boundary condition is

$$[\![-p + \mathbf{n} \cdot 2\mu\boldsymbol{S}\mathbf{n}]\!] = \sigma\kappa \tag{B.11}$$

and the tangential stress boundary condition is

$$[\![\mathbf{t}_k \cdot 2\mu\boldsymbol{S}\mathbf{n}]\!] = \mathbf{t}_k \cdot \nabla_s\sigma, \quad k = 1, 2, \tag{B.12}$$

where $\mathbf{t}_1$ and $\mathbf{t}_2$ are two unit vectors that are tangent to Σ and orthogonal to $\mathbf{n}$. When the surface tension coefficient is constant, (B.12) simplifies to

$$[\![\mathbf{t}_k \cdot 2\mu\boldsymbol{S}\mathbf{n}]\!] = 0, \quad k = 1, 2, \tag{B.13}$$

which shows that the tangential stress is continuous across the interface and, if $\mu_c \neq \mu_d$, then the rate of strain $\boldsymbol{S}$ is discontinuous at the interface.

B.3 Balance equation of kinetic energy

To derive the kinetic energy balance equation for $\mathcal{V}$ we begin with the momentum conservation equation (B.9) for $\mathcal{V}_c$ and $\mathcal{V}_d$,

$$\rho\frac{\mathrm{d}\mathbf{u}}{\mathrm{d}t} = \nabla \cdot \boldsymbol{\tau}, \quad \mathbf{x} \in \mathcal{V}_c \text{ or } \mathcal{V}_d, \tag{B.14}$$

and take the dot product of (B.14) with $\mathbf{u}$

$$\rho\frac{\mathrm{d}(\mathbf{u} \cdot \mathbf{u})/2}{\mathrm{d}t} = (\nabla \cdot \boldsymbol{\tau}) \cdot \mathbf{u}, \quad \mathbf{x} \in \mathcal{V}_c \text{ or } \mathcal{V}_d. \tag{B.15}$$

We integrate (B.15) over $\mathcal{V}_c$ and $\mathcal{V}_d$, use the identity $\mathbf{u} \cdot (\nabla \cdot \boldsymbol{\tau}) = \nabla \cdot (\boldsymbol{\tau}\mathbf{u}) - \boldsymbol{\tau} : \nabla\mathbf{u}$ and use the divergence theorem to obtain

$$\begin{aligned} \int_{\mathcal{V}_c} \rho\frac{\mathrm{d}(\mathbf{u} \cdot \mathbf{u})/2}{\mathrm{d}t}\,\mathrm{d}\mathcal{V} &= \int_{\partial\mathcal{V}_c} \boldsymbol{\tau}\mathbf{u} \cdot \mathbf{n}_c\,\mathrm{d}\mathcal{A} - \int_{\mathcal{V}_c} \boldsymbol{\tau} : \nabla\mathbf{u}\,\mathrm{d}\mathcal{V} \\ \int_{\mathcal{V}_d} \rho\frac{\mathrm{d}(\mathbf{u} \cdot \mathbf{u})/2}{\mathrm{d}t}\,\mathrm{d}\mathcal{V} &= \int_{\partial\mathcal{V}_d} \boldsymbol{\tau}\mathbf{u} \cdot \mathbf{n}_d\,\mathrm{d}\mathcal{A} - \int_{\mathcal{V}_d} \boldsymbol{\tau} : \nabla\mathbf{u}\,\mathrm{d}\mathcal{V} \end{aligned} \tag{B.16}$$

Adding together the kinetic energy equations for the carrier and droplet fluid in (B.16) yields the evolution equation for the kinetic energy of $\mathcal{V}$

$$\int_{\mathcal{V}} \rho \frac{\mathrm{d}(\mathbf{u}\cdot\mathbf{u})/2}{\mathrm{d}t}\,\mathrm{d}\mathcal{V} = \int_{\partial\mathcal{V}_c} \boldsymbol{\tau}\mathbf{u}\cdot\mathbf{n}_c\,\mathrm{d}\mathcal{A} + \int_{\partial\mathcal{V}_d} \boldsymbol{\tau}\mathbf{u}\cdot\mathbf{n}_d\,\mathrm{d}\mathcal{A} - \int_{\mathcal{V}} \boldsymbol{\tau} : \nabla\mathbf{u}\,\mathrm{d}\mathcal{V}. \tag{B.17}$$

We then use the following transformation to account for the jump in $\boldsymbol{\tau}$ at the interface:

$$\begin{aligned} \int_{\partial\mathcal{V}} \boldsymbol{\tau}\mathbf{u}\cdot\mathbf{n}\,\mathrm{d}\mathcal{A} &= \int_{\partial\mathcal{V}_c} \boldsymbol{\tau}\mathbf{u}\cdot\mathbf{n}_c\,\mathrm{d}\mathcal{A} + \int_{\partial\mathcal{V}_d} \boldsymbol{\tau}\mathbf{u}\cdot\mathbf{n}_d\,\mathrm{d}\mathcal{A} \\ &\quad - \int_{\Sigma} (\boldsymbol{\tau}\mathbf{u})_c\cdot\mathbf{n}_c\,\mathrm{d}\mathcal{A} - \int_{\Sigma} (\boldsymbol{\tau}\mathbf{u})_d\cdot\mathbf{n}_d\,\mathrm{d}\mathcal{A} \\ &= \int_{\partial\mathcal{V}_c} \boldsymbol{\tau}\mathbf{u}\cdot\mathbf{n}_c\,\mathrm{d}\mathcal{A} + \int_{\partial\mathcal{V}_d} \boldsymbol{\tau}\mathbf{u}\cdot\mathbf{n}_d\,\mathrm{d}\mathcal{A} \\ &\quad - \int_{\Sigma} (\boldsymbol{\tau}\mathbf{u})_c\cdot\mathbf{n}\,\mathrm{d}\mathcal{A} + \int_{\Sigma} (\boldsymbol{\tau}\mathbf{u})_d\cdot\mathbf{n}\,\mathrm{d}\mathcal{A} \\ &= \int_{\partial\mathcal{V}_c} \boldsymbol{\tau}\mathbf{u}\cdot\mathbf{n}_c\,\mathrm{d}\mathcal{A} + \int_{\partial\mathcal{V}_d} \boldsymbol{\tau}\mathbf{u}\cdot\mathbf{n}_d\,\mathrm{d}\mathcal{A} - \int_{\Sigma} [\![\boldsymbol{\tau}\mathbf{u}]\!]\cdot\mathbf{n}\,\mathrm{d}\mathcal{A}. \end{aligned} \tag{B.18}$$

where in the second line we have used the fact that $\mathbf{n}_c = \mathbf{n}$ and $\mathbf{n}_d = -\mathbf{n}$ for $\mathbf{x} \in \Sigma$. Combining (B.17) and (B.18) yields

$$\int_{\mathcal{V}} \rho \frac{\mathrm{d}(\mathbf{u}\cdot\mathbf{u})/2}{\mathrm{d}t}\,\mathrm{d}\mathcal{V} = \int_{\partial\mathcal{V}} \boldsymbol{\tau}\mathbf{u}\cdot\mathbf{n}\,\mathrm{d}\mathcal{A} + \int_{\mathcal{V}} \boldsymbol{\tau} : \nabla\mathbf{u}\,\mathrm{d}\mathcal{V} + \int_{\Sigma} [\![\boldsymbol{\tau}\mathbf{u}]\!]\cdot\mathbf{n}\,\mathrm{d}\mathcal{A}. \tag{B.19}$$

The work due to surface tension contributes to the last term on the right-hand side of (B.19). This is made clear by dotting equation (B.10) with $\mathbf{u}$,

$$[\![\boldsymbol{\tau}\mathbf{u}]\!]\cdot\mathbf{n} = \mathbf{u}\cdot\nabla_s\sigma + \kappa\sigma\mathbf{u}\cdot\mathbf{n}, \quad \mathbf{x}\in\Sigma, \tag{B.20}$$

where we have used (B.3). Combining (B.19) and (B.20) and using the divergence theorem yields the integral form of the kinetic energy equation for a two-fluid flow

$$\begin{aligned} 0 &= \int_{\mathcal{V}} \left(\rho \frac{\mathrm{d}(\mathbf{u}\cdot\mathbf{u})/2}{\mathrm{d}t} - \nabla\cdot(\boldsymbol{\tau}\mathbf{u}) + \boldsymbol{\tau} : \nabla\mathbf{u}\right)\,\mathrm{d}\mathcal{V} \\ &\quad + \int_{\Sigma} \left(\mathbf{u}\cdot\nabla_s\sigma + \kappa\sigma\mathbf{u}\cdot\mathbf{n}\right)\,\mathrm{d}\mathcal{A}. \end{aligned} \tag{B.21}$$

Appendix C

TURBULENCE KINETIC ENERGY EQUATIONS IN DROPLET-LADEN ISOTROPIC TURBULENCE

We now derive the balance equations for the turbulence kinetic energy (TKE) of the carrier fluid $\mathcal{V}_c$, droplet fluid $\mathcal{V}_d$, and combined fluid $\mathcal{V}$. We consider decaying homogeneous isotropic turbulence laden with droplets with constant surface tension coefficient, σ, in a periodic domain. Up until now, we have considered only two volumes of fluid, $\mathcal{V}_c$ and $\mathcal{V}_d$, separated by an interface as depicted in figure B.1. When deriving TKE equations for droplet-laden turbulence, we take the control volume $\mathcal{V}$ to be the two-fluid flow, which includes N_d droplets with volumes $\mathcal{V}_d^{(1)}, \mathcal{V}_d^{(2)}, \ldots, \mathcal{V}_d^{(N_d)}$ immersed in the carrier-fluid volume $\mathcal{V}_c$. An example of this configuration with $N_d = 4$ is shown in figure C.1.

The two-fluid TKE, k, is defined as the spatial average of the kinetic energy (per unit volume) of the fluctuating velocity field, $\mathbf{u}(\mathbf{x}, t)$, (i.e. $\mathbf{u} = \mathbf{U} - \langle \mathbf{U} \rangle$, where $\mathbf{U}$ is the full velocity and $\langle \mathbf{U} \rangle$ is its mean),

$$k \equiv \frac{1}{2}\frac{1}{\mathcal{V}} \int_{\mathcal{V}} \rho \mathbf{u} \cdot \mathbf{u} \, \mathrm{d}\mathcal{V} = \frac{1}{2} \langle \rho \mathbf{u} \cdot \mathbf{u} \rangle, \tag{C.1}$$

where $\langle \cdots \rangle$ denotes spatial averaging of the enclosed quantity. Likewise, we define the carrier-fluid TKE as

$$k_c \equiv \frac{1}{2}\frac{1}{\mathcal{V}_c} \int_{\mathcal{V}_c} \rho_c \mathbf{u} \cdot \mathbf{u} \, \mathrm{d}\mathcal{V} = \frac{1}{2} \langle \rho_c \mathbf{u} \cdot \mathbf{u} \rangle_c, \tag{C.2}$$

and the droplet-fluid TKE as

$$k_d \equiv \frac{1}{2}\frac{1}{\mathcal{V}_d} \sum_{n=1}^{N_d} \int_{\mathcal{V}_d^{(n)}} \rho_d \mathbf{u} \cdot \mathbf{u} \, \mathrm{d}\mathcal{V} = \frac{1}{2} \langle \rho_d \mathbf{u} \cdot \mathbf{u} \rangle_d, \tag{C.3}$$

where $\mathcal{V}_d^{(n)}$ is the volume of the n-th droplet and $\mathcal{V}_d$ is the total volume of the droplet fluid (i.e. $\mathcal{V}_d = \sum_{n=1}^{N_d} \mathcal{V}_d^{(n)}$). The summation is performed over the total number of droplets N_d.

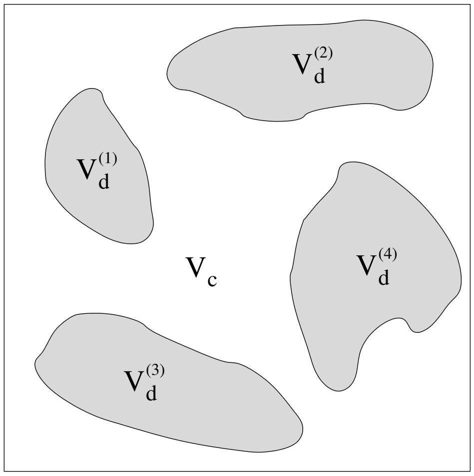

Figure C.1: Illustration showing the cross-section of a representative control volume $\mathcal{V}$ which comprises the two-fluid system: the carrier fluid $\mathcal{V}_c$ and the droplets $\mathcal{V}_d^{(1)}, \mathcal{V}_d^{(2)}, \ldots, \mathcal{V}_d^{(4)}$.

We first derive the TKE evolution equation for the carrier fluid. From (B.16) and invoking incompressibility ($\mathrm{d}\rho/\mathrm{d}t = 0$) yields

$$\int_{\mathcal{V}_c} \frac{\partial(\rho_c u_j u_j)/2}{\partial t}\,\mathrm{d}\mathcal{V} + \int_{\mathcal{V}_c} \frac{\partial(\rho_c u_i u_j u_j)/2}{\partial x_i}\,\mathrm{d}\mathcal{V} = \int_{\partial\mathcal{V}_c} \tau_{ij} u_j n_{i,c}\,\mathrm{d}\mathcal{A} - \int_{\mathcal{V}_c} \tau_{ij}\frac{\partial u_i}{\partial x_j}\,\mathrm{d}\mathcal{V}. \tag{C.4}$$

Then, by applying the divergence theorem to the first term on the right-hand side of (C.4) and using (B.6) we obtain

$$\begin{aligned}\int_{\mathcal{V}_c} \frac{\partial(\rho_c u_j u_j)/2}{\partial t}\,\mathrm{d}\mathcal{V} + \int_{\mathcal{V}_c} \frac{\partial(\rho_c u_i u_j u_j)/2}{\partial x_i}\,\mathrm{d}\mathcal{V} = &-\int_{\mathcal{V}_c} \mathsf{T}_{ij}\mathsf{S}_{ij}\,\mathrm{d}\mathcal{V} \\ &+\int_{\mathcal{V}_c}\left[\frac{\partial(\mathsf{T}_{ij}u_j)}{\partial x_i} - \frac{\partial(u_j p)}{\partial x_j}\right]\mathrm{d}\mathcal{V},\end{aligned} \tag{C.5}$$

where $\mathsf{T}_{ij} = 2\mu\mathsf{S}_{ij}$. For immiscible fluids, there is no convective transport of TKE between the carrier fluid and droplet fluid, and therefore, the second term on the left-hand side of (C.5) is zero. By dividing (C.5) by $\mathcal{V}_c$, and rewriting the resulting equation in non-dimensional form, we get

$$\underbrace{\frac{\mathrm{d}k_c}{\mathrm{d}t}}_{\substack{\text{rate of change of}\\ \text{carrier-fluid TKE}}} = -\underbrace{\varepsilon_c}_{\substack{\text{carrier-fluid}\\ \text{dissipation rate}}} + \underbrace{T_{\nu,c}}_{\substack{\text{carrier-fluid}\\ \text{viscous power}}} + \underbrace{T_{p,c}}_{\substack{\text{carrier-fluid}\\ \text{pressure power}}}, \tag{C.6}$$

where

$$\varepsilon_c \equiv \frac{1}{\mathrm{Re}}\langle \mathsf{T}_{ij}\mathsf{S}_{ij}\rangle_c, \quad T_{\nu,c} \equiv \frac{1}{\mathrm{Re}}\frac{\partial\langle \mathsf{T}_{ij}u_j\rangle_c}{\partial x_i}, \quad T_{p,c} \equiv -\frac{\partial\langle u_j p\rangle_c}{\partial x_j}. \tag{C.7}$$

The terms in (C.6) are, from left to right, the rate of change of carrier-fluid TKE, the dissipation rate of TKE in the carrier fluid, the pressure power of the carrier fluid (transport of TKE due to pressure) and the viscous power of the carrier fluid (transport of TKE due to viscous stresses). The TKE equation for the droplet-fluid is found by writing the TKE equation for each droplet and then summing over all droplets. The final result is

$$\underbrace{\frac{\mathrm{d}k_d}{\mathrm{d}t}}_{\substack{\text{rate of change of}\\ \text{droplet-fluid TKE}}} = -\underbrace{\varepsilon_d}_{\substack{\text{droplet-fluid}\\ \text{dissipation rate}}} + \underbrace{T_{\nu,d}}_{\substack{\text{droplet-fluid}\\ \text{viscous power}}} + \underbrace{T_{p,d}}_{\substack{\text{droplet-fluid}\\ \text{pressure power}}}, \tag{C.8}$$

The TKE equation for the two-fluid flow, which includes the interface, is found by adding the two equations of (B.16), resulting in

$$\int_{\mathcal{V}} \rho \frac{\mathrm{d}(\mathbf{u}\cdot\mathbf{u})/2}{\mathrm{d}t}\,\mathrm{d}\mathcal{V} = \int_{\partial\mathcal{V}_c} \boldsymbol{\tau}\mathbf{u}\cdot\mathbf{n}_c\,\mathrm{d}\mathcal{A} + \int_{\partial\mathcal{V}_d} \boldsymbol{\tau}\mathbf{u}\cdot\mathbf{n}_d\,\mathrm{d}\mathcal{A} - \int_{\mathcal{V}} \boldsymbol{\tau} : \nabla\mathbf{u}\,\mathrm{d}\mathcal{V}. \tag{C.9}$$

Because $\mathcal{V}$ is periodic, the left-hand side of (B.18) is zero such that

$$\int_{\partial\mathcal{V}_c} \boldsymbol{\tau}\mathbf{u}\cdot\mathbf{n}_c\,\mathrm{d}\mathcal{A} + \int_{\partial\mathcal{V}_d} \boldsymbol{\tau}\mathbf{u}\cdot\mathbf{n}_d\,\mathrm{d}\mathcal{A} = \int_{\Sigma} [\![\boldsymbol{\tau}\mathbf{u}]\!]\cdot\mathbf{n}\,\mathrm{d}\mathcal{A}. \tag{C.10}$$

For constant σ, integration of (B.20) over Σ gives

$$\int_{\Sigma} [\![\boldsymbol{\tau}\mathbf{u}]\!]\mathbf{n}\,\mathrm{d}\mathcal{A} = \int_{\Sigma} \kappa\sigma\mathbf{u}\cdot\mathbf{n}\,\mathrm{d}\mathcal{A}. \tag{C.11}$$

Substituting (C.11) in (C.10) yields

$$\int_{\partial\mathcal{V}_c} \boldsymbol{\tau}\mathbf{u}\cdot\mathbf{n}_c\,\mathrm{d}\mathcal{A} + \int_{\partial\mathcal{V}_d} \boldsymbol{\tau}\mathbf{u}\cdot\mathbf{n}_d\,\mathrm{d}\mathcal{A} = \int_{\Sigma} \kappa\sigma\mathbf{u}\cdot\mathbf{n}\,\mathrm{d}\mathcal{A}, \tag{C.12}$$

and substituting (C.12) into (C.9) gives

$$\begin{aligned}\int_{\mathcal{V}} \rho \frac{\mathrm{d}(\mathbf{u}\cdot\mathbf{u})/2}{\mathrm{d}t}\,\mathrm{d}\mathcal{V} &= -\int_{\mathcal{V}} \boldsymbol{\tau} : \nabla\mathbf{u}\,\mathrm{d}\mathcal{V} + \int_{\Sigma} \kappa\sigma\mathbf{u}\cdot\mathbf{n}\,\mathrm{d}\mathcal{A}\\ \int_{\mathcal{V}} \left[\rho\frac{\partial(\mathbf{u}\cdot\mathbf{u})/2}{\partial t} + \mathbf{u}\cdot\nabla(\mathbf{u}\cdot\mathbf{u})/2\right]\mathrm{d}\mathcal{V} &= -\int_{\mathcal{V}} \boldsymbol{\tau} : \nabla\mathbf{u}\,\mathrm{d}\mathcal{V} + \int_{\Sigma} \kappa\sigma\mathbf{u}\cdot\mathbf{n}\,\mathrm{d}\mathcal{A}.\end{aligned} \tag{C.13}$$

We transform the last term in (C.13) from a surface integral to a volume integral as

$$\int_{\Sigma} \kappa\sigma \mathbf{u}\cdot\mathbf{n}\ \mathrm{d}\mathcal{A} = \int_{\mathcal{V}} \mathbf{u}\cdot\mathbf{f}_\sigma\ \mathrm{d}\mathcal{V}, \tag{C.14}$$

where we recall that $\mathbf{f}_\sigma \equiv \kappa\sigma\delta(s)\mathbf{n}$ is the surface tension force. By using (C.14) in (C.13), invoking incompressibility and noting that, for homogeneous isotropic turbulence, the convective term in (C.13),

$$\int_{\mathcal{V}} \mathbf{u}\cdot\nabla(\mathbf{u}\cdot\mathbf{u})/2\ \mathrm{d}\mathcal{V} = 0, \tag{C.15}$$

we obtain

$$\int_{\mathcal{V}} \frac{\partial(\rho u_j u_j)/2}{\partial t}\ \mathrm{d}\mathcal{V} = -\int_{\mathcal{V}} \mathsf{T}_{ij}\mathsf{S}_{ij}\ \mathrm{d}\mathcal{V} + \int_{\mathcal{V}} u_j f_{\sigma,j}\ \mathrm{d}\mathcal{V}. \tag{C.16}$$

Because $\mathcal{V}$ was not chosen arbitrarily in this derivation, the integrals in (C.16) must be retained. By dividing (C.16) through by $\mathcal{V}$, rewriting the equation in non-dimensional form and noting that the time differentiation and integration commute, we obtain the TKE evolution equation for the two-fluid flow

$$\underbrace{\frac{\mathrm{d}k}{\mathrm{d}t}}_{\substack{\text{rate of change}\\ \text{of TKE}}} = -\underbrace{\varepsilon}_{\text{dissipation rate}} + \underbrace{\Psi_\sigma}_{\substack{\text{power of the}\\ \text{surface tension}}}, \tag{C.17}$$

where

$$\varepsilon \equiv \frac{1}{\mathrm{Re}}\langle \mathsf{T}_{ij}\mathsf{S}_{ij}\rangle, \quad \Psi_\sigma \equiv \frac{1}{\mathrm{We}}\langle u_j f_{\sigma,j}\rangle. \tag{C.18}$$

The terms in (C.17) are, from left to right, the rate of change of TKE for the two-fluid flow, the dissipation rate of TKE for the two-fluid flow and the power of the surface tension. To summarize, we have derived the TKE evolution equations for the

(i) carrier fluid

$$\frac{\mathrm{d}k_c}{\mathrm{d}t} = -\varepsilon_c + T_{\nu,c} + T_{p,c}, \tag{C.19}$$

(ii) droplet fluid

$$\frac{\mathrm{d}k_d}{\mathrm{d}t} = -\varepsilon_d + T_{\nu,d} + T_{p,d}, \tag{C.20}$$

(iii) two-fluid flow

$$\frac{\mathrm{d}k}{\mathrm{d}t} = -\varepsilon + \mathit{\Psi}_\sigma. \tag{C.21}$$

A useful identity, which comes from using (C.14) in (C.12), and by invoking the divergence theorem, is

$$\mathcal{V}\,\mathit{\Psi}_\sigma = \mathcal{V}_c(T_{\nu,c} + T_{p,c}) + \mathcal{V}_d(T_{\nu,d} + T_{p,d}), \tag{C.22}$$

and after dividing (C.22) throughout by $\mathcal{V}$, we get

$$\mathit{\Psi}_\sigma = (1 - \phi_v)(T_{\nu,c} + T_{p,c}) + \phi_v(T_{\nu,d} + T_{p,d}), \tag{C.23}$$

where $\phi_v \equiv \mathcal{V}_d/\mathcal{V}$ is the droplet volume fraction. (C.23) shows that the power of the surface tension is equal to the sum of the volume weighted carrier and droplet fluid viscous and pressure powers.

Appendix D

RELATIONSHIP BETWEEN THE RATE OF CHANGE OF TOTAL INTERFACIAL SURFACE AREA AND THE POWER OF THE SURFACE TENSION FOR CLOSED SURFACES

In this section, we derive the relationship between the rate of change of interfacial surface energy ($\frac{\mathrm{d}}{\mathrm{d}t}\int_\Sigma \sigma \; \mathrm{d}\mathcal{A}$) and the power of the surface tension ($\mathit{\Psi}_\sigma$). We begin be deriving the relationship for a single droplet and then generalize it for an arbitrary number of droplets N_d. Starting from the analog of the Reynolds transport theorem for a surface [86, p. 230], under the assumption that fluid parcels do not cross the interface, Joseph [85, p. 243] derived the following transport equation for the surface tension:

$$\frac{\mathrm{d}}{\mathrm{d}t}\int_{\Sigma^{(n)}} \sigma \; \mathrm{d}\mathcal{A} = \int_{\Sigma^{(n)}} \left(\frac{\partial \sigma}{\partial t} - \mathbf{u}_\Sigma \cdot \nabla_s \sigma - \kappa \sigma \mathbf{u}_\Sigma \cdot \mathbf{n} \right) \; \mathrm{d}\mathcal{A} + \int_{\partial\Sigma^{(n)}} \sigma \mathbf{u}_\Sigma \cdot \mathbf{m} \; \mathrm{d}\ell, \tag{D.1}$$

where $\Sigma^{(n)}$, in our case, is the interface of the n-th droplet, and the $\partial\Sigma^{(n)}$ is the contact line as defined in Appendix B and figure B.1. Because $\Sigma^{(n)}$ forms a closed surface, $\partial\Sigma^{(n)}$ is inexistent, and therefore, the last term in (D.1) is null. Also, if the surface tension coefficient is constant in space and time (i.e. $\sigma(\mathbf{x}, t) = \sigma$), then (D.1) reduces to

$$\sigma \frac{\mathrm{d}A^{(n)}}{\mathrm{d}t} = \int_{\Sigma^{(n)}} -\kappa \sigma \mathbf{u}_\Sigma \cdot \mathbf{n} \; \mathrm{d}\mathcal{A}. \tag{D.2}$$

where $A^{(n)} = \int_{\Sigma^{(n)}} \mathrm{d}\mathcal{A}$ is the surface area of $\Sigma^{(n)}$. We can also transform the right-hand side of (D.2) from a surface integral to a volume integral using (C.14) to obtain

$$\sigma \frac{\mathrm{d}A^{(n)}}{\mathrm{d}t} = -\int_{\mathcal{V}^{(n)}} \mathbf{u} \cdot \mathbf{f}_\sigma \; \mathrm{d}\mathcal{V}, \tag{D.3}$$

which relates the rate of change of surface area of droplet n to the power of the surface tension. To derive a relationship for the more general case of multiple droplets, we sum over

N_d droplets:

$$\sum_{n=1}^{N_d}\left(\sigma\frac{\mathrm{d}A^{(n)}}{\mathrm{d}t}\right)=-\sum_{n=1}^{N_d}\left(\int_{\mathcal{V}^{(n)}}\mathbf{u}\cdot\mathbf{f}_\sigma\ \mathrm{d}\mathcal{V}\right). \tag{D.4}$$

Interchanging the summation and differentiation and defining $A\equiv\sum_{n=1}^{N_d}A^{(n)}$ and $\mathcal{V}\equiv\sum_{n=1}^{N_d}\mathcal{V}^{(n)}$ in (D.4) yields

$$\sigma\frac{\mathrm{d}A}{\mathrm{d}t}=-\int_{\mathcal{V}}\mathbf{u}\cdot\mathbf{f}_\sigma\ \mathrm{d}\mathcal{V}, \tag{D.5}$$

Using $\langle\cdots\rangle$ to denote spatial averaging, and dividing (D.5) by $\mathcal{V}$ yields

$$\sigma\frac{1}{\mathcal{V}}\frac{\mathrm{d}A}{\mathrm{d}t}=-\langle\mathbf{u}\cdot\mathbf{f}_\sigma\rangle \tag{D.6}$$

thus using the definition of the power of the surface tension (3.7), we obtain

$$-\sigma\frac{1}{\mathcal{V}}\frac{\mathrm{d}A}{\mathrm{d}t}=\Psi_\sigma, \tag{D.7}$$

and then recalling that $\sigma=1/\mathrm{We}$ (§2.1), (D.7) becomes

$$-\frac{1}{\mathrm{We}}\frac{1}{\mathcal{V}}\frac{\mathrm{d}A}{\mathrm{d}t}=\Psi_\sigma. \tag{D.8}$$

Appendix E

DECOMPOSITION OF THE DROPLET KINETIC ENERGY

The kinetic energy of the n-th droplet per unit volume is

$$k_d^{(n)} = \frac{1}{2}\frac{1}{\mathcal{V}_d^{(n)}}\int_{\mathcal{V}_d^{(n)}} \rho_d \mathbf{u}\cdot\mathbf{u}\;\mathrm{d}\mathcal{V}. \tag{E.1}$$

The droplet kinetic energy can be computed in terms of kinetic energy associated with translation, rotation and internal circulation by decomposing the velocity field into mean translation, mean rotation, and internal circulation as

$$\mathbf{u}(\mathbf{x},t) = \mathbf{V}_d^{(n)}(t) + \mathbf{u}_r^{(n)}(\mathbf{x},t) + \mathbf{u}_i^{(n)}(\mathbf{x},t), \tag{E.2}$$

where

$$\mathbf{V}_d^{(n)}(t) = \frac{1}{\mathcal{V}_d^{(n)}}\int_{\mathcal{V}_d^{(n)}} \mathbf{u}\;\mathrm{d}\mathcal{V}, \tag{E.3a}$$

$$\mathbf{u}_r^{(n)}(\mathbf{x},t) = \mathbf{\Omega}_d^{(n)} \times \mathbf{r}(\mathbf{x},t), \tag{E.3b}$$

where $\mathbf{r} = \mathbf{x} - \mathbf{x_d}$ is the position vector $\mathbf{x}$ relative to the droplet center of mass, $\mathbf{x}_d$, and $\mathbf{\Omega}_d^{(n)}(t)$ is the mean angular velocity of the n-th droplet given by

$$\mathbf{\Omega}_d^{(n)}(t) = \frac{1}{2}\frac{1}{\mathcal{V}_d^{(n)}}\int_{\mathcal{V}_d^{(n)}} \boldsymbol{\omega}\;\mathrm{d}\mathcal{V}, \tag{E.4}$$

where $\boldsymbol{\omega} = \nabla\times\mathbf{u}$ is the vorticity. With $\mathbf{u}$, $\mathbf{V}_d^{(n)}$ and $\mathbf{u}_r^{(n)}$ known, $\mathbf{u}_i^{(n)}$ is given by

$$\mathbf{u}_i^{(n)}(\mathbf{x},t) = \mathbf{u}(\mathbf{x},t) - \mathbf{V}_d^{(n)}(t) - \mathbf{u}_r^{(n)}(\mathbf{x},t). \tag{E.5}$$

Decomposing the velocity in (E.1) using (E.2) yields

$$\begin{aligned} k_d^{(n)} &= \frac{1}{2}\frac{1}{\mathcal{V}_d^{(n)}}\int_{\mathcal{V}_d^{(n)}} \rho_d \left(\mathbf{V}_d^{(n)} + \mathbf{u}_r^{(n)} + \mathbf{u}_i^{(n)}\right)\cdot\left(\mathbf{V}_d^{(n)} + \mathbf{u}_r^{(n)} + \mathbf{u}_i^{(n)}\right) \mathrm{d}\mathcal{V} \\ &= \frac{1}{2}\rho_d \mathbf{V}_d^{(n)}\cdot\mathbf{V}_d^{(n)} + \frac{1}{\mathcal{V}_d^{(n)}}\int_{\mathcal{V}_d^{(n)}} \rho_d \mathbf{V}_d^{(n)}\cdot\left(\mathbf{u}_r^{(n)} + \mathbf{u}_i^{(n)}\right)\mathrm{d}\mathcal{V} \\ &+ \frac{1}{2}\frac{1}{\mathcal{V}_d^{(n)}}\int_{\mathcal{V}_d^{(n)}} \rho_d\left(\mathbf{u}_r^{(n)} + \mathbf{u}_i^{(n)}\right)\cdot\left(\mathbf{u}_r^{(n)} + \mathbf{u}_i^{(n)}\right)\mathrm{d}\mathcal{V} \end{aligned} \tag{E.6}$$

For a constant density droplet and noticing that $\mathbf{V}_d^{(n)}(t)$ is only a function of time, thus it can be taken out of the droplet volume integrals in (E.6),

$$\begin{aligned} k_d^{(n)} &= \frac{1}{2}\rho_d \mathbf{V}_d^{(n)}\cdot\mathbf{V}_d^{(n)} + \frac{1}{\mathcal{V}_d^{(n)}}\rho_d \mathbf{V}_d^{(n)}\cdot\int_{\mathcal{V}_d^{(n)}} \mathbf{u}_r^{(n)} + \mathbf{u}_i^{(n)}\mathrm{d}\mathcal{V} \\ &+ \frac{1}{2}\frac{1}{\mathcal{V}_d^{(n)}}\int_{\mathcal{V}_d^{(n)}} \rho_d\left(\mathbf{u}_r^{(n)} + \mathbf{u}_i^{(n)}\right)\cdot\left(\mathbf{u}_r^{(n)} + \mathbf{u}_i^{(n)}\right)\mathrm{d}\mathcal{V}. \end{aligned} \tag{E.7}$$

The second term on the right-hand side of (E.7) is zero because $\mathbf{u}_r^{(n)} + \mathbf{u}_i^{(n)}$ has zero mean. Then, the kinetic energy of a constant density droplet can be written as

$$\begin{aligned} k_d^{(n)} &= \underbrace{\frac{1}{2}\rho_d \mathbf{V}_d^{(n)}\cdot\mathbf{V}_d^{(n)}}_{k_{d,\mathrm{trans}}^{(n)}} + \underbrace{\frac{1}{2}\int_{\mathcal{V}_d^{(n)}} \rho_d \mathbf{u}_r^{(n)}\cdot\mathbf{u}_r^{(n)}\mathrm{d}\mathcal{V}}_{k_{d,\mathrm{rot}}^{(n)}} \\ &+ \underbrace{\int_{\mathcal{V}_d^{(n)}} \rho_d \mathbf{u}_r^{(n)}\cdot\mathbf{u}_i^{(n)}\mathrm{d}\mathcal{V} + \frac{1}{2}\int_{\mathcal{V}_d^{(n)}} \rho_d \mathbf{u}_i^{(n)}\cdot\mathbf{u}_i^{(n)}\mathrm{d}\mathcal{V}}_{k_{d,\mathrm{int}}^{(n)}} \end{aligned} \tag{E.8}$$

If instead of spatially averaging over a single droplet as in (E.8), we spatially average over all the droplet fluid or alternatively by summing up (E.8) over all the droplets $\sum_n = 1...N_d$, we obtain

$$k_d = k_{d,\mathrm{trans}} + k_{d,\mathrm{rot}} + k_{d,\mathrm{int}} \tag{E.9}$$

where the kinetic energy associated with translation, rotation and internal circulation are

$$\begin{aligned} k_{d,\mathrm{trans}} &= \frac{1}{2}\langle \rho_d \mathbf{V}_d^{(n)}\cdot\mathbf{V}_d^{(n)}\rangle_d, \quad k_{d,\mathrm{rot}} = \frac{1}{2}\langle \rho_d \mathbf{u}_r^{(n)}\cdot\mathbf{u}_r^{(n)}\rangle_d, \\ k_{d,\mathrm{int}} &= \langle \rho_d \mathbf{u}_r^{(n)}\cdot\mathbf{u}_i^{(n)} + \tfrac{1}{2}\rho_d \mathbf{u}_i^{(n)}\cdot\mathbf{u}_i^{(n)}\rangle_d, \end{aligned} \tag{E.10}$$

and where the droplet spatial average, $\langle\ldots\rangle_d$, is defined in (C.3).

Appendix F

DERIVATION OF LOW-MACH NUMBER GOVERNING EQUATIONS IN GAS-LIQUID FLOWS

Under the following assumptions:

- neglect Soret-Dufour effects
- neglect body forces
- neglect radiant heat transfer
- Fickian diffusion
- the gas phase is a calorically perfect gas (ideal gas and constant specific heats)

The compressible form of the Navier-Stokes equations (mass, momentum, and thermal energy) and the equation of state in dimensionless form are

$$\frac{\partial \rho}{\partial t} + \nabla \cdot (\rho \mathbf{u}) = 0 \tag{F.1}$$

$$\rho \left(\frac{\partial \mathbf{u}}{\partial t} + (\mathbf{u} \cdot \nabla)\mathbf{u} \right) = -\frac{1}{\gamma \mathrm{Ma}^2} \nabla p + \frac{1}{\mathrm{Re}} \nabla \cdot \left[\mu \left(\nabla \mathbf{u} + \nabla \mathbf{u}^T - \frac{2}{3}(\nabla \cdot \mathbf{u})\mathbf{I} \right) \right] + \frac{1}{\mathrm{We}} \mathbf{f}_\sigma \tag{F.2}$$

$$\rho c_p \left(\frac{\partial T}{\partial t} + (\mathbf{u} \cdot \nabla)T \right) = \frac{\gamma - 1}{\gamma} \left(\frac{\partial p}{\partial t} + (\mathbf{u} \cdot \nabla)p \right) + \frac{1}{\mathrm{RePr}} \nabla \cdot (k \nabla T) + \frac{(\gamma - 1)\mathrm{Ma}^2}{\mathrm{Re}} \Phi - \frac{1}{\mathrm{Ste}} \dot{m}. \tag{F.3}$$

$$p = \frac{\rho T}{\overline{\overline{M}}} \tag{F.4}$$

We expand the dependent variables as a power series in Ma^2

$$\rho(\mathrm{Ma}^2, \mathbf{x}, t) = \rho^{(0)}(\mathbf{x}, t) + \mathrm{Ma}^2 \rho^{(1)}(\mathbf{x}, t) + \mathcal{O}(\mathrm{Ma}^4), \tag{F.5a}$$

$$\mathbf{u}(\mathrm{Ma}^2, \mathbf{x}, t) = \mathbf{u}^{(0)}(\mathbf{x}, t) + \mathrm{Ma}^2 \mathbf{u}^{(1)}(\mathbf{x}, t) + \mathcal{O}(\mathrm{Ma}^4), \tag{F.5b}$$

$$p(\mathrm{Ma}^2, \mathbf{x}, t) = p^{(0)}(\mathbf{x}, t) + \mathrm{Ma}^2 p^{(1)}(\mathbf{x}, t) + \mathcal{O}(\mathrm{Ma}^4), \tag{F.5c}$$

$$T(\mathrm{Ma}^2, \mathbf{x}, t) = T^{(0)}(\mathbf{x}, t) + \mathrm{Ma}^2 T^{(1)}(\mathbf{x}, t) + \mathcal{O}(\mathrm{Ma}^4). \tag{F.5d}$$

Substituting these expansions into Eq. (F.1) and collecting like powers of Ma yields

$$\frac{\partial \rho^{(0)}}{\partial t} + \nabla \cdot \left(\rho^{(0)} \mathbf{u}^{(0)}\right) + \mathrm{Ma}^2 \left[\frac{\partial \rho^{(1)}}{\partial t} + \nabla \cdot \left(\rho^{(1)} \mathbf{u}^{(0)}\right) + \nabla \cdot \left(\rho^{(0)} \mathbf{u}^{(1)}\right)\right] + \mathcal{O}(\mathrm{Ma}^4) = 0 \tag{F.6}$$

The only way (F.6) holds for any value of Ma is if the coefficients are zero, i.e.,

$$\frac{\partial \rho^{(0)}}{\partial t} + \nabla \cdot \left(\rho^{(0)} \mathbf{u}^{(0)}\right) = 0, \tag{F.7a}$$

$$\frac{\partial \rho^{(1)}}{\partial t} + \nabla \cdot \left(\rho^{(1)} \mathbf{u}^{(0)}\right) + \nabla \cdot \left(\rho^{(0)} \mathbf{u}^{(1)}\right) = 0. \tag{F.7b}$$

Substituting the power series into (F.2) yields

$$\begin{aligned}
&\frac{1}{\gamma \mathrm{Ma}^2} \nabla p^{(0)} \\
&+ \rho^{(0)} \left(\frac{\partial \mathbf{u}^{(0)}}{\partial t} + (\mathbf{u}^{(0)} \cdot \nabla) \mathbf{u}^{(0)}\right) + \nabla p^{(1)} \\
&- \frac{1}{\mathrm{Re}} \nabla \cdot \left[\mu \left(\nabla \mathbf{u}^{(0)} + \nabla (\mathbf{u}^{(0)})^T - \frac{2}{3} (\nabla \cdot \mathbf{u}^{(0)}) \mathbf{I}\right)\right] - \frac{1}{\mathrm{We}} \mathbf{f}_\sigma \\
&+ \mathcal{O}(\mathrm{Ma}^2) = 0.
\end{aligned} \tag{F.8}$$

Again, setting the coefficients to zero gives

$$\nabla p^{(0)} = 0, \tag{F.9a}$$

$$\begin{aligned}
&\rho^{(0)} \left(\frac{\partial \mathbf{u}^{(0)}}{\partial t} + (\mathbf{u}^{(0)} \cdot \nabla) \mathbf{u}^{(0)}\right) = -\nabla p^{(1)} \\
&+ \frac{1}{\mathrm{Re}} \nabla \cdot \left[\mu \left(\nabla \mathbf{u}^{(0)} + \nabla (\mathbf{u}^{(0)})^T - \frac{2}{3} (\nabla \cdot \mathbf{u}^{(0)}) \mathbf{I}\right)\right] + \frac{1}{\mathrm{We}} \mathbf{f}_\sigma.
\end{aligned} \tag{F.9b}$$

Equation (F.9a) implies that $p^{(0)}$ is constant in space ($p^{(0)}(\mathbf{x}, t) = p^{(0)}(t)$), and is interpreted $p^{(0)}$ is constant in space as the thermodynamic pressure, which is the pressure that appears in the equation of state (Eq. (F.4)). The other pressure, $p^{(1)}$, is the dynamic pressure that is familiar to those that work in incompressible flows. Substituting Eqs. (F.5) into Eq. (F.3) gives

$$\rho^{(0)}c_p\frac{DT^{(0)}}{Dt}-\frac{\gamma-1}{\gamma}\frac{\mathrm{d}p^{(0)}}{\mathrm{d}t}-\frac{1}{\mathrm{RePr}}\left[\nabla\cdot\left(k\nabla T^{(0)}\right)\right]+\frac{1}{\mathrm{Ste}}\dot{m}'''+\mathcal{O}(\mathrm{Ma}^2)=0. \tag{F.10}$$

Collecting like terms in Ma^2 and equating the coefficients to zero gives the zeroth-order thermal energy balance equation:

$$\rho^{(0)}c_p\frac{DT^{(0)}}{Dt}=\frac{\gamma-1}{\gamma}\frac{\mathrm{d}p^{(0)}}{\mathrm{d}t}+\frac{1}{\mathrm{RePr}}\left[\nabla\cdot\left(k\nabla T^{(0)}\right)\right]-\frac{1}{\mathrm{Ste}}\dot{m}'''. \tag{F.11}$$

Here we emphasize that Eq. (F.11) governs the temperature field in both the gas and liquid phase. The temperature equation for the gas phase can be obtained by dropping the source term at the interface to give

$$\rho^{(0)}c_p\frac{DT^{(0)}}{Dt}=\frac{\gamma-1}{\gamma}\frac{\mathrm{d}p^{(0)}}{\mathrm{d}t}+\frac{1}{\mathrm{RePr}}\left[\nabla\cdot\left(k\nabla T^{(0)}\right)\right], \tag{F.12}$$

and the temperature equation for the liquid phase is obtained by taking $\gamma=1$

$$\rho^{(0)}c_p\frac{DT^{(0)}}{Dt}=\frac{1}{\mathrm{RePr}}\left[\nabla\cdot\left(k\nabla T^{(0)}\right)\right]. \tag{F.13}$$

Our task now is to obtain an expression for $\nabla\cdot\mathbf{u}^{(0)}$ in the gas phase. We first take the material derivative of the equation of state (Eq. (F.4)) to obtain expression for dp^0/dt

$$\frac{dp^{(0)}}{dt}=\frac{T^{(0)}}{\overline{M}}\frac{D\rho^{(0)}}{Dt}+\frac{\rho^{(0)}}{\overline{M}}\frac{DT^{(0)}}{Dt}-\frac{\rho^{(0)}T^{(0)}}{\overline{M}^2}\frac{D\overline{M}}{Dt}. \tag{F.14}$$

Then by using the continuity equation (F.7a) in (F.14) and writing $D\overline{M}/Dt$ for a binary mixture, we obtain

$$\nabla\cdot\mathbf{u}^{(0)}=-\frac{1}{p^{(0)}}\frac{dp^{(0)}}{dt}+\frac{1}{T^{(0)}}\frac{DT^{(0)}}{Dt}+\overline{M}\left(\frac{1}{M_v}-\frac{1}{M_a}\right)\frac{DY_v}{Dt}. \tag{F.15}$$

Appendix G

LOW MACH NUMBER FORMULATION IN A CLOSED DOMAIN

In a periodic or closed domain, the velocity field is subject to the following kinematic constraint

$$\int_{\mathcal{V}} \nabla \cdot \mathbf{u}^{(0)} \; \mathrm{d}\mathcal{V} = 0, \tag{G.1}$$

which states that the rate of change of the volume of the control volume is zero. In other words, all the sources and sinks of volume must sum to zero. In the present gas-liquid flow, there are two sources and sinks of $\nabla \cdot \mathbf{u}^{(0)}$ in the domain. The first is expansion (compression) due to evaporation (condensation) at the interface, and the other is the corresponding compression (expansion) in the gas phase such that the total volume is constant. Adding these two sources and sinks yields

$$\begin{aligned} &\int_{\mathcal{V}} \frac{1}{\mathrm{Re\ Sc}} \dot{m} \left(\frac{1}{\rho_g} - \frac{1}{\rho_l} \right) \; \mathrm{d}\mathcal{V} \\ &+ \int_{\mathcal{V}_g} \left[-\frac{1}{p^{(0)}} \frac{dp^{(0)}}{dt} + \frac{1}{T^{(0)}} \frac{DT^{(0)}}{Dt} + \overline{M} \left(\frac{1}{M_v} - \frac{1}{M_a} \right) \frac{DY_v}{Dt} \right] \mathrm{d}\mathcal{V} = 0. \end{aligned} \tag{G.2}$$

By noting that $p^{(0)} = p^{(0)}(t)$, we can obtain an ordinary differential equation for $\mathrm{d}p^{(0)}/\mathrm{d}t$

$$\begin{aligned} \frac{\mathrm{d}p^{(0)}}{\mathrm{d}t} = \frac{p^{(0)}}{\mathcal{V}_g} \Bigg\{ &\int_{\mathcal{V}} \frac{1}{\mathrm{Re\ Sc}} \dot{m} \left(\frac{1}{\rho_g} - \frac{1}{\rho_l} \right) \; \mathrm{d}\mathcal{V} \\ &+ \int_{\mathcal{V}_g} \left[\frac{1}{T^{(0)}} \frac{DT^{(0)}}{Dt} + \overline{M} \left(\frac{1}{M_v} - \frac{1}{M_a} \right) \frac{DY_v}{Dt} \right] \mathrm{d}\mathcal{V} \Bigg\} \end{aligned} \tag{G.3}$$

Analyzing Eq. (G.3), we note that if there is no phase change ($\dot{m} = 0$), the flow is isothermal ($DT/Dt = 0$), and there is no mass transport due to species diffusion ($M_v/M_a = 1$ or $DY_v/Dt = 0$) then the thermodynamic pressure remains constant ($\mathrm{d}p^{(0)}/\mathrm{d}t = 0$).